Measurement of π^0 and η mesons in pp collisions at $\sqrt{s} = 13$ TeV with ALICE Photon Spectrometer at CERN Large Hadron Collider

PhD Thesis

Oleksandr Kovalenko

Supervisor: Prof. dr hab. Teodor Siemiarczuk

National Centre for Nuclear Research
Warsaw, Poland

February 2020

Abstract

The goal of this thesis was the measurement and the analysis of π^0 and η mesons spectra in pp collisions at $\sqrt{s} = 13$ TeV with the highly segmented ALICE photon spectrometer at the CERN Large Hadron Collider. These are the first measurements of light, neutral mesons at the highest energy ever attained in the Collider experiments.

The potential of using the π^0 and η spectra extends from testing the QCD and setting constraints on the theoretical models in both perturbative and nonperturbative regimes, to bettering the Monte-Carlo event generators and evaluating the reference distributions for direct photon studies.

The data presented in this thesis were taken in 2016–2018. The quality and stability of the data were studied on a run-by-run basis. Only the runs satisfying the stringent quality criteria, 1.5 billion pp collisions in total, were taken for further analysis.

The π^0 and η meson spectra were reconstructed up to 20 GeV/c transverse momentum via the two-photon decay channels: $\pi^0 \to \gamma\gamma$, $\eta \to \gamma\gamma$. The π^0 and η yields were extracted by integrating the background-subtracted $\gamma\gamma$ invariant mass distribution in subsequent p_{T} intervals. The detailed study of various corrections and different sources of systematic uncertainties is described.

The obtained invariant differential cross-sections were compared with Tsallis and Two-Component-Model predictions. The latter did somewhat better in the entire range of the transverse momentum, confirming the observations at lower energies. The PYTHIA 6 describes our π^0 data reasonably well for p_{T} larger than 7 GeV/c but overpredicts the yield at lower transverse momenta. For the η meson, PYTHIA 6 overpredicts low-p_{T} momentum yields and underpredicts the high-momentum part of the spectrum. The η/π^0 yield ratio was studied as a function of the transverse momentum and compared with the lower energy ratios compiled for this analysis in the 13.6 GeV $< \sqrt{s} <$ 13 TeV energy interval. The η/π^0 ratio exhibits remarkable similarity in the entire energy range studied with a common saturation value of about 0.46. The pQCD calculations using CTEQ parton distribution function and available fragmentation functions, extracted from the LEP data, significantly overpredicted our results. The $\sqrt{s} = 13$ TeV pp data together with our other LHC pp measurements were used to calculate the x_{T}-scaling exponent n. The obtained value $n \sim 5$ is in agreement with pQCD calculations. We also tested our 13 TeV data for m_{T}-scaling, and no significant departure from its predictions was observed.

Streszczenie

Celem pracy był pomiar i analiza widm mezonów π^0 i η w zderzeniach pp przy energii $\sqrt{s} = 13$ TeV z użyciem spektrometru fotonów o wysokiej rozdzielczości w eksperymencie ALICE w CERN na Dużym Zderzaczu Hadronów. Są to pierwsze pomiary produkcji lekkich, neutralnych mezonów przy najwyższej energii, jaką kiedykolwiek osiągnięto w eksperymentach na zderzaczach.

Potencjał wykorzystania widm π^0 i η rozciąga się od testowania QCD i nałożenia ograniczeń na modele teoretyczne w reżimach zarówno perturbacyjnym jak i nieperturbacyjnym, do ulepszenia generatorów zdarzeń metodą Monte-Carlo i konstrukcji rozkładów referencyjnych dla badań fotonów bezpośrednich.

Dane przedstawione w pracy zostały zebrane w latach 2016–2018. Jakość i stabilność danych zbadano na zasadzie "run-by-run". Tylko pomiary spełniające rygorystyczne kryteria jakości, łącznie 1.5 miliarda zderzeń pp, wzięto do dalszej analizy. Widma mezonów π^0 i η zrekonstruowano w obszarze pędu poprzecznego do 20 GeV/c przy pomocy kanałów rozpadu na dwa fotony: $\pi^0 \to \gamma\gamma$ i $\eta \to \gamma\gamma$. Przekroje różniczkowe mezonów π^0 i η otrzymano poprzez całkowanie rozkładu masy efektywnej $\gamma\gamma$ w kolejnych przedziałach p_{T} po odjęciu tła. W pracy przedstawiono szczegółowy opis wyznaczenia poprawek i błędów systematycznych.

Uzyskane niezmiennicze różniczkowe przekroje czynne porównano z rozkładem Tsallisa i przewidywaniami modelu dwuskładnikowego. Ten ostatni wypadł nieco lepiej w całym zakresie pędu poprzecznego, potwierdzając obserwacje przy niższych energiach. PYTHIA 6 dość dobrze opisuje widmo π^0 dla $p_{\mathrm{T}} > 7$ GeV/c, ale przewiduje większy przekrój czynny przy małych pędach poprzecznych. W przypadku mezonu η, PYTHIA 6 daje za duże przekroje czynne przy niskich i za małe przy wysokich pędach poprzecznych. Zbadano stosunek widm η/π^0 w funkcji pędu poprzecznego i porównywano z wynikami przy niższych energiach zestawionych dla tej analizy w przedziale 13.6 GeV $< \sqrt{s} <$ 13 TeV. Stosunek η/π^0 wykazuje duże podobieństwo w całym badanym zakresie energii ze wspólna wartością nasycenia około 0.46. Obliczenia pQCD z wykorzystaniem funkcji rozkładu partonów CTEQ i dostępnej funkcji fragmentacji, uzyskanej z danych LEP, znacząco przewyższały nasze wyniki. Pomiary dla $\sqrt{s} = 13$ TeV pp wraz z naszymi wcześniejszymi pomiarami na LHC przy niższych energiach zostały użyte do obliczenia wykładnika n skalowania w zmiennej x_{T}. Uzyskana wartość $n \sim 5$ jest zgodna z obliczeniami pQCD. Przetestowaliśmy występowanie skalowania w masie poprzecznej m_{T} w naszych danych pp przy $\sqrt{s} = 13$ TeV. Nie zaobserwowano znaczącego odstępstwa od przewidywań skalowania.

Contents

1 Introduction **4**
- 1.1 Standard Model . . . 4
- 1.2 Quantum Chromodynamics . . . 5
- 1.3 Measurements of neutral mesons . . . 7
- 1.4 Particle Production in High Energy Collisions . . . 8
  - 1.4.1 Particle distribution functions . . . 9
  - 1.4.2 Fragmentation functions . . . 10
- 1.5 Experimental results . . . 12
  - 1.5.1 Results from RHIC . . . 12
  - 1.5.2 The most recent results from the LHC . . . 13
  - 1.5.3 m_{T} scaling . . . 17
  - 1.5.4 x_{T} scaling . . . 19
- 1.6 Physics motivation . . . 21

2 Setup **23**
- 2.1 The Large Hadron Collider . . . 23
- 2.2 ALICE experiment . . . 25
- 2.3 Detectors . . . 27
  - 2.3.1 VZERO (V0) . . . 27
  - 2.3.2 Inner Tracking System (ITS) . . . 27
  - 2.3.3 The Time Projection Chamber (TPC) . . . 28
  - 2.3.4 Trigger system . . . 30
  - 2.3.5 The PHOton Spectrometer (PHOS) . . . 31

3 Analysis **35**
- 3.1 Data Condition . . . 35
  - 3.1.1 Beam Condition . . . 35
  - 3.1.2 Event selection . . . 36
  - 3.1.3 Run selection . . . 36
  - 3.1.4 Channel selection . . . 38
- 3.2 Neutral meson reconstruction . . . 39
  - 3.2.1 Cluster selection . . . 39
  - 3.2.2 Raw yield extraction . . . 40
  - 3.2.3 Timing cut efficiency . . . 45
  - 3.2.4 Reconstruction efficiency . . . 48
  - 3.2.5 Feed-down correction . . . 53
  - 3.2.6 Corrected yield . . . 56

4 Evaluation of systematic uncertainties **58**
- 4.1 Raw yield extraction algorithm . . . 58
- 4.2 Nonlinearity of PHOS energy response . . . 61
- 4.3 Acceptance . . . 63
- 4.4 Time of flight cut . . . 64

4.5 Material budget . . . 65
4.6 Feed-down correction . . . 65
4.7 Global energy scale . . . 65
4.8 Summary of systematic uncertainties . . . 68

5 Experimental distributions and their properties 70
5.1 Comparison with the lower LHC energies . . . 70
5.2 Phenomenological description . . . 71
5.3 Comparison with the pQCD calculations . . . 80
5.4 η/π^0 ratio . . . 82
5.5 m_{T}-scaling . . . 85
5.6 x_{T} scaling . . . 87

6 Conclusions and outlook 91

A List of good runs 93
A.1 LHC16 . . . 93
A.2 LHC17 . . . 95
A.3 LHC18 . . . 98

B PHOS QA plots: Cluster Averages 101
B.1 LHC16 . . . 101
B.2 LHC17 . . . 106
B.3 LHC18 . . . 111

C Invariant mass fits of pp data at $\sqrt{s} = 13$ TeV 117

D Invariant mass fits of Single Particle Monte-Carlo 120

Chapter 1

Introduction

The goal of this thesis is to report the first measurements of π^0 and η meson spectra in pp collisions obtained at CERN LHC at $\sqrt{s} = 13$ TeV, the highest energy attained so far in colliders. This chapter gives a brief overview of the theoretical aspects and experimental results on hadron spectroscopy. The discussion starts with a short introduction to the theory of elementary particles, the Standard Model.

1.1 Standard Model

The theory that describes strong, electromagnetic and weak interactions of elementary particles is called the Standard Model (SM). According to this theory, all particles can be divided into two categories: the force carriers and the matter.

The gauge bosons belong to the first type of particles. They have integer spins, and they mediate the interactions. For example, electromagnetic interactions between charged particles are governed by photons. The particles of different flavours that interact weakly exchange the massive bosons $W^{\pm}$ and Z^0. The strong interaction occurs between colour-charged particles and is mediated by massless gluons. The recent discovery of Higgs Boson at LHC [1, 2] confirms the existence of corresponding fields predicted by SM. The Higgs mechanism is the way to explain the masses of $W^{\pm}$ and Z^0 bosons. This discovery proved SM to be a self-consistent theory of interaction of elementary particles.

The second type of particles consists of quarks and leptons. They are the building blocks of the universe in the sense that all visible matter consists of these particles. Both quarks and leptons have half-integer spins and come in three generations consisting of two quarks, two leptons and their antiparticles. The first generation consists of up (u), down (d) quarks, electron, and an electron neutrino. They are the lightest fermions. The second generation consists of charm(c), strange(s) quarks, muon, and a muon neutrino. The third generation consists of bottom(b), top (t) quark, tau and tau neutrino. Each antiparticle has the same mass, opposite electric charge, and opposite additive quantum numbers (such as strangeness, baryon number, lepton number etc.). The elementary particles together with their properties are summarised in Fig. 1.1.

Quarks are confined inside colourless structures called hadrons. It is a broad class of particles that participate in strong interactions. The simplest hadrons, mesons, consist of quark-antiquark pairs. They were introduced by Yukawa to describe the forces that keep protons inside the nuclei. Protons and neutrons themselves are examples of three-quark structures called baryons. The baryonic number is a special quantum number that indicates the quark-contents of a particle. The baryon number of every meson is 0 whereas the baryonic number of baryons is 1. Most of the visible matter is composed of baryons.

There are still several phenomena that can not be explained by the SM: the problem of quantisation of gravity, the problem of dark matter and dark energy, the asymmetry between matter and anti-matter as in the observed universe, the problem of neutrino mass (according to the SM the neutrino mass is 0, which contradicts the observation of neutrino

oscillations which implies that the neutrino mass is larger than 0 [3]). There are many possible extensions beyond the Standard Model proposed to explain these issues. These theories are being tested in the proton-proton collisions at the Large Hadron Collider (LHC) [4].

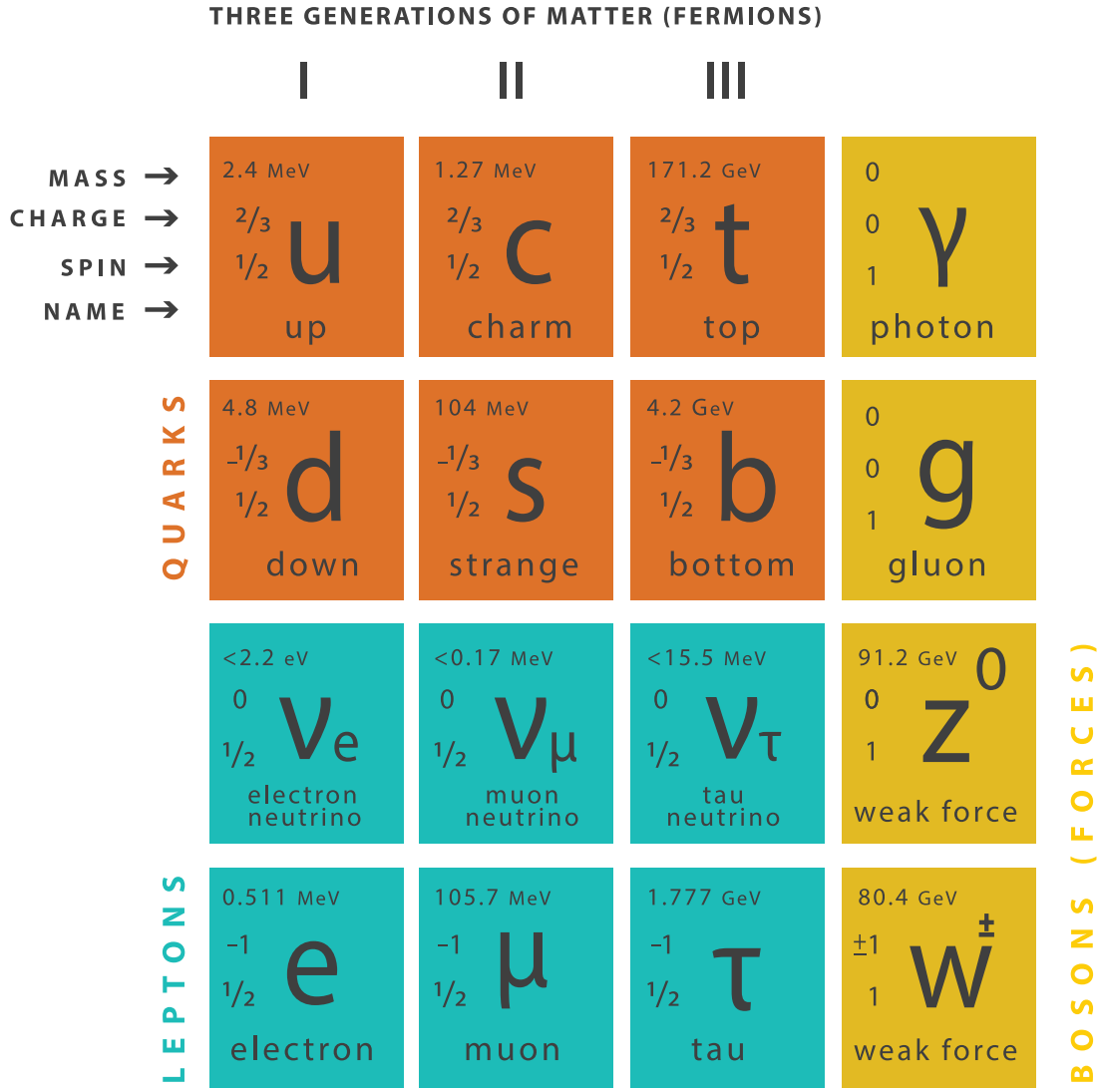

Figure 1.1: The elementary particles of the Standard Model.

The theories of electromagnetic and weak forces provide precise calculations of the corresponding physical processes. Their predictions were confirmed with high accuracy. At the same time, the theory of strong interactions still needs to be studied in more details due to its internal complexity. The following sections introduce the theoretical framework that describes physical processes governed by the strong force.

1.2 Quantum Chromodynamics

The strong interaction is the most intensive fundamental force at the scale of the order of 1 femtometer (10^{-15} m). According to the Standard Model, the strong interactions are described by quantum chromodynamics (QCD) which considers quarks and gluons as constituents of the hadronic matter. The QCD is defined by the following Lagrangian density:

$$\mathcal{L}_{\text{QCD}} = \bar{\psi}_i \left(i(\gamma^\mu D_\mu)_{ij} - m\,\delta_{ij} \right) \psi_j - \frac{1}{4} G^a_{\mu\nu} G^{\mu\nu}_a,$$

where $\psi_i(x)$ is the quark fields, in the fundamental representation of the SU(3) group; the latin indices i, j correspond to quarks; D_μ is the covariant derivative; the γ_μ are Dirac matrices. The symbol $G^a_{\mu\nu}$ is a gluon field strength tensor. It is defined in the following way:

$$G^a_{\mu\nu} = \partial_\mu \mathcal{A}^a_\nu - \partial_\nu \mathcal{A}^a_\mu + g f^{abc} \mathcal{A}^b_\mu \mathcal{A}^c_\nu \,,$$

where $\mathcal{A}^a_\mu(x)$ are the gluon fields in the adjoint representation of the SU(3) group, indexed by a, b, c and g is the gaugle coupling parameter. The symbols f_{abc} are the structure constants of SU(3) that define connections between generators T^X of the group

$$[T^a, T^b] = i f_{abc} T^c.$$

The strength of any interaction is defined by its coupling constant. The coupling constant of strong interactions $\alpha_s \equiv g/4\pi$ can be described as a function of the renormalization scale μ_R^2. It should satisfy the renormalisation group equation in order to describe a physical system in terms of the β-function:

$$\mu_R^2 \frac{\partial \alpha_s(\mu_R)}{\partial \mu_R} = \beta(\alpha_s) = -\frac{\beta_0}{2\pi}\alpha_s^2 - \frac{\beta_1}{2\pi^2}\alpha_s^3 - \frac{\beta_2}{2\pi^3}\alpha_s^4 + \ldots$$

In perturbative QCD renormalization scale μ_R^2 is chosen to be equal to the square four-momentum transfer Q^2. Therefore the coupling constant of strong interactions α_s depends on Q^2, and for its large values, the following approximation becomes accurate:

$$\alpha_s(Q^2) \approx \frac{12\pi}{(33 - 2n_f)\log\left(Q^2/\Lambda^2_{\mathrm{QCD}}\right)},$$

where n_f is the number of quark flavours, Λ_{QCD} is the QCD scale a free parameter of the theory. This parameter can not be calculated by means of QCD and the numerical value of $\Lambda_{\mathrm{QCD}} \approx 200$ MeV was obtained in the experiment [5].

The approximation indicates that the coupling constant decreases as a function of the momentum transfer. For large Q^2 values, the coupling constant α_s asymptotically approaches 0. This effect is called "asymptotic freedom". It is a distinctive trait of strong interactions. In contrast, the coupling constant α_s increases at low Q^2. This makes it impossible to apply perturbative calculations for the systems with low four-momentum transfer.

Yet another important feature of the strong interactions is "colour confinement". The phenomenological potential of quark-quark interaction at a distance r can be written in the following way:

$$V_s(r) = \frac{4}{3}\frac{\alpha_s \hbar c}{r} + kr.$$

This potential and hence the magnitude of the corresponding force increases with r. It is possible to increase the distance between quarks by applying external forces. This will create a strong tension between the particles. When the energy of such tension becomes twice as large as the rest mass of a quark, a new particle-antiparticle pair will be created. For these reasons, quarks can not be separated. This fact agrees with the experiments in which we observe only colourless quark structures [5].

The study of the properties of quarks and gluons is a very challenging problem as it is impossible to isolate a single parton and determine the properties of free particles. At the same time, the hadron spectrometry gives a natural possibility to study the dynamics of strong interactions. The inclusive cross-sections can be measured with high accuracy experimentally, and the very same quantities can be derived from the perturbative QCD calculations. The next sections of this chapter describe the theoretical framework and the most recent results on the spectrometry of light neutral mesons.

1.3 Measurements of neutral mesons

The experimental part of this thesis is devoted to the measurements of the light neutral meson spectra. This section gives a historical overview of the discovery of π^0 and η mesons and their properties.

The neutral particles do not have an electrical charge, and they do not leave tracks in detectors. This complicates the detection of such particles in experiments. The neutral pion was discovered in cyclotron experiments in 1950 via double photon decay channel [6]. The masses of charged pions and the π^0 are nearly identical. Their numeric values were measured with high precision and are 139.57061 ± 0.00024 MeV/c^2 and 134.9770 ± 0.0005 MeV/c^2 for charged and neutral pions, respectively [7]. Neutral pion is the lightest known meson.

Each pion has the same quark content and therefore the same isospin value $I = 1$. The wave functions of the particles are combinations of u and d quark-antiquark states that correspond to different eigenvalues of the third component of isospin ($I_3 = 1, 0, -1$). Neutral and charged pions from an isospin triplet which corresponds to an adjoint representation of $SU(2)$ group. The π^0 wave function can be written as the linear combination of $u\bar{u}$ and $d\bar{d}$ states:

$$\pi^0 = \frac{1}{\sqrt{2}} \left(u\bar{u} - d\bar{d} \right).$$

Such definition follows from the quark model directly as it is a unique way to represent electrically neutral, colorless state with zero spin and odd spatial parity composed only of u and d quarks.

The η meson was discovered in 1961 at the Bevatron accelerator [8] in Lawrence Berkeley National Laboratory. It was reconstructed in the $\eta \to \pi^+ + \pi^- + \pi^0$ decay channel [9]. This particle has zero spin, no electric charge and is ~ 4 times heavier than the π^0. The measurements report $m_\eta = 547.862 \pm 0.017$ MeV/c^2 [7]. The large mass indicates that besides u, d quarks it contains strange quark-antiquark combinations. The quark theory predicts the existence of two states that have zero strangeness and electric charge:

$$\eta_1 = \frac{1}{\sqrt{3}} \left(u\bar{u} + d\bar{d} + s\bar{s} \right)$$

and

$$\eta_8 = \frac{1}{\sqrt{6}} \left(u\bar{u} + d\bar{d} - 2s\bar{s} \right).$$

These states are not observed experimentally due to the contribution of weak iteraction. It is responsible for the quark flavour transition. The measured particle state corresponds to the linear combination of eigenstates

$$\begin{pmatrix} \eta \\ \eta' \end{pmatrix} = \begin{pmatrix} \cos\theta_{\mathrm{P}} & -\sin\theta_{\mathrm{P}} \\ \sin\theta_{\mathrm{P}} & \cos\theta_{\mathrm{P}} \end{pmatrix} \begin{pmatrix} \eta_8 \\ \eta_1 \end{pmatrix},$$

where $\theta_{\mathrm{P}} = -11.5^\circ$ is a pseudoscalar mixing angle [7]. The π^0, η_8 and η_1 states are mutually orthogonal states that describe mesons with zero electric charges and zero strangeness. Mesons that contain u, d, and s quark form an octet of pseudoscalar mesons. These particles have zero spin and odd spatial parity. Charged and neutral pions, kaons, η and η' form a nonet of light pseudoscalar mesons. These particles have different masses, electric charge Q and strangeness S. The corresponding wave functions form the flavour symmetry group which belongs to the adjoint representation of $SU(3)$. Neutral pions and η mesons have even C parity. This means that they are their own antiparticles.

The quantum properties of neutral π^0 and η mesons are well studied in low energy experiments [7]. These particles are copiously produced in hadron-hadron collisions, and

hence the mesons themselves can be used as a tool to study the particle production mechanisms and dynamics of the collisions. The following chapters give an introduction to the theoretical description of the neutral-meson spectra in hadron-hadron collisions. The subsequent sections present a brief overview of the experimental results on π^0 and η meson measurements.

1.4 Particle Production in High Energy Collisions

The hadron production at high energies can be calculated by means of quantum chromodynamics. The matrix elements of such processes involve long-range interactions. The factorisation theorem needs to be used to decompose the cross-section of a QCD process into separate matrix elements that come from different subprocesses. The theorem applies to the domain of perturbative QCD which corresponds to a particle production with a high four-momentum transfer.

The inclusive hadron production in hadron-hadron hard scattering can be symbolically written as:

$$\mathrm{A} + \mathrm{B} \rightarrow h_\mathrm{C} + \mathrm{X},$$

where A and B are the incoming particles, X denotes all the particles in the final state that are not measured in the experiment and h_C is a generated particle that is measured in the experiment. According to factorisation theorem, the cross-section of such a process can be written as:

$$d\sigma^{\mathrm{AB}\rightarrow h_\mathrm{C}\mathrm{X}} = f_a(x_a,\mu^2) \otimes f_b(x_b,\mu^2) \otimes d\hat{\sigma}_{ab\rightarrow cx} \otimes D_c^{h_\mathrm{C}}(z_c,\mu^2), \tag{1.1}$$

where $f_a(x_a,\mu^2)$ is the parton distribution function that has a meaning of the probability to find a parton a with the momentum fraction x_a ($x_a = p_a/p_A$) inside a hadron A, $f_b(x_b,\mu^2)$ has the same meaning but corresponds to another incoming hadron B, $d\hat{\sigma}_{ab\rightarrow c\mathrm{x}}$ term denotes the corss-section of the interaction between partons a and b with production of c. The last term $D_c^{h_\mathrm{C}}(z_c,\mu^2)$ is a fragmentation function (FF). It has the meaning of the probability for a parton c to form a hadron h_C with the momentum fraction $z_c = p_h/p_c$.

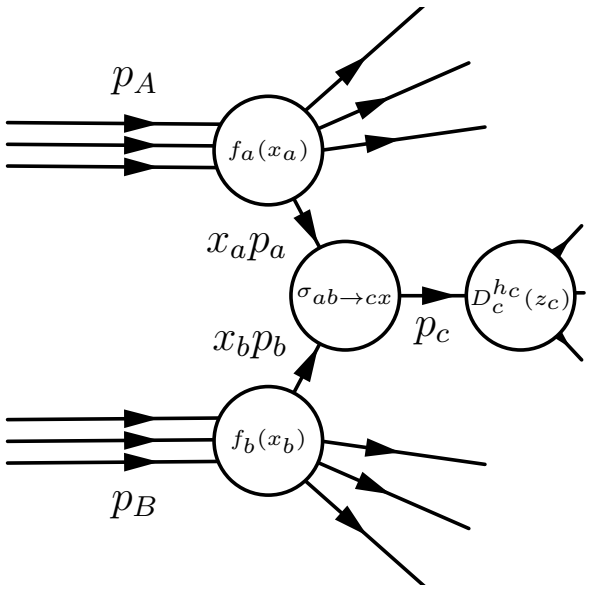

Figure 1.2: The process of generation of hadron C in A and B collisions.

The formula above (1.1) factorizes the parton distribution functions $f(x,\mu^2)$ and fragmentation functions $D_{h_\mathrm{C}}(z,\mu^2)$. They correspond to the long-range interactions and can not be computed within the framework of perturbative chromodynamics. Whereas

$d\hat{\sigma}_{ab\to cx}$ corresponds to the parton-parton interactions such as quark-quark scattering $q_1 + q_2 \to q_1 + q_2$, quark-antiquark anihilation $q + \bar{q} \to q + g$ and quark-gluon Compton scattering $q + g \to \gamma g$. The cross-sections of these processes can be obtained from the Feynman rules.

From the above one follows that the precise knowledge of parton distribution and fragmentation functions is vital to describe single-particle spectra. These functions can be extracted from the experimental data on deep inelastic scattering and inclusive hadron spectra measured so far.

1.4.1 Particle distribution functions

The cross-section of Deep Inelastic Scattering (DIS) can be written in the following form:

$$\frac{d\sigma}{d\Omega dE} = \left(\frac{d\sigma}{d\Omega}\right)_{\text{Mott}} \cdot \left(W_2(\nu, Q^2) + 2W_1(\nu, Q^2)\tan^2\theta/2\right),$$

where $\left(\frac{d\sigma}{d\Omega}\right)_{\text{Mott}}$ is the corss-section of Mott scattering, $W_1(x, Q^2)$ and $W_2(x, Q^2)$ are the structure functions, θ and E are the scattered angle and energy of the electron. Kinematic variables Q^2 and ν denote squared four-momentum transfer and energy loss of the electron, respectively. In the Bjorken limit, for infinitely high values of Q^2 and ν under condition $Q^2/\nu \approx$ constant, the structure functions depend on a Bjorken x-variable:

$$W_1(Q^2, \nu) = F_1(x), \quad \nu W(Q^2, \nu) = MF_2(x).$$

The Bjorken variable x describe the momentum fraction of incoming hadron carried out by its parton. It is defined in the following way:

$$x = \frac{Q^2}{2M \cdot \nu}.$$

This definition implies no Q^2 dependence in the Bjorken limit, which is known as Bjorken scaling. This corresponds to the situation when a nucleon is composed of point-like particles that carry momentum fraction x of the entire nucleon. For point-like paritlces with spin 1/2 the sctructure functions $F_1(x)$ and $F_2(x)$ are not independent. This is known as Callan-Gross relation [10]:

$$2xF_1(x) = F_2(x).$$

The SLAC-MIT group has studied $2xF_1/F_2$ ratio. Their measurement showed that this ratio is consistent with unity within the uncertainties of the experiment [11]. This result confirms the hypothesis that nucleons consist of point-like particles with spin 1/2. These particles are referred to as "partons", and therefore the model is known as "parton model".

The QCD higher-order corrections violate the Bjorken-scaling. Perturbative QCD allows computing these effects by means of Dokshitzer–Gribov–Lipatov–Altarelli–Parisi (DGLAP) equations [12, 13]. In fact, the data show that structure-function exhibits Q^2 dependence at low x and can be well described by the theory. The structure-functions can be written in terms of Parton Distribution Functions (PDFs):

$$F_2(x, Q^2) = x\sum_q e_q \left(f_q(x, Q^2) + \bar{f}_q(x, Q^2)\right),$$

where the sum runs over partons (quarks and gluons), $f_q(x, Q^2)$ corresponds to the probability to find a parton in a nucleon that carries momentum fraction x. The functions $f_q(x, Q^2)$ can be obtained experimentally from the DIS data in lepton-lepton and lepton-hadron collisions. Usually, they are measured for the limited Q^2 and x regions. To extend

the PDFs for the entire phase space, these distributions are substituted with parametrisations that can be estimated from fitting. The MSTW collaboration has done such calculations. They obtained the parton distribution functions as a function of x for a fixed value of Q^2 [14]. The example of PDFs at different momentum transfers $Q^2 = 10$ GeV^2 and $Q^2 = 10^4$ GeV^2 are shown in Fig. 1.3.

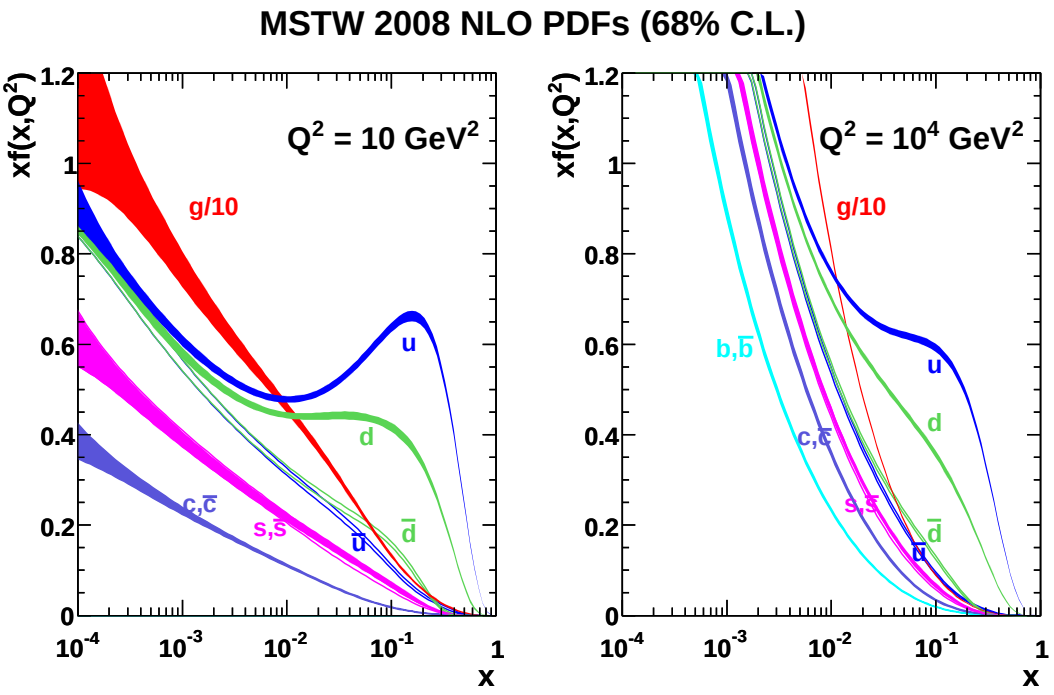

Figure 1.3: The Parton Distribution Function for gluon and different quark flavours as calculated by NNLO pQCD with DGLAP evolution equation. The figure is taken from [14].

The gluon contribution dominates at the low x region since these particles are massless and they can emit new gluons themselves. Such type of processes is described by QCD as the Feynman rules for this theory allow self-interactions of gluon fields.

Nuclear environment modifies the parton distribution functions. Therefore probability to find a parton inside a nucleus A is given by

$$f_q^A(x, Q^2) = R_q^A(x, Q^2) f_q(x, Q^2),$$

where $R_q^A(x, Q^2)$ is the nucleus modification factor. It takes into account the different effects in the bound nucleon.

1.4.2 Fragmentation functions

In the high energy collisions, the partons that undergo interactions with high four-momentum transfer (large values of Q^2) can be scattered into opposite directions. As colour confinement forbids existing coloured structures outside hadrons, the scattered partons produce more coloured particles to form hadrons. These hadrons are observed along the paths of incoming particles. The process of creating new particles is called hadronisation and a group of hadrons located in a small solid angle that corresponds to a scattered parton is known as "jet". The longitudinal momenta of hadrons in a jet are proportional to the momenta of the generating partons whereas their transverse momenta are small being of the order of hundreds MeV. Jets that are formed from quarks and gluons have a different width. The radius of the gluon jet is larger as gluon fields have a larger probability of forming new particles.

Quantitatively hadronisation is described by "Fragmentation Function" (FF). It is denoted as $D_f^h(z_{\mathrm{T}})$ and has a meaning of probability for a parton f to produce a hadron h that carries a fraction $z_{\mathrm{T}} = p_{\mathrm{T}}^h / p_{\mathrm{T}}^f$ of the original parton momentum.

The single-particle inclusive spectrum of hadron h can be expressed in terms of fragmentation functions

$$\frac{1}{\hat{p_{\mathrm{T}}}} \frac{d^2\sigma(\hat{p_{\mathrm{T}}}, z_{\mathrm{T}})}{d\hat{p_{\mathrm{T}}} dz_{\mathrm{T}}} = \frac{1}{\hat{p_{\mathrm{T}}}} \frac{d\hat{\sigma}}{d\hat{p_{\mathrm{T}}}} \times D_f^h(z_{\mathrm{T}}),$$

where p_{T} denotes the traverse momentum of the hadron, $\hat{p_{\mathrm{T}}}$ corresponds to the momentum of the initial parton which coincides with the jet transverse momentum, $d\hat{\sigma}/d\hat{p_{\mathrm{T}}}$ the initial parton spectrum which can be calculated in perturbative chromodynamics and $D_f^h(z_{\mathrm{T}})$ is the fragmentation function of the parton f. This equation shows that FFs can be obtained indirectly from the experimental data on single-particle production cross-section. Fragmentation functions can be also studied in e^+e^- collisions. They can be extracted from events containing two and more jets as the electrons and positrons can annihilate and create quark-antiquark pairs. Such pairs produce final-state hadrons and jets that can be measured in the experiment.

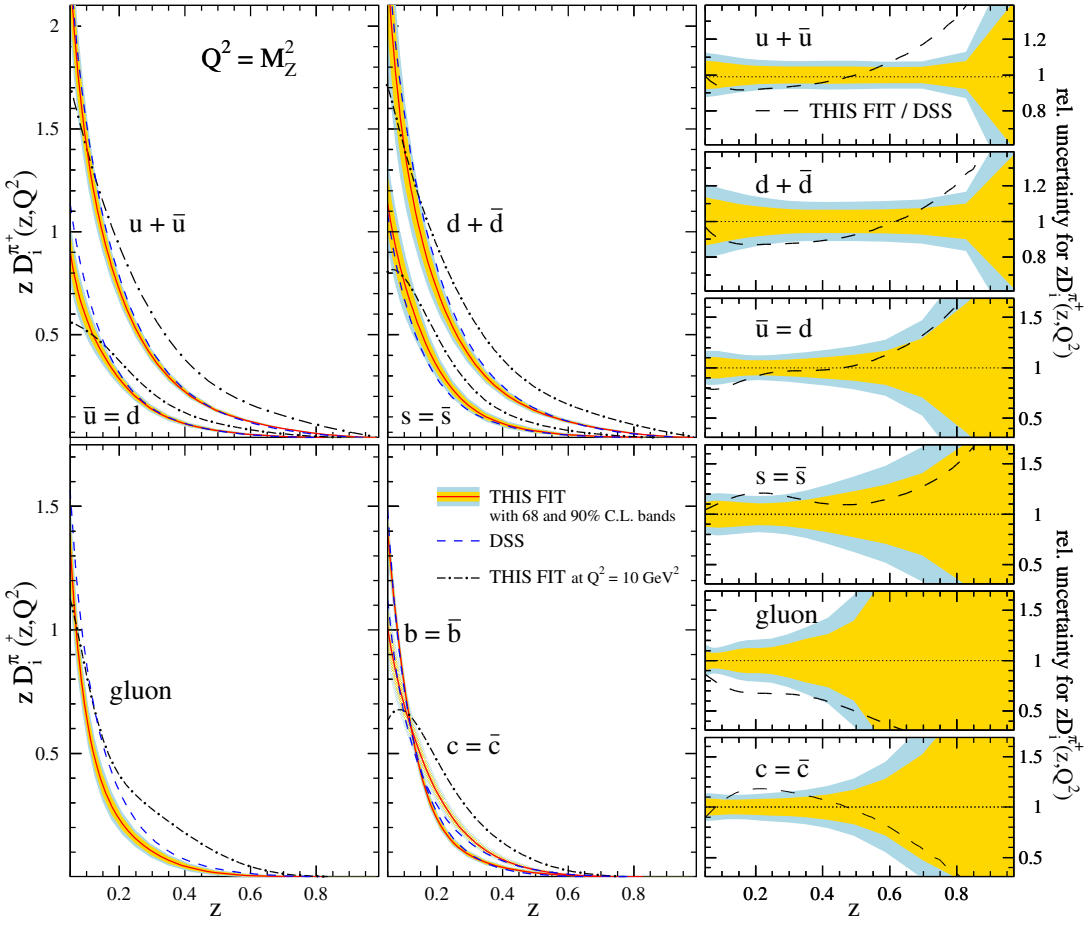

Figure 1.4: The Fragmentation Functions together with uncertainties calculated for charged pions in the DSS analysis. The figure is taken from [15].

The data on inclusive hadron, as well as jets production in e^+e^- collisions, are necessary to determine the fragmentation functions. Several phenomenological groups are working in this direction. One of the most famous analyses in this field was done by D. de Florian, R. Sassot and M. Stratmann (so-called DSS fit) [16, 17, 15]. The examples of the extracted fragmentation functions is shows in Fig. 1.4.

1.5 Experimental results

The inclusive neutral meson and photon spectra in high energy hadron-hadron collisions were studied at entergies from $\sqrt{s} = 13.8$ GeV up to $\sqrt{s} = 8$ TeV [18]. In this section, the overview is limited to the most recent measurements at $\sqrt{s} > 200$ GeV as those results are closely related to the subject of this thesis.

1.5.1 Results from RHIC

The PHENIX experiment at RHIC has measured light neutral mesons spectra in pp collisions at $\sqrt{s} = 200$ GeV and $\sqrt{s} = 510$ GeV. Their results show a good agreement with next-to-leading order pQCD calculations for neutral pions [19, 20, 21, 22]. The measurements at $\sqrt{s} = 200$ GeV were used as a baseline to study the suppression patterns in d–Au collisions at the same collision energy [23]. The reported invariant yields for π^0 and η mesons are shown in Fig. 1.5 for different centrality classes.

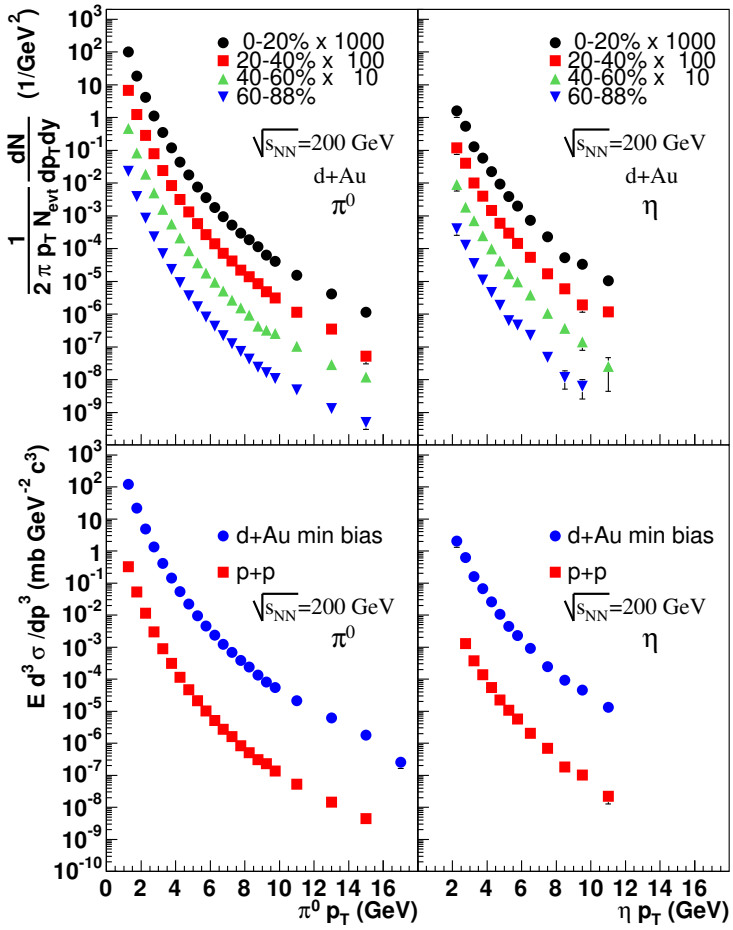

Figure 1.5: Top: invariant yields at for π^0 (left) and η (right) in d–Au collisions as a function of p_{T} for different centrality classses. Bottom: invariant cross section at mid-rapidity for π^0 (left) and η (right) in pp and d–Au collisions as a function of p_{T}. The figure is taken from [24].

The d–Au measurements show no modification of π^0 and η meson spectra with respect to the pp collisions [24]. In contrast, the data collected in Au–Au collisions at $\sqrt{s}_{\mathrm{NN}} = 200$ GeV show a strong suppression in particle production [25, 26, 27]. This agrees with the previous observations made for Au–Au system at $\sqrt{s}_{\mathrm{NN}} = 130$ GeV [28]. The inclusive particle spectra measured in pp collisions at RHIC served as an input for phenomenological analyses of light hadron spectra that will be presented later in this chapter.

1.5.2 The most recent results from the LHC

The ALICE experiment at CERN has measured the spectra of neutral mesons at $\sqrt{s}$ = 0.9, 2.76, 7 and 8 TeV [30, 31, 32, 33]. The neutral meson production cross-sections are shown in Fig. 1.6 The predictions of PYTHIA 8.2 Monte-Carlo generator [34] with Monash 2013 tune describe the data at high p_{T} but deviate from the data at moderate p_{T} at the higher energies. The perturbative QCD calculations in next-to-leading order

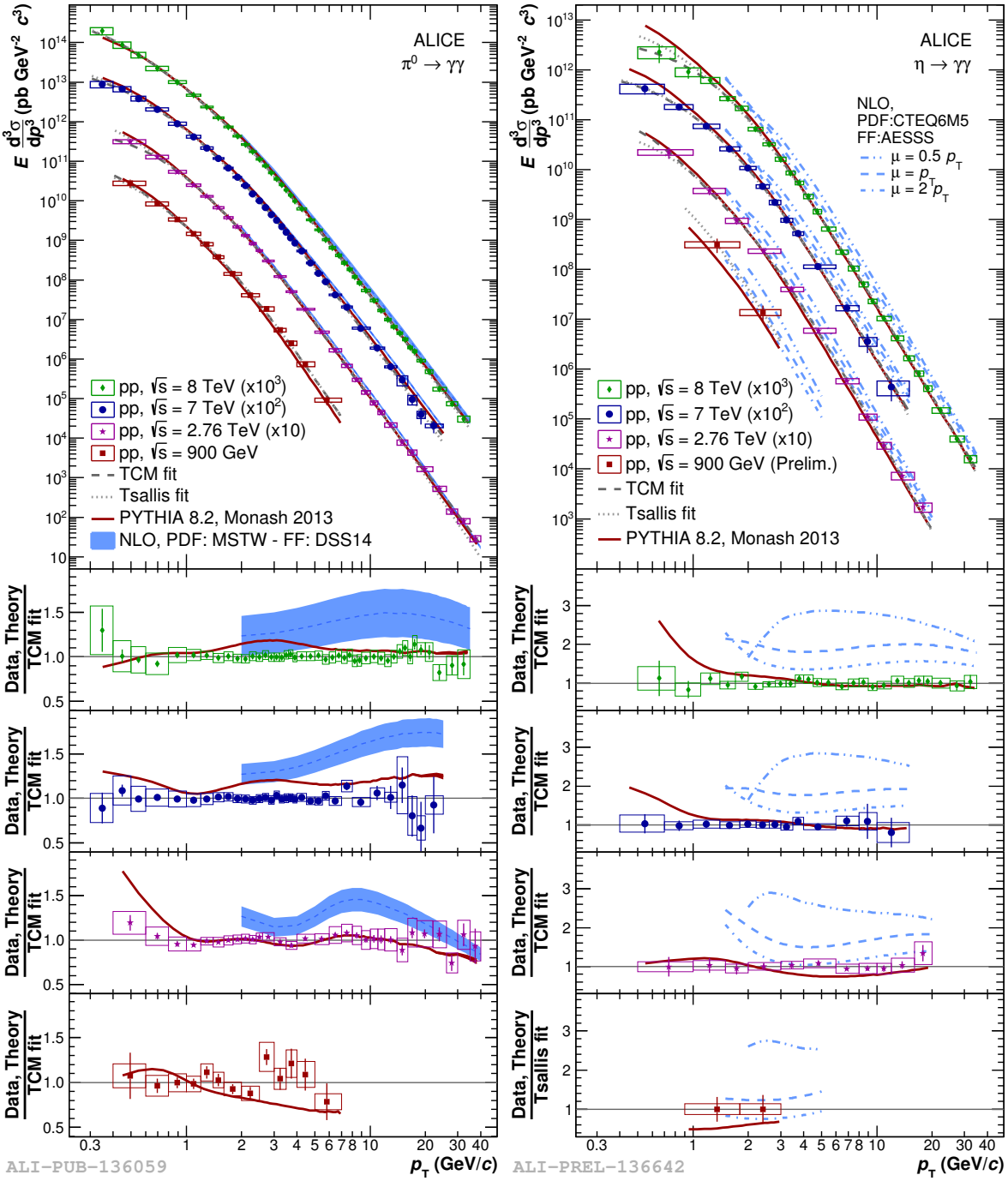

Figure 1.6: Neutral pion spectrum at $\sqrt{s} = 0.9, 2.76, 7$ and 8 TeV [30, 31, 32, 35, 33]. The spectrum is compared to PYTHIA8 [34] event generator and NLO pQCD calculations. The ratios of data and predictions to two-component model (TCM) fit [36] are shown on the bottom panels for each energy separately.

(NLO) [15, 37, 38] predict 20–60% higher yield, and the difference increases with p_{T}. The measured η meson production spectra show similar patterns: PYTHIA 8.2 with Monash 2013 tune reproduces the data, whereas NLO pQCD calculations predict 50–100% higher yield at all colliding energies.

The ratios of the measured data to the corresponding fit are shown in the bottom panels of Fig. 1.6 The data measured at $\sqrt{s} = 0.9$ and 2.76 TeV show a good agreement with NLO pQCD calculations. However, the discrepancy between the data and theory increases with energy. The effect is stronger for larger p_{T}.

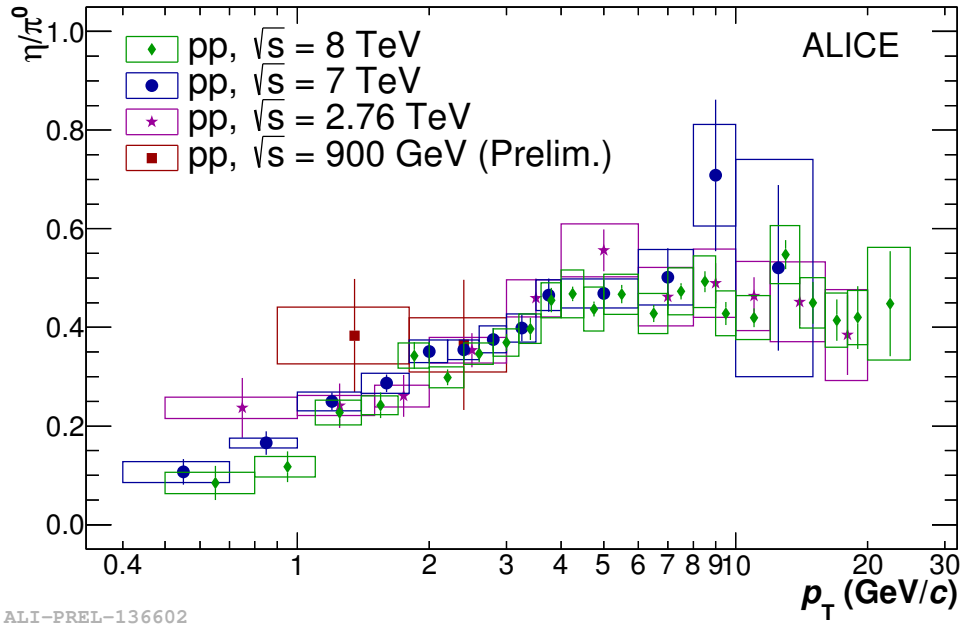

Figure 1.7: The comparison of the η/π^0 production cross-section ratio for pp collisions at $\sqrt{s} = 0.9,\ 2.76,\ 7$ and 8 TeV [32, 30, 33].

The comparison of the η/π^0 production cross-section ratio for pp collisions at $\sqrt{s} = 0.9,\ 2.76,\ 7$ and 8 TeV [32, 30, 33] is shown in Fig. 1.7. The measurements are consistent with each other. The η/π^0 ratio shows no energy dependence which is confirmed in low-energy experiments [39].

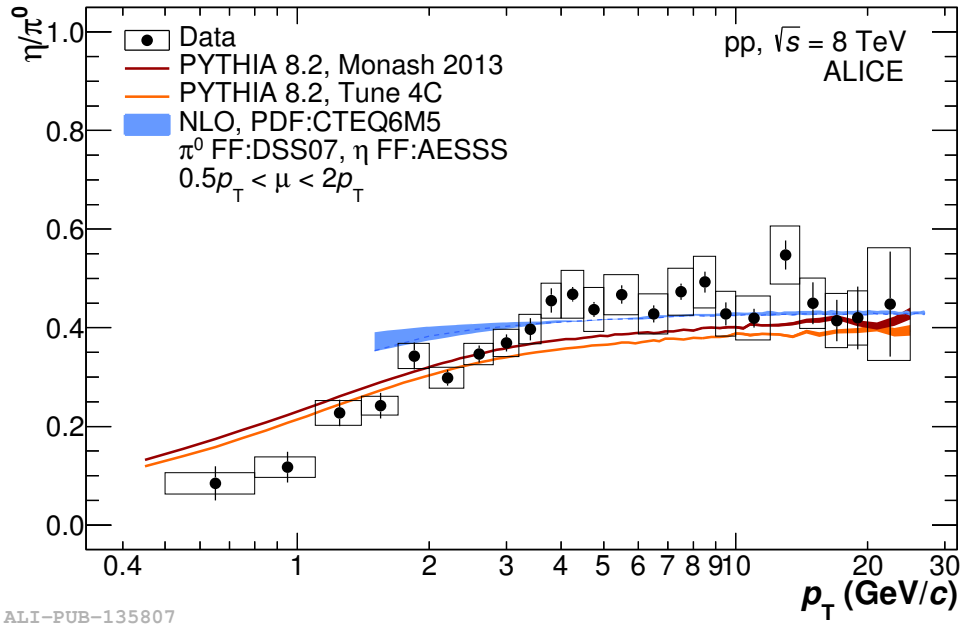

Figure 1.8: The η/π^0 yield ratio in proton-proton collisions at $\sqrt{s} = 8$ TeV [33] compared to theoretical predictions. The brown band corresponds to PYTHIA 8 Monash tune [40] and the red one represents 4C tune [41]. The blue band represents NLO pQCD calculations with CTEQ6M5 [37] as PDF combined with DSS07 [15] for pions and AESSS [38] as FF for η mesons.

The η/π^0 ratio depends on transverse momentum. It increases from ~ 0.1 at $p_{\mathrm{T}} < 2$ GeV/c to ~ 0.5 at p_{T} larger than 5 GeV/c. The data indicate that the η/π^0 ratio saturates at higher p_{T} and the distributions are often fitted with a zero-degree polynomial in that region.

The experimental values of η/π^0 ratio measured in pp collisions by ALICE are well reproduced by PYTHIA 8 Monte-Carlo simulations with Monash [40] and 4C tunes [41]. The data also agrees with the NLO calculations based on CTEQ6M5 [37] PDFs combined with DSS07 [15] fragmentation functions for pions and AESSS [38] as FF for η mesons. The comparison between the theoretical predictions and the experimental values of η/π^0 ratio measured in pp collisions at $\sqrt{s} = 8$ TeV [33] in Fig. 1.8. This is the first measurement of light neutral meson spectra at the highest collision energy so far. PYTHIA 8 shows a good description of the data in the high-p_{T} region and is above the experimental points below 1 GeV/c. As seen from the bottom panels in Fig. 1.6 the same pQCD calculations significantly deviate from the individual spectra, however, they well reproduce the η/π^0 ratio.

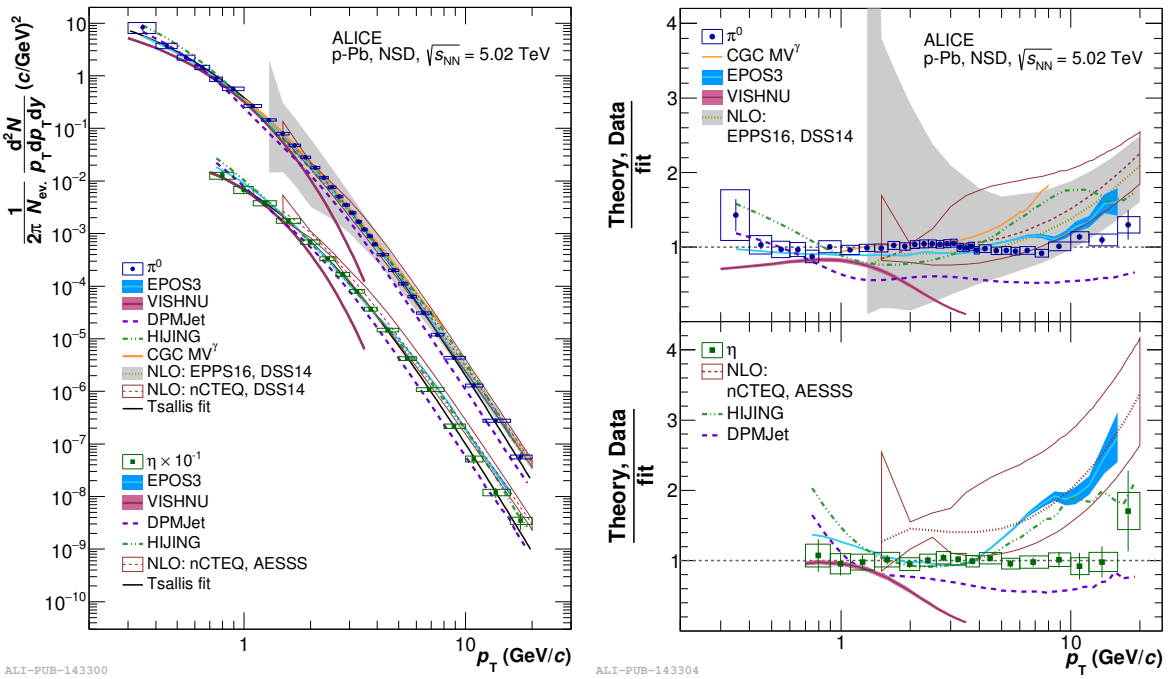

Figure 1.9: Left plot: π^0 and η spectra measured in p–Pb collisions at $\sqrt{s}_{\mathrm{NN}} = 5.02$ TeV [42]. Right plot: the ratio of the data to fit. The data are comparedand to DPMJET [43], VISHNU [44], HIJING [45], EPOS [46], CGC [47] models and to scaled NLO pQCD calculations [15, 48].

The ALICE experiment has also reported the neutral pion and η meson cross sections in proton-lead collisions at $\sqrt{s}_{\mathrm{NN}} = 5.02$ TeV [42]. The spectra have a power-like shape similar to ones measured in pp collisions. The Tsallis parametrisations [**?**] in the entire p_{T} range. The data and the ratios to the fit functions are shown in Fig. 1.9. The NLO pQCD calculations [15, 48] scaled with the number of binary nucleon-nucleon collisions well describe the π^0 cross-section in the entire p_{T} range and overpredict the η spectrum at high p_{T}. EPOS [46] Monte Carlo reproduces the π^0 spectrum and η spectrum below 3 GeV/c, but overpredicts it at high transverse momentum. Hydrodynamic model VISHNU[44] provides a good description at low p_{T}. HIJING[45] and DPMJET [43] models predictions do not reproduce the data for p_{T} larger than 4 GeV/c and well describe spectra below ~ 5 GeV/c. The π^0 cross-section data agrees with the CGC [47] calculations at low and moderate p_{T} and departs high from the data starting from 4 GeV/c.

ALICE measured the spectrum of neutral pions in Pb–Pb collisions at $\sqrt{s}_{\mathrm{NN}} = 2.76$ TeV in the range $0.6 < p_{\mathrm{T}} < 12$ GeV/c with the data collected in 2010 [31]. The

neutral pion yield shows power-law behaviour as a function of p_{T}. The cross-section data can be described by the Tsallis fits. The data collected in 2010 and 2011 years were combined together to extend the range of π^0 spectrum up to 20 GeV/c and to measure η meson spectra in narrower centrality classes [35]. The π^0 and η meson yields, together with theoretical predictions, are shown in Fig. 1.10. Two versions of stochastic hadronisation model [51] reproduce the shape of the π^0 spectrum at low p_{T}. For the η mesons, the nonequilibrium variation of SHM underestimates the yield at the low-p_{T} region.

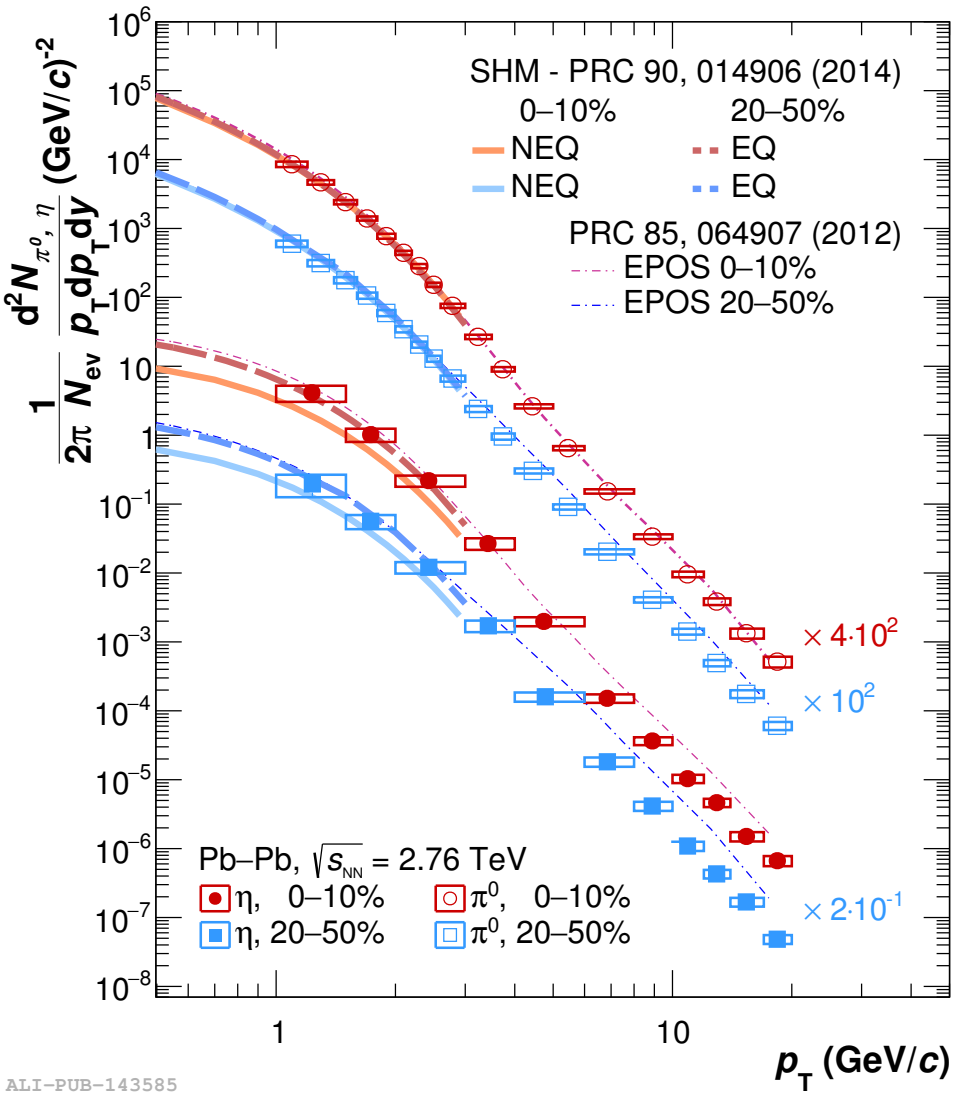

Figure 1.10: The π^0 (open symbols) and η (closed symbols) meson production cross-section measured in 0-10% (red) and 20-50% (blue) centrality clasess in lead-lead collisions for the center-of-mass energy $\sqrt{s}_{\mathrm{NN}} = 2.76$ TeV [31]. The measurements are compared to predictions of EPOS [52] (dash-dotted line) and two versions of SHM the equilibrium (EQ) one plotted with the dashed line and nonequilibrium one (NEQ) represented with the solid line.

The nuclear modification factor R_{AA} is defined as a ratio of the meson yield in Pb–Pb collisions divided by the meson production cross-section in pp collisions at the same energy scaled with the nuclear overlap function. The simultaneous measurement of π^0 and η spectra in pp and Pb–Pb collisions at $\sqrt{s}_{\mathrm{NN}} = 2.76$ TeV allowed extraction the nuclear modification factor [31]. The absence of the nuclear medium effects corresponds to $R_{\mathrm{AA}} = 1$. For Pb–Pb collisions at $\sqrt{s}_{\mathrm{NN}} = 2.76$ TeV nuclear modification factor attains its minimum $R_{\mathrm{AA}} \sim 0.1$ at $p_{\mathrm{T}} \sim 7$ GeV/c. This reflects strong energy loss by partons in the hot quark-gluon matter. This observation also shows that R_{AA} increases with p_{T}. The nuclear modification factor for π^0 and η agrees with that for $\pi^{\pm}$ and $K^{\pm}$[53]. The

R_{AA} decreases with increasing centrality. This indicates that the medium effects are most prominent in the most central collisions which agrees with the previous measurements at RHIC [27].

1.5.3 m_{T} scaling

The colliding experiments show that the spectra of the final state hadrons (h) show similar behavior if calculated as a function of transverse mass $m_{\mathrm{T}} = \sqrt{p_{\mathrm{T}}^2 + m_h^2}$ where m_h is the mass of a particle and p_{T}– its transverse momentum. This means that the spectral shapes $f(m_{\mathrm{T}})$ are identical and differ by the normalization constant C_h that correspond to different hadron species:

$$E\frac{d^3\sigma}{dp^3}(h) = C_h f(m_{\mathrm{T}}).$$

The phenomenon above is called m_{T} scaling [54]. This effect was discovered in pp data at ISR energies [55, 56]. The similar pattern was observed in heavy-ion collisions. The data on Au–Au collisions at $\sqrt{s}_{\mathrm{NN}} = 130$ GeV from RHIC demonstrates m_{T}-scaling [57]. Scaling of the π^0 and η spectral shapes was reported in S–Au, S–S collisions at 200 GeV by WA80 [58]. The m_{T}-scaling was reported in pp collisions at RHIC energies as well. Transverse-mass spectra were measured by STAR and PHENIX experiments for $\pi^{\pm}, K^{+}, K^0_s, \Lambda, \pi^0$ and Ξ for $\sqrt{s} = 200$ GeV and $\sqrt{s} = 510$ GeV [22, 59]. Those results indicate similarity between shapes of the spectra corresponding to different particle species up to $m_{\mathrm{T}} \sim 2$ GeV/c^2. This measurement revealed that at higher transverse mass baryon

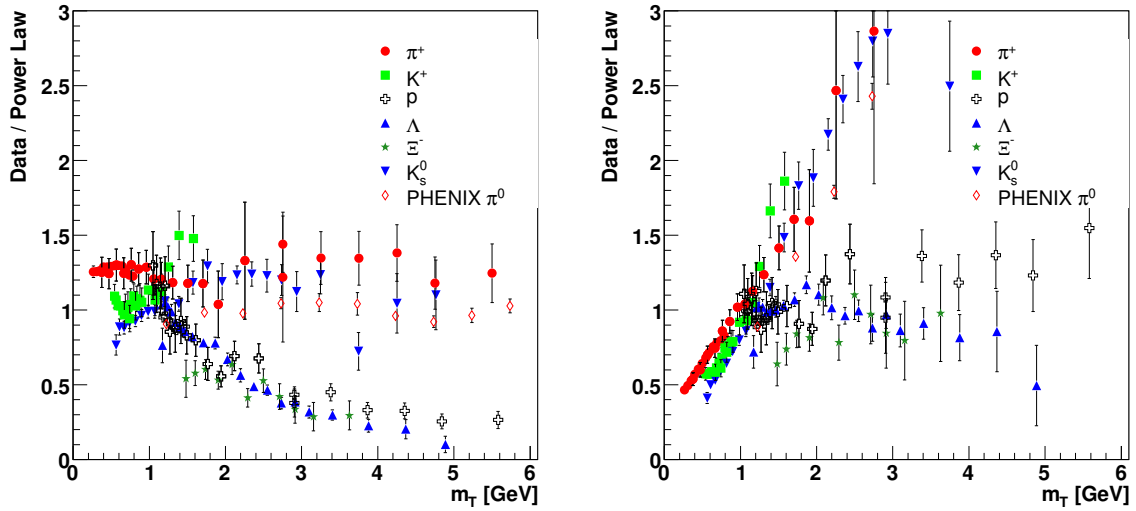

Figure 1.11: Left plot: Ratio of data to meson power-law fit for each particle species. Right plot: Ratio of data to baryon power-law fit for each particle species measured in pp collisions at $\sqrt{s} = 200$ GeV. The figure is taken from [39].

spectra show steeper behaviour and differences between meson and baryon cross-section is more apparent [39]. The agreement between different shapes was tested by a power-law function fits, as it well represents the data. Then the spectra were divided by the parametrisation in order to test the agreement. The ratios of hadron spectra to the power-law fits are given in Fig. 1.11. It confirms the effect of meson-baryon separation at high transverse mass. These results indicate that meson production dominates baryon generation at high transverse momentum. The scaling is universal for all particle species for m_{T} below 2 GeV/c^2 in pp collisions at $\sqrt{s} = 200$ GeV. These phenomena might be an effect of thermal particle production in hadron-hadron collisions.

The ratio of π^0 to η spectra is a convenient experimental variable since it allows experimentalists to exclude some of the systematic errors (for example the one connected

to the normalisation). This variable can be derived from m_{T}-scaling as well. Previous observations show power-law fits $f(m_{\mathrm{T}}) = (m_{\mathrm{T}} + a)^{-n}$ well describe the experimental data in the range $0.2 < m_{\mathrm{T}} < 14$ GeV/c^2. The ratio of invariant cross-section of neutral pion and η meson can be written in the form

$$R_{\eta/\pi^0}(p_{\mathrm{T}}) = R_{\eta/\pi^0} \left(\frac{a + \sqrt{m_\eta^2 + p_{\mathrm{T}}^2}}{a + \sqrt{m_{\pi^0}^2 + p_{\mathrm{T}}^2}} \right)^{-n},$$

where $R_{\eta/\pi^0} = C_\eta / C_\pi^0$ – is the relative normalization constant, that corresponds to the asymptotic value of η/π^0 ratio. Various low-energy experiments have reported the η/π^0 ratio. These results for hadron-hadron collisions for energy range $13.8 < \sqrt{s} < 1800$ GeV are show in Fig. 1.12 [60]. The values of η/π^0 spectra ratio increase exponentially as a function of transverse momentum. Above $p_{\mathrm{T}} \sim 3$ GeV the η/π^0 ratio saturates at the level of $0.3 - 0.6$.

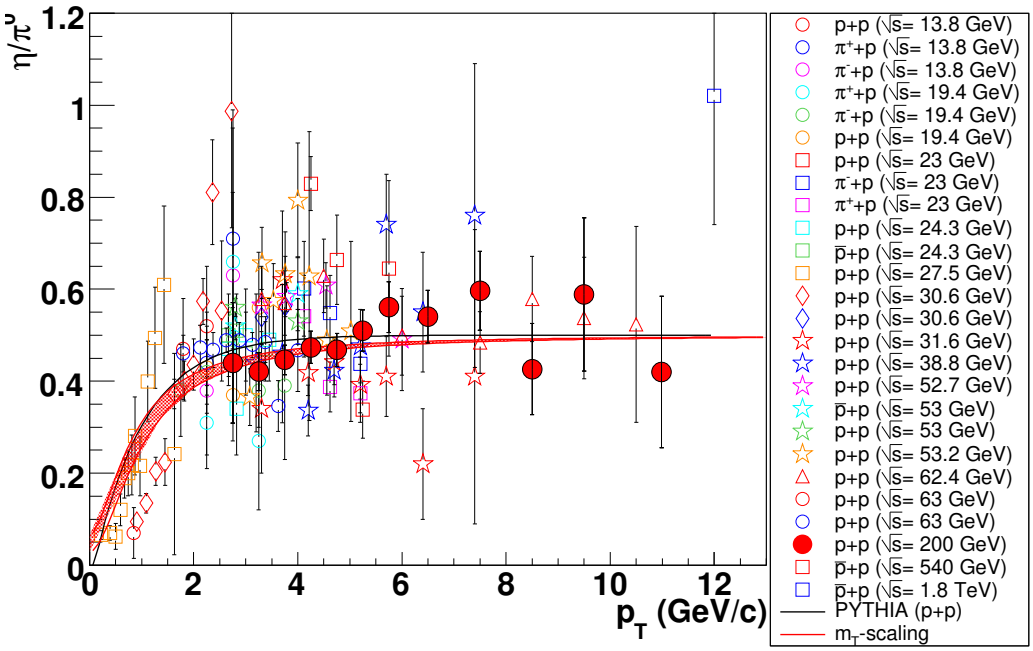

Figure 1.12: Values of the η over π^0 spectra ratios as a function of transverse momentum measured in the hadron-hadron collisions. The black curve is the prediction of PYTHIA 6 [61] for the ratio in pp at $\sqrt{s} = 200$ GeV, and the red shaded area indicates the empirical m_{T}-scaling with fixed $a = 1.2$, power-law exponent $n = 10. - 14.$, and an asymptotic η/π^0 ratio of 0.5. The figure is taken from [60].

It is important to note that a black solid line in Fig. 1.12 corresponds to the PYTHIA 6 Monte-Carlo predictions [61] for pp collisions at $\sqrt{s} = 200$ GeV. It shows a good description of all the points presented in Fig. 1.12. The agreement between different energy and consistency of the data with the PYTHIA 6 predictions indicate that η/π^0 ratio depends on the meson fragmentation functions and is invariant to the initial conditions of the collision.

The red-shaded area in Fig. 1.12 is m_{T}-scaling parametrization for the parameters $a = 1.2$ and $10 < n < 14$ and asymptotic value is taken $R_{\eta/\pi^0} = 0.5$. The m_{T}-scaled curve approximates all the data points and indicates that the scaling is preserved in various systems and different energies at $p_{\mathrm{T}} > 2$ GeV/c. However, at low p_{T} (below 1 GeV/c), there is a discrepancy between m_{T} scaling and the data. The weak decay contribution can partially explain this at low m_{T} part (below 0.4 GeV/c^2) of the pion cross-section. This can be accounted for by the more complex parametrisations.

The convergence of the predictions from PYTHIA 6 Monte-Carlo generator and m_{T} scaling formula originates from the string fragmentation function used by PYTHIA 6. It models the m_{T} dependence explicitly [61].

There are many low energy measurements of η/π^0 cross-section ratio, but they lack statistics to test the m_{T} scaling with high confidence. The points with the highest accuracy below $p_{\mathrm{T}} < 1.6$ GeV/c are measurd by NA27 [62] experiment in pp collisions. The highest precision at high-p_{T} (above 2.25 GeV/c) is achieved by PHENIX collaboration in pp collisions at $\sqrt{s} = 200$ GeV. In both cases, the correction that accounts contribution of secondary decays (feed-down correction) is not applied. Its contribution is rather small and is more prominent in LHC energies. Therefore it should be taken into consideration while analysing the data from ALICE.

Below $p_{\mathrm{T}} \sim 1$ GeV/c, m_{T} scaling predicts significantly higher values than the data points. However, the precision of that data does not allow to conclude strong m_{T} scaling violation at low p_{T}. In heavy-ion collisions this effect is more prominent [60]. It is expected that collective effects such as collective radial flow [63] can alter the hadron spectra for $p_{\mathrm{T}} < 1.5$ GeV/c. The hydrodynamic flow predicts an increase in the yield of heavy particles and therefore larger η/π^0 spectrum ratio in heavy-ion collisions if compared to hadron-hadron experiments. The violation of m_{T}-scaling is expected below $p_{\mathrm{T}} < 2$ GeV/c as η meson is several times heavier than π^0 [64]. However, this can not be measured with PHOS detector alone as the acceptance of the detector allows measurements of η only at $p_{\mathrm{T}} > 2$ GeV/c at $\sqrt{s} = 13$ TeV.

1.5.4 x_{T} scaling

Historically, the hypothesis about the parton structure of a proton was suggested in [65]. It was motivated by the scaling of the parton structure functions in deep inelastic scattering. Originally, partons were assumed to interact electromagnetically [66], therefore, the invariant cross-section for hadron production in pp scattering in a general form can be written as:

$$E\frac{d^3\sigma}{dp^3}\left(p + p \to h + X\right) = \frac{4\pi\alpha^2}{p_{\mathrm{T}}^4} F\left(-\frac{u}{s} - \frac{t}{s}\right).$$

where $4\pi\alpha^2/p_{\mathrm{T}}^4$ factor comes from the assumption of a single photon exchange, F – is the form factor and it depends only on the energy. The measurements of hadron production at large p_{T} in pp collisions at $\sqrt{s} = 31$ GeV and 63 GeV by ISR showed that the data [67] indicated the a violation of $1/p_{\mathrm{T}}^4$ behaviour and followed $\sim 1/p_{\mathrm{T}}^8$ law. The constituents interchange model was designed to describe the steeper behaviour of final-state hadron spectra [68]. Within this framework the inclusive hadron production cross-section in pp collisions can be written as:

$$E\frac{d^3\sigma}{dp^3}\left(p + p \to h + X\right) = \left(\frac{2}{\sqrt{s}x_{\mathrm{T}}}\right)^n F(x_{\mathrm{T}}), \tag{1.2}$$

where n – is the power that models the interaction and $x_{\mathrm{T}} \equiv p_{\mathrm{T}}/\sqrt{s}$ – is the x_{T} variable. The choice of a new kinematic parameter x_{T} is motivated by the fact that the maximal value of p_{T} is $\sqrt{s}/2$. Hence, the resulting variable is dimensionless and bounded $0 < x_{\mathrm{T}} < 1$. The QCD analogue of the equation 1.2 can be written in the following form [69]:

$$E\frac{d^3\sigma}{dp^3}\left(p + p \to h + X\right) = \frac{1}{\left(\sqrt{s}\right)^{n(x_{\mathrm{T}},\sqrt{s})}} G(x_{\mathrm{T}}),$$

where $G(x_{\mathrm{T}})$ – is the dimensionless form factor that contains structure and fragmentation functions and all dimensionless variables, $n(x_{\mathrm{T}}, \sqrt{s})$ – is the effective index, which takes into account the fact that the original n variable depends on the collision energy and x_{T} [69]. The limiting value of $n = 4$ corresponds to the QED scenario. It

is expected that n is grater at higher energies (it should grow with momentum transfer) due to the contribution of higher-order perturbative processes. The invariant cross-section as a function of x_{T} in Fig. 1.13

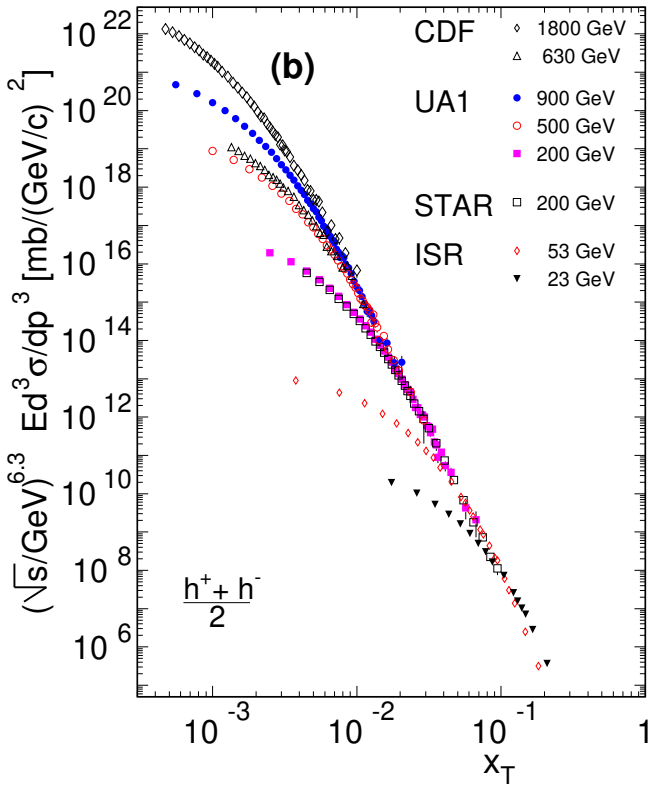

Figure 1.13: The invariant cross section multiplied by $(\sqrt{s})^{6.3}$ plotted as a function of x_{T} for seven center of mass energies from different experiments [70, 71, 72, 73]. The figure is taken from [74].

The invariant cross-section at low x_{T} shows almost no correlation with the collision energy. This can be explained by soft processes that have a larger contribution in that kinematic region. However, for higher values of x_{T}, the spectra have similar shapes, that indicates a strong dependence on collision energy, as hard processes dominate at large x_{T}.

Since the form factor $G(x_{\mathrm{T}})$ does not depend on the collision energy, it can be used to write an equation that connects invariant cross-section measured for different energies. The formula for the calculation of scaling parameter n can be written as

$$n(x_{\mathrm{T}}, \sqrt{s}_1, \sqrt{s}_2) = \frac{\ln\left(\sigma(x_{\mathrm{T}}, \sqrt{s}_2)/\sigma(x_{\mathrm{T}}, \sqrt{s}_1)\right)}{\ln\left(\sqrt{s}_1/\sqrt{s}_2\right)},$$

where $\sqrt{s}_{1,2}$ – are the collision energies of the measurements and $\sigma_i = Ed^3\sigma/dp^3$ – the correspoding invariant cross-section measurement. It is important to mention that in order to estimate the $n(x_{\mathrm{T}})$, it is necessary to have at least two sets of measurements at different collision energies.

It is expected that x_{T} scaling applies for heavy-ion collisions as well. The resulting n values should be the same in case if high p_{T} particles come from hard-scattering described by QCD. This effect can be explained by scaling of the structure and fragmentation functions which also leads to different form factors $G(x_{\mathrm{T}})$. The difference in the suppression of high-p_{T} particles in heavy-ion collisions with respect to pp collisions should be studied.

As it indicates shadowing of the structure functions [75], gluon saturation [29] and rather eliminates the final state interaction with the hot and dense matter.

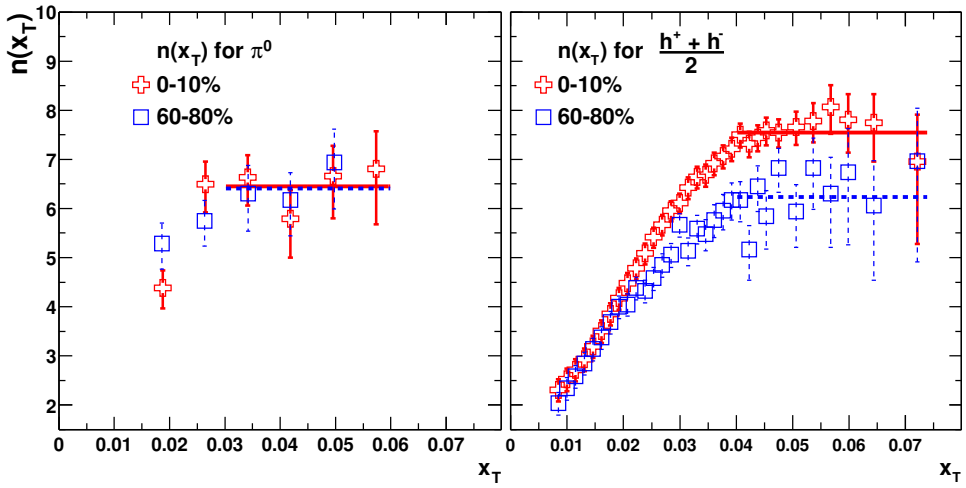

Figure 1.14: The x_{T} scaling power $n(x_{\mathrm{T}})$ plotted as function of x_{T} calculated for π^0 (left panel) and $(h^+ + h^-)/2$ (right panel) in central (0-10%) and peripheral (60-80%) collisions. The solid (and dashed) lines indicate a constant fit along to the central (and peripheral) $n(x_{\mathrm{T}}, \sqrt{s})$ data. The values of $n(x_{\mathrm{T}})$ are dirived from charged hadron spectra measured in Au–Au collisions at $\sqrt{s}_{\mathrm{NN}} = 130$ GeV and $\sqrt{s}_{\mathrm{NN}} = 200$ GeV. The figure is taken from [74].

An example of $n(x_{\mathrm{T}})$ distributions derived from the experimental data is presented in Fig. 1.14. It is calculated from charged hadron spectra measured in Au–Au collisions at $\sqrt{s}_{\mathrm{NN}} = 130$ GeV and $\sqrt{s}_{\mathrm{NN}} = 200$ GeV [74]. For neutral pions x_{T} scaling is visible at $x_{\mathrm{T}} > 0.03$ and does not depend on centrality while for charged hadrons $n(x_{\mathrm{T}})$ flattens at $x_{\mathrm{T}} > 0.04$. The scaling factor for neutral pions was found to be $n = 6.33 \pm 0.54$ in peripheral collisions and $n = 6.41 \pm 0.55$ for central ones. Those values are in agreement with the data obtained from pp at $\sqrt{s} = 200$ GeV which shows $n \sim 6.4$ [76]. For the charged hadrons there is a significant difference between peripheral ($n = 6.12 \pm 0.49$) and central ($n = 7.53 \pm 0.44$) collisions. The saturation region at $0.01 < x_{\mathrm{T}} < 0.03$ corresponds to the transition from the soft to hard kinematic region.

1.6 Physics motivation

The precise measurement of light neutral meson spectra is required for the understanding of the particle production mechanism at high energies. This section shows that perturbative quantum chromodynamics provides a theoretical description of π^0 and η cross-sections. The pQCD calculations are based on fragmentation functions $D_f^h(z)$ that were obtained from the low-energy experiments. By measuring π^0 and η meson production, it is possible to test the pQCD predictions.

The spectra themselves can be used to better constrain the FFs and improve the accuracy of the theoretical calculation. The neutral pion and η meson yields are the unique instruments for such analysis as pQCD provides accurate calculations only at high transverse momenta ($p_{\mathrm{T}} > 3$ GeV/c) and at the same time, experimental measurement of charged hadrons is limited to a few GeV/c due to the limitations of gas detectors. Also, the π^0 and η meson spectra, serve as a validation tool for Monte-Carlo algorithms that are used in experimental physics to estimate the hadron contribution to particle spectra.

Additionally, π^0 and η mesons are the dominant sources of photons in hadron-hadron collisions. For this reason, the light neutral meson spectra serve as an input for the analysis of prompt photons, all the photons that do not originate from particle decays.

Since they mostly come from hard processes at high p_{T}, their spectra can be calculated within the pQCD framework [77]. Also, it was observed in heavy-ion collisions that low p_{T} part of the prompt photon spectra contains thermal photons that come from the hot nuclear medium [78, 79, 80].

The aim of this thesis is to report the first measurements of π^0 and η spectra in pp collisions at $\sqrt{s} = 13$ TeV.

Chapter 2

Setup

2.1 The Large Hadron Collider

The Large Hadron Collider (LHC) is a superconducting hadron accelerator which is located at CERN (European Organization for Nuclear Research). The LHC mainly consists of dedicated CERN accelerator complex [81, 82, 83]. The tunnel of the LHC is 26.7 km long. The depth of cavern varies from 45 m to 175 m below the sea level [84]. The tunnel consists of eight arcs and the same amount of straight sections, four of which have beam crossing points. There are 858 quadrupole magnets with 233 T/m field along straight sections. The quadrupole magnets are used to focus the beam. The arc sections are covered with 1232 superconducting dipole magnets with 8.33 T field and 14.3 m long. The dipole magnets are used to bend the beam.

The LHC was designed to deliver stable protons beams with energy $\sqrt{s} = 14$ TeV with high luminosity of $L = 10^{34}$ cm$^{-2}s^{-1}$ and Pb-Pb beams with the luminosity $L = 10^{27}$ cm$^{-2}s^{-1}$ at the energy of $\sqrt{s}_{\,\mathrm{NN}} = 5$ TeV. In the heavy ion (Pb-Pb) mode, the designed luminosity is $L = 10^{27}$ cm$^{-2}s^{-1}$ and highest collision energy per nucleon is $\sqrt{s}_{\,\mathrm{NN}} = 5.02$ TeV.

The accelerator chain consists of the Linear accelerator (Linac 2) and Linac 3 for lead beams, Proton Synchrotron Booster (PSB), Proton Synchrotron (PS), Super Proton Synchrotron (SPS) and LHC itself. All the steps in the chain are shown in Fig. 2.1.

The collision processes are initiated at Linac 2 where a strong magnetic field separates electrons from hydrogen atoms to produce ions that are used to form the beam. Then the ions are grouped into bunches using radio-frequency quadrupoles. The Linac 3 accelerates the nuclei up to 50 MeV then the beam is injected into Proton Synchrotron Booster where each beam attains energy of 1.4 GeV. The beams increase their energy up to 25 GeV in the Proton Synchrotron afterwards where the final bunches are shaped. Each beam is divided into 72 bunches with a length of 4 ns. After that, all bunches are injected into the SPS which accelerates the beams to the energy of 450 GeV and finally injects them into the LHC. The quality of the beam can be expressed in terms of the transverse emittance ε and the amplitude function β. These quantities are strongly dependent. The transverse emittance is a spatial characteristic of the beam that corresponds to the smallest opening angle that fits the beam with a given energy. The amplitude function is usually calculated as $\pi\sigma^2/\varepsilon$ where σ the bunch cross-section size. The low values of β correspond to compact beams that are suitable for collisions. For these reasons, the most important detectors are located low β points at the LHC.

There are four such points at the LHC ring that corresponds to the largest experiments are ALICE (A Large Ion Collider Experiment), LHCb (Large Hadron Collider beauty), CMS (Compact Muon Solenoid) and ATLAS (A Toroidal LHC ApparatuS). There are smaller experiments that accompany the main detectors: the LHCf (LHC forward), the TOTEM (TOTal Elastic and diffractive cross section Measurement) and the MoEDAL (Monopole and Exotics Detector at the LHC) experiments.

The ALICE experiment [85] is a dedicated heavy-ion experiment that is focused on the strong interaction of QCD properties of matter. A part of its physics program is the analysis of the pp data which serve as a baseline for proton-lead and lead-lead measurements. More details on the ALICE experiment will be given in the following sections.

The CMS [86] and the ATLAS experiments [87] are aimed to test the standard model and search for the beyond-standard-model physics. One of the main physics targes for these experiments is a Higgs boson search. Therefore these experiments are designed to record data at high luminosity proton-proton collisions.

The LHCb experiment [88] is a forward rapidity experiment. It is specialized in the heavy flavour physics in pp collisions. One of the main physics objectives of the LHCb experiment is the study of CP-violation in the decays of hadrons containing c and b quarks.

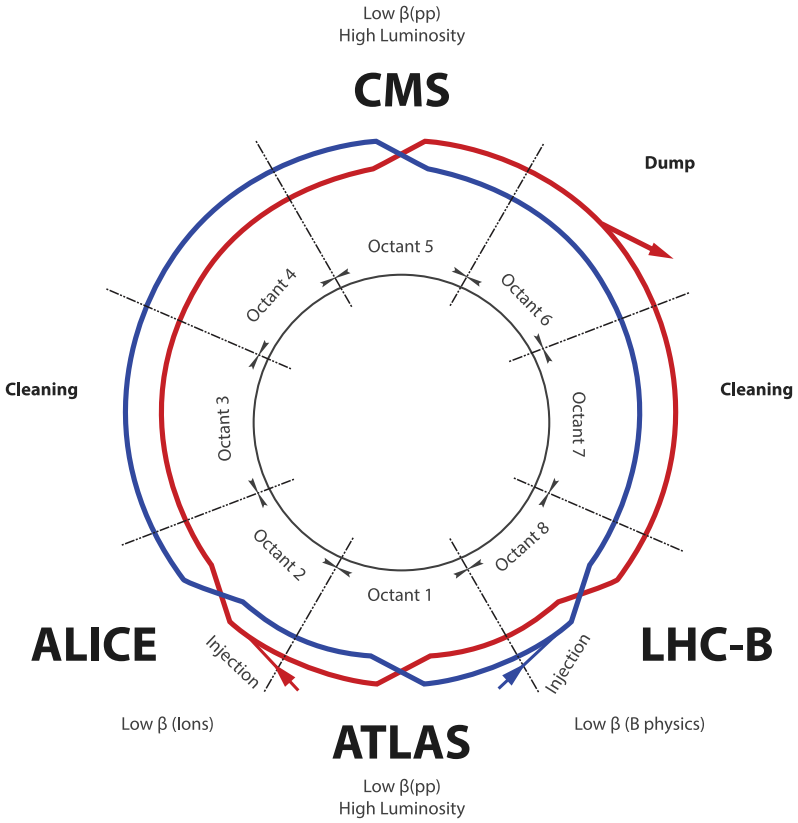

Figure 2.1: The schematic view of the LHC acceleration complex. The red and blue rings contain the bunches that are circulating in the opposite directions marked with the arrows. The points with where the circles cross have the lowest values of amplitude function β. They correspond to the largest experiments at LHC.

The LHCf experiment [89] is a forward physics experiment which focuses on particles that merely decline from the beam line ($|\eta| > 8.4$) in proton-proton collisions. This experiment is targeted to study the hadron interaction models. This is a part of the extremely high-energy cosmic-rays investigation. The LHCf experiment is located at ± 140 m far from the ATLAS detector.

The TOTEM experiment [90] designed to measure the elastic and inelastic cross sections in proton-proton collisions. One of the most important missions of TOTEM is to study diffraction processes in proton-proton collisions.

The MoEDAL experiment [91] is a high-precision, single-arm experiment. It is constructed for the magnetic monopoles and exotic (massive) particles search.

2.2 ALICE experiment

ALICE (A Large Ion Collider Experiment) is one of the largest experiments at the LHC. High-energy QCD matter is the subject of studies of the ALICE experiment. The ALICE detector is constructed to operate under extremely high multiplicities (when the number of charged particles is higher than several thousand) in lead-lead collisions. It is a modular apparatus that consists of almost 20 smaller detectors. All these detecting devices together can cover wide rapidity and momentum ranges. The ALICE setup has a unique particle identification potential. There are three categories of subsystems: forward, central-barrel detectors and muon spectrometer with muon trigger.

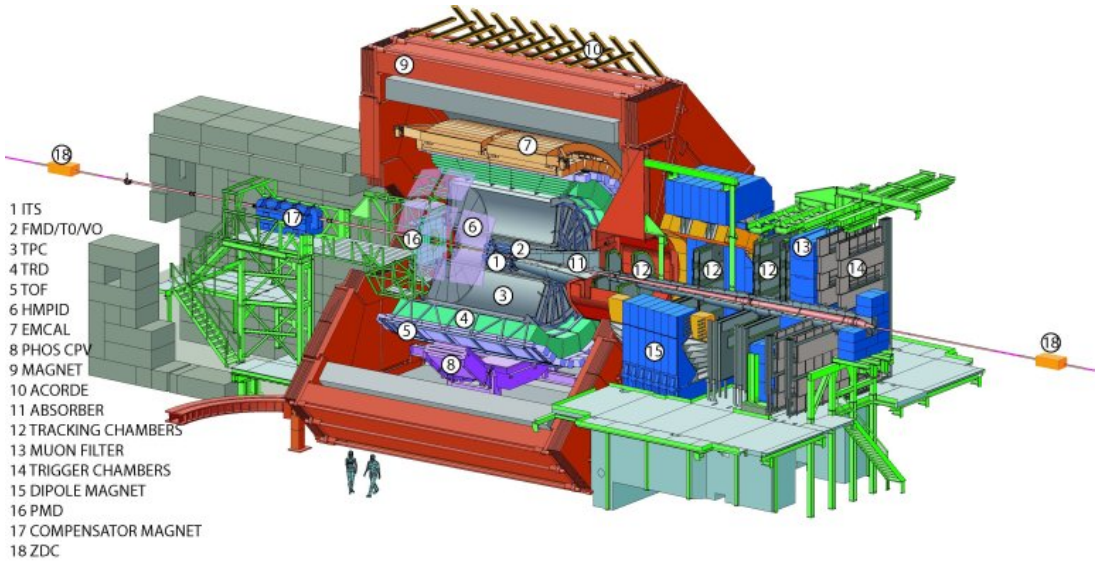

Figure 2.2: The schematic overview of the ALICE experiment

The trigger and forward detectors are responsible for the event properties and the experimental conditions. All the detectors do not record data continuously, but they are turned on when the actual event occurs. To trigger the event and to start counting the time of the event, the TZERO (T0) and VZERO (V0) detector are used. The T0 detector has a very good timing resolution (< 25 ns) which allows monitoring the instantaneous luminosity. The VZERO detector is responsible for the minimum-bias (MB) trigger. It reduces the background in collisions, and it provides the data for the event plane estimation. The Zero Degree Calorimeter (ZDC) triggers events and is used for the centrality determination. It is located ~ 112 m away from the nominal interaction point.

The main readout detectors belong to the central-barrel group of detectors and are enclosed in the L3 solenoid magnet [85]. The operational magnetic field of the L3 solenoid is of the order of $0.2-0.5$ T which is small if compared to the other LHC experiments. This configuration allows high precision measurement of low transverse momentum particles.

The central-barrel detectors cover pseudorapidity $|\eta| < 0.9$ and the momentum in the range $0.1 < p_{\mathrm{T}} < 100$ GeV/c for charged particles. The Inner Tracking System (ITS) is the most precise detector, which is the closest to the beam pipe. The Time Projection Chamber (TPC) encloses the ITS and is the main tracking device of ALICE. The Transition Radiation Detector (TRD) is located outside the TPC. For charged particle identification, the Time-of-Flight (TOF) and the High Momentum Particle Identification Detector (HMPID) are used.

The electromagnetic calorimeters of the ElecroMagnetic CALorimeter (EMCAL) and the PHOton Spectrometer (PHOS) belong to the central barrel as well. These detectors can measure photons with the transverse momentum of the order of 100 GeV/c. The electromagnetic calorimeters can also serve as an electron (positron) identification tool.

The muon spectrometer covers the forward rapidity region $-2.5 < \eta < -4.0$. The main purpose of this detector is to measure muons coming from proton-proton collisions. It consists of two parts the muon tracking chamber and muon trigger. The muon tracking system consists of a hadron absorber and a tracking chamber called Muon CHamber (MCH). It is a single-arm detector that is adjacent to the beam pipe and is far from the interaction point $-14.2 < z < -5.4$ m. It is used for tracking to reduce hadron contamination. The Muon TRigger system is used for particle identification at analysis time, and the signal from this detector serves as inputs to the central trigger system to select events with high energy muons. It is also a single-arm detector that is located at the edge of the ALICE apparatus with the distance to the interaction point of $-17.1 < z < -16.1$ m.

Detector	φ	maximal $\lvert\eta\rvert$ value	Δr, cm	description
SPD layer 1	Full	2.0	3.9	Tracking
SPD layer 2	Full	1.4	7.6	Vertex Tracking
SDD layer 1	Full	0.9	15.0	Vertex Tracking
SDD layer 2	Full	0.9	23.9	PID Tracking
SSD layer 1	Full	0.9	38	PID Tracking
SSD layer 2	Full	0.9	43	PID Tracking
TPC	Full	0.9	85	PID Tracking
TRD	Full	0.8	290	PID Tracking
TOF	Full	0.9	370	PID ($e\pm$)
PHOS	$250^\circ < \varphi < 320^\circ$	0.12	460	PID Photon
EMCal	$80^\circ < \varphi < 187^\circ$	0.7	430	Photon and Jet
HMPID	$1^\circ < \varphi < 59^\circ$	0.6	490	PID
ACORDE	$30^\circ < \varphi < 150^\circ$	1.3	850	Cosmic
Forward Detector	φ	η	Δz, cm	description
T01	Full	$4.6 < \eta < 4.9$	370	Charged particle
T02	Full	$-3.3 < \eta < -3.0$	-70	Charged particle
FMD1	Full	$3.6 < \eta < 5.0$	320	Charged particle
FMD2	Full	$1.7 < \eta < 3.7$	80	Charged particle
FMD3	Full	$-3.4 < \eta < -1.7$	-70	Charged particle
PMD	Full	$2.3 < \eta < 3.9$	367	Photon
V01	Full	$2.8 < \eta < 5.1$	329	Charged particle
V02	Full	$-3.7 < \eta < -1.7$	-88	Charged particle
ZDC (ZN)	Full	$\lvert\eta\rvert > 8.8$	$\pm$113	Forward neutron
ZDC (ZP)	$\lvert\varphi\rvert < 10^\circ$	$6.5 < \lvert\eta\rvert < 7.5$	$\pm$113	Forward proton
ZDC (ZEM)	$\lvert 2\varphi\rvert < 32^\circ$	$4.8 < \lvert\eta\rvert < 5.7$	$\pm$7.3	Forward Photon
MCH	$-4.0 < \eta < -2.5$	Full		Muon tracking
MTR	$-4.0 < \eta < -2.5$	Full		Muon trigger

Table 2.1: Summary of central barrel detectors (the upper part) and the forward detectors (the bottom part) of ALICE experiment.

The summary of the detector systems in the ALICE experiment is given in table 2.2. The coordinates r, φ, η in this thesis are defined with respect to the nominal interaction point (IP). The positive values of z-axis correspond to the clockwise direction of the LHC beam. Next sections give a more detailed description of the key detectors involved in the light neutral meson analysis.

2.3 Detectors

2.3.1 VZERO (V0)

The VZERO (V0) detector is a forward detector that supplies ALICE with the trigger, multiplicity and centrality information. The detector consists of two arrays of scintillator counters [92]. Each counter is installed on the opposite sides (V0A and V0C) of interaction point along the beamline.

The V0 is asymmetric detector with V0A covering $2.8 < \eta < 5.1$, while V0C $-3.7 < \eta < -1.7$ in full azimuth angle. Both V0A and V0C consist of 4 rings that are divided into eight sectors in the azimuthal direction. The detector consists of an array of plastic scintillators that are connected to the photomultiplier. The VZERO detector can trigger beam-beam interaction and separate it from beam-gas events thanks to a high timing resolution of 1 ns.

The amount of light produced by the scintillator (and hence the signal in the detector) is proportional to the number of tracks that penetrated the detector surface. The V0 signal is used as a tool for multiplicity measurement. In lead-lead collisions, the charged particle multiplicity is an estimator for the event centrality.

2.3.2 Inner Tracking System (ITS)

The Inner Tracking System is the closest to the beam pipe detector. It is composed of silicon semiconductors [93]. This detector is designed for high precision measurement (the spatial resolution is less than 100 μm) of the collision point. The ITS allows reconstruction of the secondary vertices produced by the weak decaying particles (heavy-flavour hadrons). It is also used for tracking and charged particle identification.

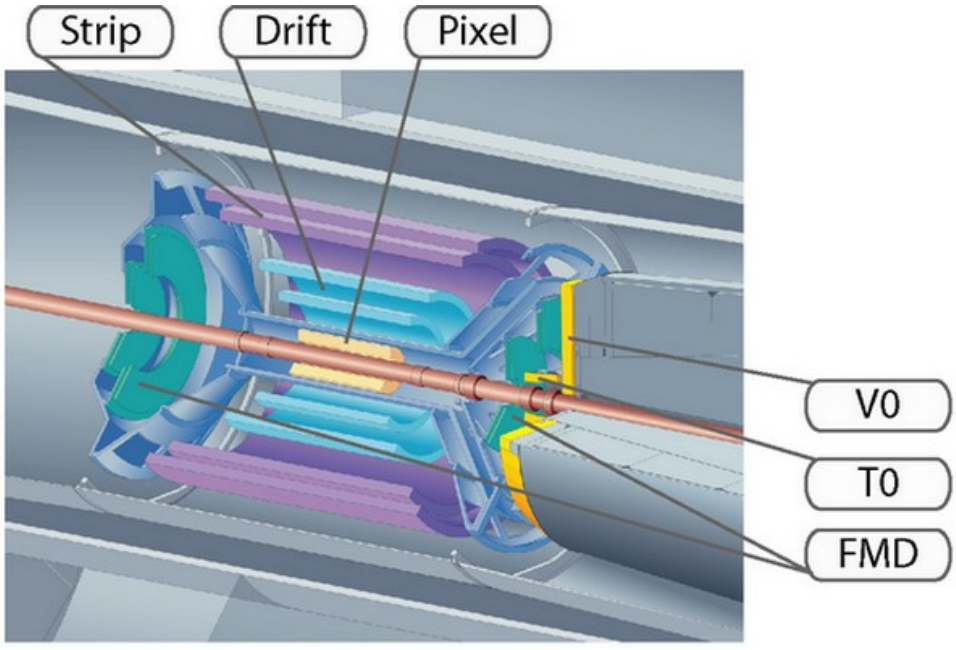

Figure 2.3: Inner Tracking System layout. The innermost layers correspond to the SPD, two next layers are parts of SPD, and the outermost layers belong to the SDD detector.

The ITS consists of three cylindrical detectors based on different technologies. It is adjacent to the beam pipe (the radius of the first layer is 3.9 cm). The last layer of the detector has a radius of 43 cm.

The innermost part of the ITS is the Silicon Pixel Detector (SPD) which consists of two layers of silicon pixels which cover pseudorapidity range of $|\eta| < 2.0$ and $|\eta| < 1.2$ and

full azimuthal range. The pixel technology provides a high spatial resolution of 100 μm in $r\varphi$ and 12 μm in z direction.

The line that connects two hits in the different layers of the SPD is called a tracklet. The information about the spatial density of tracklets is used to reconstruct the interaction point and the primary vertex. The number of tracklets (provided that it is a function of the number of charged particles produced in the collision) is used as an estimator for the event-by-event multiplicity calculation.

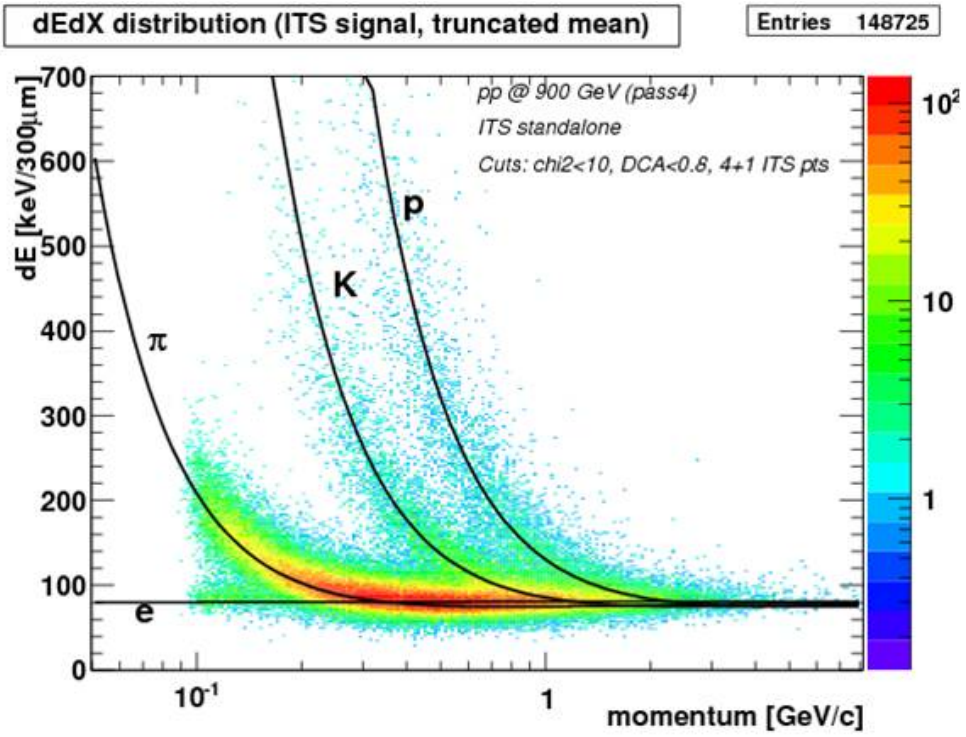

Figure 2.4: Specific energy loss as a function of a particle momentum measured in the Inner Tracking Sytem.

Two middle layers of the ITS are the Silicon Drift Detector (SDD) they designed to cover full azimuthal range and pseudorapidity range of $|\eta| < 0.9$. The resolution of these two layers is 25×35 μm^2 in $r \times \varphi$. Two outermost layers are the Silicon Strip Detector (SSD). It has a resolution of 830×20 μm^2 in $r \times \varphi$.

The specific energy loss dE/dx in the SDD and SSD detectors can be used for particle identification (PID). Energy loss in the ITS is shown as the function of the momentum of a charged particle in Fig. 2.4. The electron signal can be separated from the charged pions up to ~ 0.2 GeV/c. Kaons can be distinguished from pions up to ~ 1 GeV/c and pions and protons can be identified below ~ 2 GeV/c.

2.3.3 The Time Projection Chamber (TPC)

The Time Projection Chamber (TPC) is the largest detector in the central barrel [94]. It is a main tracking device of the ALICE experiment, and it also provides specific energy loss dE/dx for particle identification.

The TPC has a cylindrical shape, and it is filled with the gas mixture that consists of 90% of Ne and 10% of CO_2. The inner and outer radii of the detector are 85 and 247 cm, respectively. The height of the TPC barrel is 500 cm (along the beam axis). The volume of the detector is divided into two parts by the higher voltage (HV) electrode in the middle. Bases of the TPC cylinder are covered with the readout pads. The electrode is supplied with the voltage of -100 kV to create a 400 V/cm drift field towards the centre of the

TPC. Charged particles that transverse the detector ionize the gas atoms and generate electron-ion pairs. The drift field separates electrons and ions. Electrons float with the speed of ~ 2.7 cm/μs towards the readout pads at the sides of the TPC. The drift speed of ions is three orders of magnitude smaller. All the ions are moving to the centre of the detector in the HV electrode direction. Each readout pad consists of 18 trapezoidal shaped sectors. All the sectors cover 20° of azimuth angle.

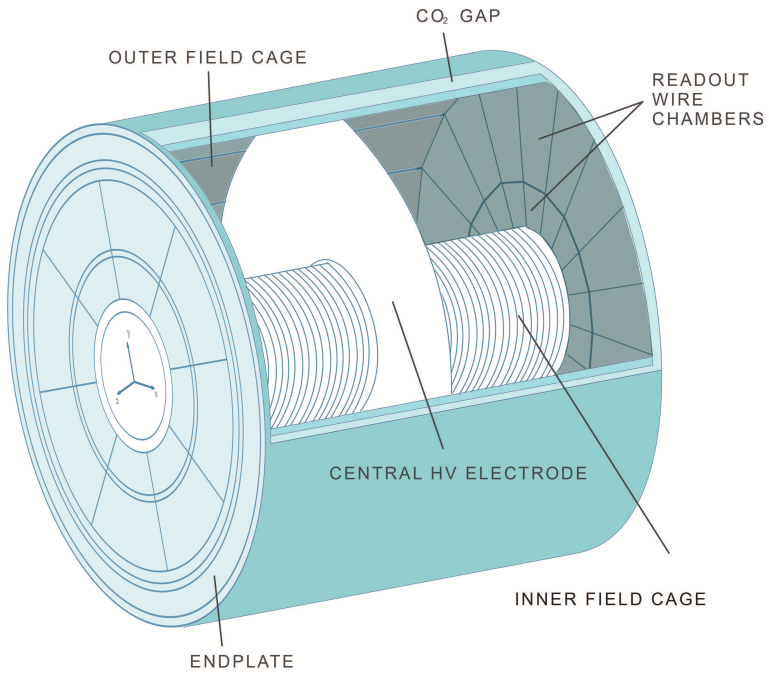

Figure 2.5: The layout of the Time Projection Chamber of ALICE experiment.

The track density in the radial direction decreases as $1/r^2$ (here r is the distance to the beamline). The parts of readout plates that are closer to the beam have a higher load than the outermost pads. Trapezoidal readout chambers are divided into two parts to provide better performance for differently charged track multiplicities. The Inner Read-Out Chambers (IROCs) and the Outer ReadOut charged (OROCs). The IROCs have better granularity and consist of 5504 readout pads of 4×7.5 mm^2 surface which forms 63 rows. The OROCs are composed of 6×10 mm^2 pads that are organized in 64 rows and 6×15 mm^2 outer pads that form 32 rows. The schematic layout of the TPC barrel is presented in Fig. 2.5.

The TPC can measure charged particles in the full azimuth range. It measures the tracks with the full radial lenght within $|\eta| < 0.9$ range while for thracks of 1/3 radial lenght it can measure up to $|\eta| < 1.5$. The spatial resolution of the detector is 1100-800 μm in $r\varphi$ and 1250-1100 μm in z direction.

The TPC reconstructs particles in a wide momentum range with $0.1 < p_{\mathrm{T}} < 100$ GeV/c with high precision. The momentum resolution of the TPC reaches 1% for tracks with 1 GeV/c, and it drops to 6.5% for particles with p_{T} below 10 GeV/c.

Charged particles that transverse the volume of the detector loses energy in ionization processes along their trajectories. The charge that is collected on the electrodes of the TPC is proportional to the energy loss of the measured tracks. Therefore energy loss dE/dx can be calculated using the TPC signal. It is presented in Fig. 2.6 as a function of charged particle momentum.

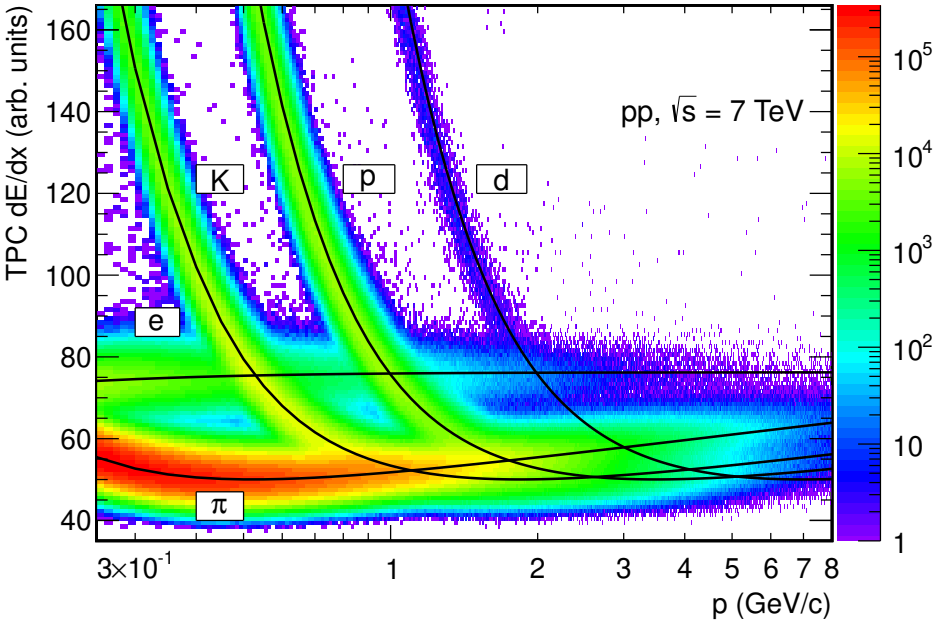

Figure 2.6: Specific energy loss measured by TPC as a function of a charged particle momentum. The black solid lines represent trend parametrizations by the Bethe-Bloch curves [95].

2.3.4 Trigger system

The trigger system is responsible for the selection of interesting physics events. It is designed to optimize the usage of ALICE subsystems that have different readout time and reduce the overall data rate. There are two major parts of the ALICE Trigger System: The Central Trigger Processor (CTP) and Trigger Distribution Network (TDN). The CTP generates the trigger signals based on the information provides by the trigger detectors [96]. These signals are then distributed across the detectors using the trigger distribution network [97].

All the subsystems of the ALICE detector are designed to work as a trigger detector and as a readout detector. The triggering detector is a device that provides data for a trigger decision. The readout detector takes part in the data recording. It's possible to use a subsystem as a trigger detector and as a readout detector at the same time.

All triggering detectors which are listed in table 2.2 send their signals to the ALICE trigger system which makes decisions and selects the event. Then it sends the trigger decision to the readout subsystems.

The detectors that are organized in readout (or trigger) clusters. The slowest detector (the one with the largest dead time) in the cluster defines the dead time of a cluster The clusters have similar configurations and parameters of the sub-detectors.

Due to the physical requirements and constraints on electronics of the detectors, the triggers are separated into three groups (levels). The fastest trigger decision is L0. It is delivered in ~ 0.9 μs after the beginning of the event. This is a very short period of time; therefore, not all the detectors can meet this requirement. If the L0-trigger decision was positive, then L1-trigger is evaluated. The L1 signal is generated within ~ 6.5 μs. This time defined by the computation times in EMCal, TRD and ZDC systems.

The final step in the triggering is the L2 signal. It takes ~ 90 μs to generate the L2 trigger. This limitation is caused by the drift time of the TPC after the collision. The final trigger signals are sent to the readout system together with the LHC clock. The successful trigger decision signals the Data Acquisition (DAQ) system to record the data.

A minimum-bias event (MB) is an event that satisfied the minimum-bias trigger. There are two definitions of the minimum-bias trigger: $\mathrm{MB_{OR}}$ and $\mathrm{MB_{AND}}$. The $\mathrm{MB_{OR}}$ is fired if the event contains at least one hit in both V0 (either V0A or V0C) and SPD detectors. The $\mathrm{MB_{AND}}$ has the same definition, but it requires hits on both sides of V0. This trigger suppresses the beam-gas interactions, but its efficiency is lower. There are many other triggers that are designed to selects events with special properties. For example, the muon trigger is fired when high energy muon hits the surface of the muon system. The PHOS trigger selects events that contain high energy photons ($E > 4$ GeV) that were registered in PHOS. These events allow enhancing the number of reconstructed neutral mesons in the high-p_{T} region.

2.3.5 The PHOton Spectrometer (PHOS)

The PHOton Spectrometer (PHOS) is an electromagnetic calorimeter with high spatial resolution [98]. This detector is designed to measure the energy and position of photons and electrons with high accuracy. The signals provided by PHOS are the main input to the analysis in this thesis.

The detector consists of 4 modules (3 and a half) that are installed at a distance of 4.6 m from the nominal interaction point. The fourth module was installed in 2015 and contains fewer cells than the previous ones. This is a significant change in PHOS construction in comparison to the LHC Run 1 configuration. The spectrometer has a relatively small solid angle if viewed from the interaction point. The acceptance of PHOS corresponds to $|\eta| < 0.13$ and $250 < \varphi < 320^\circ$ in azimuthal angle. The modules are adjacent to each other and are located radially, so each module covers $\Delta\varphi = 20^\circ$ and the same rapidity region.

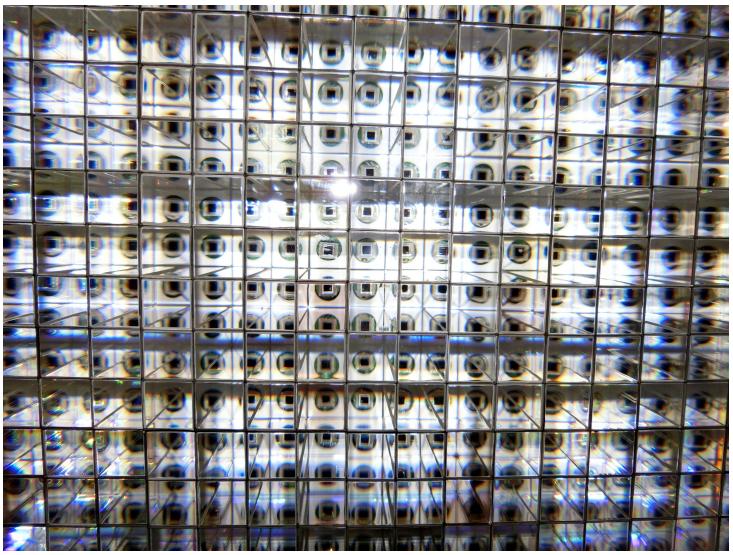

Figure 2.7: The scintillation crystals with avalanche photodiode assembled into a module grid that corresponds to a fragment of one of the modules.

All PHOS modules, by design, consist of 64×56 channel grids. An element of a single PHOS module is shown in Fig. 2.7. There are $12,544$ sensitive elements in the entire detector. The detection channels consist of the scintillation crystals and photodiodes attached to the preamplifiers. The scintillation crystals are made of $PbWO_4$ (lead tungsten or PWO). It has a surface area of 2.2×2.2 cm^2 which is approximately equal to the Moliere's radius ($\sim$ 2 cm for PWO). Photons deposit energy in several adjacent cells making a photon cluster. The total active area of the PHOS detector, including all modules, is 6 m^2. The density of lead tungsten is ~ 8.29 g/cm^3 and the radiation length

of this material X_0 is ~ 0.89 cm. The crystal has a length of 18 cm, which is equal to 20 radiation lengths.

The light yield of PWO material decreases with temperature with a rate of 2% per 1 $^{\circ}C$. The PWO material has three times higher light yield at -25 $^{\circ}C$ if compared to normal conditions. For this reason, the operational temperature of PHOS remains at the same level with a precision of 0.3% [99]. The crystals are connected to the Avalanche PhotoDiode (APD). The APD signals are amplified with a low-noise Charged-Sensitive Preamplifier (CSP). Both APD and the preamplifier are connected to the lower edges of the scintillation crystals with the transparent glue with a high refractive index. The detection cell, together with its parts, is shown in Fig. 2.8.

Figure 2.8: The avalanche photodiode connected to the scintillation cell.

The active area of a single photodiode is 5×5 mm^2 while the surface area of the preamplifier corresponds to 19×19 mm^2. Signals from detection channels are collected and processed in the front-end-electronics (FEE) cards. The electronics of PHOS implement digitization and trigger logic for generating the inputs for L0 and L1 level triggers [100]. Each energy shaper channel outputs two signals with low and high amplification that are digitized in two separate analogue-to-digital converters. These outputs are called low- and high-gain channels. This division is necessary to be able to measure the signals dynamically in the broad energy ranges. The upper limit of the low-gain channels is 5 GeV and 80 GeV for high-gain channels. The amplification rate changes significantly across different channels. The voltage distribution and control system allows the gain of each APD to be tuned by setting the bias voltage individually. The gain of each APD is tuned by channels the bias voltage separately for each unit. The accuracy of the voltage control is 0.2 V. This corresponds to $\sim 0.5\%$ variations in APD gain variations. The information about cell timing is calculated in the offline pulse-shape analysis.

The energy resolution of the spectrometer depends on the energy of the incoming particles. Empirically, the relative energy resolution can be described by the following function:

$$\frac{\sigma_E}{E} = \sqrt{\left(\frac{a}{E}\right)^2 + \left(\frac{b}{\sqrt{E}}\right)^2 + c^2}, \tag{2.1}$$

where E is the energy of a fired cluster measured in GeV, a represents noise contribution that dominates at low p_{T}, b takes into account characteristic effects of detector dominated at high p_{T} and the constant c describes the calibration error. These parameters were calculated in an electron beam tests with PHOS prototype composed of a single 3×3 cell detector [101]. The resulting parameters are presented in table 2.2. The relative energy

resolution as a function of cluster energy is shown in Fig. 2.9. The same quantity was also studied in the dedicated Monte-Carlo simulations that show a good agreement with the measured data.

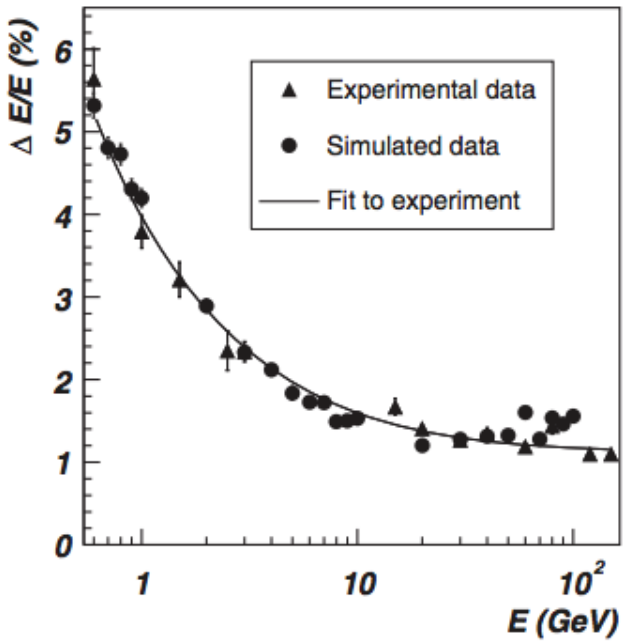

Figure 2.9: The relative energy resolution of PHOS detector as a function of incoming photon energy E measured in the electron beam tests [101]. The black triangles correspond to the experimental data. They were fitted with an empirical formula 2.1. The black dots represent the Monte-Carlo simulations.

parameter	value	uncertainty
a (GeV)	0.0130	0.0007
b	0.036	0.002
c (GeV$^{1/2}$)	1.12	0.30%

Table 2.2: The parameters of the empirical function 2.1 that describe the relative energy resolution measured experimentally [101].

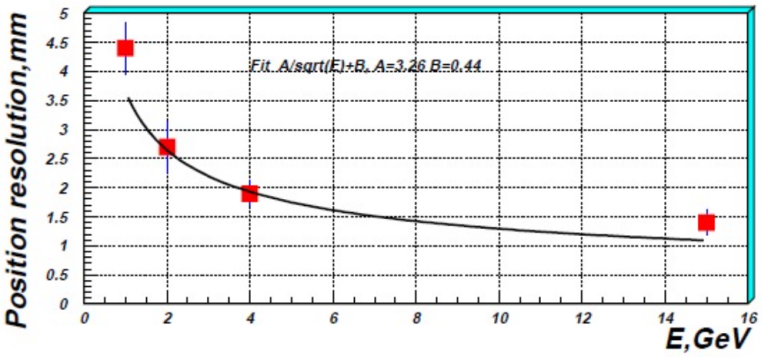

Figure 2.10: The spatial resolution of the PHOS detector as a function of the incoming particle energy E, measured in the electron beam tests [101] (red squares). The solid black line corresponds to the fit with an empirical function 2.2.

The spatial resolution of a neutral meson reconstruction in a photon spectrometer depends on the energy of the incoming meson. This is connected to the position of a

cluster created by the decay photons in the detector. At low energies, the photon signal is distributed more uniformly among the adjacent cells, and it is harder to determine the exact location of the cluster. The photons with higher energy tend to leave up to 80% of their energy in a single cell that simplifies their spatial reconstruction. This was studied experimentally in the electron beam tests as well [101]. It was observed that the spatial resolution of neutral pion reconstruction could be approximated in the following way:

$$\sigma_{x,y} = \frac{A}{\sqrt{E}} + B, \tag{2.2}$$

where A and B are free parameters which were determined from the fit. The numeric values of these parametrs are: $A = 3.26$ mm and $B = 0.44$ mm for neutral pions. The spatial resolution of the PHOS detector as a function the incoming particle energy is presented in Fig. 2.10.

Chapter 3

Analysis

This chapter presents the measurements of photons and the extraction procedure of the invariant cross-section of π^0 and η mesons as a function of p_{T} in proton-proton collisions at $\sqrt{s} = 13$ TeV with PHOS photon spectrometer. It is divided into three parts. The first section is devoted to the data description and the event selection. The second one describes the quality assurance (QA) analysis which considers PHOS performance in time. The last section of this chapter is about the neutral meson reconstruction in the two-photon decay channel.

3.1 Data Condition

3.1.1 Beam Condition

The experimental data on proton-proton collisions at $\sqrt{s} = 13$ TeV taken in 2016, 2017 and 2018 is the subject of the analysis reported in this thesis. The collisions (bunches) at LHC are described with the filling scheme. The sample of the filling scheme in 2016-2018 is `25ns_2076b_2064_1717_1767_96bpi_23inj`. The first number in this scheme corresponds to the time spacing between the main bunches, which is 25 ns. The second entry of it `2076b` refers to the total number of bunches in the LHC. This information is followed by the number of bunches colliding in ATLAS and IP4. This number is the same for both experiments as they are located at IP1 and IP4, which are opposite on the LHC circle. The next two digits correspond to the number of colliding bunches inside ALICE and LHCb detectors, respectively. The last digits on this symbol represent the technical information about the beam formation. There were 23 injections into LHC, 96 bunches each. The working intensity of each bunch at the LHC in this period was $\sim 1.15 \times 10^{11}$ protons per beam. Such configuration shows that the ALICE experiment has the smallest number of colliding bunches. This translates directly to the lowest luminosity. ALICE is designed to study strong interactions that have several orders of magnitude higher cross-sections and therefore requires fewer data to be collected.

The integrated luminosity is used to compare the statistics collected at colliding experiments it is defined as:

$$\mathcal{L}_{\mathrm{int}}^{\mathrm{MB}} = \frac{N_{\mathrm{pp}}^{\mathrm{MB}}}{\sigma_{\mathrm{pp}}^{\mathrm{MB}}},$$

where $\sigma_{\mathrm{pp}}^{\mathrm{MB}}$ is the minimum-bias cross section estimated with the V0 trigger. The minimum bias event in pp collisions is defined as that with a signal in both sides of the V0 detector: V0-A and V0-C. The value of $\sigma_{\mathrm{MB}}^{\mathrm{or}} = 57.8 \pm 1.2$ mb was determined experimentally with the pp Van Der Meer scan [103, 104]. The integrated luminosity of minimum bias data $\mathcal{L}_{\mathrm{int}}^{\mathrm{MB}} = 7.87 \pm 0.40$ nb^{-1} [102]. This corresponds to an average number of visible proton-proton interactions per bunch crossing equal to ~ 0.0065 for most of the runs.

3.1.2 Event selection

The minimum-bias trigger described above is defined to catch any interaction inside the central barrel detectors. Most of the time, this information is not useful. There are noise events that originate from beam-gas and gas-gas interactions. This type of data contains no useful information for the analysis and should be filtered out. Also, some of the recorded data may have high reconstruction errors. For these reasons, the additional selection of the processed events should be applied.

The position of a PHOS cluster is determined with respect to the primary collision vertex. It is important to select events with a well-defined position of the primary collision. Otherwise, a large systematic bias will be introduced in the photon momentum reconstruction procedure. The primary vertex of the collisions is measured by a silicon pixel detector (SPD) which is a part of the Inner Tracking System. SPD is able to determine the position of the primary vertex with precision which is higher than 300 μm in proton-proton collisions. The primary vertex can not be reconstructed properly if it is close to the edges of the detector. In order to increase the reliability of the measurement, the cut on the position of the vertex along the beam axis was used. Events with a single primary vertex reconstructed within 10 cm from the nominal interaction point are considered in the current analysis.

A pile-up event is an event that contains more than one proton pair collision in a single bunch crossing. It is important to take into account such events that are expected to occur as the collision probability per a bunch crossing, μ, is at the level of ~ 0.0064. The pile-up events are detected by SPD algorithms based on tracklet distributions. Such events are not considered in the current analysis as we are not able to estimate the cross-section of such event precisely.

Another source of background is beam-gas interaction. Events triggered by the beam-gas interactions are also removed from the analysis based on the signal from the V0 detector.

3.1.3 Run selection

Events recorded by ALICE are taken in runs, which are defined as a period when the detector was continuously recording the data. Each change of the LHC configuration requires the interruption of the data-taking. The data-taking can also be stopped when some problems with the detector were noticed, such as high busy time, software glitch or problems with the trigger. Within a single run, the configuration and the performance of the detectors must be constant. Only negligible variations of the efficiencies are allowed in the runs; otherwise, that run is marked as bad.

The number of bunches in the LHC, the bunch spacing (filling scheme in general) the intensity of the beams and the energy are changing. The intervals of time during which the LHC had the same configuration called run periods. The detectors are adjusted for the changes in beam conditions. The time scale of these periods varies from a couple of weeks to months. Usually, the detector teams can perform several detector runs within a single run period.

The analysis described in this chapter is based on the experimental data measured in proton-proton collisions at $\sqrt{s} = 13$ TeV. All the periods used in the analysis were reconstructed in `pass1` reconstruction, which is the first available reconstruction that includes all the detectors that are needed for physics extraction. The total list of runs per period can be found in Appendix A.

The status of the ALICE detector and hence the quality of the data is constantly changing in time. Therefore the first step of each physics analysis is the Quality Assurance of the measured data. One of the goals of this study is to find the parts of a dataset where the PHOS detector performance was uniform. There might occur a situation when

parts of a detector (cells or even entire blocks of cells) can break down and give wrong measurements. Such situations should be detected and fixed as even a couple of broken cells can distort the invariant mass spectrum of two photons. In the context of this analysis, the parts of the dataset that showed similar behaviour in time of physical quantities were selected for further analysis. All the cells that cause deviations were removed from the dataset or studied separately. The physics quantities that were used for run selection are the average energy of a cluster, the average number of clusters per event and the average number of cells per cluster.

In the QA analysis clusters were selected according to the same selection criteria as in physics analysis. The cut on the minimum cluster energy $E_{\text{cluster}} > 0.3$ GeV was applied to remove the minimum ionizing particles which can imitate photons in the detector medium. The minimal number of cells in the cluster was 3, as clusters made of 1 or 2 cells originate mainly from electrons. This requirement also suppresses the noise in the detector as the probability to have more than one noisy channel in a cluster is low. The example of such run-by-run distributions is shown in Fig. 3.1.

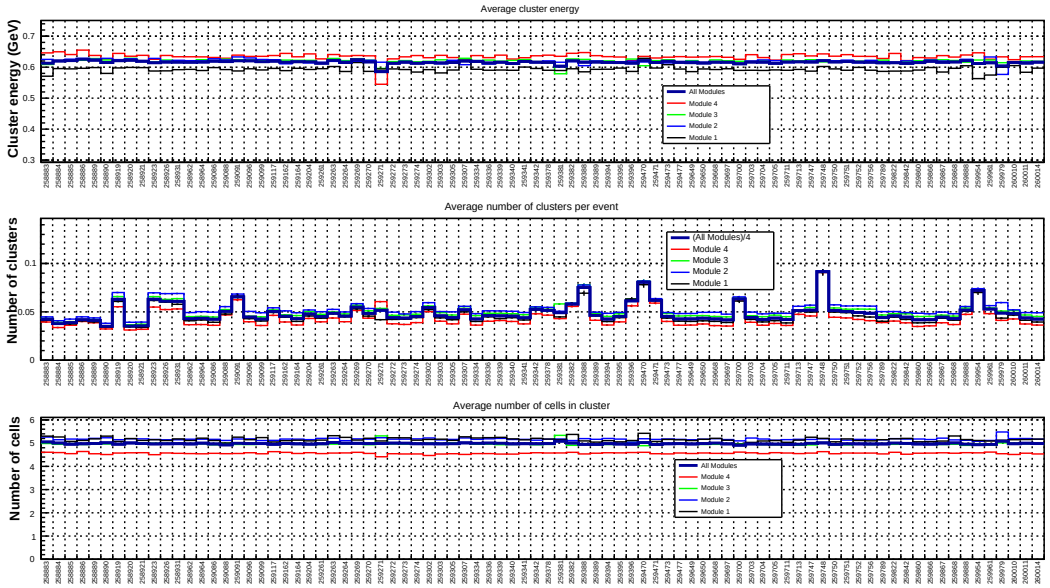

Figure 3.1: The upper plot shows the average energy in a PHOS cluster in the LHC16l run period. The middle plot corresponds to the average number of clusters per event. The bottom histogram shows the average energy of a cluster. All quantities are shown as a function of the run number that represents chronological order.

The horizontal axis in Fig. 3.1 corresponds to the run number, and it is the same for all plots presented. Three histograms show average cluster energy, averages the number of clusters per event and the average number of cells per cluster, respectively. One can see that the average number of clusters per event changes slightly in all four PHOS modules simultaneously. This is the effect of luminosity change. The intensity of the beams drops, therefore, the run taken at the beginning of the LHC fill will have a higher intensity and a larger number of pile-up events that contribute to the noise in PHOS. This also impacts the average cluster energy. The number of cells per run in module 4 is lower if compared to the average trend. This is connected with the acceptance of this module containing a smaller number of working channels. Looking at this plot one can conclude that the overall performance of PHOS was stable. The small changes in different runs look-alike in all modules. Only the runs that are close to the average trend of the performance histograms are considered in this analysis. The runs that have extreme values of cluster averages in a single module after bad channel extraction were excluded from the analysis. The same plots for all run periods can be found in Appendix B.

3.1.4 Channel selection

Cluster averages plots for PHOS detector sometimes show abnormal behavior for a particular module. For example, there are runs where the average number of clusters per event in a module is higher than the average, whereas average energy in the same module is lower than the general trend. This may indicate that there are some noisy channels in that run. An example of such behaviour can be shown in Fig. 3.1. This is a trending plot for a `LHC16l` period before removing noisy channels. The run `259271` has a significantly higher number of clusters on average than the other modules. At the same time, the average energy is lower. This is a clear indication that some noisy channels that contribute to the signal are present in the dataset.

Manual detection of such noisy channels is impossible due to the large size of the sample. To cope with this problem, a special algorithm for PHOS bad channel detection was used [105]. It counts the number of times a cell was in a cluster and the total energy of a cluster that the cell contributed to. For both quantities, a dimensionless "factor" is calculated. The factor is defined in the following way:

$$\text{factor} = \frac{\text{value for a cell}}{\text{average over cells}}.$$

In current analysis factor is calcuated for both quantities and in two energy regions. The low energy region includes photons in the range $0.3 < E < 1$ GeV. The high energy region considers photons with $E > 1$ GeV. Division in two energy intervals is necessary because the statistics of high energy clusters is smaller than the statistics for low energy region. Consequently, it would be difficult to detect some noise in high energy clusters as they would be less significant. An example of factor distribution in `LHC16l` is shown in Fig. 3.2.

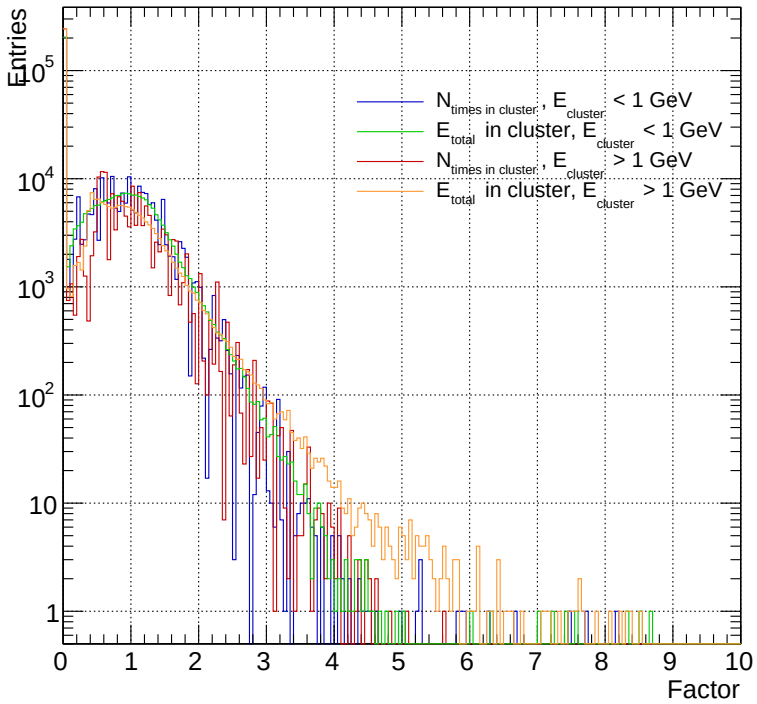

Figure 3.2: The factor distribution in the LHC16l run period. The number of times a cell participated in low (high) energy clusters are represented by blue (red) lines. The total energy of a cluster at low/high energies are plotted with green (yellow) lines.

The distributions in Fig. 3.2 are asymmetric. The moderate values of a factor were chosen for neutral meson measurement to remove the bad cells. The upper limit on the factor values was taken as 3.5. The lower limit is chosen to be 0.05, which removes only the completely inactive cells. If a cell shows an abnormal behaviour in 90% of runs, then the cell is considered as a bad one. Such cells then are marked as bad, and their signals are excluded from the analysis.

The described algorithm is iterative as the average will change after removing some cells. The limits were chosen to increase the convergence speed of the procedure as it requires reanalyzing of the entire dataset. The process of a good run and channel selections are connected as a change in the number of cells affects the runwise distributions and vice-versa. Both calculations are performed simultaneously. The cluster averages calculated after excluding all the noisy cells are shown in Appendix B.

3.2 Neutral meson reconstruction

3.2.1 Cluster selection

A high energy photon that enters the PHOS detector creates electromagnetic avalanche inside the PHOS cells. The signal appears when electrons and visible photons reach the sensitive photodiodes that are attached at the end of the scintillation crystals. The main mechanism of electron creation is e^+e^- pair production wich is the dominant process for at $E_\gamma > 1$ GeV in lead tungstate medium. The created electrons emit high energy photons that are able to produce electron-positron pairs by themselves. Particles that are created in the electromagnetic showers expand in all directions. Therefore a single photon can leave a signal in several neighbouring cells. All adjacent cells that have signal exceeding the noise threshold are grouped into a cluster [106].

There is some ambiguity in the cluster definition as they may originate from photons, electrons, neutrons or simply from the noise. Additional requirements for such clusters should be imposed to filter the data suitable for the analysis. Photon candidates are required to pass the following criteria:

- Low energy threshold. In this analysis $E_{\text{min}} = 0.3$ GeV. This value was used to remove minimum ionizing particles that have energy close to 0.25 GeV.
- Cluster size cut. Only clusters that have a number of cells greater than 3 are considered in order to reduce the contamination from clusters that do not belong to photons.
- Timing cut. In the LHC Run2, the bunch spacing is 25 ns but the exposition time of PHOS is ~ 6 μs. This means that PHOS measures photons that are coming from different bunch crossings. Since it was impossible to determine the cross-section of such events, the photons that are coming from other bunch crossings should be removed. The clusters that are measured within 12.5 ns (half of the bunch spacing time) are considered in the analysis.
- Bad channels. The clusters that contain a bad channel are removed from the analysis as the energy estimation is not reliable in this case.

The low energy threshold puts a limit on the lowest accessible energy in PHOS. The constraint on a cluster size reduces the background. The efficiency of both cuts was estimated through Monte-Carlo simulations. The timing window significantly reduces the number of measured clusters, and the spectra were corrected for the cut efficiency, which was calculated from the data itself. Channels excluded in the analysis define the

acceptance of PHOS. It was studied together with reconstruction efficiency in the Monte-Carlo simulations. The standard bin-by-bin correction technique was applied to the raw yield in the analysis. The calorimeters of ALICE have different sizes, and it is difficult to compare the performance of such detectors directly. To circumvent this complication the acceptance of a detector A is calculated simultaneously with the reconstruction efficiency ε. This results in a composite quantity $\varepsilon \cdot A$ which can be estimated using Monte-Carlo simulations. Another advantage of this approach is the simplicity of computations. By definition, $\varepsilon \cdot A$ corresponds to a ratio of generated to reconstructed particle spectra.

3.2.2 Raw yield extraction

The uncorrected spectra of π^0 and η were reconstructed by calculating the area under the invariant-mass peak of PHOS cluster pairs. Invariant mass histograms were constructed for different p_{T} bins and contain all possible combinations of two clusters that were detected in the event and passed the cuts. Examples of such distributions for π^0 and η mesons are shown in Fig. 3.3.

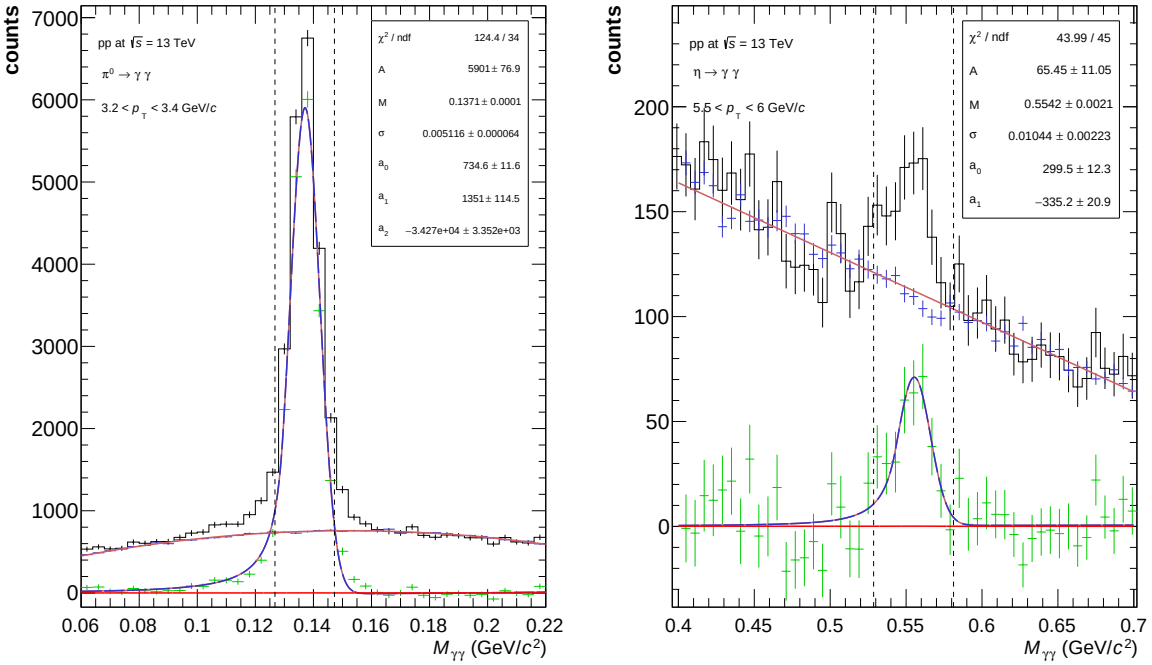

Figure 3.3: The black points correspond to the two-cluster invariant mass distribution, the blue points represent the combinatorial background estimated with the mixing-event technique, the solid red line corresponds to the background approximation (second-degree polynomial with a_i parameters for π^0 and linear fit for η meson), green points refer to the signal distribution after the background subtraction and the solid blue line shows the Crystal Ball [107] approximation of the signal distribution.

The number of mesons can be extracted from the area under gaussian-like peaks near the meson masses, but invariant-mass distributions calculated in this way contain the combinatorial background which should be subtracted. To estimate the background contribution, the "mixing" technique was used.

The idea behind this method is to calculate invariant mass distributions with clusters that come from different events. Their single-particle distributions will have a similar shape, whereas the peaks from neutral mesons will be absent as clusters from different events are uncorrelated. The mixing-event distribution was normalized and subtracted from the real one to obtain a signal distribution. The experimental and the mixed-event

distributions of invariant masses of PHOS clusters are shown in Fig. 3.3 by black and blue colours respectively. The combinatorial background was fitted with a second-degree polynomial for the neutral pions and with a linear function for the η mesons.

In the next step, both raw and signal two-gamma mass distribution peaks were fitted with the Crystal Ball function [107]. It is a modified version of the normal distribution that has an asymmetric shape:

$$f(m;\alpha,n,m_{\text{meson}},\sigma) = N \cdot \begin{cases} A \cdot (B - \frac{m-m_{\text{meson}}}{\sigma})^{-n}, & \text{for } \frac{m-m_{\text{meson}}}{\sigma} \leq -\alpha \\ \exp\left(-\frac{(m-m_{\text{meson}})^2}{2\sigma^2}\right), & \text{for } \frac{m-m_{\text{meson}}}{\sigma} > -\alpha \end{cases} \tag{3.1}$$

where α and n are the parameters of the fit, N – is the normalization constant, A, B coefficients are defined in the following way:

$$A = \left(\frac{n}{|\alpha|}\right)^n \cdot \exp\left(-\frac{|\alpha|^2}{2}\right),$$

$$B = \frac{n}{|\alpha|} - |\alpha|\,.$$

Free parameters α and n have physical interpretations. These parameters describe energy loss in the PHOS detector. Parts of electron shower can spread across several neighbouring cells if the energy fraction of the shower in a particular cell is lower than the threshold energy E_{zero}. Such a cell is not taken into account, and the fraction of energy deposited in it is lost. The values of these parameters were determined from the experimental data. For each p_{T} bin invariant mass spectrum was fitted with free α and n. These parameters were fitted with a zero degree polynomial in p_{T} as shown in Fig. 3.4. It can be seen from

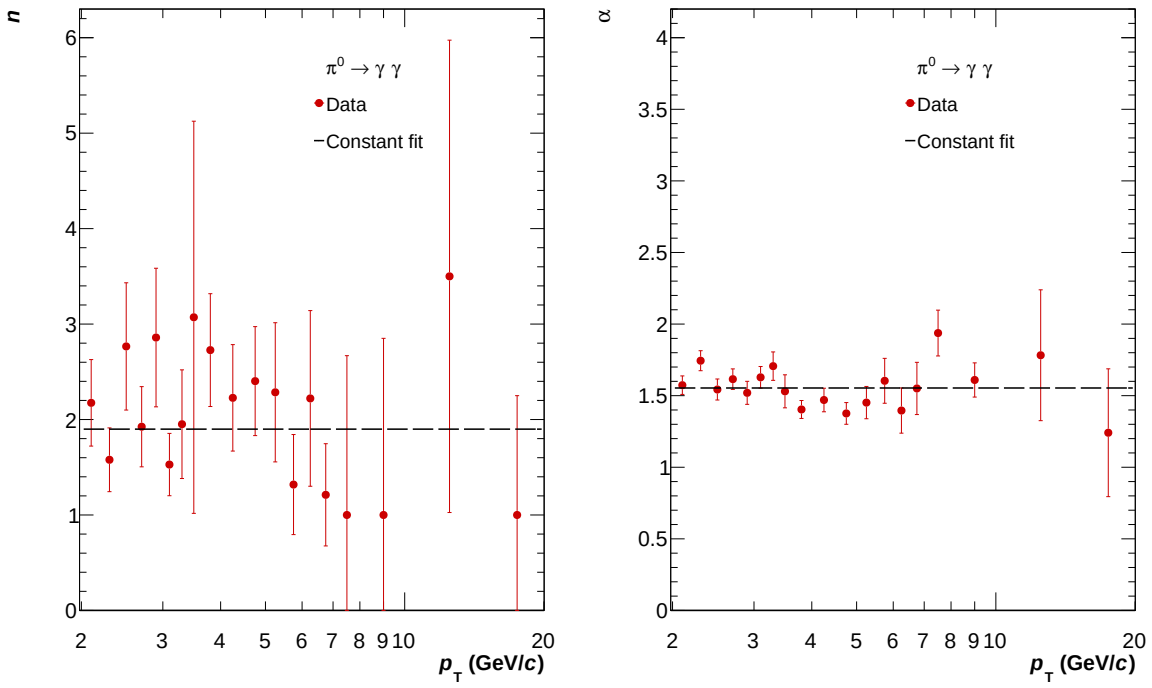

Figure 3.4: Crystal Ball (3.1) parameters n and α as a function of p_{T} estimated from π^0 peaks. The dashed lines correspond to constant fits.

this figure that parameter n has large errors. It is sensitive to small changes in the data. The parameter α is more stable to the fluctuations. The two-photon distributions for η meson have the order of magnitude fewer entries and the Crystal Ball parameters α and n estimated from the fits have larger fluctuations than in the π^0 case. Since these parameters

describe energy loss in the same detector under the same conditions, their values should be identical. The final values of α and n parameters extracted from the linear fits are listed in table 3.2.2. It is possible to describe both peaks with the generalized version of

quantity	value
α	1.554
$\Delta\alpha$	0.021
χ^2/ndf	1.82
n	1.899
Δn	0.132
χ^2/ndf	0.79

Table 3.1: The parameters n and α of the Crystal Ball approximation for π^0 peaks obtained with a linear fit in the $0 < p_{\mathrm{T}} < 20$ GeV/c interval in pp collisions at $\sqrt{s} =$ 13 TeV.

the Crystal Ball 3.1 function with all parameters free. This option produces better fits in each p_{T} bin, however, it leads to higher systematic errors. The neutral meson peaks can also be approximated by Gaussian functions. This approach yields almost the same results, but the quality of fits in each p_{T} bin is somewhat lower. Additionally, this leads to an increase in a systematic error. A more detailed discussion of systematic uncertainties is presented in the following chapters.

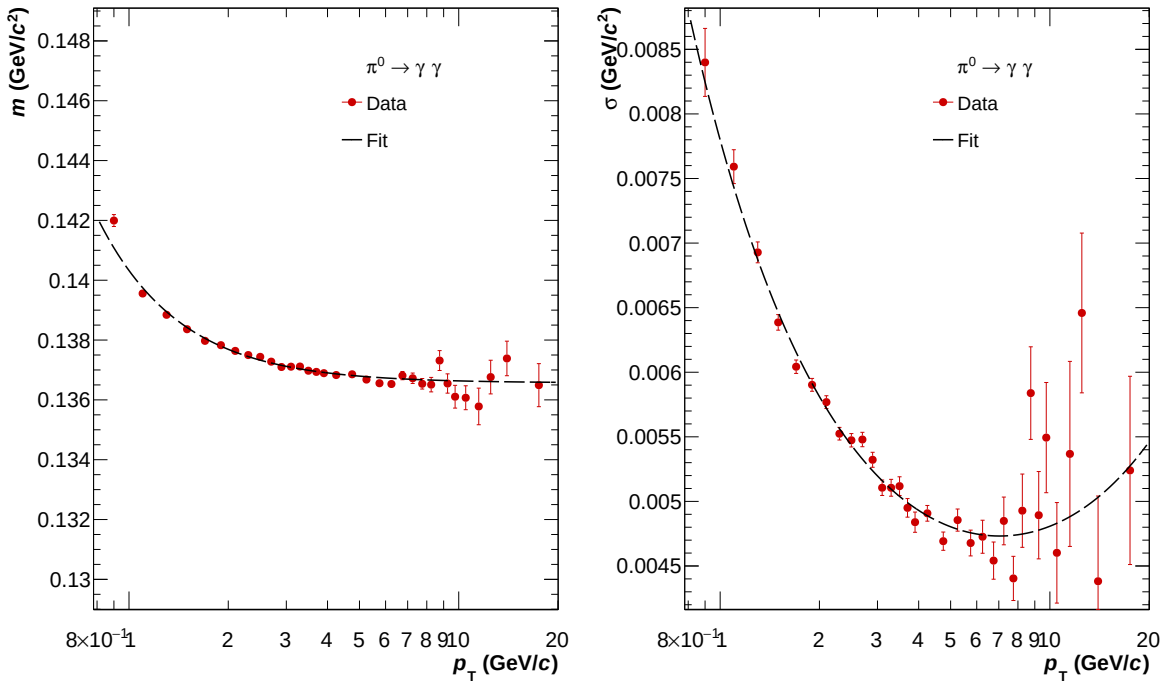

Figure 3.5: The neutral pion peak position m (left plot) and width σ (right plot) as a function of p_{T}. The red dots correspond to experimental data calculated in pp collisions at $\sqrt{s} = 13$ TeV while the black dashed line represent smooth approximations of the distributions.

The position of the neutral meson peak corresponding to a mass of the meson depends on the transverse momentum. This is caused by energy loss in the detector. As described above, high energy photon fires more cells, but some of the signals from those cells happen to be below the detection threshold. Hence the peak positions and widths measured can depend on the transverse momentum of mesons. The dependence of the peak parameters

on p_{T} are shown in Fig. 3.5 for π^0 and in Fig. 3.6 for η meson. One can notice the difference in mass and width parameters for the π^0 and η due to the different background contributions. The mass of π^0 decreases with p_{T} and levels off at the value close to that of the Particle Data Group (PDG) [7]. This is explained by the energy loss caused by thresholds in readout electronics. Since high energy cluster consists of more cells, more energy is lost during the signal digitalization. The mass of the π^0 is larger for the low p_{T} as the low-energy photons trigger fewer cells leading to the smaller energy loss. PHOS is calibrated to reproduce the expected value of π^0 mass at higher p_{T}. The absolute value of the meson mass is, however, not important for this analysis as soon as it is the same in the Monte-Carlo simulations used to calculate the efficiency. This effect is not visible for η meson mass (see the left plot in Fig. 3.5). The lowest accessible energy for η reconstruction is 2 GeV/c, which is already in the saturation region of the mass distribution. The shape of the width of the neutral meson peak can be explained by the spatial and energy resolutions of photon measurements. Their precision increases with p_{T} and reaches its maximum at $p_{\mathrm{T}} \sim 9$ GeV/c. At higher energies, the contribution of the noise from readout electronics leading to the increase of the π^0 width. This effect is negligible for η mesons due to statistics at high p_{T}.

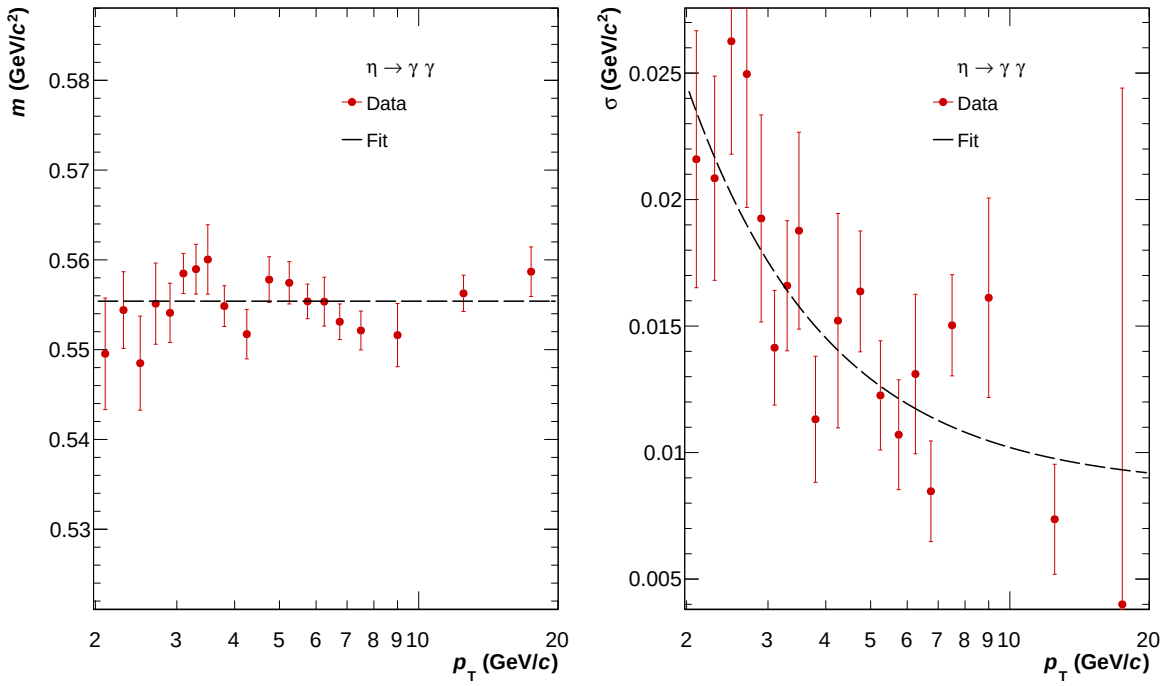

Figure 3.6: Crystal Ball (3.1) parameters n and α as a function of p_{T} estimated from η peaks. The dashed lines correspond to the approximations.

The parameters estimated from invariant-mass distribution are very sensitive to small changes in the input data and the initial values of the parameters. The fluctuations in raw yields influence the peak parameters significantly. This contributes to systematic errors. Smooth representations of neutral meson mass position m and width σ are used to solve the problem with numerical stability of the fits. These parameterizations are purely empirical and only account for the detector effects. The continuous representation of π^0 mass dependence on p_{T} can be approximated with:

$$m_{\pi^0}(p_{\mathrm{T}}) = (a \cdot p_{\mathrm{T}})^{-b} + c,$$

where a corresponds to the scale, b is the power-law exponent and c is the asymptotic mass value at high p_{T}. These are free parameters, and they are extracted from the fit.

This function takes into account the power-law behaviour of PHOS energy response at low p_{T} and describes saturation at the higher transverse momenta. The smooth parameterization of η mass is defined as $m_{\eta}(p_{\mathrm{T}}) = c$. The position of η meson peak m_{η} is the same for different p_{T} bins as the experimental distribution starts at $p_{\mathrm{T}} = 2$ GeV/c. These parameterizations are presented as the dashed lines in Fig. 3.5. They show a good agreement with the experimental data. The optimal values of the parameters are listed in table 3.2.

Since the π^0 peak width σ has a similar dependence on p_{T}, it can be parameterized with a similar function:

$$\sigma_{\pi^0}(p_{\mathrm{T}}) = (a \cdot p_{\mathrm{T}})^{-b} + d \cdot p_{\mathrm{T}} + c,$$

where a, b, c – are the free parameters that were determined from the fits. The additional linear term $d \cdot p_{\mathrm{T}}$ describes a slight increase of π^0 peak width at high p_{T}. The η meson peak parameterization is similar to that of pions, except for the linear term, whose contribution was found to be close to zero and was discarded in η meson analysis. The dashed lines in Fig. 3.5 and Fig. 3.6 represent the peak width continuous parametrizations for π^0 and η meson respectively. The exact values of the parameters obtained from the fits are listed in table 3.2.

The obtained from the fit experimental π^0 to η meson mass ratio $m_{\pi^0}/m_{\eta} = 0.24685 \pm 0.00843$ (stat.) is close the the PDG value of $m_{\pi^0}/m_{\eta} \sim 0.24636$ [7]. This is an indication of a good spatial calibration of PHOS. It should be noted that this estimate of m_{π^0}/m_{η} contains only statistical error. The systematic uncertainty of this quantity was not calculated as the exact values of the meson masses do not change the final spectra. The comparison to the PDG serves as a consistency check for this analysis.

peak position m	π^0	η
a (GeV/c^{-1})	$2.4658 \times 10^1 \pm 3.542$	
b	$1.742 \pm 7.6 \times 10^{-2}$	
c (GeV/c^2)	$1.37 \times 10^{-1} \pm 4.67 \times 10^{-3}$	$5.55 \times 10^{-1} \pm 1 \times 10^{-3}$
χ^2/ndf	2.19	0.98

peak width σ	π^0	η
a (GeV/c^{-1})	$2.745\,34 \times 10^2 \pm 1.251\,30 \times 10^2$	$9.107 \pm 1.2942 \times 10^1$
b	$9.74 \times 10^{-1} \pm 8.8 \times 10^{-2}$	$1.426 \pm 7.01 \times 10^{-1}$
c (GeV/c^2)	$3 \times 10^{-3} \pm 1 \times 10^{-5}$	$9 \times 10^{-3} \pm 3 \times 10^{-3}$
d (c^{-1})	$1 \times 10^{-3} \pm 1 \times 10^{-4}$	
χ^2/ndf	1.92	1.24

Table 3.2: The parameters of peak position m and width σ distributions approximations, extracted from the fit of π^0 and η meson data.

The number of mesons in particular p_{T} bin is calculated using the bin counting technique in the region near the peak centre $m(p_{\mathrm{T}})$. The size of this window is taken to be $2\sigma(p_{\mathrm{T}})$. The widths of the integration region are the same for π^0 and η mesons. The choice of the integration region of 2σ was found to be optimal. Other possibilities up to 5σ were studied, and a 2σ window appeared to be the best tradeoff between the accuracy and precision giving the central values with the smallest systematic uncertainties. Different parameterizations of π^0 and η meson masses and widths were studied as well, but the presented ones provide the smallest χ^2/ndf and the highest stability of the final results. A more detailed description of the systematic uncertainties connected with the raw yield extraction is presented in the next chapter.

The raw yields of the neutral mesons are defined as the number of neutral mesons reconstructed in a given p_{T} bin $\Delta N_{\mathrm{rec}}(p_{\mathrm{T}})$ normalized by the width of that bin Δp_{T} and

divided by the number of events $N_{\rm ev}$ that passed event-selection criteria described earlier:

$$\frac{dN_{\rm rec}}{dp_{\rm T}}(p_{\rm T}) = \frac{1}{N_{\rm ev}} \frac{\Delta N_{\rm rec}(p_{\rm T})}{\Delta p_{\rm T}(p_{\rm T})}.$$

The raw uncorrected yields for neutral pion and η mesons are presented in Fig. 3.7. The error bars shown correspond to statistical uncertainties obtained from the bin-counting procedure.

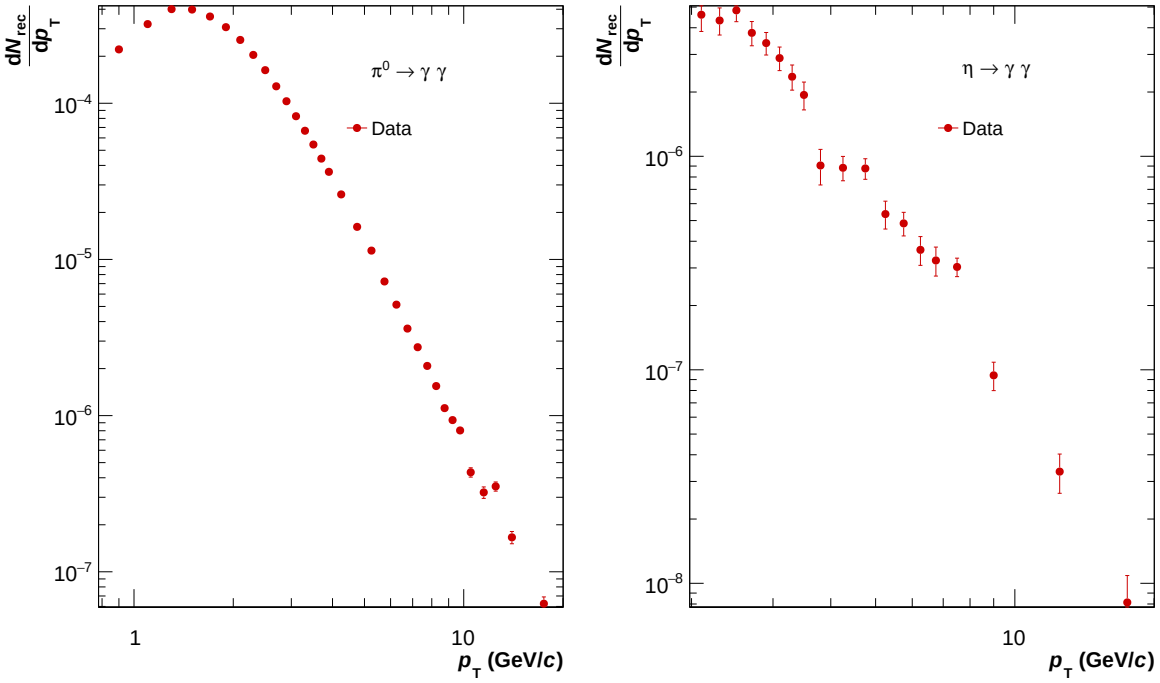

Figure 3.7: The raw uncorrected yields for neutral pion (left plot) and η mesons (right plot). Only statistical errors are presented.

The lowest $p_{\rm T}$ bin for π^0 measurement is 0.8 GeV/c. It is determined by the minimum ionizing particles cut of 0.3 GeV on the energy of the cluster. For η meson, the lowest $p_{\rm T}$ measured is 2 GeV/c because of the PHOS acceptance for the angle between two decay photons. The number of η mesons in each $p_{\rm T}$ region is significantly lower than that for neutral pions. The bin-by-bin fits of invariant masses in different $p_{\rm T}$ ranges are presented in Appendix C

3.2.3 Timing cut efficiency

As it was mentioned earlier, the exposition time of PHOS ($\sim$ 6 μs) is much larger than the distance between LHC bunches (25 μs). Consequently, PHOS can measure clusters originated from different bunch crossings. To remove the clusters that do not belong to the triggered event, the timing cut of 12.5 ns was applied. The procedure was as follows: the cell in a PHOS cluster that has the highest amplitude in avalanche photodiode (APD) counts was called the leading cell. It contains the maximum fraction of energy deposited by a particle in this cluster. The timing of the leading cell was adopted as the timing of the cluster. Consequently, it depends on the cluster energy. The time resolution decreases with energy as it is more difficult to measure a time of flight with respect to the cell with a low signal amplitude corresponding to a low energy particle. The time distributions of clusters as a function of energy is shown in Fig. 3.8. The horizontal axis in that plots corresponds to the cluster energy while the vertical one represents the time in nanoseconds.

The peak at zero nanoseconds corresponds to the triggered bunch crossings. It contains all the clusters that are coming from the main bunch-bunch interactions. The secondary peaks originate from the neighbour bunch crossings, and the distance between them is exactly 25 ns.

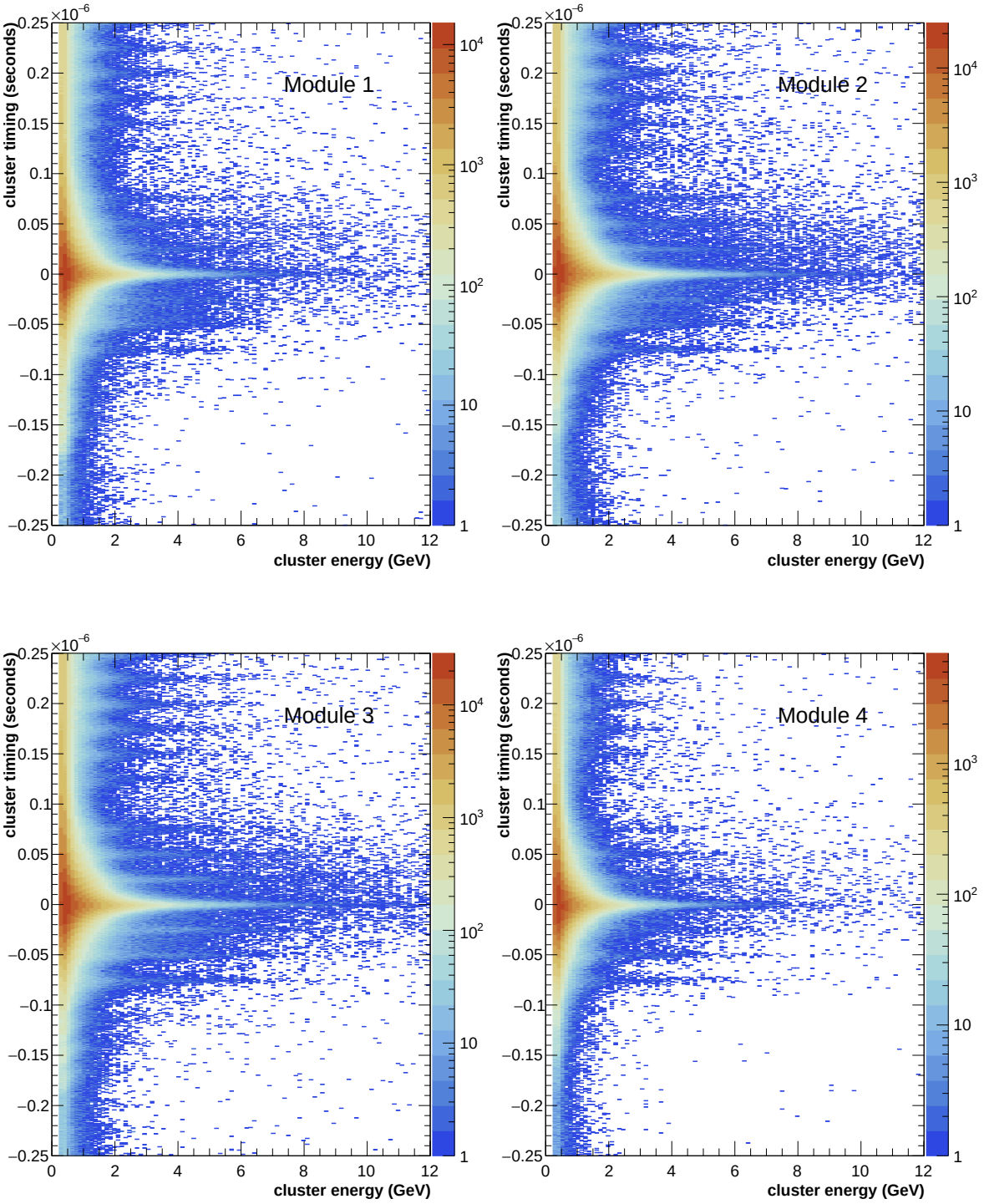

Figure 3.8: The cluster timing distributions in different PHOS modules as a function of the cluster energy. The peaks at 25 ns intervals correspond to the different bunch crossings. The resolution increases with the energy of a cluster.

The cluster time distributions in Fig. 3.8 are not symmetric. The peaks in the negative part of the time axis correspond to the bunch crossings that occurred before the triggered event. They contain fewer statistics than the distributions in the positive part of the time axis. This is connected to the trigger system and readout electronics of PHOS.

The differences in the distributions are the result of the small variations in modules energy calibration. They can be disregarded as in the previous section, and it has been demonstrated that both π^0 and η mesons can be reconstructed with a high resolution.

The performance of the timing cut is not uniform. It can be seen in Fig. 3.8 that the number of points in the vicinity of ± 12.5 ns lines depends on the position on the horizontal axis. The efficiency of this cut strongly depends on the energy of the cluster measured by PHOS. Since the magnitude of timing resolution varies significantly, this correction can not be neglected.

The efficiency of timing cut was defined as a ratio of the number of clusters that come from the same bunch crossings relative to the total amount of particles. The direct calculation of this quantity is systematically biased by the noise particles. The ratio, however, is less sensitive to the noise in the invariant mass distributions of a pair of photons. This observation was used in formulating the tag and probe technique which is more accurate and resistant to the noise. The main idea of this method is to select photons from neutral pion decays to reduce the background.

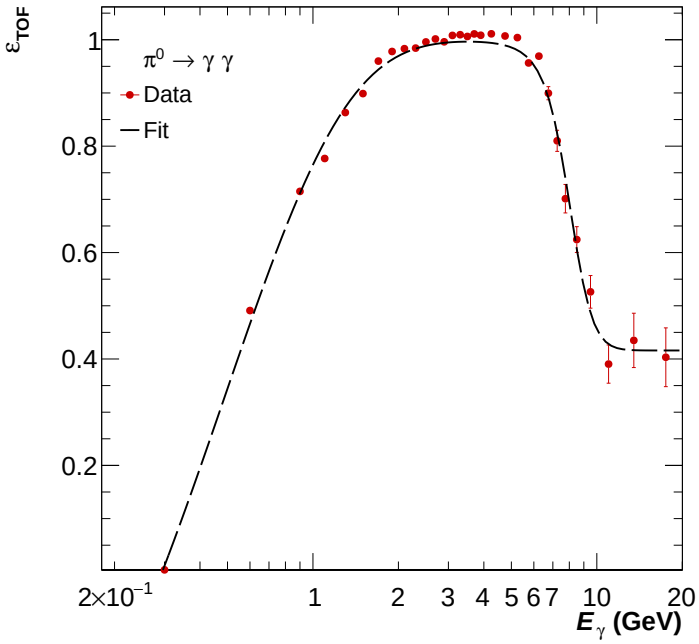

Figure 3.9: The timing cut efficiency as a function of cluster energy estimated with the tag and probe method in pp collisions at $\sqrt{s} = 13$ TeV. The dashed line corresponds to a continuous parametrization. The uncertainties in each p_{T} bin correspond to binomial errors propagated from tag and probe signals ratio.

The algorithm is as follows: a photon that passes 12.5 ns timing cut is selected as a "tagged cluster". It is used to construct invariant mass combinations, and it defines the point where the cut should be applied. The probe clusters are defined as all photons that form a system with the tagged clusters and an invariant mass close to the π^0 signal in the region $0.11 < m_{\gamma\gamma} < 0.13$ GeV/c^2. All combinations of tagged and probe photons are considered. In the final stage of the computation, the invariant mass of such a system was taken within the 2σ range near the π^0 peak, and the signal was extracted. The timing cut efficiency estimated by the tag and probe method is defined in the following way:

$$\varepsilon_{\mathrm{TOF}} = \frac{\text{spectrum of probe photons that pass 12.5 } n\text{s cut}}{\text{spectrum of all probe photons,}},$$

where the numerator of $\varepsilon_{\mathrm{TOF}}$ takes into account combinations of clusters that both pass the timing cut, at the same moment the denominator consists of the combinations were

only tagged photon comes from the triggered bunch crossing. Clusters originating from different events will not contribute to the π^0 peak. Both quantities measure the number of neutral pions in the same bunch crossing, but the denominator also contains the combination rejected by the timing cut (e.g. fraction of lost mesons due to timing constraint). In the perfect detector, the number of such combinations should be equal to zero, making thus the ratio equal to one. The efficiency of timing cut calculated in pp collisions at $\sqrt{s} = 13$ TeV with tag and probe method is presented in Fig. 3.9.

The timing cut efficiency $\varepsilon_{\mathrm{TOF}}$ is small at low p_{T}. This is a reflection of the fact that time distributions at low cluster energies are wider (as seen from Fig. 3.8). The efficiency improves with p_{T} and drops above $p_{\mathrm{T}} \sim 6$ GeV/c. This is connected with the switch to high gain channels of PHOS readout electronics (the upper threshold for low gain channels is 5 GeV). This $\varepsilon_{\mathrm{TOF}}$ at low p_{T} is significantly smaller than at $p_{\mathrm{T}} \sim 6$ GeV/c as low gain channels give smaller amplification of the signal leading to worse resolution.

The $\varepsilon_{\mathrm{TOF}}$ is approximated with a smooth function defined as:

$$\varepsilon_{\mathrm{TOF}}\left(E_\gamma\right) = 1 - \frac{c}{\exp\left(a \cdot E_\gamma + b\right) + 1} - e \cdot \exp\left(E_\gamma \cdot d\right),$$

where $a,\ b,\ c,\ d$ and e – are the free parameters that are constrained from the fit. The exponential part corresponds to the increase of the efficiency at low p_{T}. The sigmoidal term describes the switch to the high gain channels, and the constant term takes into account a levelling at the highest p_{T}. The unweighted log-likelihood minimization procedure was applied to fit the data as it gives well defined $\tilde{\chi}$-loss landscape in this case. The values of the fit parameters are summarized in table 3.3.

parameter	value	uncertainty
a (GeV/c^{-1})	-1.259	4.536
b	9.979	33.601
c	0.584	0.605
d (GeV/c^{-1})	1.830	3.089
e	-2.053	3.318
$\tilde{\chi}^2$/ndf	0.00519	

Table 3.3: Parameters of the fit of the timing cut efficiency parameterizations $\varepsilon_{\mathrm{TOF}}(E_\gamma)$ obtained by minimizing the unweighted $\tilde{\chi}^2$/ndf distance between the smooth representation and the experimental data.

The efficiency is applied to each cluster pair combination. The measurements of two different photons are assumed to be independent. Each two-cluster combination in $(m_{\gamma^1\gamma^2}, p_{\mathrm{T}})$ space is weighed with $1/\varepsilon^1_{\mathrm{TOF}} \times 1/\varepsilon^2_{\mathrm{TOF}}$ factor, where $\varepsilon^i_{\mathrm{TOF}}$ corresponds to the timing cut efficiency of the i-th photon cluster.

3.2.4 Reconstruction efficiency

The cuts that were introduced at the beginning of this section remove background and noise clusters. However, they also remove real photons that originate from π^0 or η decays. Therefore the measured raw yield is several orders of magnitude smaller than the real physical one. Also, a fraction of mesons is lost because of the detector acceptance. The final spectra should be corrected for the detector effects of the measurement. It is also important to know the differences in performances of ALICE calorimeters when combining the measurements from different subdetectors. The reconstruction schemes differ for different detectors to take advantage of each scheme in the corresponding kinematic region. It is hard to compare the performance of all the calorimeters directly as their sizes vary significantly. For example, photons reconstructed via photon conversion method (PCM)

use TPC, which covers most of the phase space whereas PHOS occupies only a small fraction of the phase space and is located outside the central barrel. The product of reconstruction efficiency ε and the detector acceptance A is used to relate the performance of the different systems. Each particle (or decay) channel has it is own definition of $\varepsilon \cdot A$ quantity as it takes into account all the cuts applied at the reconstruction level which have different impacts on various particle species. For neutral mesons, $\varepsilon \cdot A$ factor is defined as a fraction of all reconstructed to all incoming particles. This definition is very simple, and it corresponds to the normalization factor that should be applied to the raw yield to remove the detector effects. Unfortunately, it can not be estimated precisely with data-driven methods. That is why the Monte-Carlo simulations are widely used to determine the $\varepsilon \cdot A$ values in ALICE calorimeters [30, 32, 35, 33, 50]. This method can be divided into two steps: event generation and propagation through the material of the detector. The event generators produce the particles with their momenta according to the lower orders of perturbation theories or phenomenological models. The most commonly used Monte-Carlo event generators for pp collisions are PYTHIA [61, 34] and EPOS [52]. The passage of the generated particles through the material of the detector is calculated employing transport packages. ALICE experiment uses GEANT [108, 109] simulation framework. It calculates the energy loss of each particle in the material of the detectors that allows reconstruction of particles in Monte-Carlo generated events.

In the case of PHOS the efficiency estimation based on the PYTHIA 8 [34] and EPOS [52] Monte-Carlo generators suffer from high statistical uncertainty. These productions contained $\sim$ 280 and 90 million minimum bias events respectively and were generated centrally by the ALICE collaboration. The number of particles decreases with energy exponentially. In the high p_{T} region ($p_{\mathrm{T}} > 5$ GeV/c) the signal drops significantly. This effect is very strong for PHOS as it has the smallest acceptance if compared to other calorimeters.

In order to solve the problems with the statistical significance, the dedicated single-particle Monte-Carlo production was generated for PHOS analyses. Each event in such simulation contains only one primary meson with the transverse momentum sampled from the uniform distribution. Since there is always only one type of particles available, the higher statistical significance can be achieved with the same volume of data.

The standard Monte-Carlo event generators such as PYTHIA 8 are not suitable for this analysis as they always favour low energy particles. Another disadvantage of such an approach is the shape of the single-particle spectra. Previous measurements show that PYTHIA Monte-Carlo production can overpredict the light meson spectra up to 60% [30, 33]. The reconstruction efficiency does not depend on the generated signal spectrum directly. However, the generated spectra have a large impact on the shape of the combinatorial background. This means that large changes in the shape of the particle yield as a function of p_{T} lead to a high systematic bias of the measurement. The differences in the spectral shapes can be fixed by re-weighting the generated distributions.

In this analysis, a flat p_{T} distribution has an advantage as the weighting function, in this case, corresponds to the smooth approximation of the corrected yield. The procedure of re-weighting of the Monte-Carlo production was iterative. It starts with the uncorrected signal, which is used to calculate the efficiency. Then the corrected yield is extracted and fitted with a smooth function to obtain the weights for the next iteration. The process is repeated until the differences in weight function parameters in two subsequent iterations are of the order of the errors obtained from the fit. In the case of the uniform distribution, the convergence is very fast. It takes only three iterations to obtain the stable parametrizations for both neutral pion and η yields. The spectra of π^0 and η mesons before and after re-weighting are shown in Fig. 3.10. The final parameters of smooth parametrizations, together with the definitions, are presented in the last chapter of the thesis.

In the low-p_{T} region, the reconstruction efficiency is significantly lower due to the acceptance. The opening angle between two-photon is large, and it gets smaller with the energy of the decaying particle. Hence the low p_{T} part of the spectrum requires higher statistics to obtain reliable estimates of the reconstruction efficiencies. For this reason, the single-particle Monte-Carlo production was generated in two regions. The low p_{T} region was $0 < p_{\mathrm{T}} < 8$ GeV/c for π^0 and $0 < p_{\mathrm{T}} < 10$ GeV/c for η mesons. The poductions contain $\sim 1.2 \times 10^8$ events for both particles. The high p_{T} part of the spectra are generated in $4 < p_{\mathrm{T}} < 100$ GeV/c range and contain $\sim 4.0 \times 10^7$ and $\sim 3.5 \times 10^7$ events for η and π^0, respectively.

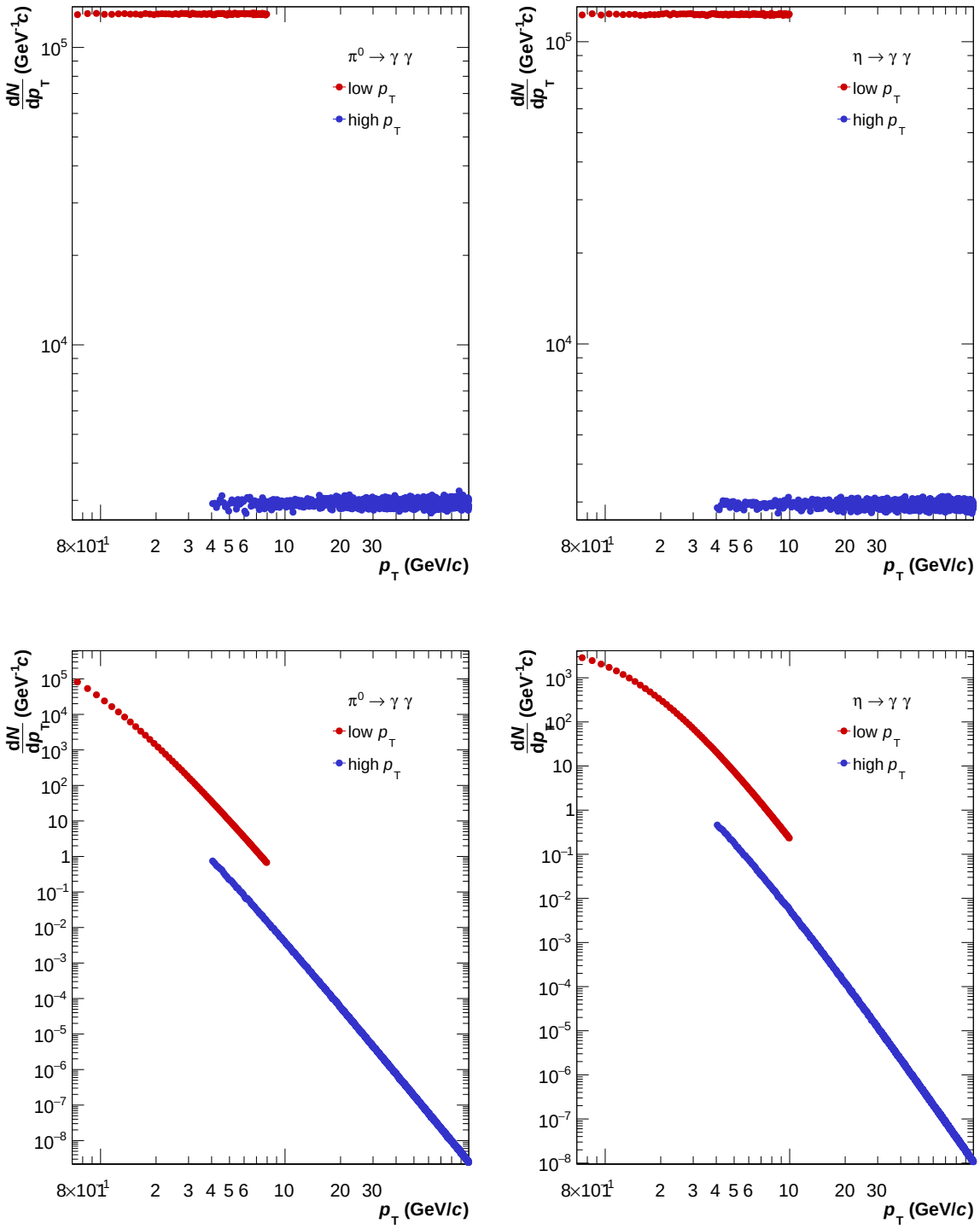

Figure 3.10: Generated p_{T} spectra of π^0 and η meson in the Single Particle Monte-Carlo production, no weights applied. Generated p_{T} spectra of π^0 and η meson in the Single Particle Monte-Carlo production weighted with the Tsallis function [49].

The splitting of the dataset into two parts was performed as a part of the memory and CPU optimizations. The storage for this type of analysis is limited, and this was required to be done to fit within the quota. The red and blue points in Fig. 3.10 correspond to low and high p_{T} regions, respectively. The transport of the generated particles through the material of the detector is a highly intensive CPU task. Also, the hits from these tracks require additional disc space. For these reasons, mesons in single-particle MC simulations were generated in the solid angle that corresponds to PHOS acceptance with additional margin to take into account the edge effects. Both π^0 and η meson signals were limited to $|y| < 0.15$ and $3\pi/2 < \varphi < 2\pi$. The two-dimensional distribution in polar angle-rapidity coordinates for photons reconstructed from neutral mesons decays is shown in Fig. 3.11.

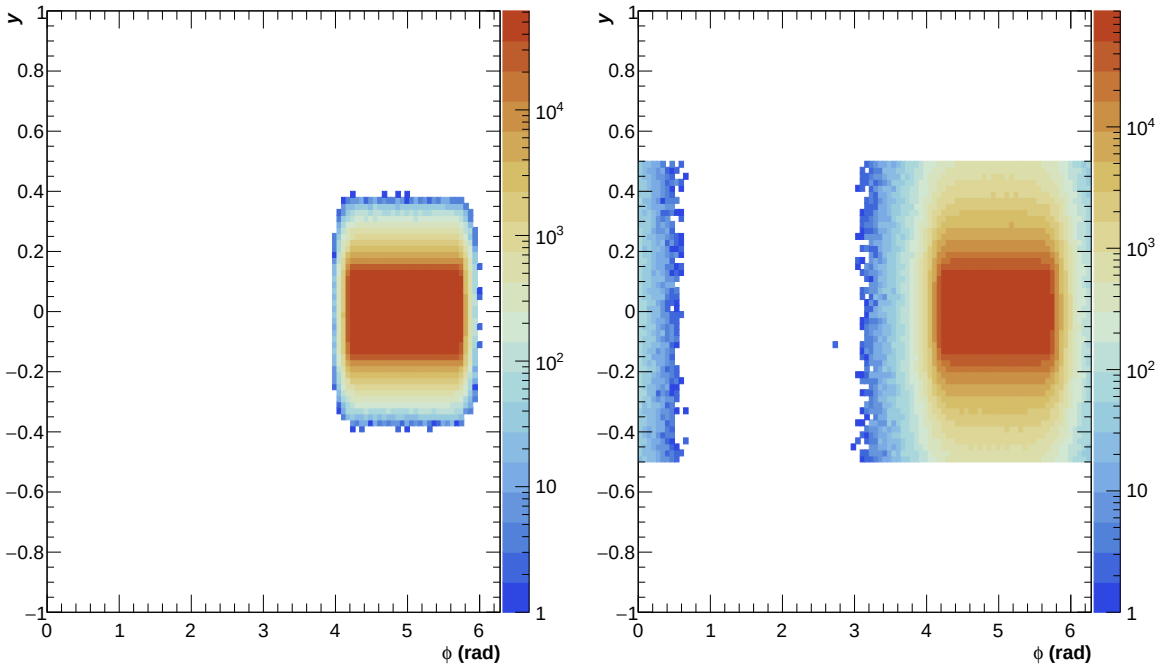

Figure 3.11: The phase-space covered by photons coming from meson decays in terms of rapidity y and polar angle φ. The two-dimensional distributions correspond to the single-particle Monte-Carlo production for π^0 (left plot) and η meson (right plot). The colors represent logarithm of the particle counts at the given point.

The distributions in Fig. 3.11 are the sum of low and high p_{T} productions. The spread of photons is larger for η mesons. This is caused by the wider opening angle between the decay photons. This figure demonstrates the difference between π^0 and η reconstruction with PHOS.

The part of the phase-space not covered by the single-particle Monte-Carlo production has no impact on the detector performance and the efficiency calculated with this method is the correct estimate. Other conditions and configurations of these productions were the same as in PYTHIA 8 simulations. The definition of single-particle Monte-Carlo simulations implies that they are suitable for efficiency calculations at different collision energies as there are no physical models or energy-dependent assumptions involved. The re-weighting of the generated p_{T} spectrum according to the experimental distributions was applied during the offline analysis as described above.

The efficiencies times acceptance $\varepsilon \cdot A$ are calculated separately for low and high p_{T} productions. Then they were merged by taking all the points below $p_{\mathrm{T}}^{\mathrm{treshold}}$ from the low p_{T} production and the points above these values were taken from the high p_{T} region. The value of $p_{\mathrm{T}}^{\mathrm{treshold}}$ for single π^0 MC production is equal to $p_{\mathrm{T}}^{\mathrm{treshold}} = 6$ GeV/c and for η simulations it is $p_{\mathrm{T}}^{\mathrm{treshold}} = 7$ GeV/c as they correspond to the centers of the overlap

regions in the corresponding productions.

It was already mentioned that the absolute values of the meson mass and width are not important in this analysis. However, it is necessary for these quantities to be reproduced by Monte-Carlo simulations. The peak positions and widths for different productions and the data are shown in Fig. 3.12.

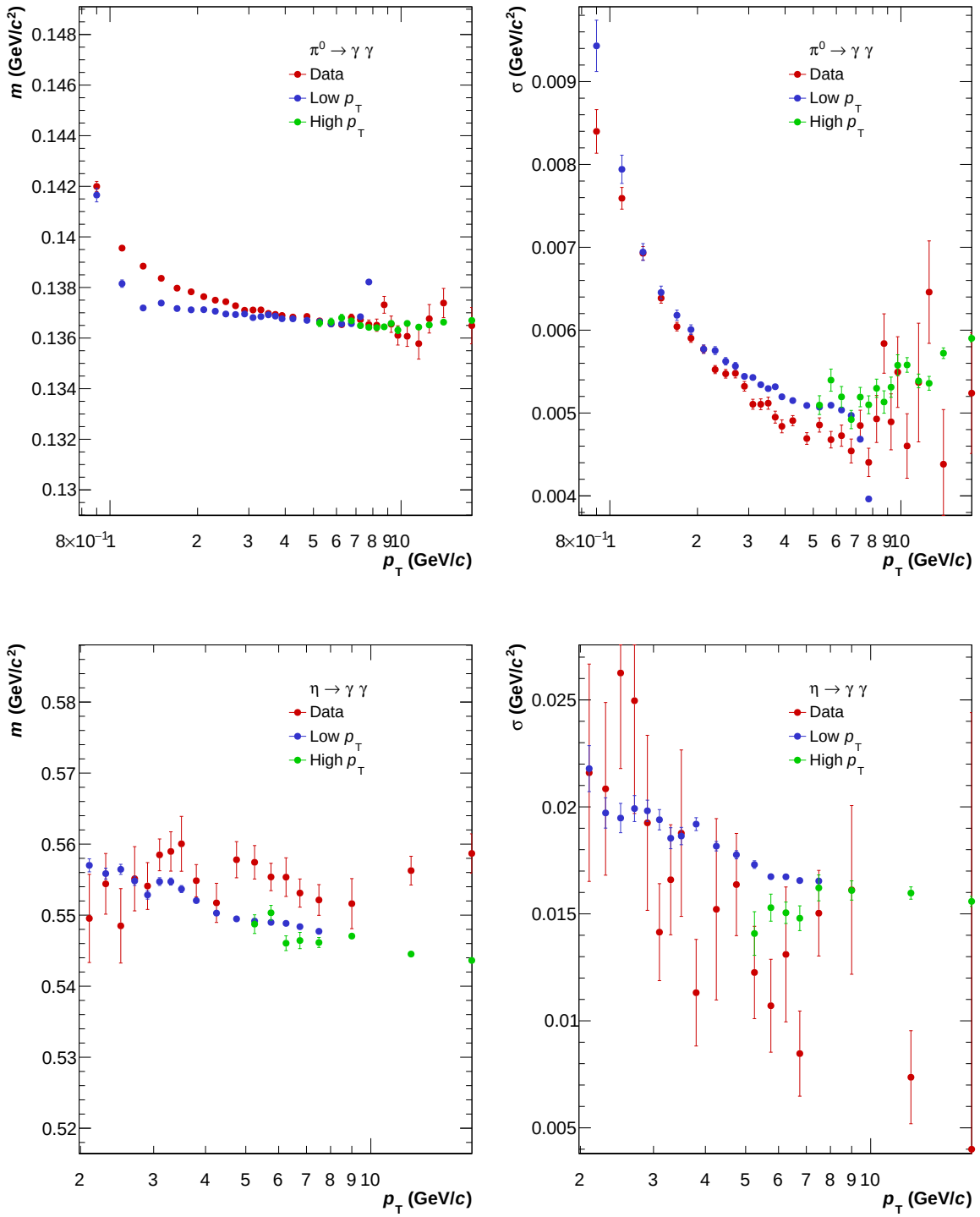

Figure 3.12: The peak position m and width σ for π^0 (upper plots) and η meson (bottom plots) in the Single Particle Monte-Carlo production.

The red points in Fig. 3.12 correspond to quantities obtained from the real data while the blue and green points represent low and high p_T productions, respectively. The peak positions and widths of the data and the Monte-Carlo are in reasonable agreement in the overlap region. This confirms the self-consistency of the two datasets. The efficiency

times acceptance calculated from these productions are merged in the overlap region. The invariant-mass plots used for the signal reconstruction in Monte-Carlo productions are presented in Appendix D.

The efficiency times acceptance was calculated from the single-particle Monte-Carlo production described above with the following formula:

$$\varepsilon \cdot A = \frac{\Delta y \Delta \varphi}{2\pi} \frac{\text{Number of mesons reconstructed in PHOS}}{\text{Number of mesons generated}},$$

where Δy and $\Delta\varphi$ are the azimuthal angle and rapidity regions covered by the simulations and 2π factor is used to extend the corrected spectra to the entire φ range. The reconstruction efficiency after all the corrections for neutral pions and η mesons are presented in Fig. 3.13.

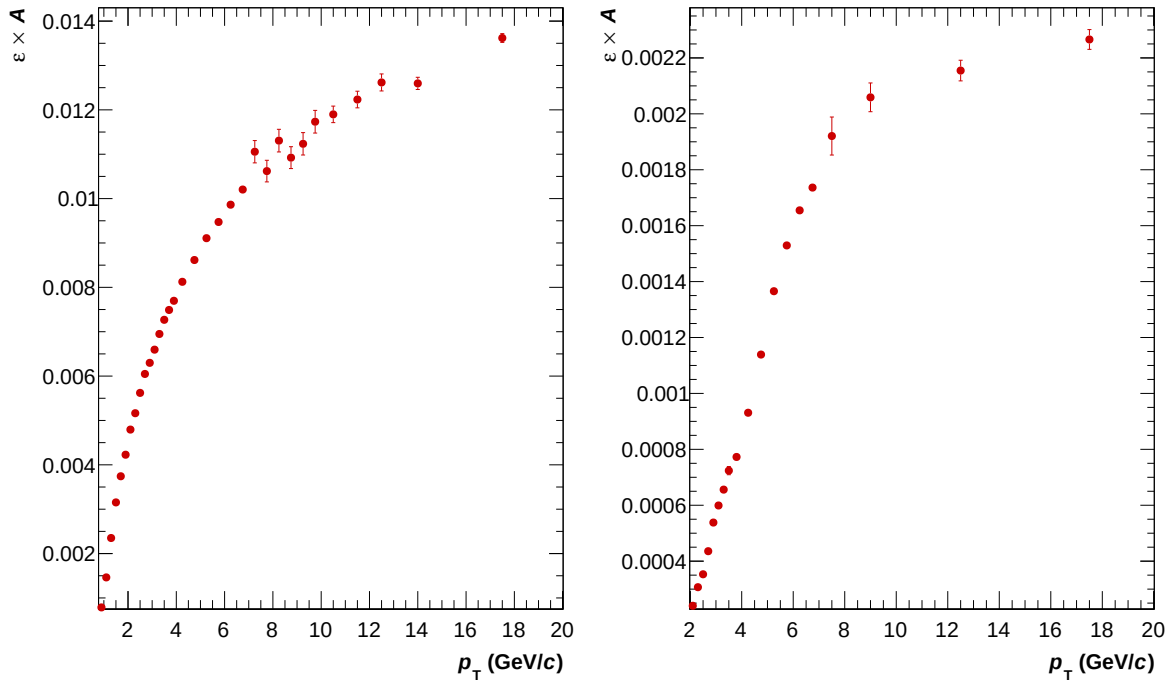

Figure 3.13: The reconstruction efficiency ε times acceptance A for π^0 (left plot) and η mesons (right plot) calculated from Monte-Carlo simulations.

The obtained values of $\varepsilon \cdot A$ values are of the order of 0.001 and 0.0002 at the lowest p_{T} bins for π^0 and η mesons, respectively. This quantity increases with the p_{T} as the opening angle between a pair of photons that are products of neutral meson decays decreases with the energy of the decaying particle. This also explains the difference between $\varepsilon \cdot A$ factor for π^0 and η mesons. The mass of η is almost four times larger than the mass of a neutral pion, and the opening angle between η decay products is always larger at the same p_{T} as demonstrated in Fig. 3.11. The reconstruction efficiency is expected to grow for p_{T} up to $25 - 30$ GeV/c. At larger p_{T}, the opening angle becomes small enough, so the showers coming from different photons overlap in the detector. The larger error bars at higher p_{T} have a purely statistical origin. The points above $p_{\mathrm{T}} > 7$ GeV/c are extracted from high p_{T} Monte-Carlo production that contains fewer events.

3.2.5 Feed-down correction

The PHOS detector can measure all neutral mesons in the final state. A fraction of these particles originates from the weak decays of strange hadrons. For example, $K^0_s \to \pi^0 + \pi^0$

and $\Lambda \to n + \pi^0$ are the most dominant sources of secondary particles. The two-pion decay channel of K_s^0 has branching ratio of 30.69% and $c\tau \sim 2.7$ cm while Λ into π^0 decay channel has branching ratio of 35.8% and corresponding $c\tau = 7.9$ cm. The contribution from the latter one is too small and was disregarded in this analysis. Since K_s^0 have $c\tau$ larger than the size of the inner tracking system, the secondary pions are created far from the nominal interacting point. The reconstructed mass of such pions will be underestimated, and their invariant mass distribution will be shifted to the left. Such pions are called feed-down pions. The current analysis focuses on the measurements of primary pions, therefore, feed-down particles should be removed from the final result.

The contribution of the feed-down particles was estimated with PYTHIA Monte-Carlo simulations. It is known that the PYTHIA generator is not able to reproduce true relative yields of kaons and pions (the $K^{\pm}/\pi^{\pm}$ ratio). Therefore, the kaon spectrum needs to be reweighed to reflect true kaon and pion distributions. The most recent ALICE measurements [110] were used to determine the deviation of the PYTHIA generator from the real data. The comparison of $K^{\pm}/\pi^{\pm}$ spectrum ratio is shown in Fig. 3.14.

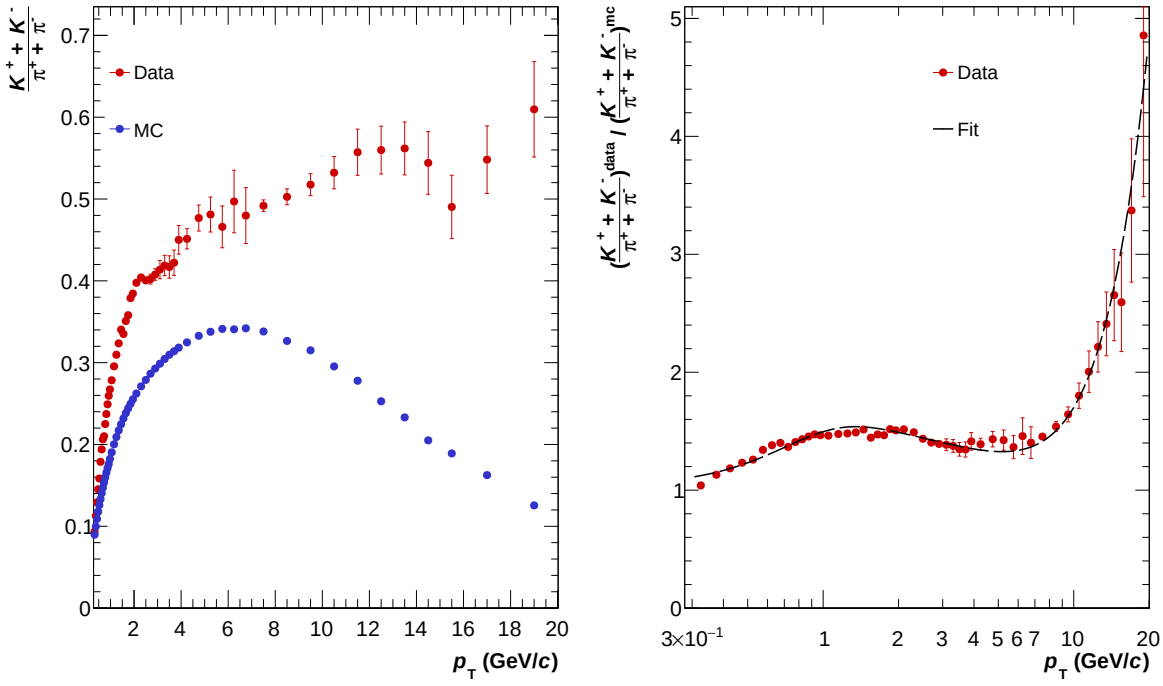

Figure 3.14: The ratio of charged kaon and pion production yields in the data and PYTHIA 8 Monte-Carlo (left plot) and their ratio (right plot). The dashed line corresponds to a smooth parameterization of the double ratio.

The number of kaons generated at a given p_{T} is significantly underestimated by PYTHIA 8. The difference between the data and Monte-Carlo simulations depends on the transverse momentum of the particles. It increases at $p_{\mathrm{T}} > 10$ GeV as PYTHIA generates more pions at high p_{T}. The double ratio of the $K^{\pm}/\pi^{\pm}$ spectra was approximated with a smooth parametrization:

$$f(p_{\mathrm{T}}) = A \cdot \left(1 + B \cdot \exp\left(-p_{\mathrm{T}}^2/\sigma\right)\right) + (C + D) \cdot p_{\mathrm{T}}^2 + D \cdot p_{\mathrm{T}},$$

where A, B, σ, C and D are the free parameters that were extracted from the fit. The dashed line on the right plot in Fig. 3.14 corresponds to the parameterized double ratio. The values of the parametrs are presented in table 3.4. This parameterization is used to scale the spectrum of the generated particles and two-cluster combinations that are used to construct invariant-mass distributions for the yield extraction. The feed-down pions

parameter	value	uncertainty
A	1.760	0.533
B	-0.403	0.570
σ $(\mathrm{GeV}/c)^{-1}$	0.546	1.763
C $(\mathrm{GeV}/c)^{-1}$	-0.151	0.147
D $(\mathrm{GeV}/c)^{-1}$	0.167	0.155
χ^2/ndf	0.01	

Table 3.4: The parameters of the double $K^{\pm}/\pi^{\pm}$ ratio obtained from PYTHIA 8 [34] Monte-Carlo simulations and the real data.

were calculated as a fraction of pions that are coming from K^s_0 decays divided by the total number of neutral mesons measured by PHOS:

$$p_{\mathrm{feeddown}} = \frac{N^{\pi^0 \leftarrow K^s_0}_{\mathrm{rec}}}{N^{\mathrm{all}}_{\mathrm{rec}}} \times \frac{((K^+ + K^-)/(\pi^+ + \pi^-))^{\mathrm{DATA}}}{((K^+ + K^-)/(\pi^+ + \pi^-))^{\mathrm{MC}}},$$

where the first part in the product corresponds to the contribution of neutral pions that originate from the weak decays, and the second term is the correction factor induced by the difference in the kaon yield in the real data and the Monte-Carlo simulations. The resulting feed-down correction for neutral pion spectrum in pp collisions at $\sqrt{s} = 13$ TeV is shown in Fig. 3.15

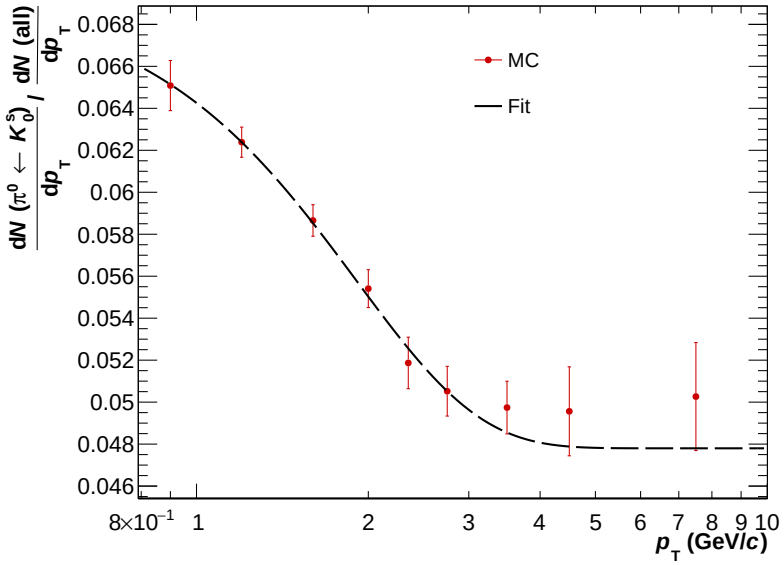

Figure 3.15: The feed-down correction factor as a function of p_{T} estimated from the PYTHIA 8 Monte-Carlo production. The dashed line is the approximation of the feed-down spectrum with a smooth function.

The correction was calculated independently from the raw yield and reconstruction efficiency. It was applied as the final correction factor to the efficiency-scaled yield. A smooth function was used in order to extend the result for the arbitrary binning of the corrected yield:

$$\frac{dN_{\text{feed-down}}}{dp_{\mathrm{T}}}(p_{\mathrm{T}}) = A \cdot \left(1 + \alpha \cdot \exp\left\{\left(\frac{-p^2_{\mathrm{T}}}{2d^2}\right)\right\}\right),$$

where A, α and d are the free parameters to be obtained from the fit. The feed-down function is represented as a dashed line in Fig. 3.15. The optimal parameters and the

parameter	value	uncertainty
A	0.048	0.001
α	0.453	0.031
σ (GeV/c)$^{-1}$	1.350	0.002
χ^2/ndf	0.33	

Table 3.5: The values of the feed-down function parameters estimated from PYTHIA 8 simulations.

χ^2/ndf values are shown in table 3.5. The corection due to the fraction of secondary pion decays is at the level of 6% at low p_{T} and it decreases with p_{T} to almost 5%. This correction is small, the contributions from more rare decays are negligible as the absolute value of those contributions is significantly smaller than the statistical and systematic errors of their extraction.

3.2.6 Corrected yield

This subsection presents the neutral pion and η meson signal extraction in pp collisions at $\sqrt{s} = 13$ TeV with PHOS.

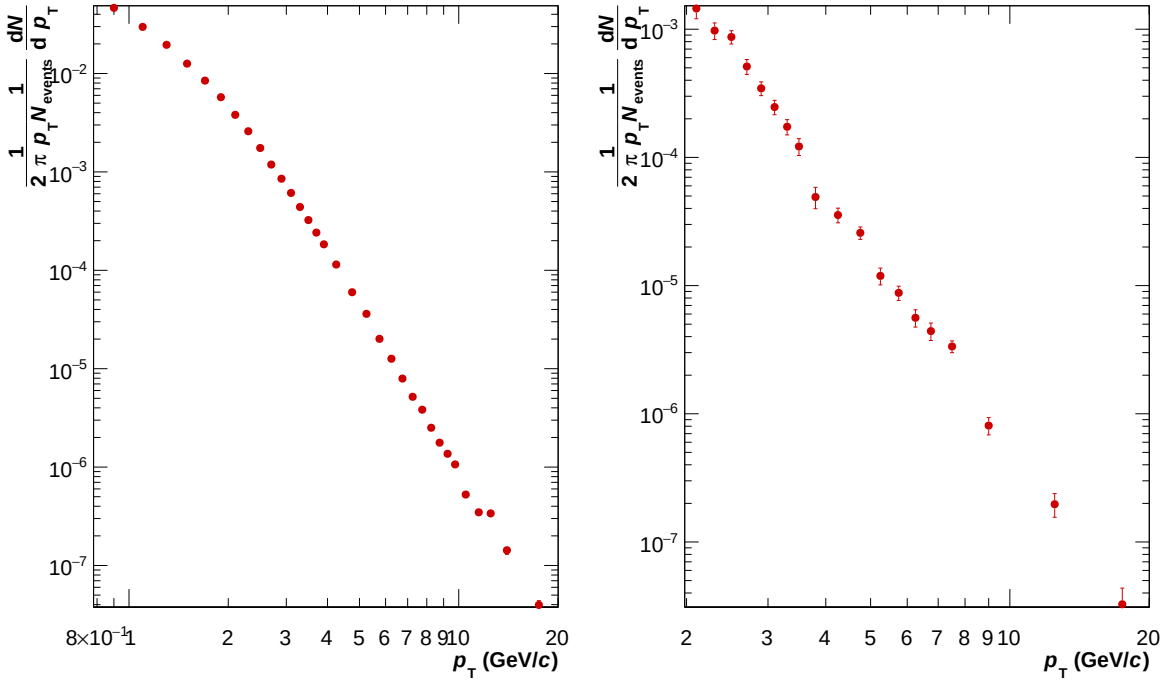

Figure 3.16: The corrected yields of neutral pions (left plot) and η mesons (right plot) measured with full available statistics in pp collisions at $\sqrt{s} = 13$ TeV.

The raw spectra were calculated as the area near the meson peak in two-photon invariant mass distributions in a given p_{T} bin. The photons are reconstructed from electromagnetic showers in the calorimeter. The clusters used in the analysis were selected according to the scheme described above. It reduces the systematic bias from the noise-clusters, but it also removes some physical particles. The acceptance of the PHOS detector is relatively small. There are a fraction of neutral mesons that escape the calorimeter because of the detector size. Also, the neutral meson signal can be lost when one of the photons hits a bad channel. The cut on the timing of the clusters rejects a significant amount of the neutral mesons. All these factors influence the measured spectra of neutral mesons. The

efficiency times acceptance $\varepsilon \cdot A$, the timing cut efficiency $\varepsilon_{\mathrm{TOF}}$, feed-down corrections, described in the previous sections, are necessary to produce the detector independent differential cross-sections. The timing efficiency was used to weight the cluster pairs to correct the probabilities of two-photon combinations. Other factors were applied as the bin-by-bin normalization factors.

The corrected yield for netural mesons can be written in the following way:

$$\frac{dN}{dp_{\mathrm{T}}}(p_{\mathrm{T}}) = \frac{dN_{\mathrm{rec}}^{\mathrm{tof}}}{dp_{\mathrm{T}}} \frac{1}{\varepsilon \cdot A} \times \left(1 - \frac{dN_{\text{feed-down}}}{dp_{\mathrm{T}}} / \frac{dN_{\mathrm{all}}}{dp_{\mathrm{T}}}\right),$$

where $dN_{\mathrm{rec}}^{\mathrm{tof}}/dp_{\mathrm{T}}$ is a raw yield cacluated with reweighting by timing cut efficiency of each photon pair, efficiency times acceptance $\varepsilon \cdot A$ factor is calculated from single-particle productions and $dN_{\text{feed-down}}/dp_{\mathrm{T}}$ corresponds to the feed-down correction. This contribution, as discussed above, is of the order of a few per cent in the π^0 case and was negligible for the η spectrum. The fully corrected spectra of neutral mesons are shown in Fig. 3.16.

The presented spectra are normalized to the number of events and the total φ range. The error bars on both plots are the statistical errors propagated from the bin counting procedure. The systematic uncertainties are discussed in the next chapter.

Chapter 4

Evaluation of systematic uncertainties

This chapter gives a summary of the calculation of the systematic uncertainties of the neutral meson production cross-sections in proton-proton collisions at $\sqrt{s} = 13$ TeV measured with PHOS. The chapter is divided into subsections that correspond to separate contributions to the total uncertainty. The main sources of the systematic uncertainties in the neutral meson analysis are:

- Raw yield extraction algorithm
- Estimation of PHOS nonlinearity of the energy response
- The absolute scale of cluster energy measured by PHOS
- Timing cut uncertainties
- Acceptance
- Feed-down correction uncertainty
- Material budget uncertainty

4.1 Raw yield extraction algorithm

As described in section 3.2.2, the raw yield extraction algorithm consists of multiple steps that involve various parameters. For example, the number of mesons in each p_{T} bin is calculated as an area under the invariant mass histogram around the meson peak within 2σ. Another parameter of this analysis is the function used to describe the peak. As it was discussed earlier, the current analysis uses Crystal Ball function, but other parametrizations can be used. Any particular choice of parameters can lead to small changes in the extracted yield. The main goal of systematic uncertainty is to provide a confidence interval for the target variable induced by the ambiguities of the measurement process. To estimate this uncertainty, one can look at all possible combinations of the parameters of the yield extraction procedure. Each spectrum produced with a unique combination of parameters is considered as an independent measurement. The mean and Root Mean Square (RMS) calculated for all those measurements allow constructing a statistic that reflects the ambiguities of the reconstruction algorithm. In particular, neutral pion signal distribution (invariant mass after combinatorial background subtraction) was approximated with the Crystal Ball and with normal distribution functions. Different integration regions for the number of mesons estimation were used to calculate the number of entries in the neutral meson peaks. For π^0 yield extraction, these regions were $\pm 2\sigma$ and $\pm 3\sigma$ from the meson mass position. Linear function and second-degree polynomial functions were fitted to scale the ratio of mixed-event to experimental distributions. This gives the background uncertainty. The calculation of systematic uncertainty of the

spectrum extraction algorithm requires the efficiency corrected yields. For these reasons, the efficiency calculation parameters were changed as well. Namely, the same integration ranges and fitting functions were used simultaneously to estimate the impact of particular parameters on the results. The parameters varied in the π^0 analysis can be summarized in the following way:

- The function fitted to the signal: Crystal Ball, Gausian function
- Background function: linear, quadratic
- Three different fit regions:
  - "wide": $0.06 < M_{\gamma\gamma} < 0.22$ GeV/c^2
  - "mid": $0.04 < M_{\gamma\gamma} < 0.20$ GeV/c^2
  - "low": $0.08 < M_{\gamma\gamma} < 0.20$ GeV/c^2
- Integration regions: $\pm 2\sigma$, $\pm 3\sigma$

The obtained yields were averaged over all the combinations of parameters and RMS were calculated. The ratio of RMS to the mean values in particular p_{T} bin was considered as a measure of systematic uncertainty in that bin. The invariant π^0 yield and the distribution of this ratio of as a function of p_{T} for the neutral pion yield extraction are shown in Fig. 4.1.

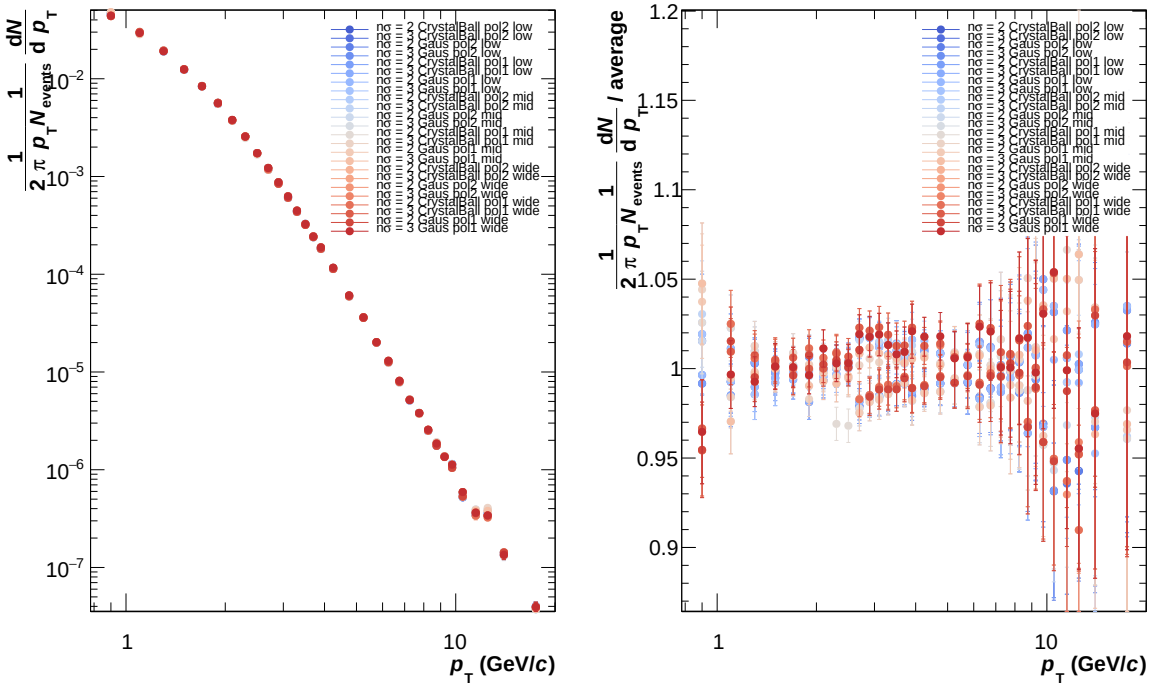

Figure 4.1: Left plot: Invariant π^0 yields calculated with different configurations of the extraction algorithm. Different colours and markers correspond to a particular set of parameters. Each colour corresponds to a set of parameters that differs in fitting function, background function, fitting or integrating regions. Right plot: Ratio of RMS of the π^0 yield to the averaged yield calculated for the different sets of parameters.

Yield extraction uncertainty attains its maximum at $p_{\mathrm{T}} = 10$–12 GeV/c and is equal to 6.5%. This can be explained by a large background at a low p_{T}.

The shape of the η peak is somewhat different. It is slightly wider. Also, the background around η peak behaves differently and generally should be described with higher

degree polynomials, but in this analysis, it is limited to second-degree polynomial. Also, the peak position and width have different dependence. For this reason, the systematic error for η meson yield extraction was estimated separately and follow the same algorithm. The main difference in the configuration is the fitting range since the η meson peak is slightly wider. It also requires a larger p_{T} region to estimate the parameters of the background. The summary of parameters varied in the η analysis:

- The function fitted to the signal: Crystal Ball, Gausian function
- Background function: linear, quadratic
- Three different fit regions:
  - "wide": $0.35 < M_{\gamma\gamma} < 0.65$ GeV/c^2
  - "mid": $0.40 < M_{\gamma\gamma} < 0.70$ GeV/c^2
  - "low": $0.45 < M_{\gamma\gamma} < 0.78$ GeV/c^2
- Integration regions: $\pm 2\sigma$, $\pm 3\sigma$

The same set of parameters were applied for the efficiency calculation. The feed-down correction for η meson is negligible and was disregarded. The RMS value divided by the mean η yield is shown in Fig. 4.2, this quantity was taken as a contribution to the uncertainty due to the yield extraction.

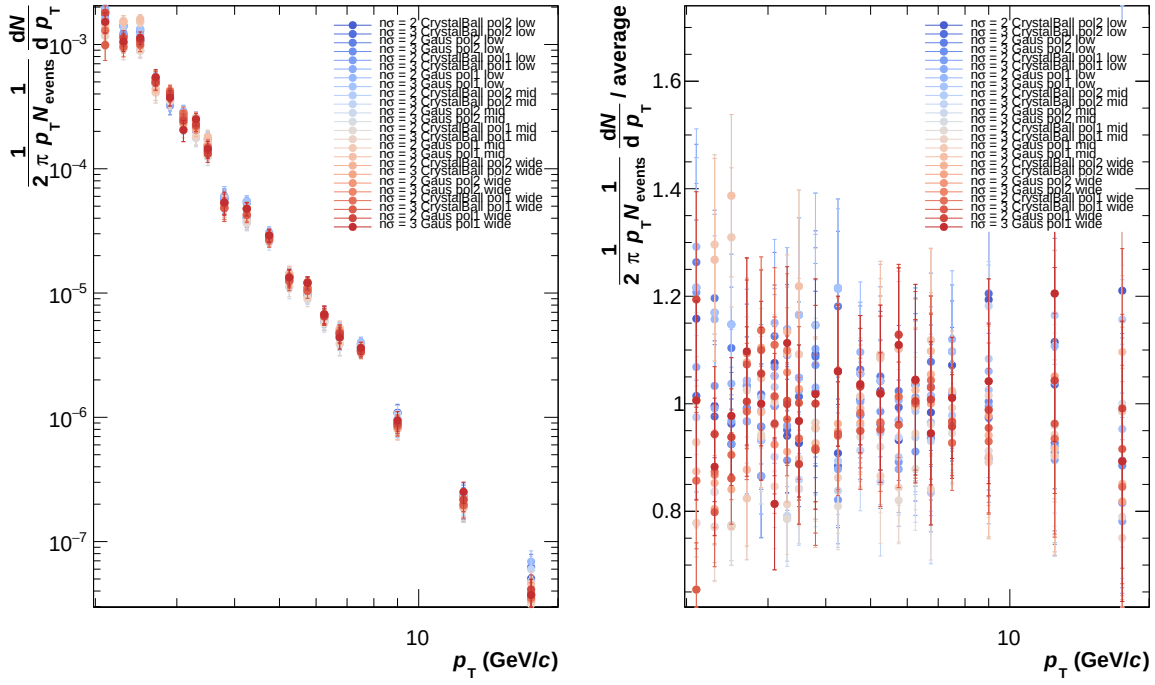

Figure 4.2: Left plot: Invariant η yields calculated with different configurations of the extraction algorithm. Different colours and markers correspond to a particular set of parameters. Each colour corresponds to each set of parameters differs in fitting function, background function, fitting or integrating regions. Right plot: Ratio of RMS of the η yield to the averaged yield calculated for the different sets of parameters.

The largest uncertainty of $\sim 22\%$ at $p_{\mathrm{T}} = 16$ GeV/c corresponds to smallest statistics in that particular bin. The errors decrease at the moderate p_{T} and increase at < 4 GeV/c as the background increases. The uncertainty at the lowest p_{T} bin is $\sim 18\%$, which can be explained by the weak η signal at that region due to limited acceptance.

4.2 Nonlinearity of PHOS energy response

It was shown in section 3.2.2, the position of neutral mesons peaks measured in PHOS depend on the transverse momentum. This can be explained by the PHOS nonlinear energy response [111, 112]. It is caused by the light attenuation in PWO material, electronic thresholds, amplitude digitalization and electromagnetic shower leakage to other crystals. The reconstructed efficiency was calculated from the Monte-Carlo simulation. It was tuned in such a way that the π^0 mass position as a function of p_{T} agreed with the real data. The exact value of a meson mass is not important for the yield extraction as soon as we are able to reproduce it in the simulation and estimate the efficiency properly. The tuning process corresponds to the rescaling of the measured energy of a cluster in the Monte-Carlo simulation [113]:

$$E_{\mathrm{corr}} = \begin{cases} aE + b\sqrt{E} + c + d/\sqrt{E} + e/E, & E \leq E_0 \\ \alpha E + \beta\sqrt{E}, & E > E_0 \end{cases}$$

where α and β are fixed to ensure a smoothnes at the point $E = E_0$ and $a,\ b,\ c,\ d,\ e,\ E_0$ are free parameters. These parameters were estimated by fitting the ratio of the tabular value of neutral pion mass taken from PDG [7] to the measured one. The resulting set of parameters are summarized in table 4.2. Here, the a paramter represents a global

parameter	value	error
a	1.02	0.01
b (GeV$^{1/2}$)	-0.2548	0.0005
c (GeV	0.648	0.001
d (GeV$^{3/2}$)	-0.4550	0.0002
e (GeV^2)	0.1338	0.0005
E_0 (GeV)	5.17	0.01

Table 4.1: Parameters of the PHOS energy response nonlinearity estimated from the pp $\sqrt{s} = 13$ TeV data [113]

energy sale, the parameter b can be interpreted as a small correction to the global energy scale, the parameter c – represents a constant shift of the nonlinearity respons. The two remaining parameters, d and e have a major impact on the shape of the spectrum and were studied separately. They were estimated by minimizing the χ^2 distribution between the constant value of π^0 peak position and the data corrected for nonlinearity [113].

The error of the energy response in PHOS comes from the uncertainties of the nonlinearity parameters. A standard error-propagation technique can not be applied since there is no analytic expression for the nonlinearity dependence of the corrected yield and a change in nonlinearity leads to changes in the two-photon invariant mass distributions. Since the shape of the nonlinearity function strongly depends on parameters e and d, they were selected as a main target for the systematic uncertainty study. The rate of change of the nonlinearity function with respect to other parameters, varied within their uncertainties, is negligible.

The systematic uncertainty was extracted from the single π^0 Monte-Carlo simulations as it has the largest statistics if compared to other MC productions. Both parameters, e and d, were varied simultaneously within their systematic uncertainties to construct different efficiencies with different π^0 mass positions. Since these changes do not alter the raw yield and feed-down correction, they were disregarded in this analysis. The computations are highly expensive, and therefore, the entire parameter range was discretized into 9 bins for each of the parameters. For each combination of parameters, an acceptance times efficiency factor $\varepsilon \cdot A$ was calculated. This corresponds to 9×9 different efficiency

distributions. The differences in the parameter values allow a probing the nonlinearity parameterization in the vicinity of optimal parameters obtained in [113]. The resulting distributions are shown in Fig. 4.3. The average value of the efficiencies in each p_{T} bin was calculated. Then each of the measurements is normalized to the mean efficiency (see the right plot in Fig. 4.3). Each colour represents a different set of parameters. The lighter points correspond to the central values of e and d that are used in this analysis. The efficiencies times acceptance values $\varepsilon \cdot A$ are divergent in the low p_{T} region. This is an expected effect as the parameters e and b have the largest impact at the smallest cluster energies. The discrepancy decreases as a function of p_{T}. This is reflected in the right plot in Fig. 4.3, which shows RMS of $\varepsilon \cdot A$ divided by the averaged $\varepsilon \cdot A$ over all combinations of parameters. This ratio has a larger variance at low p_{T} and is almost close to one at $p_{\mathrm{T}} > 10$ GeV/c. The error bars in this plot are a few times larger at $p_{\mathrm{T}} > 6$ GeV/c. This is a pure statistical effect that is connected to the fact that the high-p_{T} region of single-particle Monte-Carlo simulations has fewer events generated.

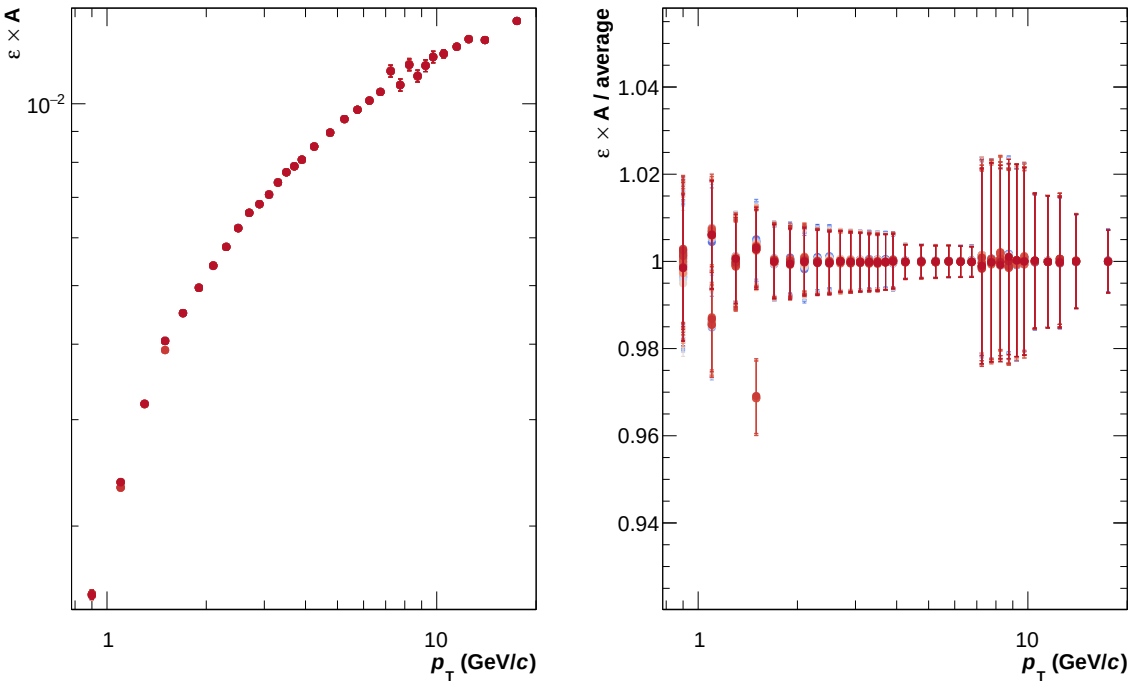

Figure 4.3: Left plot: Efficiency times acceptance $\varepsilon \cdot A$ calculated with single-particle Monte-Carlo production. Right plot: The ratio of RMS to the mean value of $\varepsilon \cdot A$ obtained with the different combinations of parameters e and d. Each color represents a different combination of e and d parameters correspond to 9 equidistant points from -0.4550 ± 0.0002 GeV$^{3/2}$ and 0.1338 ± 0.0005 GeV^2 intervals respectively.

The relative systematic uncertainty of PHOS energy response is defined as a maximum deviation from the unity of the ratio of the RMS to the mean value of the efficiency in a given p_{T} bin.

The final systematic error due to PHOS energy response is presented in section 4.8, together with other sources of uncertainties. The nonlinearity parameters for η meson are the same, as they describe the same detector, and therefore systematic uncertainty should be the same.

4.3 Acceptance

Some channels of PHOS had either a software glitch or were physically damaged during the measurements. Problematic channels were identified and excluded from the analysis. Section 3.1.4 describes the procedure of dead and noisy channels extraction. The described algorithm has some ambiguities, and therefore a cell can be labelled as bad while it was, in fact, a good one. The systematic uncertainty due to the detector acceptance corresponds to the sensitivity of the measurement to the damaged channels identification.

This uncertainty can be calculated by altering the sensitive area of the detector. It would be very inefficient to physically remove the cells during the data taking. However, the same result can be achieved on the analysis level by simply varying the minimal allowed distance to the closest bad channel. The default configuration corresponds to the zero distance (only clusters that have a centre in the channels that were labelled as noisy). The raw yield and efficiency were obtained for minimal distances of 1 and 2 cm to a bad channel. The ratio of the corrected yields to the averaged yield extracted with different distance-cuts is shown in Fig. 4.4. The resulting distributions show some fluctuations.

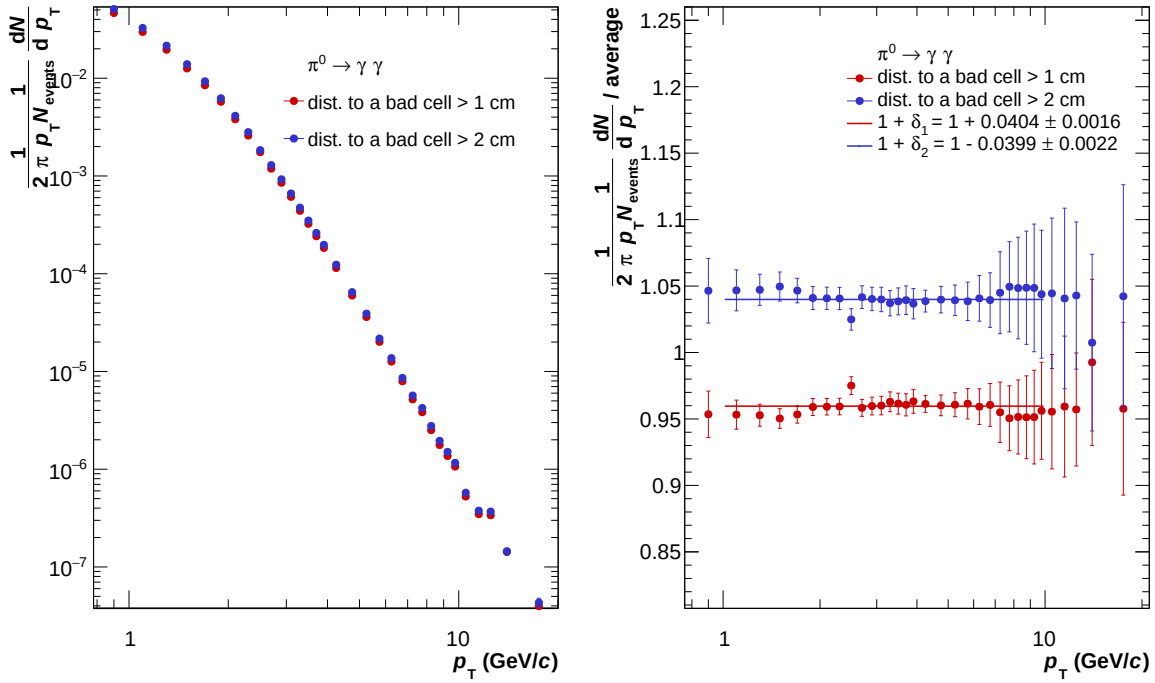

Figure 4.4: Left plot: Invariant π^0 yields calculated with 1 and 2 cm minimal distances to a bad channel. Right plot: Ratio of π^0 yields obtained with the different distance cuts to the averaged π^0 yield. They were fitted with the zero-degree polynomials in the form $1 + \delta_i$, where δ_i describes the deviation from the unity.

To estimate the general thrend they were fitted with a zero-degree-polynomials of the form $1 + \delta_i$ in the range $2 < p_{\mathrm{T}} < 10$ GeV/c. The maximum absolute deviation of the fitted curves from unity $max(|\delta_i|)$ corresponds to the uncertainty of PHOS acceptance estimation. The largest value of such deviation is 4.04 %. This value is taken as the final acceptance contribution to the systematic uncertainty.

Neutral pion and η meson analyses share the same map of bad channels, and therefore these measurements have the same systematic uncertainty due to acceptance.

4.4 Time of flight cut

Another source of systematic uncertainties is an inter-bunch pileup. The cut on the time of flight of the clusters removes photons that come from different bunch-crossings as described in section 3.2.3.

The uncertainty in time-of-flight efficiency determination can be estimated by comparison of the corrected spectrum with that with efficiency equal to unity by definition. If the timing cut is perfect, then the ratio of production spectra with and without the cut should produce the same results. This can be written as:

$$R_{\mathrm{TOF}} = \frac{\text{number of } \pi^0 \text{ with 12.5 } ns \text{ cut, corrected for TOF}}{\text{number of } \pi^0 \text{ without cut and without corrections}}$$

For a perfect detector the quantity R_{TOF} is equal to one by construction. The maximal deviation from unity is used as an estimate of systematics uncertainty of the timing cut efficiency.

There were several runs during 2016 data-taking (appendix A) with a bunch-crossing interval greater than 1000 ns. For such runs, the ± 500 ns timing cut corresponds to 100% efficiency of the cluster detection. These runs were used to construct the denominator for the R_{TOF} quantity, while all other runs considered in this analysis were used to calculate the numerator.

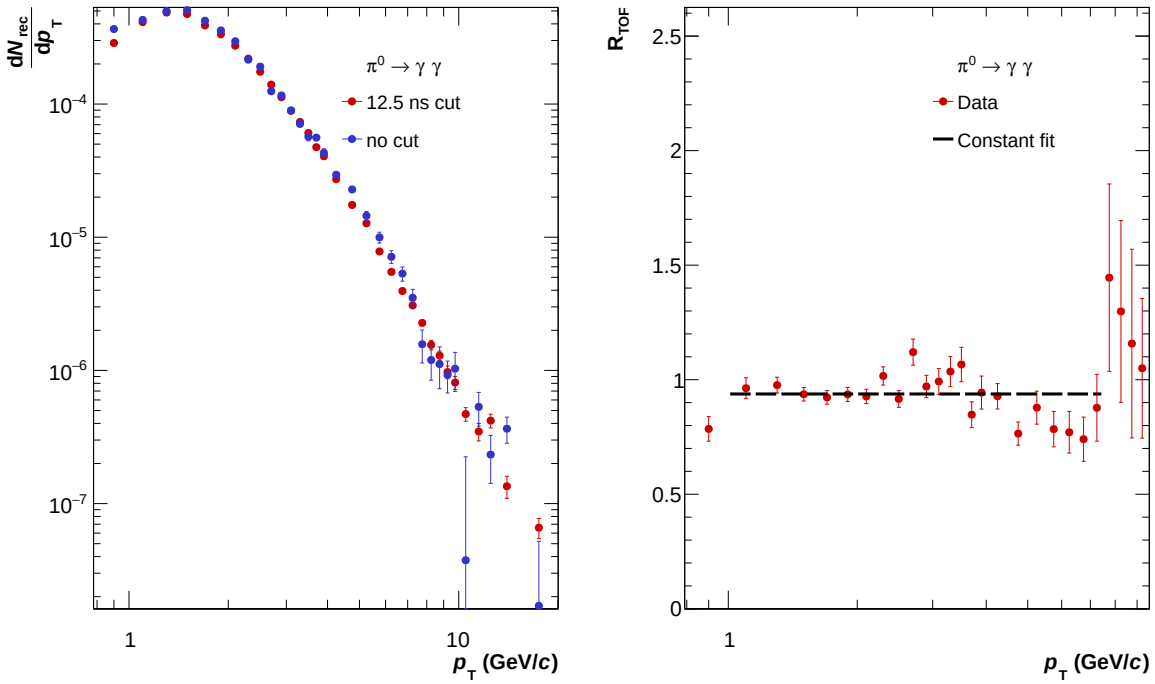

Figure 4.5: Left plot: The TOF corrected neutral pion yield calculated with 25 ns bunch-spacing data (red points) and the yield measured for runs with bunch spacing greater than 1000 ns (blue points) and without corrections. Right plot: The ratio of π^0 yields is shown as red points, the dashed line coresponds to the constant fit in the $1 < p_{\mathrm{T}} < 7.5$ GeV/c region.

The red points on the left part of Fig. 4.5 correspond to π^0 yield calculated for runs that have bunch spacing equal to 25 ns, the blue points represent π^0 yield in runs with larger bunch spacing and without TOF correction. The statistics of the latter are more than 1000 times smaller, and the spectrum extraction for such a small dataset might be unstable. The ratio of these two spectra was then fitted with a constant function in the $1 < p_{\mathrm{T}} < 7.5$ GeV/c interval (see the right part of Fig. 4.5). The neutral pion spectrum

below 1 GeV/c has large background contribution and π^0 peak is not distinct. The region above 7.5 GeV/c has very low statistics. The fit yields a value of $1-R_{\rm TOF} = 0.062\pm0.010$. It is assigned to the systematic uncertainty of the timing cut correction, and it is the same for all $p_{\rm T}$ bins. This value is also used in the η meson analysis.

4.5 Material budget

The ALICE detector was designed in such a way that the amount of the material in front of the PHOS detector is minimal. However, TPC barrel, elements of the installation are still present. The uncertainty due to the material budget can be calculated by comparing neutral pion yields reconstructed for the runs with and without magnetic field generated by the ALICE solenoid. In the absence of the magnetic field, e^+e^- the pairs that come from the photon conversion can be reconstructed as photon candidates increasing the neutral pion yield.

The setup of the ALICE detector was not changing during the entire Run2. Therefore the systematic uncertainty due to material budget in front of PHOS is the same for all collision energies. Previous analysis of proton-proton data at $\sqrt{s} = 5.02$ TeV [114] shows that this value is 2% for the Run2 data.

4.6 Feed-down correction

In section 3.2.5 it was mentioned that final π^0 yield was corrected for the contribution coming from strange hadrons. This correction has its own systematic uncertainty. It was adopted from $K^{\pm}/\pi^{\pm}$ data which has 12.6% systematic error at maximum. Following the standard rules of error propagation that quantity should be multiplied by the $N_{\rm rec}^{\pi^0\leftarrow K^s_0}/N_{\rm rec}^{\rm all}$ which is about ~ 0.1. This leads to the final uncertainty of the feed-down correction of 1.26%.

The analogous uncertainty for η meson can be safely ignored as the contribution from the strange hadrons to the η spectrum is negligible as described in section 3.2.5.

4.7 Global energy scale

In this section, we will estimate the uncertainty related to the energy measurement. This can be achieved by comparing particle energy in two different detectors. The most suitable detector in the current setup is TPC, as it is adjacent to PHOS and it allows the selection of the same particles measured simultaneously in both detectors. We construct a ratio of electron energy E deposited in PHOS to electron momentum p reconstructed by TPC. This ratio (E/p) should be somewhat less than unity due to the electron energy loss in the material of the detectors.

The electrons were indentified in TPC using specific energy loss parametrizations dE/dx as shown in Fig. 2.6. To identify particles, the reconstructed dE/dx values are compared to the Bethe-Bloch parametrizations corresponding to different particle species. The measured energy loss at given momentum p is calculated in the units of standard deviation σ of the dE/dx distribution:

$$n\sigma(p) = \frac{(dE/dx(p))^{\rm meas.} - (dE/dx(p))^{\rm param.}}{\sigma(p)}.$$

The electron candidates correspond to a particle that match the criterion $2 < n\sigma_e < 3$. The same conditions and cuts as in photon analysis were applied to select electron clusters in PHOS. Additionally, electron clusters in PHOS required to have a matched track in

TPC to eliminate neutral particles from the analysis. A cut on the cluster shape was applied as well. The latter is needed to enhance the electron signal in the detector. Hadrons lose their energy mostly through ionization while electrons and photons create electron-positron pairs in the material. This causes the difference in electron shower spread and thus in the shape of PHOS clusters. The parameters of cluster shapes where studied in the real data and Monte-Carlo simulations [115]. Each PHOS cluster was approximated with an ellipse, and then a cut on the main ellipse axes was applied to distinguish between different shapes. As it has been demonstrated in [114, 115, 116] a cut on the smaller axis $R_2 < 2.5$ selects mostly photon and electron candidates.

The distributions of E/p in different p_{T}-bins were fitted with a sum of the Gaussian function and the second-degree polynomial. The resulting positions of E/p peak as a function of p_{T} are presented in Fig. 4.6.

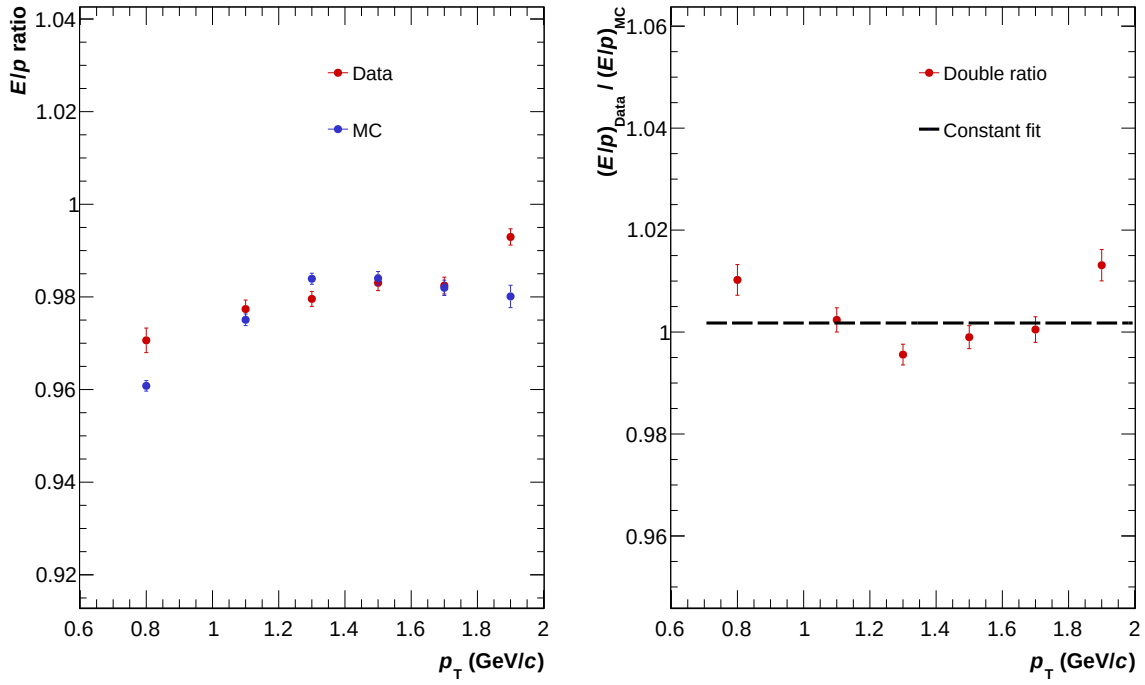

Figure 4.6: Left plot: The electron energy E deposited in PHOS divided by momentum p reconstructed in TPC in data (red points) and estimated from PYTHIA 8 [34] Monte-Carlo simulations. Right plot: The double ratio of (E/p) ratio measured and that obtained from PYTHIA 8 Monte-Carlo production (red points). The black dashed line corresponds to the fit of the constant function $(E/p)_{\mathrm{Data}}/(E/p)_{\mathrm{MC}} = 1+\delta p_{\mathrm{T}}/p_{\mathrm{T}}$ in $0.7 < p_{\mathrm{T}} < 2$ GeV/c range.

The red points in Fig. 4.6 (right plot) correspond to the E/p calculated from data, and the blue points are obtained from PYTHIA 8 Monte-Carlo production. The ratio was extracted in $0.7 < p_{\mathrm{T}} < 2$ GeV/c range, as the electron statistics vanishes faster than that of photons. The double ratio of E/p values calculated from data to that calculated with Monte-Carlo simulations is presented as red points in Fig. 4.6 (right plot). It can be seen that this quantity is consistent with unity. This indicates that the calibration of the PHOS detector well describes the data.

The level of disagreement between the data and Monte-Carlo simulations determines the uncertainty of efficiency calculations and the corrected yield reconstruction. The deviation from unity of the double E/p ratio is estimated by fitting a constant function of the form $(E/p)_{\mathrm{Data}}/(E/p)_{\mathrm{MC}} = 1+\delta p_{\mathrm{T}}/p_{\mathrm{T}}$ in $0.7 < p_{\mathrm{T}} < 2$ GeV/c range. The resulting value is equal to $1 + \delta p_{\mathrm{T}}/p_{\mathrm{T}} = 1.002 \pm 0.001$ which demonstrates a very good energy calibration of PHOS. The deviation of the double ratio of $\delta p_{\mathrm{T}}/p_{\mathrm{T}}$ from unity is taken as

the uncertainty of the global energy calibration of PHOS. Since the energy calibration for π^0 and η meson is the same, the value of the systematics uncertainty of global energy estimation was taken $\delta p_{\mathrm{T}}/p_{\mathrm{T}} \sim 0.2\%$ for both particle species.

The uncertainty in global energy scale determination does not translate directly to an error in the differential yield extraction. The yield extraction procedure does not involve the δp_{T} term explicitly. This term is responsible for p_{T}-bin determination. The change in the global energy scale leads to a parallel shift along the p_{T} axis of the differential cross-section if plotted as a function of p_{T}. To estimate the ambiguity caused by the global energy scale error, it was compared to the change of yields caused by altering the p_{T} values. This can be done using a smooth parametrization of the p_{T} spectrum and changing its argument.

In this analysis, the systematic uncertainty of differential yield extraction connected with the global energy scale error was determined as a maximum deviation from the unity of the meson spectrum divided by the shifted one:

$$\Delta_E = \max \left| 1 \mp \frac{f(p_{\mathrm{T}} \pm \delta p_{\mathrm{T}})}{f(p_{\mathrm{T}})} \right|$$

where Δ_E – the systematic uncertainty, δp_{T} – global energy scale uncertainty, $f(p_{\mathrm{T}})$ – a smooth representation of spectrum with Tsallis function [49]. The sign "$\pm$" reflects the fact that the distribution should be shifted in either direction. The ratio of the spectra as a function of p_{T} are shown in Fig. 4.6 for the π^0 and η yields. The systematic uncertainty

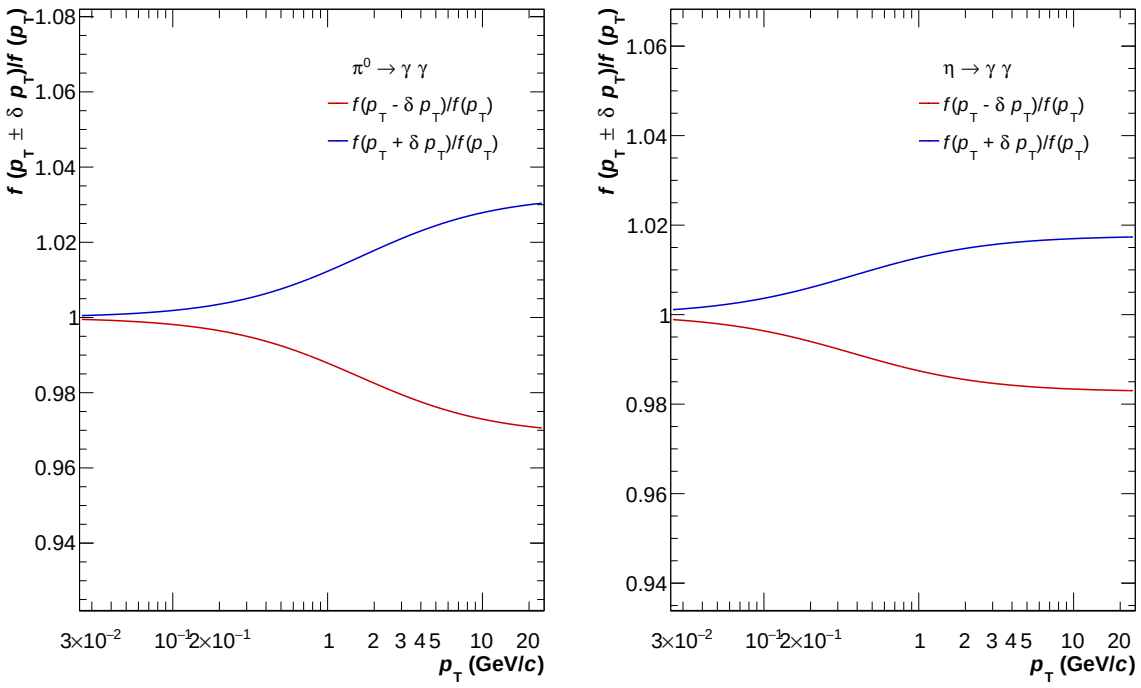

Figure 4.7: The ratio of smooth parameterization of differential π^0 (left plot) and η (right plot) yields to the $\delta p_{\mathrm{T}}/p_{\mathrm{T}}$-shifted versions of that distributions. The function f corresponds to the Tsallis parameterization [49] of the meson spectra.

of the cross-section extraction connected with the global energy scale calibration Δ_E is different for π^0 and for η mesons. This is due to the difference in p_{T} binning, the width of the peak, and the yield itself, which is reflected in Fig. 4.6: it can be seen that the η meson spectra change less than that of π^0 with respect to p_{T} shifts as it has a larger integration region.

The final values of systematic uncertainties due to global energy scale extraction are presented in the last section of this chapter.

4.8 Summary of systematic uncertainties

This section is devoted to the discussion of systematic uncertainties of light neutral meson yield extraction. As described, in previous sections, π^0 and η meson have the same sources of systematic uncertainties, the only difference is the feed-down correction. It is absent in the η meson case, as the contribution from strange particle decays is negligible. All the sources of systematic uncertainties, together with the total systematic error, are shown in Fig. 4.8.

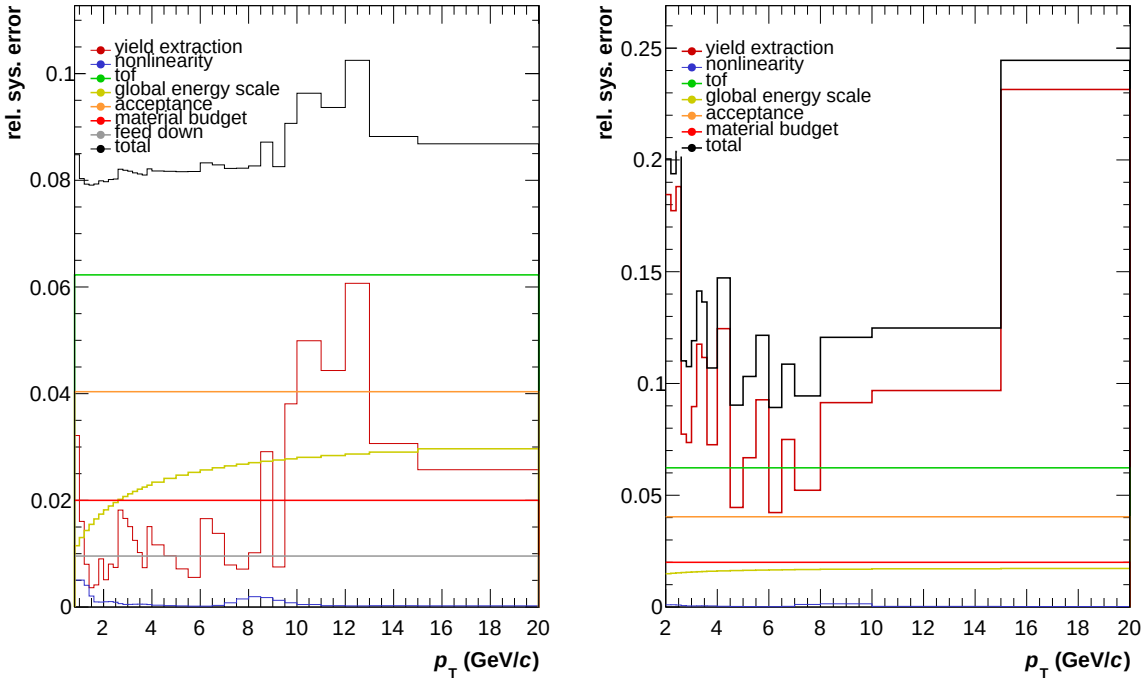

Figure 4.8: Sources of the systematics uncertainties of the neutral pion (left plot) and η (right plot) meson reconstruction in pp collisions at $\sqrt{s} = 13$ TeV. The coloured lines correspond to the different sources. The black solid line represents the listed contributions added in quadratures.

The dominant contribution to the total uncertainty corresponds to the yield extraction error for both π^0 and η measurements. At low p_{T}, it is of the level of 3% for π^0 and 18% for the η meson spectrum. The difference between these numbers corresponds to the fact that η meson peaks have a lower signal to noise ratio. Generally, the statistics of π^0 two-photon distributions are few orders of magnitude larger, making pion signal well defined. At the same time, the η meson signal has fewer statistics, and the ambiguity of extraction algorithm parameters is way higher. At moderate p_{T} the uncertainty decreases down to $\sim 0.5\%$ for neutral pions and $\sim 6\%$ for η meson. This region is rich in statistics, and the noise is quite low. The increase of the uncertainty up to $\sim 9\%$ at higher p_{T} for both mesons can be explained by two factors: the decrease of statistics in data, and smaller statistics in single-particle Monte-Carlo simulations. This makes the peaks less pronounced leading to larger uncertainties.

The error connected with the global energy scale uncertainty increases with p_{T}. It grows above $\sim 3\%$ for π^0 and up to $\sim 2\%$ for η mesons. As it was discussed in section 4.7, η meson analysis is more stable to the global energy uncertainties due to the bin width and the larger integration window in each p_{T} bin.

The uncertainty of timing cut efficiency estimation is the same for both mesons. It does not depend on p_{T} and is equal to $\sim 3\%$. This error reflects the PHOS timing calibration.

The systematic uncertainty due to the nonlinearity of the PHOS energy response is estimated to be at above $\sim 0.006\%$ on average. It attains the largest value of 0.018% at $p_{\mathrm{T}} \sim 2$ GeV/c and it decreases with p_{T}. This is mainly caused by the functional form of the nonlinearity calibration function described in section 4.2. Both neutral pion and η meson signals have the same nonlinearity uncertainty as they use the same calibration.

The contributions from material budget and acceptance are below 2%, and they do not depend on p_{T}. This value is shared for both π^0 and η meson measurements.

It is assumed that the correlation between different sources of systematic uncertainties can be neglected. The black curve in Fig. 4.8 corresponds to the total systematic uncertainties of neutral pion and η meson measurements. It is obtained by adding in quadratures all the contributions presented in Fig. 4.8.

Chapter 5

Experimental distributions and their properties

Previous chapters describe the procedure of neutral meson invariant-yield extraction from the data taken by ALICE at $\sqrt{s} = 13$ TeV. Fig. 5.1 summarizes π^0 and η yields together with their statistical and systematic uncertainties. The invariant differential cross-section is given by multiplying the invariant yield by the collision cross-section:

$$E\frac{d^3\sigma}{dp^3} = \frac{1}{2\pi}\frac{\sigma^{\rm or}_{\rm MB}}{N_{\rm nevents}}\frac{1}{p_{\rm T}}\frac{1}{\varepsilon\cdot A}\frac{N^{\rm part}}{\Delta y \Delta p_{\rm T}},$$

where $\sigma^{\rm or}_{\rm MB}$ is the cross section for the minimum bias interactions in pp collisions, $N_{\rm events}$ is the number of minimum bias ($\rm MB_{OR}$) events. $N^{\rm part}$ stands for the number of reconstructed particles (in the current analysis it corresponds to the number of neutral pions and η mesons), Δy is the rapidity range of the measurements, $\Delta p_{\rm T}$ is the width of the transverse momentum bin analyzed and the term $\varepsilon \cdot A$ is the reconstruction efficiency ε multiplied by the acceptance A.

The minimum-bias cross section for proton-proton collisions at $\sqrt{s} = 13$ TeV is $\sigma^{\rm or}_{\rm MB} = 57.8 \pm 1.2$ mb [104]. It has been determined by using the Van Der Meer scans [103, 104].

The invariant cross section for inclusive neutral pion production covers transverse momentum range of $0.8 < p_{\rm T} < 20$ GeV/c while η meson is measured in $2 < p_{\rm T} < 20$ GeV/c range. The total uncertainties are calculated by adding the statistical and systematic uncertainties in quadratures. These errors are at the level of 8% for the π^0 and 20% for the η meson in most of the $p_{\rm T}$ bins presented in this analysis. The uncertainties increase at the edges of the distributions. At high $p_{\rm T}$, it happens due to statistics, whereas at low $p_{\rm T}$ ($p_{\rm T} < 3$ GeV) because of the worse time resolution and a smaller signal to noise ratio.

5.1 Comparison with the lower LHC energies

The final neutral pion invariant cross sections reconstructed in pp collisions at $\sqrt{s} =$ 13 TeV together with the most recent measuremnts at $\sqrt{s} = 0.9,\ 2.76,\ 7$ and 8 TeV [32, 30, 33] are shown in Fig. 5.1. The red points correspond to the neutral meson spectra at $\sqrt{s} = 13$ TeV. This is the first measurement so far of neutral meson inclusive spectra at the highest LHC energy. Some of the previous ALICE measurements were done in the wider $p_{\rm T}$ regions. For example, neutral meson spectrum measured at $\sqrt{s} = 2.76$ TeV extends up to $p_{\rm T} \sim 40$ GeV/c and the data from $\sqrt{s} = 7$ TeV reaches down to $p_{\rm T} \sim 0.3$ GeV/c. The reason is that ALICE has reported the combined measurements of neutral meson production obtained from different detectors. In addition to the PHOS detector, the data from TPC and EMCal were used. As all the detectors have different efficiency and acceptance depending on $p_{\rm T}$, combining their data from different detectors, one can extend the lowest and the highest accessible $p_{\rm T}$ ranges and reduce the uncertainties in the overlapping regions.

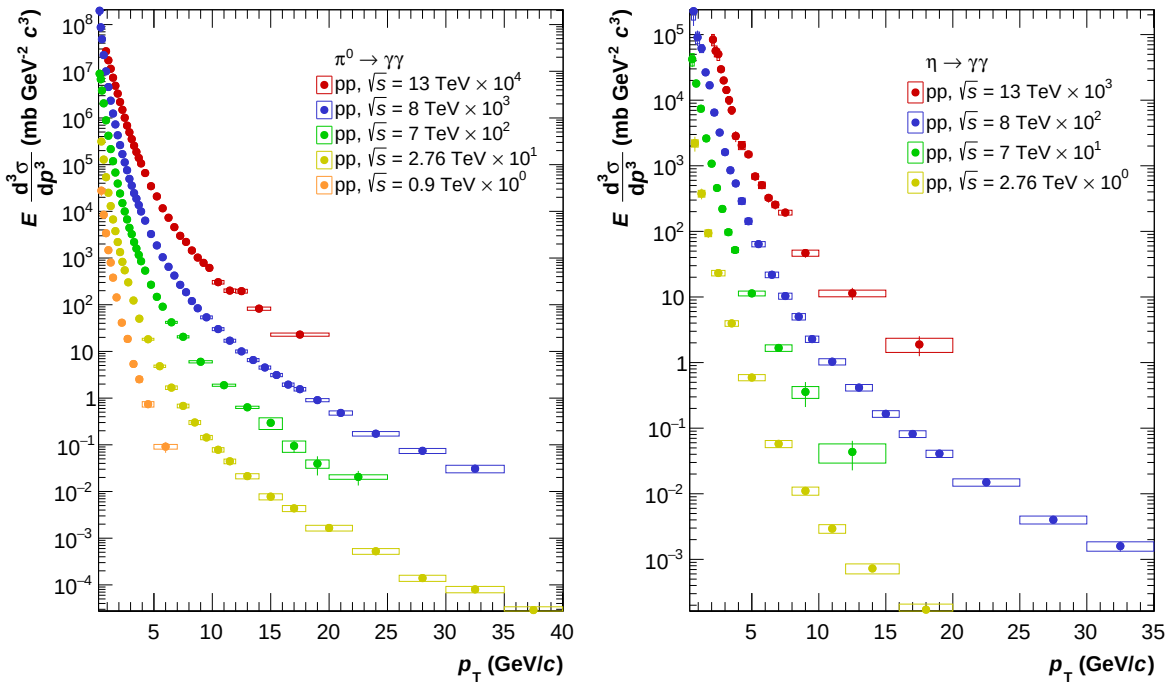

Figure 5.1: The differential cross section for inclusive π^0 (left plot) and η meson (right plot) production in pp collisions at $\sqrt{s} = 13$ TeV (red points) and the most recent measuremnts at $\sqrt{s} = 0.9,\ 2.76,\ 7$ and 8 TeV [32, 30, 33]. The vertical bars and open squares correspond to the statistical and systematic errors, respectively.

The highest accessible p_T bin in the current analysis is determined by the statistics in that region. The number of high-energy particles drops sharply with p_T, as it can be seen from Fig. 5.1. The lowest p_T for π^0 spectrum is 0.8 GeV/c while for η meson differential cross secction it is $p_T = 2$ GeV/c. These values are determined by the acceptance of the photon spectrometer. The opening angle between decay photons decreases with the energy of the particle. It becomes large at low p_T, so at least one of the photons escapes PHOS.

The analyses of the η to π^0 spectra and their ratio will be presented in the subsequent sections.

5.2 Phenomenological description

The description of the hadron transverse momentum spectra in hadron and nuclear collision provide information on the dynamics of the system. The theoretical approach based on perturbative QCD calculations is not applicable at low p_T, and the transition point between the soft and hard p_T region is not well defined. For these reasons, the alternative phenomenological approaches are used in hadron spectroscopy. The thermal models that assume the creation of the stationary hadron gas use Boltzmann distribution to describe the data at low p_T [117, 118, 119, 120]. These models underpredict the data at very high p_T, which shows power-law behaviour that well agrees with the quark model [121, 122].

The classical thermodynamics describes the states of physical systems with a set of potentials that can be expressed through the macroscopic variables, state functions, that are related to the system. The temperature of a system in equilibrium, number of particles and entropy S are the examples of state functions. The connection between the macroscopic and microscopic description of the physical systems was established with the

introduction of the statistical definition of entropy:

$$S = -k \sum_{i=0}^{W} p_i \log(p_i),$$

where W are the number of all possible microstates of the system, p_i is the probability of finding the system in a microstate i and k is the Boltzmann's factor. This definition of entropy assumes independence of p_i which implies the absence of correlation between the microstates making it suitable for the description of the systems with almost no interactions between its particles such as ideal gas. The probability of the microstates can be derived from the maximum entropy principle. For the isolated system in thermal equilibrium at a constant temperature that has no particle exchange with the surroundings, the probabilities, p_i are mutually exclusive. Mathematically it can be expressed as

$$\sum_{i=0}^{W} p_i = 1.$$

The only observable in such a simple system is energy, however, experimentally one measures its average over many repeated experiments. In order to make a connection to the theory, an assumption should be made that the average over measurements of the same system equals the averaging over measurements on the collection of independent systems. This is the ergodic hypothesis. It is applicable mostly for the systems in thermal equilibrium. Once it holds, the average energy of the system is a subject to a constraint

$$\sum_{i=0}^{W} p_i E_i = \text{const.}$$

The maximum entropy principle, which implies that the probability distribution that describes the data best has the largest entropy, equipped with the constraints described above, immediately gives the formula for the probability to find a system in the microstate i:

$$p_i = \frac{1}{Z} e^{-E_i/kT},$$

where the normalization factor $Z = \sum_{i=0}^{W} e^{-E_i/kT}$ is called a partition function. Such an approach, regarded as Boltzmann-Gibbs statistics, was successful in describing many physical systems. In particular, at the early stages of the strong interaction phenomenology, there were arguments that particle transverse spectra at high energies should follow Boltzmann-Gibbs law [123]

$$f(p_{\mathrm{T}}) \propto e^{-p_{\mathrm{T}}/T},$$

where T is the temperature of the hadron system created in the collisions. However, the spectra measured in collider experiments showed steeper behaviour at higher p_{T} then predicted by Boltzmann law. and the development of the phenomenology of strong interactions lead to the modified expression for the asymptotic distribution [124]:

$$f(p_{\mathrm{T}}) \propto \left(1 + \frac{p_{\mathrm{T}}}{p_o}\right)^{-n},$$

where p_0 and n are the free parameters, that are usually deduced from the fit to the experimental data. This parameterization is referred to as the Hagedorn function. This function recovers Boltzmann distribution $f(p_{\mathrm{T}}) \propto e^{-p_{\mathrm{T}}/p_0}$ at $p_{\mathrm{T}} \to 0$ and the power law $f(p_{\mathrm{T}}) \propto (p/p_0)^{-n}$ at $p_{\mathrm{T}} \to \infty$. However, whereas the power-law dependence is inspired by QCD predictions for the high p_{T} part of the hadron spectra, the Hagedorn formula is purely phenomenological, and a suitable statistical model is still required.

One of the possible generalizations of the Boltzmann-Gibbs thermodynamics [49] postulates the entropy in the form of:

$$S_q = k\frac{1-\sum_{i=0}^{W} p_i^q}{1-q}.$$

In the literature this function is called Tsallis entropy. It has an additional parameter q – the entropic index, which reflects the intrinsic properties of the underlying system. Such a definition of entropy is able to model more complex systems as it no longer assumes the absence of correlation between the microstates. This leads to a modified summation rule. For a system that consists of two independent subsystems A and B the probability to be in any particular state is given by the product of the marginal probabilities $p(A)$ and $p(B)$, however, the entropy of such a system is equal to:

$$S_q(A+B) = S_q(A) + S_q(B) + (1-q)S_q(A)S_q(B).$$

Generally, the proposed S_q is not additive and, therefore, it is not an extensive property of a system anymore. The usual summation rule is recovered only for $q = 1$. This is not a coincidence as in the limit $q \to 1$ the Tsallis entropy converges to the Boltzmann-Gibbs entropy $S_1 = -k\sum_{i=0}^{W} p_i \ln(p_i)$ [49]. For this reason, the entropic index q is regarded as the "nonextensivity" parameter which controls the deviation from the classical formulation of statistics.

The expression for the probability of the microstates in a system equipped with the entropy S_q can be derived in the same way as it is done for Boltzmann-Gibbs formulation. The maximum entropy principle gives the Tsallis distribution, which is often written in the form:

$$f_q(p_\mathrm{T}) = C_q\left(1-(1-q)\frac{p_\mathrm{T}}{T}\right)^{\frac{1}{1-q}},$$

where C_q is the normalization constant, q is the noextensivity parameter and T can be interpreted as the effective temperature of the system. This function is a generalization of Boltzmann distribution as the usual exponential law $f_1 = C_1 e^{-p_\mathrm{T}/T}$ can be obtained from it by setting $q = 1$. On the other hand for $q \neq 1$ this function shows power-like behaviour similar to Hagedorn parametrization that was inspired by QCD [124]. Indeed, the Tsallis distribution corresponds to the Hagedorn function with parameters $n = q/(q-1)$ and $p_0 = T/(q-1)$.

Although the functional forms of both models are equivalent, the justifications differ. The Hagedorn distribution was introduced as an empirical function that agrees with the microscopic theory, while the Tsallis formula is derived from the generalization of the Boltzmann-Gibbs statistics. It assumes the existence of the equilibrium states that can be described by the temperature T and the nonextensivity parameter q.

It was shown that the entropy index q is connected to the intrinsic fluctuations [125] of temperature. For a system with nonhomogeneous heat distribution, the local temperature T_local changes around the equilibrium temperature T. The distribution of such fluctuations $g(1/T_\mathrm{local})$ can be expressed in the following way:

$$g(1/T_\mathrm{local}) = \frac{1}{\Gamma\left(\frac{1}{q-1}\right)}\frac{T}{q-1}\left(\frac{1}{q-1}\frac{T}{T_\mathrm{local}}\right)^{\frac{2-q}{q-1}}\exp\left(-\frac{1}{q-1}\frac{T}{T_\mathrm{local}}\right).$$

In this formula the parameter q comes from the evolution equation for T_local and is defined as:

$$q-1 = \frac{\mathrm{Var}[1/T_\mathrm{local}]}{\mathrm{E}[1/T_\mathrm{local}]^2}.$$

The local temperature fluctuations $g(1/T_\mathrm{local})$, averaged with Boltzmann-Gibbs distribution of states $f(p_\mathrm{T}) \sim e^{-p_\mathrm{T}/T_\mathrm{local}}$ over all possible T_local, produces the Tsallis distribution $f_q(p_\mathrm{T})$. This connects the definitions of the parameter q as an entropic index

to the rate of the local temperature variations. Such approach was successful in describing charged hadron p_{T}-spectra in proton-proton collisions at SPS (beam momenta 20, 31, 40, 80, and 158 GeV/c) [126, 127], RHIC ($\sqrt{s} = 62.4$ and 200 GeV) [128, 129, 130] and the most recent results at LHC ($\sqrt{s} = 0.9,\ 2.76,\ 7$ and 8 TeV) [130, 131, 132, 133, 127, 33] energies.

Another advantage of the statistical approach in the phenomenological description of hadron spectroscopy is that multiplicity distribution is in good agreement with this framework. In particular, for a set of particles produced with energies $E_1, E_2, \ldots, E_N$ taken from the Boltzmann-Gibbs distribution $f(E)$ the joined probability to observe such particles is

$$f(E_1, E_2, \ldots, E_N) = \frac{1}{\lambda^N} \exp\left(-\frac{1}{\lambda}\sum_{i=1}^{N} E_i\right),$$

where, the parameter λ has the meaning of the average energy fraction carried out by a single particle. The probability of finding N particles at energies less than E is given by an integral over all allowed combinations of energies, which results in Poisson distribution:

$$P(N) = \frac{\bar{N}^N}{N!} e^{-\bar{N}},$$

where $\bar{N} = E/\lambda$ is the average number of particles produced in the final state of the collision. The similar calculations can be repeated for the Tsallis distribution $f_q(E)$. In this case, the final-state multiplicity follows the Negative Binomial Distribution (NBD) [134]:

$$P(N) = \frac{\Gamma(N+k)}{\Gamma(N+1)\Gamma(k)} \frac{\left(\frac{\langle N\rangle}{k}\right)^N}{\left(1+\frac{\langle N\rangle}{k}\right)^{N+k}}, \tag{5.1}$$

where $\langle N\rangle$ is the average number of particles for NBD and $k = 1/(q-1)$. This is still a generalization of the Boltzmann-Gibbs statistics as for $q \to 1$ this formula gets reduced to Poisson distribution. In the limit, $q \to 2$ the NBD converges to geometrical distribution.

Finally, the formula 5.1 in case of large multiplicities leads to Koba-Nielsen-Olesen (KNO) scaling [135], written in the form:

$$\langle N\rangle\, P(N) \approx \psi\left(z = \frac{N}{\langle N\rangle}\right) = \frac{k^k}{\Gamma(k)} z^{k-1} \exp\left(-kz\right).$$

In this sense, the nonextensive thermodynamics not only describes the single-particle spectra, but at the same time it gives the statistical model that reflects broadening of the multiplicity distributions in proton-proton collisions [136].

It was observed experimentally that fluctuations in multiplicity distributions are much smaller than the ones in transverse or rapidity spectra [137]. The possible explanations and connections between the parameters q calculated in different dynamical systems were successfully derived within the nonextensive approach [138, 139, 140].

Previous measurements of π^0 and η meson production in pp collisions reported by ALICE [30, 31] used Tsallis-like function [49] to describe the data. These results showed that the nonextensive approach could describe the neutral meson spectra in hadron collisions at very high energies. In this analysis, the π^0 and η meson spectra were fitted with the same parameterization of the Tsallis function. For the meson with the rest mass m, the function was defined as:

$$E\frac{\mathrm{d}^3\sigma}{\mathrm{d}p^3} = \frac{A}{2\pi} \frac{(n-1)(n-2)}{nT(nT + m(n-2))} \left(1 + \frac{m_{\mathrm{T}} - m}{nT}\right)^{-n},$$

where A, n and T are the free parameters of the model obtained from the fit and $m_{\mathrm{T}} = \sqrt{p_{\mathrm{T}}^2 + m^2}$ is the transverse mass. The parameters in this formula are different from the ones that enter the expression for f_q. By making the following transformation:

$$n \to 1 + \frac{1}{q-1} \text{ and } nT \to \frac{T + m(q-1)}{q-1},$$

the formula for $E\frac{\mathrm{d}^3\sigma}{\mathrm{d}p^3}$ becomes the f_q function. Such parametrization is a matter of convenience as the parameter A related to the area under the curve has the same units as a cross-section. This simplifies the comparison with other models.

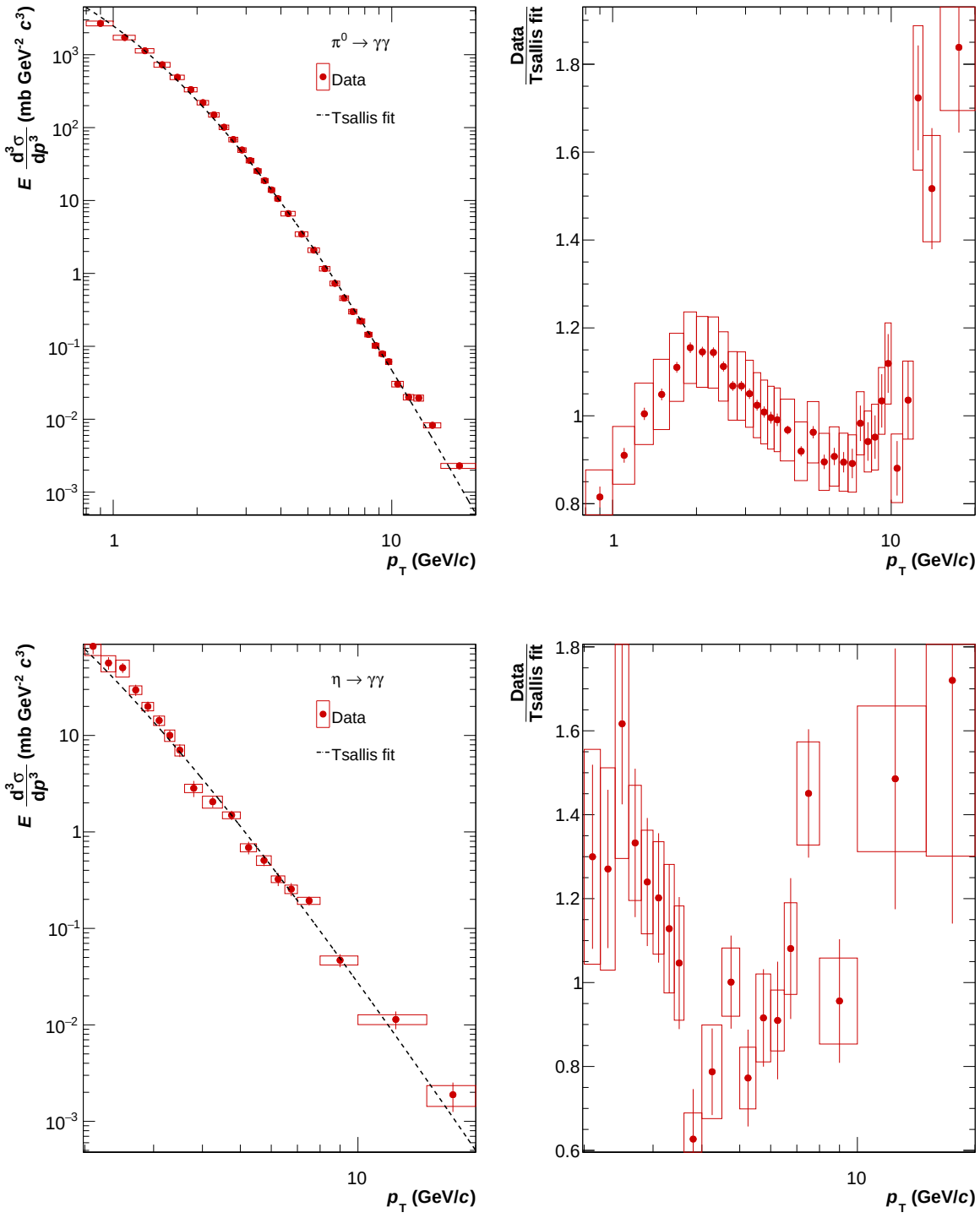

Figure 5.2: The invariant cross-section of the inclusive neutral pion and η meson production (left plots) and the ratio of the data to Tsallis fit (right plots) in pp collisions at $\sqrt{s} = 13$ TeV. The dashed black line represents the result fit of the Tsallis function [49].

The data studied in this thesis were fitted with the Tsallis function in the entire accessible p_{T}-range. Both, the neutral pion and η meson yield show systematic deviations from the fit in low and high p_{T} regions Fig. 5.2 (left plots). This results in high values of $\chi^2/\mathrm{ndf} \sim 2.42$ and $\chi^2/\mathrm{ndf} \sim 1.92$ for π^0 and η meson, respectively. The data to fit ratio is presented in Fig. 5.2 (right plots). The maximum deviation of the low p_{T} part of the spectrum from the Tsallis shape is at $p_{\mathrm{T}} \sim 2$ GeV/c. The fitted function commences to depart from the data again at $p_{\mathrm{T}} > 10$ GeV/c and increases with p_{T}. Similar disagreement was observed for neutral meson production cross section in pp collisions at $\sqrt{s} = 2.76$ and 8 TeV measured by ALICE experiment [32, 33]. The systematic study of charged hadron transverse spectra showed a similar pattern for other particles in the wide energy range [141].

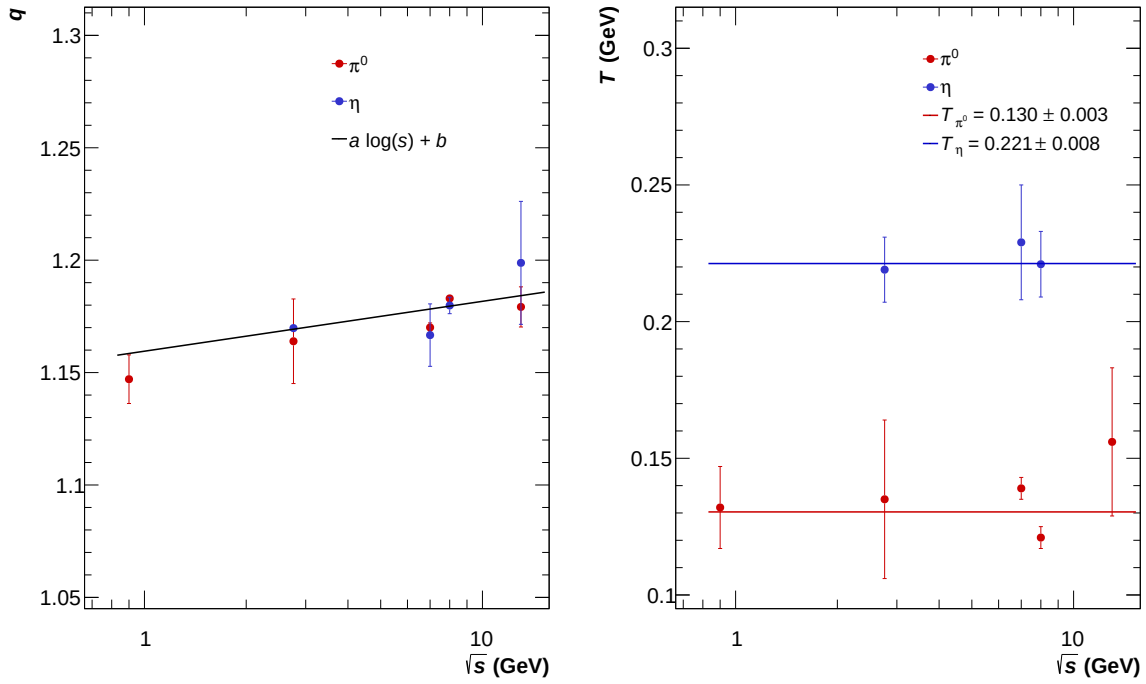

Figure 5.3: Left plot: The nonextensivity parameter q obtained for the neutral pion (red points) and η meson (blue points) inclusive production cross sections in pp collisions at LHC energies. Left plot: The Tsallis temperature T for the neutral pion (red points) and η meson (blue points) inclusive production cross sections in same collision systems.

For these reasons the fitting procedure was repeated for neutral pion and η meson spectra in a restricted transverse momentum ranges $2 < p_{\mathrm{T}} < 10$ GeV/c and $3 < p_{\mathrm{T}} < 10$ GeV/c, respectively, in order to get the reliable values of the extesivity parameters. The reduction of the kinematic region improves the quality of the π^0 fit leading to $\chi^2/\mathrm{ndf} \sim 0.23$, while for η meson $\chi^2/\mathrm{ndf} \sim 1.91$ stays almost the same. The nonextensivity parameter q and temperature T were extracted from this fit and from the data on neutral meson production cross-section measurements in pp collisions reported by ALICE at $\sqrt{s} = 0.9,\ 2.76,\ 7$ and 8 TeV [32, 30, 33]. They are presented in Fig. 5.3 as a function of the collision energy. The red and blue points represent π^0 and η parameters, respectively. The nonextensivity parameter q shows a weak energy dependence in the range $0.15 < q < 1.20$ for $0.9 - 13$ TeV energy interval. The q energy dependence of π^0 and η were fitted simultaneously with a function

$$q(\sqrt{s}) = a \log\left(\sqrt{s}\right) + b,$$

yielding $a = 0.010 \pm 0.001$ and $b = 1.160 \pm 0.002$. The fitted curve is shown in the left plot of Fig. 5.3. The dependence of Tsallis temperature on collision energy was fitted with a

zero-degree polynomial for π^0 and η mesons separately yielding $T_{\pi^0} = 0.130 \pm 0.003$ GeV and $T_\eta = 0.221 \pm 0.008$ GeV, respectively. The fitted polynomials are depicted in the right plot in Fig. 5.3. Inspection of the measured q and T distributions reveals the following behaviour of the Tsallis parameters:

1. The nonextensivity parameter q grows as a logarithm of energy changing from ~ 1.15 to ~ 1.2 in the point 0.9 TeV to 13 TeV.

2. The energy dependence of the nonextensivity parameter is the same, within the limits of errors, for π^0 and η mesons.

3. The Tsallis temperature depends strongly on the mass of the particle being for η twice as large as for π^0.

These observations may indicate that sources of different particle species exhibit similar dynamical fluctuation patterns governed by the nonextensivity parameter q.

The neutral meson cross sections measured in pp colllisions at $\sqrt{s} = 13$ TeV together with the corresponding Tsallis fits in $2 < p_{\mathrm{T}} < 10$ GeV/c region for π^0 and $3 < p_{\mathrm{T}} < 10$ GeV/c for η meson, are shown in Fig. 5.4 with dashed lines. For illustration purposes, the functions were plotted in the extended p_{T}-ranges. The parameters of the fits are presented in table 5.1.

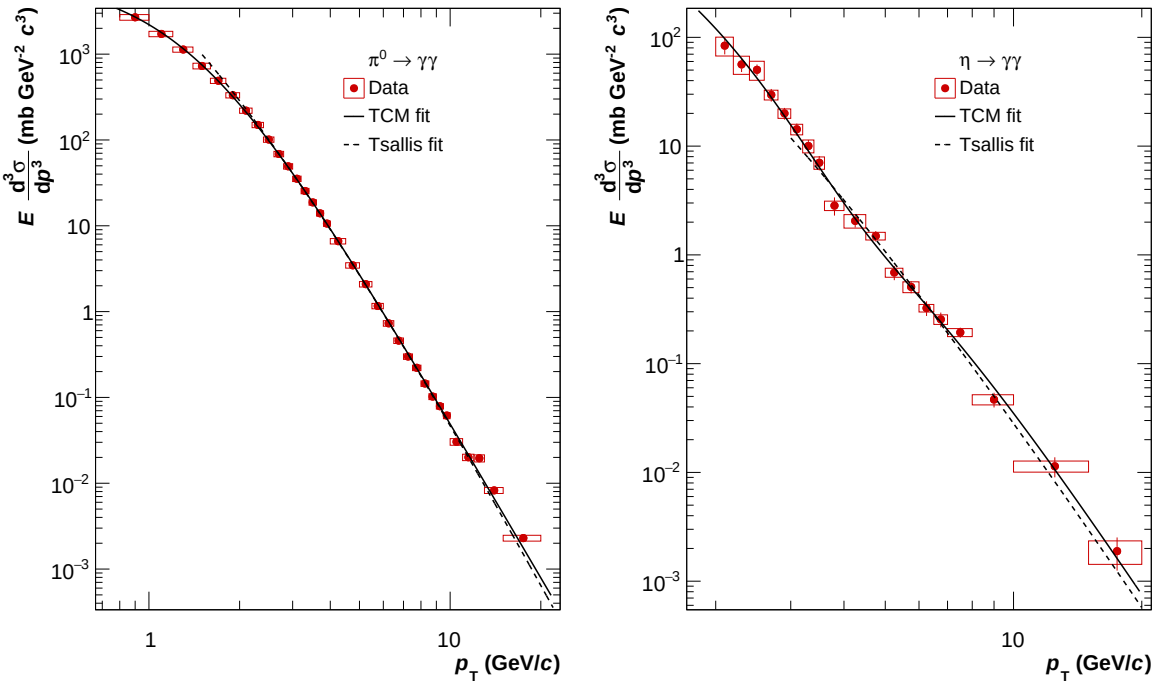

Figure 5.4: The invariant cross-section of the inclusive neutral pion (left plot) and η meson productions at $\sqrt{s} = 13$ TeV. Red points correspond to the experimental data and the solid black lines are the fit result of two-component function [36, 141] defined earlier in this section (5.2). The dashed black line represents the fits of the Tsallis parametrization [49]. The sum in quadratures of statistical and systematic uncertainties is used to obtain the final error for the fits. The vertical bars and open squares correspond to the statistical and systematic errors, respectively.

Although Tsallis function provides a reasonable description of the hadron spectra in various collision systems over the wide p_{T} ranges, this study and the recent ones demonstrate that the data commence deviating from it at high energies [141]. It was also

demonstrated that the measurements systematically depart from the theoretical predictions at low p_{T}. This observation is confirmed in the current measurement as can be seen in Fig. 5.4. The two-component model (TCM), was introduced in [141, 36] as possible improvement of the phenomenological description of the hadron spectra.

This parameterization combines a Boltzmann-Gibbs component that describes soft processes at low p_{T} and a power-law term that dominates at high p_{T} and describes mesons coming from the hard pQCD scatterings. The functional form of the TCM for a meson with a rest mass m is defined as:

$$E\frac{\mathrm{d}^3\sigma}{\mathrm{d}p^3} = A_{\mathrm{e}}\,\exp\left(-E_{\mathrm{T,kin}}/T_{\mathrm{e}}\right) + A\left(1+\frac{p_{\mathrm{T}}^2}{T^2 n}\right)^{-n}, \tag{5.2}$$

where $E_{\mathrm{T,kin}} = \sqrt{p_{\mathrm{T}}^2 + m^2} - m$ is the transverse kinetic energy and A_{e}, A, T_e, T as well as n are the free parameters that are constrained by the fit to the data. The number of parameters in this model is larger, compared to the Tsallis parametrization, that allows it to capture more complex functional dependencies. The TCM distribution has a couple of interesting properties that make it more attractive among other candidates. For example, the values of parameters T and T_e extracted from the hadron spectra in proton-proton collisions at $\sqrt{s} \leq 200$ TeV exhibit a strong correlation [36]. This indicates the existence

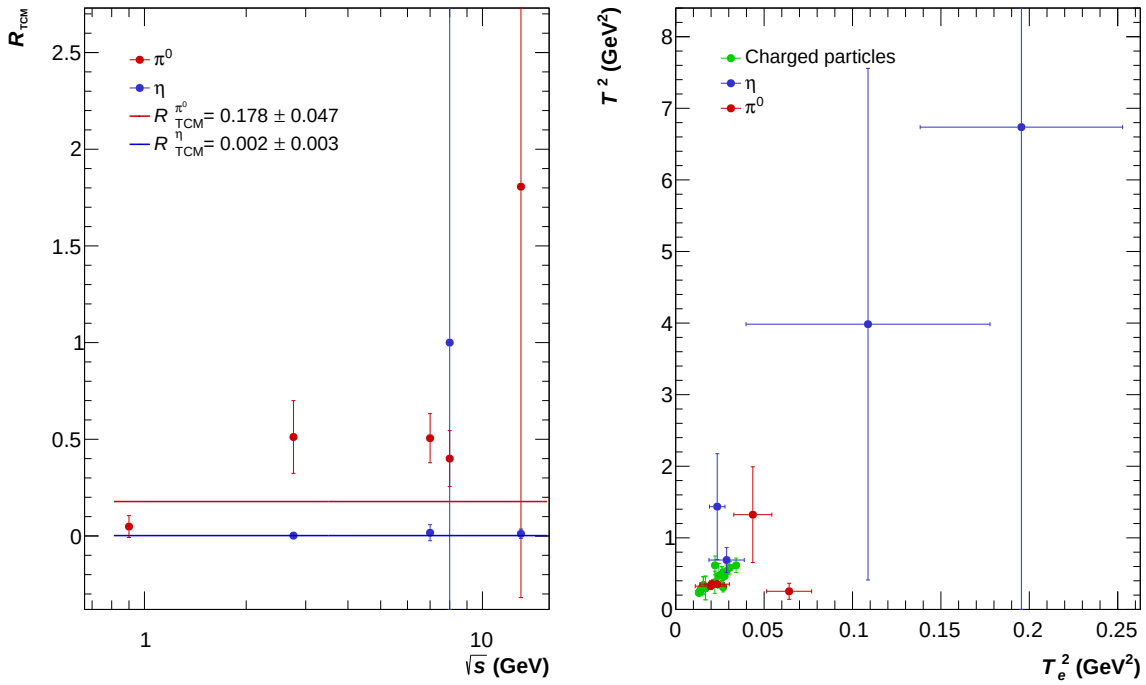

Figure 5.5: Left plot: The relative contribution of the power term to the exponential one R_{TCM} (5.3) in the two-component model [36]. The data are extracted from neutral meson spectra in pp collisions at $\sqrt{s} = 13$ TeV and previous measurements [32, 30, 33] at lower energies. Right plot: The correlation between temperature parameters in the TCM model calculated for the same collision energies. The red and blue points correspond to the π^0 and η meson data, respectively.

of the additional constraint in TCM, which practically reduces the number of free parameters. Yet another remarkable property of the TCM parameterization is the ratio of the exponential and power-law contributions R_{TCM}. It can be expressed by the formula, derived from the definition of TCM function:

$$R_{\mathrm{TCM}} = \frac{AnT}{AnT + A_e(2mT_e + 2T_e^2)(n-1)}. \tag{5.3}$$

It was demonstrated that this quantity is small and shows a weak energy dependence in proton-proton and vanishes in $\gamma\gamma$ collisions [141]. This property is a key point in understanding the physical picture encoded in the TCM invariant cross-section. The model assumes two sources of the final-state hadrons produced in the high-energy collisions. The first one is the radiation emitted by the valence quarks in the cooling hadron gas in baryon-baryon collisions. This also explains the absence of the exponential term in $\gamma\gamma$ collisions [141] as there are no valence quarks in the initial collision. The second source of hadrons is associated with the fluctuations of QCD-vacuum, which is described by a Pomeron exchange. This type of interaction naturally leads to the power-law shape of the distribution. It was shown [142] that the TCM model predicts the increase of R_{TCM} with energy and, thus, the decrease of the exponential term contribution with multiplicity in proton-proton collisions at $\sqrt{s} = 200$ GeV. This is in agreement with the hypothesis of the QCD-vacuum fluctuations, as according to it the multiplicity in hadron-hadron collisions is proportional to the number of Pomeron exchanges in the interaction [143].

The two-component model provides an alternative way to describe the hadron spectra in proton-proton, proton-antiproton, heavy-ion, and photon-photon collisions in the wide energy range (from $\sqrt{s} = 23$ GeV to $\sqrt{s} = 7$ TeV). It was also used to fit the invariant cross sections for inclusive π^0 and η meson production at $\sqrt{s} = 8$ TeV [33]. The fit of the TCM formula showed a good agreement with the data at low and high p_{T} resulting in the smaller χ^2/ndf values compared to those obtained with Tsallis fit.

Tsallis	π^0	η
A (mb GeV$^{-2}c^3$)	109749.944 ± 45484.218	7230.530 ± 3301.915
T (GeV)	0.156 ± 0.027	0.254 ± 0.050
n	6.581 ± 0.278	6.030 ± 0.692
χ^2/ndf	0.23	1.91
p_{T} range of the fit	$2 < p_{\mathrm{T}} < 10$ GeV/c	$3 < p_{\mathrm{T}} < 10$ GeV/c

TCM	π^0	η
A_{e} (mb GeV$^{-2}c^3$)	0.006 ± 596233.415	3850.156 ± 2433.814
T_{e} (GeV)	0.131 ± 1445.852	0.432 ± 0.072
A (mb GeV$^{-2}c^3$)	7924.269 ± 61.943	16.527 ± 39.579
T (GeV)	0.792 ± 0.001	2.207 ± 1.445
n	3.007 ± 0.005	2.984 ± 0.839
χ^2/ndf	0.82	0.98
p_{T} range of the fit	$0.7 < p_{\mathrm{T}} < 22$ GeV/c	$1.8 < p_{\mathrm{T}} < 20$ GeV/c

Table 5.1: Parameters of the fits to the differential invariant yields of π^0 and η meson using Tsallis [49] and two-component Bylinkin-Rostovtsev functions [141, 36]. The total uncertainties, i.e. quadratic sum of statistical and systematic uncertainties, are used for the fits.

We calculated the R_{TCM} as a function of center-of-mass energy $\sqrt{s}$ for neutral mesons in pp collisions at LHC energies [32, 30, 33]. Since these spectra cover different p_{T} limits, the fitting range was restricted to $0 < p_{\mathrm{T}} < 15$ GeV/c and $2 < p_{\mathrm{T}} < 15$ GeV/c for π^0 and η, respectively. The relative contribution of the power-law part in the two-component model, presented in Fig. 5.5 (left plot), shows weak energy dependence. This agrees with the observations made by the authors of this model [141]. Some of the parameters of this model are correlated. An example of such correlations is shown in Fig. 5.5 (right plot) for temperatures T and T_e.

In conclusion, the two-component and Tsallis models were used to describe the cross-section for the inclusive production of π^0 and η. The solid black line in Fig. 5.4 corresponds to TCM function, while the dashed one represents the Tsallis distribution fitted to $\sqrt{s} =$

13 TeV data. The resulting TCM model shows a good agreement with the experimental data, especially at lower p_{T} for the neutral pion spectrum. Both sets of parameters extracted from both the TCM and Tsallis fits are listed in Tab. 5.1.

Since the two-component model reproduces π^0 and η meson invariant cross-section data in the entire p_{T} range, it was chosen as the neutral meson spectra continuous representation in the following analyses. This observation is in agreement with previous ALICE results, where TCM describes the spectra at low and high p_{T} better than the Tsallis function [144, 33, 32]. One has to bear in mind, however, that TCM scheme has more free parameters than the Tsallis distribution.

5.3 Comparison with the pQCD calculations

In this section, the comparison of our data with PYTHIA event generators and pQCD calculations will be presented.

Most of the measurements in high energy physics rely on Monte-Carlo generators. They are used to estimate parameters of the detector, its efficiency, or to calculate likelihood functions. Generally, they are extremely complex programs containing theoretical and phenomenological models that describe the data. The Monte-Carlo generators are divided into submodules responsible for hadronization, hard process, parton showers, multiparticle interactions and particle decays. Almost all models in Monte-Carlo generators work on the three levels of perturbative theories. Sometimes next-to-leading order corrections are applied. Usually, such corrections are obtained from the hadron spectrometry. This makes the measurements of hadron spectra crucial in understanding the performance of such generators.

In particular, for pp collisions, state of the art Monte-Carlo generator is PYTHIA [61, 34]. It makes emphasis on multiparticle production in collisions between elementary particles that correspond to hard interactions in pp collisions. This program and its variations generate complete events similar to experimentally observable ones. For a single event, PYTHIA takes into account the following processes [61]:

- The early stage of a collision of two-beam particles characterized by parton distribution function that are subjected to flavour and energy constraints.
- The initial-state shower generation that consists of $q \to qg$ processes originating from the partons belonging to different particles.
- The hard processes involving incoming partons (quark-antiquark annihilation, quark-gluon Compton scattering) that may determine the main characteristics of the event.
- An optional production of short-lived resonances and their decays. For example, PYTHIA can generate decays of $Z^0/W^{\pm}$ gauge bosons.
- The final sate-showers initiated by the outgoing partons.
- Semihard interactions between spectator partons.
- The outgoing quarks and gluons are described as parts of colour neutral hadrons to satisfy QCD confinement.
- Decays of unstable hadrons.

The simulations are based on the current understanding of the underlying physical processes in the sense that they are tuned to reproduce the measurements obtained in the experiments. The quantum nature of the high-energy collisions leads to event-by-event

fluctuations. PYTHIA reproduces them with Monte-Carlo methods and ensures the correct expected values of the physical observables. This makes it one of the most widely used event generators for simulations in pp collisions at high energies.

The invariant cross-sections of inclusive π^0 and η meson productions are plotted together with PYTHIA 6 [61] calculations. The red points in Fig. 5.6 correspond to the

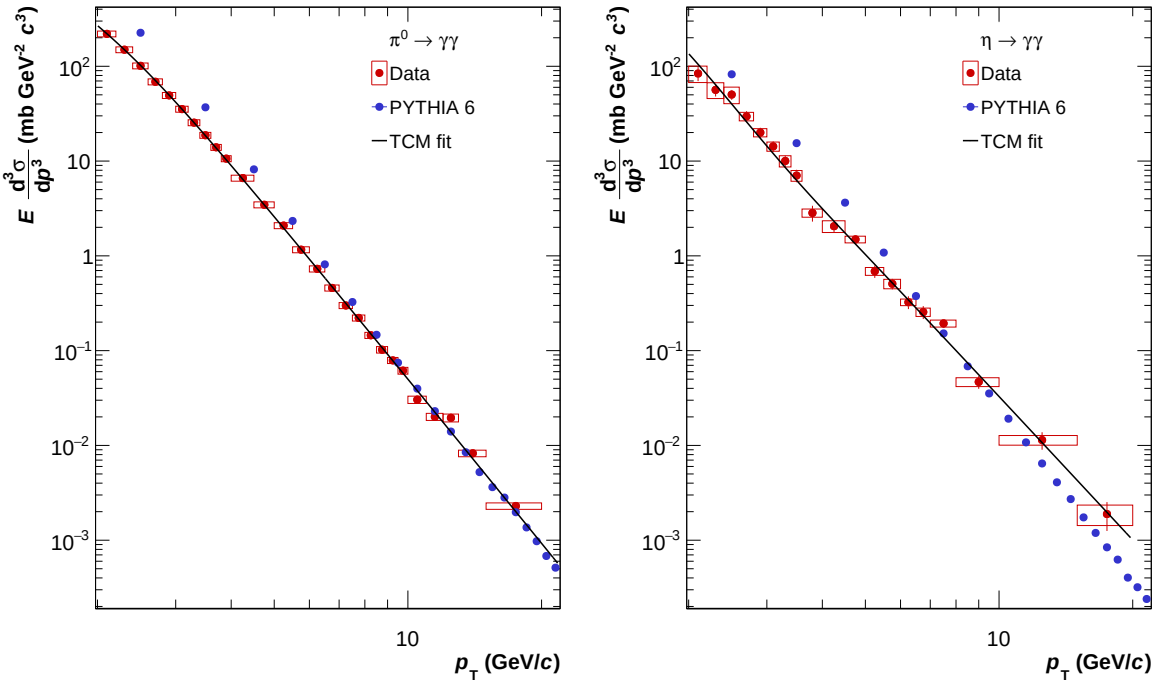

Figure 5.6: The invariant cross-section of π^0 and η meson measured at $\sqrt{s} = 13$ TeV with PHOS (red points). The error bars presented on the plot are calculated as a quadratic sum of systematic and statistical uncertainties. The blue points correspond to PYTHIA 6 predictions [61]. The solid black line corresponds to TMC fits [141, 36]. The vertical bars and open squares correspond to the statistical and systematic errors respectively.

π^0 and η spectra measured at $\sqrt{s} = 13$ TeV while blue points represent PYTHIA 6 predictions. The simulation reproduces the π^0 yield within 10% in the high p_T region (above 10 GeV/c). The PYTHIA 6 predicts significantly higher yields at $1 < p_T < 7$ GeV/c. This is not a new effect, the similar but somewhat higher disagreement was reported in the most recent measurements by ALICE. The π^0 spectrum measured at $\sqrt{s} = 2.76$ TeV show disagreement with PYTHIA predictions at the level of 150% [32, 31]. The measurement of neutral pion cross section at $\sqrt{s} = 8$ TeV [33] shows 30% deviation from PYTHIA 8.210 with tune 4C [41] and 10% with Monash 2013 tune [40].

Similar effects can be observed with the η meson production cross-section, which is below the PYTHIA 6 predictions at low p_T. It starts reproducing the data at $p_T > 7$ GeV/c. The discrepancy between predictions and measurements were observed in pp collisions at lower energies as well [30, 33, 31]. The highest deviation from the data of $\sim 300\%$ was at $\sqrt{s} = 8$ TeV at a low p_T. The difference decreases at lower energies to 200% for at $\sqrt{s} = 7$ TeV for $p_T < 2$ GeV/c. The measurement presented in this analysis confirms the discrepancy between data and PYTHIA predictions at low p_T and the good agreement for π^0 at $p_T > 7$ GeV/c whereas for η agreement is not so good at low and high p_T.

It is also important to compare the data to the QCD theory predictions itself. There exists an open-source code for direct photon and inclusive hadron production [145]. The package performs pQCD calculations based on PDFs and FFs constrained from low energy experiments [145]. It is able to estimate neutral pion inclusive production at next-to-

leading order approximation of QCD, employing CTEQ PDFs [146, 147] and NLO FF extracted from the LEP data [148] (see chapter 1.4.2 chapter of this tehsis). In Fig. 5.7, we make such a comparison presenting the ratio of the measured data and pQCD to the two-component model fit.

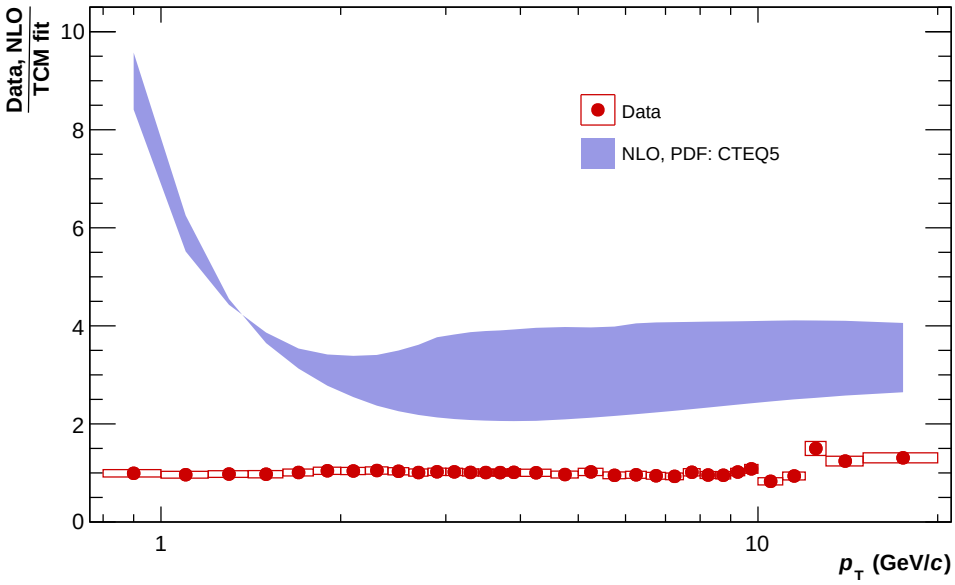

Figure 5.7: The ratio of the invariant cross section for π^0 production measured in pp collisions at $\sqrt{s} = 13$ TeV (red points) to TCM fit [141, 36]. The shaded area corresponds to the pQCD NLO predictions with CTEQ5 PDFs [146, 147] and FF extracted from LEP data [148] calculated for initial and renormaizated scale in the range $p_T/2 < \mu < 2p_T$. The vertical bars and open squares correspond to the statistical and systematic errors respectively.

The red points in Fig. 5.7 refer to the π^0 cross section. The blue-shaded region is the pQCD prediction for pp collisions at $\sqrt{s} = 13$ TeV. Its upper part corresponds to the calculations with factorization and renormalization scale $\mu = p_T/2$, while the lower part to $\mu = 2p_T$. The pQCD calculations strongly overpredict the data at low p_T and get closer to the data for $p_T > 10$ GeV/c. But even there the disagreement of 300% is observed. We reported the discrapancy $100 - 300\%$ in pp collisions at lower energies [30, 32, 33]. It should be noted that the NLO caclulations presented here are based the parton distribution functions obtained from low-energy measurements for $\sqrt{s} < 30$ GeV [149] and fragmentation functions extracted from LEP data [148]. Such a large difference between the data measured in pp collisions at $\sqrt{s} = 13$ TeV and the theoretical predictions indicates that the dynamics of high-energy collisions strongly depends on energy. This measurement can be used as an **input for the analysis of the fragmentation functions** to improve the precision of the pQCD-based models.

5.4 η/π^0 ratio

While inclusive single-particle spectra represent the dynamics of hadron production in different kinematic regions the ratio of cross-sections measured in the same collision system can reveal the possible differences in the **production of those particles and thus their constituents**. For example, it was already demonstrated in section 3.2.5 that PYTHIA is not able to reproduce $K^{\pm}/\pi^{\pm}$ ratio, and additional corrections should be made. The similar study should be repeated for π^0 and η mesons.

From experiments point of view, η/π^0 ratio has an additional advantage as it can be measured with higher precision than the spectra themselves. The systematic uncertainties

connected to the absolute energy scale in calorimeters cancel down.

The results presented in this chapter allow measurement of η/π^0 spectrum ratio R_{η/π^0} in a wide p_{T} range $2 < p_{\mathrm{T}} < 20$ GeV/c. The ratio of η meson to the neutral pion cross-sections is presented in Fig. 5.8.

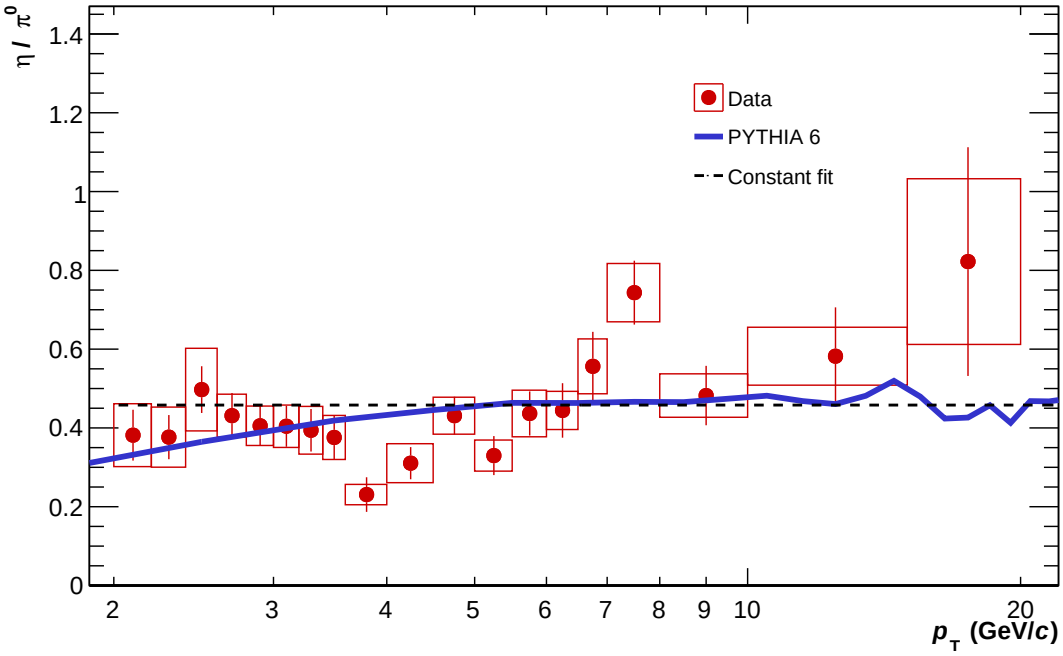

Figure 5.8: η/π^0 invariant cross section ratio R_{η/π^0} measured in pp collisions at $\sqrt{s} =$ 13 TeV (red points). The blue line corresponds to PYTHIA 6 predictions. The dashed line represents the constat $R_{\eta/\pi^0} = 0.458$ obtained from the fit to the data with $\chi^2/\mathrm{ndf} = 1.72$. The vertical bars and open squares correspond to the statistical and systematic errors respectively.

The red points in Fig. 5.8 correspond to the experimental R_{η/π^0} values calculated from $\sqrt{s} = 13$ TeV measurements presented earlier in this chapter. The dashed line is the constant parametrization of the η/π^0 invariant cross-section ratio. This constant is determined from a fit to the data in $4.5 < p_{\mathrm{T}} < 20$ GeV/c range, and is found to be $R_{\eta/\pi^0}(p_{\mathrm{T}}) = 0.458 \pm 0.030$. This value and the results obtained at lower energies are listed in table 5.4. The blue line in Fig. 5.8 represents the PYTHIA 6 prediction for $\sqrt{s} =$ 13 TeV. The good overall agreement with the experimental results is observed. The fact that PYTHIA 6 overpredicts the individual particle spectra but describes reasonably well the η/π^0 cross-section ratio shows that the hadron **production mechanisms should be tuned up whereas the relative contributions of π^0 and η signals are calculated correctly for high energies**.

There is a wealth of data on π^0 and η meson spectroscopy available in a wide energy range. It would be good to calculate and compile the η/π^0 ratio in a single report. The data summarized in table 5.4 are collected from the available publications that reported neutral pion, η meson cross-sections or their ratio in hadron-hadron collisions. Most of the η/π^0 spectra ratio available in the table has been imported from the original publications. The values R_{η/π^0} were calculated by dividing the published η and π^0 spectra reconstructed at the same energy. Their errors were summed in quadratures.

When the binning of η and π^0 spectra did not coincide, a smooth parameterization was used to replace the π^0 spectrum. In particular, in most cases, modified power function was fitted to the data [150]. The η/π^0 ratio was calculated by dividing the experimental points of the η spectrum by that obtained from the fitted π^0 p_{T}-distribution function. The uncertainties for such ratios were calculated from the published errors of the η spectrum and those of π^0 approximations [60].

System	$\sqrt{s}$ (GeV)	p_{T} range (GeV/c)	R_{η/π^0}	Collab./Exp.	Ref.
pp	13.8	$1.6 - 2.4$	0.52 ± 0.13	FNAL M2	[18]
π^+p	13.8	$1.6 - 3.$	0.49 ± 0.10	FNAL M2	[18]
π^-p	13.8	$2. - 3.$	0.41 ± 0.13	FNAL M2	[18]
π^+p	19.4	$2. - 3.5$	0.40 ± 0.07	FNAL M2	[18]
π^-p	19.4	$1.5 - 4.$	0.43 ± 0.04	FNAL M2	[18]
pp	19.4	$2. - 3.5$	0.42 ± 0.04	FNAL M2	[18]
pp	23.0	$4. - 5.5$	0.60 ± 0.04	CERN WA70	[151]
π^+p	23.0	$4. - 5.5$	0.43 ± 0.05	CERN WA70	[151]
π^-p	23.0	$4. - 5.5$	0.57 ± 0.06	CERN WA70	[151]
pp	24.3	$2.5 - 4.$	0.45 ± 0.06	CERN UA6	[152]
p$\bar{\mathrm{p}}$	24.3	$2.5 - 4.$	0.48 ± 0.04	CERN UA6	[152]
pp	30.6	$0.8 - 3.$	0.55 ± 0.04	ISR	[153]
pp	30.6	$3. - 4.$	0.54 ± 0.05	ISR	[154]
pp	31.6	$3. - 8.$	0.41 ± 0.03	FNAL 706	[155]
pp	38.8	$3. - 8.$	0.44 ± 0.03	FNAL 706	[155]
pp	52.7	$3. - 6.$	0.58 ± 0.03	ISR	[154]
p$\bar{\mathrm{p}}$	53.	$2.5 - 4.$	0.53 ± 0.03	ISR AFS	[156]
pp	53.	$2.5 - 4.$	0.55 ± 0.02	ISR AFS	[156]
pp	53.2	$3. - 6.$	0.54 ± 0.03	ISR	[153]
pp	62.4	$3. - 11.$	0.55 ± 0.03	ISR AFS	[154]
pp	63.	$0.2 - 1.5$	0.07 ± 0.055	ISR AFS	[157]
pp	63.	$2. - 4.$	0.47 ± 0.01	ISR AFS	[158]
pp	200.	$2. - 12.$	0.48 ± 0.03	PHENIX	[60]
p$\bar{\mathrm{p}}$	540.	$3. - 6.$	0.60 ± 0.16	CERN UA2	[159]
p$\bar{\mathrm{p}}$	1800.	12.0	1.02 ± 0.27	CDF	[160]
pp	2760.	$2. - 20.$	0.476 ± 0.028	ALICE	[32]
pp	7000.	$2. - 15.$	0.474 ± 0.028	ALICE	[30]
pp	8000.	$2. - 35.$	0.455 ± 0.015	ALICE	[33]
pp	13000	$2. - 20.$	0.458 ± 0.030	PHOS	this thesis

Table 5.2: The data on the R_{η/π^0} ratio in hadron-hadron collisions at various centre-of-mass energies $\sqrt{s}$. For each collision system, $\sqrt{s}$ and the p_{T} range are given. For the measurements which provide systematic and statistical uncertainties separately, the errors quoted were calculated by adding them in quadratures.

5.5 m_{T}-scaling

This section opens a discussion of m_{T}-scaling of the light meson spectra in pp collisions at $\sqrt{s} = 13$ TeV. The overview of results on the properties of transverse mass scaling obtained from various experiments is given in section 1.5.3. The same study was conducted in the current analysis. Since the TCM model well describes the data, it was used to approximate the shape of the neutral pion spectrum. The parameters of that function were fixed except for the normalization. The normalization parameter was taken from a constant fit to η/π^0 ratio above 4.5 GeV/c, see Fig. 5.9. Its value was ~ 0.458. The ratio of the data points to the TCM function was calculated.

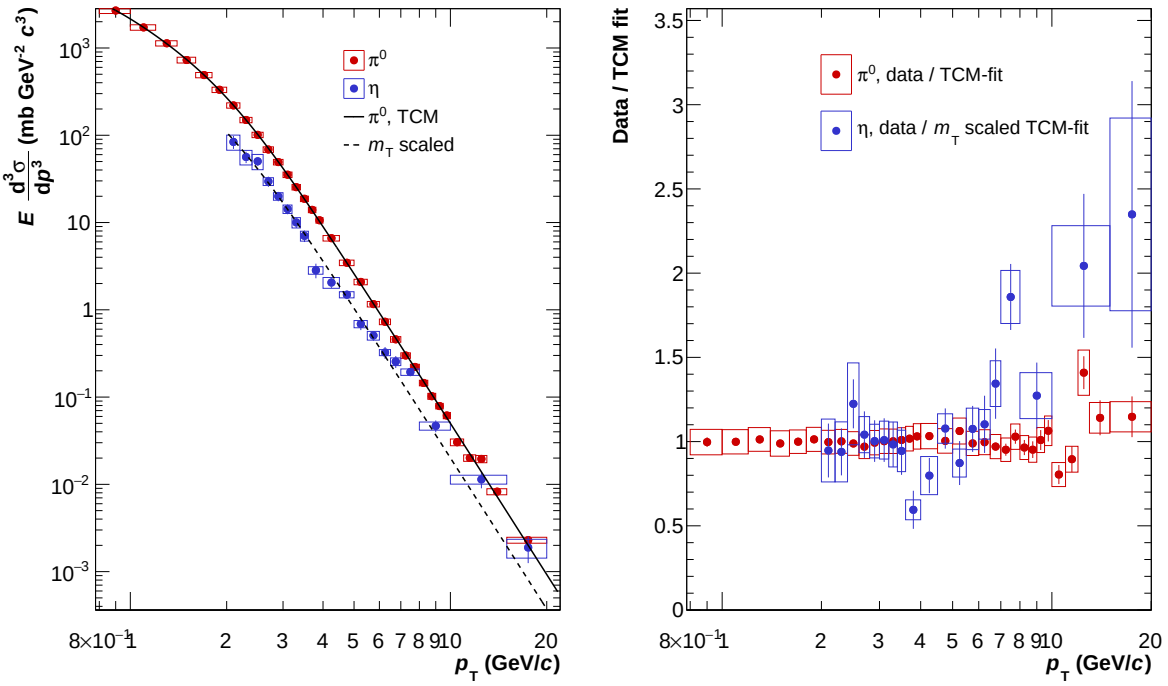

Figure 5.9: Left plot: Invariant cross-section for neutral pions (red points) and η meson (blue points). The solid black line corresponds to the TCM fit to the π^0 spectrum, the dashed line is the m_{T}-scaled invariant cross-section of η meson. Right plot: the ratio of π^0 spectrum to the TCM fit and η spectrum to the m_{T} scaled TCM parametrization. The vertical bars and open squares correspond to the statistical and systematic errors respectively.

For the π^0 spectra, such quantity represents the goodness of fit (values close to unity indicate a good approximation). In the η meson case, this ratio represents the deviation from the π^0 shape. It can be seen in Fig. 5.9 that the neutral pion and η meson invariant yields have similar shapes and only the normalization differs. So this feature is observed in pp collisions at $\sqrt{s} = 13$ TeV for p_{T} above 2 GeV/c.

Since the π^0 and η invariant cross-section can be represented with a power law for higher p_{T} ($\sim$ 3 GeV/c) the analysis [60] described in 1.5.3 can be applied to the data measured at $\sqrt{s} = 13$ TeV. The η/π^0 spectrum ratio can be expressed as the ratio of two power-like functions, and can be written in the form:

$$R_{\eta/\pi^0} = C_{\eta/\pi^0} \left(\frac{a + \sqrt{m_\eta^2 + p_{\mathrm{T}}^2}}{a + \sqrt{m_{\pi^0}^2 + p_{\mathrm{T}}^2}} \right)^{-n},$$

where C_{η/π^0} – is the limiting value of η/π^0 spectrum ratio, and a and n parametrize the m_{T} spectra for both particles (asuming m_{T} scaling is valid). The measured η/π^0

differential yield ratio together with m_{T} predictions is shown in Fig. 5.10. The parameters a and n are the same as in [60] as they were obtained from a fit to a broad range of energies. Since they are related through the formula for the average transverse mass $\langle m_{\mathrm{T}} \rangle = 2a/(n-3)$, the a parameter was fixed to $a = 1.2$. The shaded area in Fig. 5.10 corresponds to the extreme values of the power-law exponent $10 < n < 14$. The exponent of the spectrum parametrization n decreases with energy. The upper and lower edge of the m_{T} parametrization region ($n = 10$) come from a fit at $\sqrt{s} = 200$ GeV, and $\sqrt{s} = 13$ GeV data, respectively.

The functional form of R_{η/π^0} and the parameters a and n are taken from the analysis of the η/π^0 ratio in hadron-hadron collisions at energies below $\sqrt{s} = 200$ GeV [60]. The only difference between the parametrizations is the asymptotic constant C_{η/π^0}. In this thesis $C_{\eta/\pi^0} = 0.458 \pm 0.030$ was taken from the asymptotic analysis described in the previous subsection.

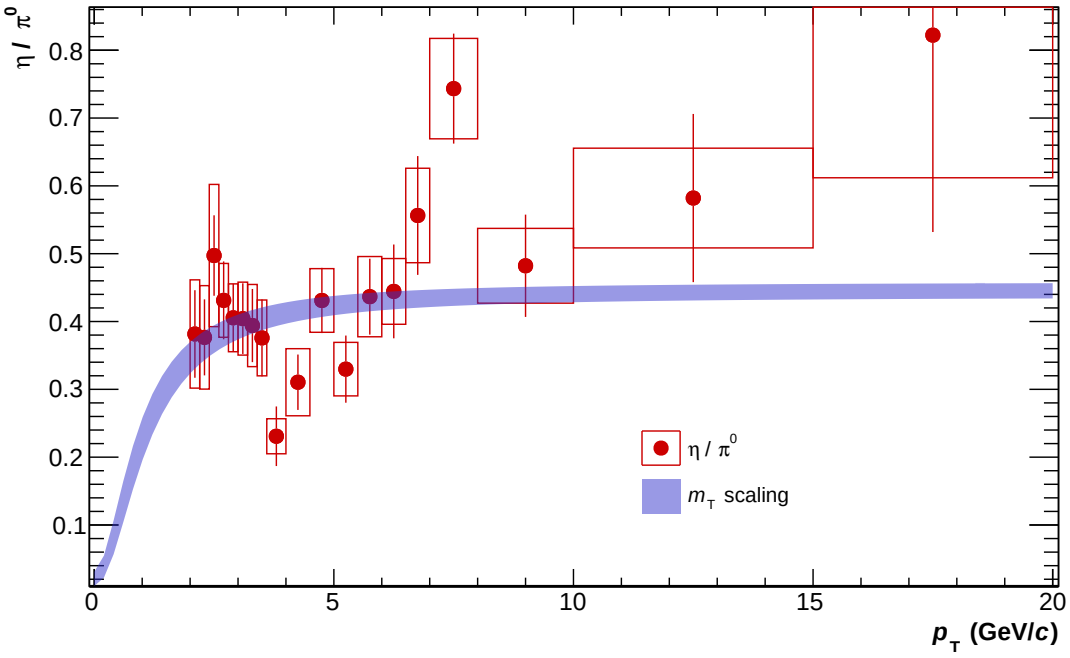

Figure 5.10: The $R_{\eta/\pi^0}(p_{\mathrm{T}})$ invariant yield ratio in pp collisions at $\sqrt{s} = 13$ TeV measured by PHOS (red points). The shaded red area corresponds to the m_{T}-scaling predictions for different power-law exponents $10 < n < 14$, $a = 1.2$ and the limiting value of η/π^0 invariant cross section ratio $C_{\eta/\pi^0} = 0.458 \pm 0.030$. The vertical bars and open squares correspond to the statistical and systematic errors, respectively.

The Pearson's χ^2 nonparametric test, applied to the data and the m_{T}-scaling predictions shown in Fig. 5.10 with the blue band, gave $\chi^2 \sim 29.70$ which is lass than $\chi^2_{\mathrm{critical}} = 32.35$ at significance level $p = 0.02$. We conclude, therefore, that our $\sqrt{s} = 13$ TeV data are consistent with the m_{T}-scaling obtained from the measurements at lower energies preserving the power-law behaviour as a function of transverse mass.

It is expected that the shape of the final-state hadrons spectra in heavy-ion collisions can be altered by collective radial flow at low p_{T} [64]. The contribution of η meson at $p_{\mathrm{T}} < 2$ GeV/c is expected to be larger than that of π^0 as the hydrodynamical flow boosts heavier particles. This results in larger values of η/π^0 ratio at low p_{T} and, consequently, the violation of m_{T} scaling. In the region above 2 GeV/c the m_{T} scaling is restored, as the radial flow effects are negligible. The most recent measurements have confirmed the same effect in pp collisions at $\sqrt{s} = 0.9,\ 2.76,\ 7$ and 8 TeV [32, 30, 33]. The reported results demonstrate the systematic deviation from m_{T} scaling predictions at $p_{\mathrm{T}} < 3.6$ GeV/c.

In this measurement, we do not see any significant indication of such an increase of the η/π^0 ratio. The p_{T}-region below 2 GeV/c is a very interesting part of the spectrum as

it allows us to check the collective properties of hadron-hadron interactions. This cannot be tested by PHOS alone due to its limited acceptance for η meson at low p_{T}. The search of the m_{T}-scaling violation at low p_{T} is the subject of the ongoing combined measurement of light neutral meson spectra with PHOS, TPC and EMCal detectors.

Concluding, we do not see any significant deviation from m_{T}-scaling in our data.

5.6 x_{T} scaling

As described in section 1.5.4, the x_{T} scaling can be expressed by the formula

$$\left(\sqrt{s}\right)^{n(x_{\mathrm{T}},\sqrt{s})} E\frac{d^3\sigma}{dp^3} = G(x_{\mathrm{T}}),$$

where $n(x_{\mathrm{T}}, \sqrt{s})$ – x_{T}-scaling power, which in the lower order approximation corresponds to the Rutherford scattering (it scales as 4-th power of inverse momentum transfer in the lowest-order calculations) [69]; $G(x_{\mathrm{T}})$ – contains fragmentation and structure functions as a function of x_{T}. The left-hand side of the equation contains all the information measured in the experiment, except the exponent, and the right-hand side of the equation contains solely theoretical quantity. The measured values of the x_{T}-scaling power n are usually larger than 4 due to higher-order effects such as the evolution of parton distribution and fragmentation functions and a running strong coupling constant α_s. This makes x_{T} scaling a sensitive tool for studying the contribution of higher-order pQCD processes to hadron spectra in pp collisions.

The x_{T} spectra of π^0 and η measured in pp collisions by the ALICE collision are shown in Fig. 5.11. The points that correspond to the different energies are aligned into

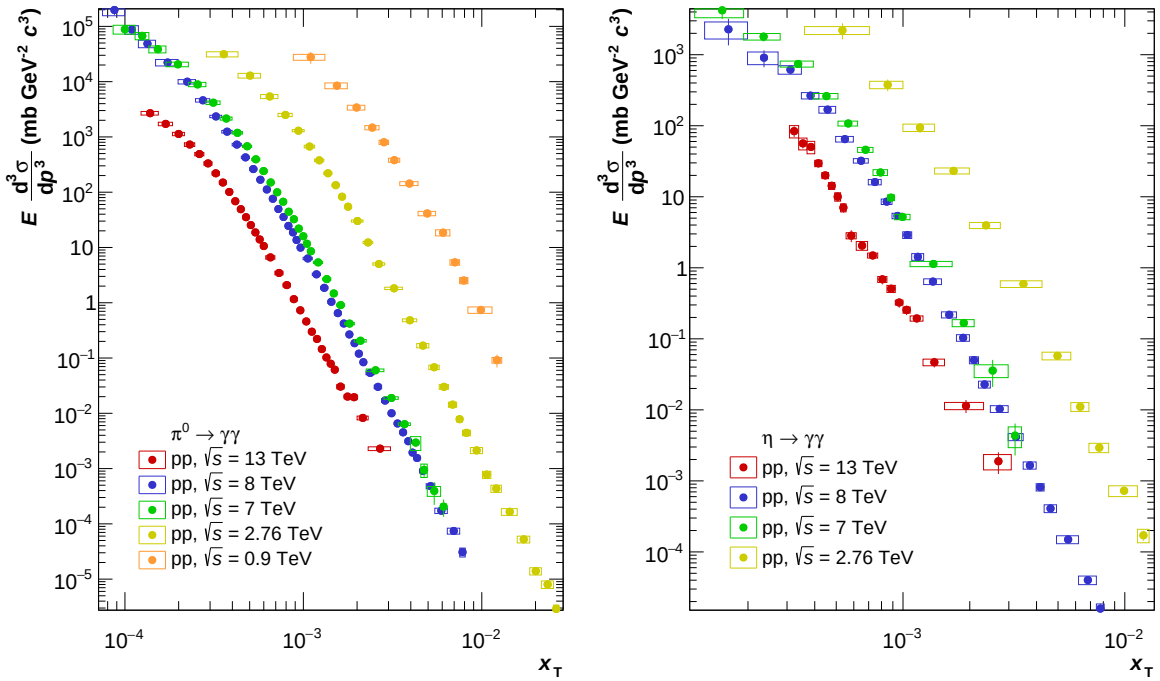

Figure 5.11: Left plot: The neutral pion invariant cross-section in pp collisions at LHC energies as a function of x_{T}. Right plot: The η meson invariant spectra in pp collisions at LHC energies as a function of x_{T}. The vertical bars and open squares correspond to the statistical and systematic errors, respectively.

distinct parallel lines. The distances between them correspond to energy dependent part of the invariant cross-section $\left(\sqrt{s}\right)^{-n(x_{\mathrm{T}})}$. To observe x_{T} scaling, one needs to divide the

spectra by these factors. The only problem is that the exponents $n(x_{\mathrm{T}})$ are unknown. To evaluate $n(x_{\mathrm{T}})$ this analysis follows the approach described in section 1.5.4 and use the mesuarements at two different energies $\sqrt{s}_1$ and $\sqrt{s}_2$:

$$n(x_{\mathrm{T}}, \sqrt{s}_1, \sqrt{s}_2) = \frac{\ln\left(\sigma(x_{\mathrm{T}}, \sqrt{s}_2)/\sigma(x_{\mathrm{T}}, \sqrt{s}_1)\right)}{\ln\left(\sqrt{s}_1/\sqrt{s}_2\right)}.$$

The resulting values of the x_{T}-scaling exponent n are shown in Fig. 5.12. Different colours correspond to the different combinations of measurements. Only the points that have small enough uncertainties are shown, other combinations are not included in the plot as they are not conclusive due to the high errors and their contribution to the average value is negligible.

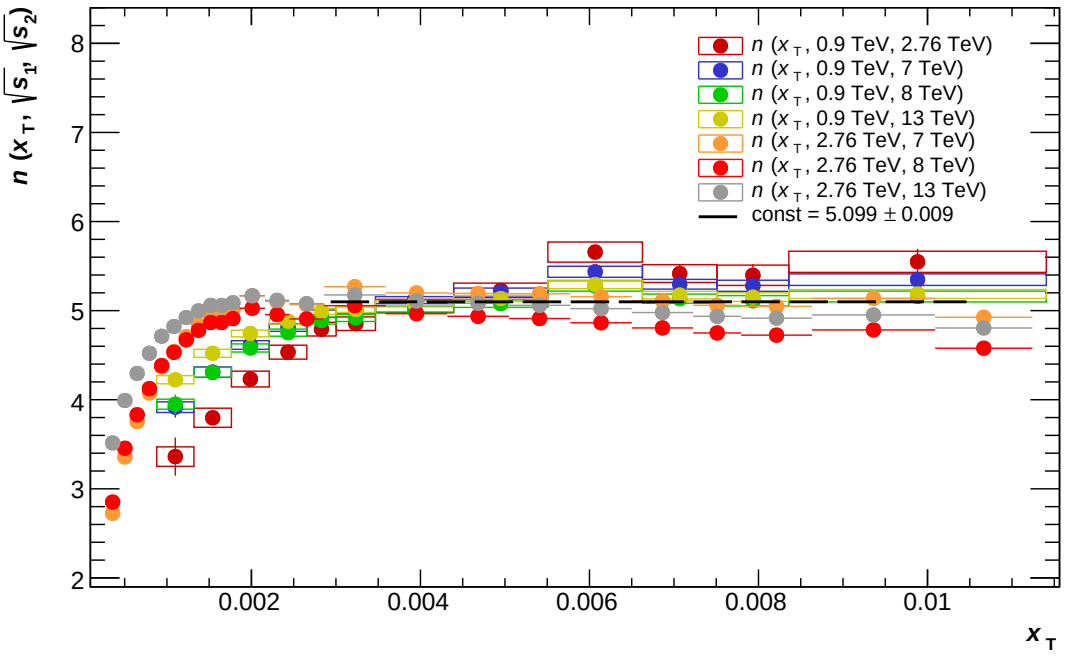

Figure 5.12: The x_{T}-scaling exponent $n(x_{\mathrm{T}}, \sqrt{s}_1, \sqrt{s}_2)$ calculated from different combination of ALICE measurements. The dashed line refers to the combined fit with a zero-degree polynomial which gave $n = 5.099 \pm 0.009$. The vertical bars and open squares correspond to the statistical and systematic errors respectively.

The dashed line corresponds to the combined fit of all the points in the $0.0029 < x_{\mathrm{T}} < 0.0105$ region with the zero-degree polynomial. It results in $n = 5.099 \pm 0.009$ with $\chi^2/\mathrm{ndf} = 4.12$. This value of n was taken as a final x_{T} scaling power in the current analysis. It was used to construct the form factors for the different energies that are plotted in Fig. 5.13.

The experimental points for all the spectra start to merge into a single line at $x_{\mathrm{T}} \sim 0.0024$ for neutral pions and at $x_{\mathrm{T}} \sim 0.0010$ for η mesons. This is a manifestation of x_{T} scaling. There are data points at each given energy that are located below the asymptotic line. This deviation shifts toward lower values of x_{T} with increasing collision energy. It corresponds to the low-p_{T} range of $1 - 3$ GeV/c, where soft-physics effects dominate over the hard processes. It can also be seen that for each energy the experimental points commence at some critical value of x_{T} to deviate from the asymptotic scaling line. Fig. 5.14 shows the dependence of the $x_{\mathrm{T}}^{\mathrm{critical}}$ on the collision energy. This quantity decreases with energy for both neutral pions and η mesons.

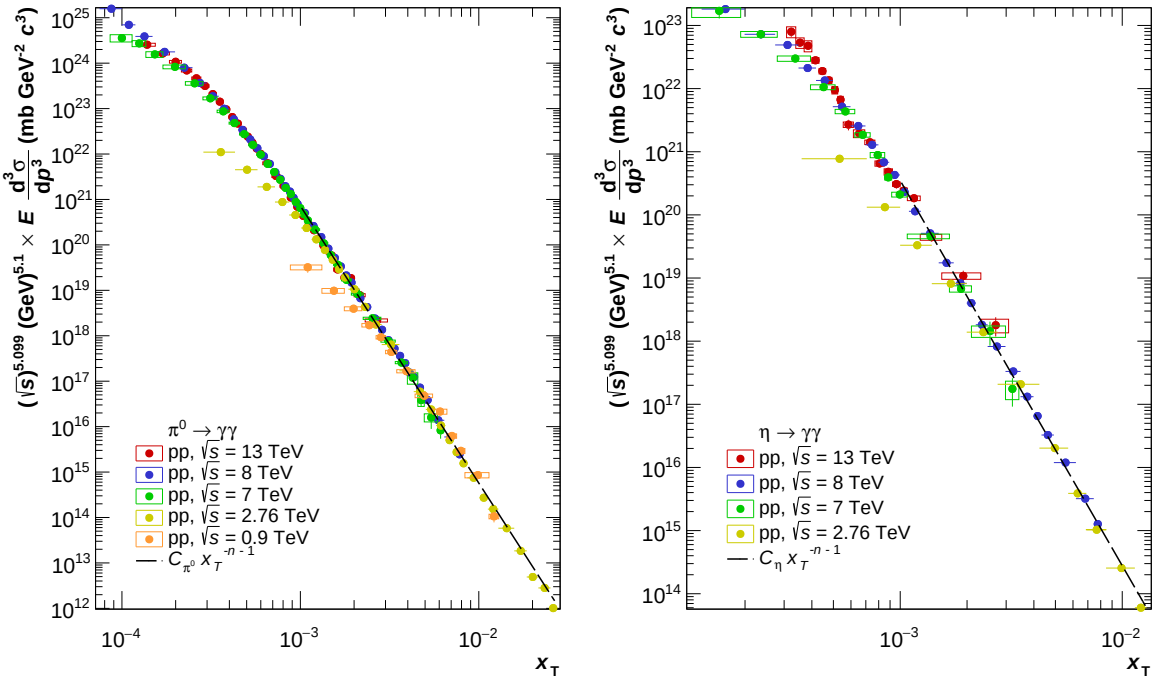

Figure 5.13: The x_{T}-scaled spectra of neutral pions (left plot) and η meson (right plot). Both particle cross-section were scaled with the same exponent $n = 5.099$ obtained from the combined fit of the ALICE data. The vertical bars and open squares correspond to the statistical and systematic errors, respectively.

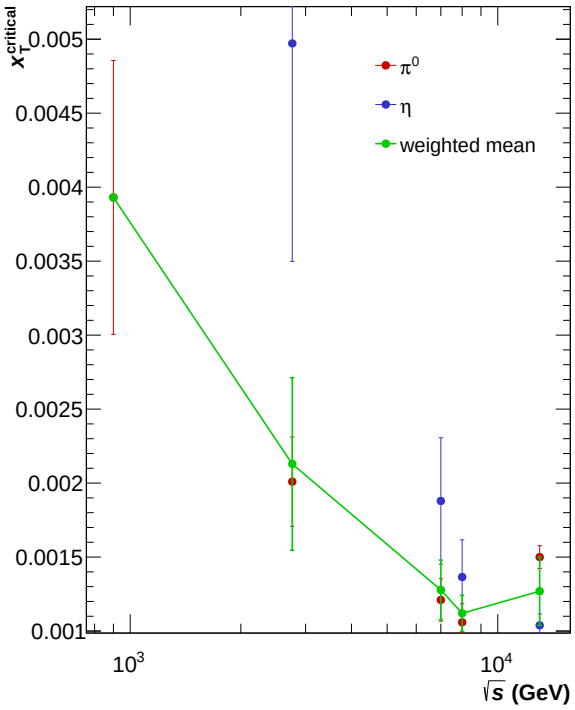

Figure 5.14: The distribution of $x_{\mathrm{T}}^{\mathrm{critical}}$, the points where x_{T} spectra reach power-law regime, in pp collisions for π^0 (red points) and η meson (blue points) as a function of $\sqrt{s}$.

The magnitude of x_{T} scaling exponent n obtained in this analysis is significantly smaller than the one measured by PHENIX [161]. They combined measuremnts of neutral pions in pp collisions at $\sqrt{s} = 62.4$ GeV and $\sqrt{s} = 200$ GeV to obtain $n = 6.41 \pm 0.55$.

This value is consistent with the results from charged particles in peripheral Au–Au collisions at $\sqrt{s}_{\rm NN} = 200$ GeV, which yielded $n = 6.12 \pm 0.49$ [74]. Current analysis shows that the value of $n \sim 5$ is the asymptotic limit for inclusive single-particle production at high energies. The obtained results are in a good agreement with the NLO pQCD predictions for the scaling exponent n [162]. These calculations are based on DSS07 [17] PDFs and BFG fragmentation functions [148]. According to NLO approximation the scaling exponent $n \sim 5$, being almost the same for all species. The deviation from the leading twist predictions $n = 4$ implies the large contribution of the higher twist processes, the direct hadron production in hard scatterings like $qg \to \pi^0 q$ or $q\bar{q} \to \pi^0 g$.

The deviation of the experimental data at $\sqrt{s} = 200$ GeV from the theoretical calculations is explained mainly by the significantly larger contribution of hard processes to the direct hadron production [162]. The proposed model predicts a smaller deviation from the NLO approximation at LHC energies due to wider $p_{\rm T}$ range and large $\sqrt{s}$. The result obtained in this thesis agrees with that prediction and supports the hypothesis that hadrons are produced mainly in the hard processes rather than in parton jet fragmentation [162].

Chapter 6

Conclusions and outlook

This thesis presents the analysis of π^0 and η mesons in pp collisions at $\sqrt{s} = 13$ TeV using the PHOS spectrometer of ALICE. This is the first measurement of light neutral mesons at the highest energy attained in collider experiments.

- The data measured during 2016-2018 were analyzed in this thesis. The runs suitable for physics analysis were extracted from the entire data recorded by ALICE. It was verified that the performance of PHOS was stable, and the data measured during different periods were obtained under the same conditions.

- The malfunctioning and noisy PHOS cells were identified and excluded from the analysis. Both time and energy calibrations were verified and have been proven to be consistent in the entire dataset.

- The raw π^0 and η meson spectra were reconstructed via the two-photon decay channel. The raw yields were calculated by counting the number of $\gamma\gamma$ combinations in the 2σ-region around the centre of π^0 and η meson peaks in the two-photon effective mass distribution.

- The reconstruction efficiency times acceptance factors were calculated from the Monte-Carlo simulations, generated for this analysis. The efficiency of the timing cut of PHOS clusters was estimated with the data-driven tag-and-probe technique.

- The systematic uncertainties of the measurement were extracted by examining the change of the final spectra resulting from the changes of the reconstruction algorithm. The obtained errors were added in quadratures with the statistical uncertainties. The average total errors are at the level of 8 for π^0 and $\sim$ 20% for η meson.

- The fully corrected yields of π^0 and η mesons were obtained in $20 < p_{\mathrm{T}} < 20$ GeV/c and $2 < p_{\mathrm{T}} < 20$ GeV/c regions, respectively. Both π^0 and η meson spectra exhibit power-like behavior observed in pp collisions at lower LHC energies.

- The measured spectra were fitted with the Tsallis function, which well agrees with the data expect some low and high-p_{T} regions. The same behaviour was observed for hadron spectra measured in high-energy collisions below 13 TeV. The nonextensivity parameter q and temperature T were extracted from the fits. It was shown that the nonextensivity parameter q grows as the logarithm of the collision energies. The temperature T shows no significant energy dependence but exhibits a distinct dependence on the mass of a particle. It is almost twice as large for η meson compared to π^0 temperature.

- The measured inclusive π^0 and η meson production cross sections were fitted with the TCM function. It combines Boltzmann-Gibbs contribution describing the low

p_{T} region and the power-law term that accounts for the hard scatterings. It was demonstrated that this model provides a good description of the light neutral meson spectra in the entire p_{T} range. The relative contribution of the power-law term to the entire spectrum was studied as a function of collision energy. This quantity shows a weak energy dependence that agrees with the observations for $\sqrt{s} < 1.8$ TeV.

- It was demonstrated that PYTHIA 6 and NLO pQCD calculations predict somewhat higher invariant cross-sections of π^0 and η mesons for $p_{\mathrm{T}} < 4$ GeV/c and agree with the data for $p_{\mathrm{T}} > 7$ GeV/c. The ratio of invariant cross-sections η/π^0 is in a good agreement with PYTHIA 6 predictions in the entire p_{T}-range. Similar behaviour was observed by ALICE collaboration in pp collisions at $\sqrt{s} = 0.9,\ 2.76,\ 7$ and 8 TeV.

- The ratio η/π^0 of neutral meson spectra agrees with the m_{T}-scaled function developed by the PHENIX collaboration to describe the data for $\sqrt{s} < 200$ GeV. The measured ratio is consistent, within errors, with the m_{T}-scaling. However, a further increase in statistics is called for. To this end, the combining of signals from different detectors could reduce experimental errors.

- The compilation of the asymptotic ratio of η/π^0 yield in hadron-hadron collisions in the energy range spanning over two orders of magnitude (13.6 GeV – 13 TeV) is presented in this thesis. This is the first compilation containing the data up to the highest LHC energies.

- The π^0 spectrum in pp collisions at $\sqrt{s} = 13$ TeV together with data at $\sqrt{s} = 0.9,\ 2.76,\ 7$ and 8 TeV were used to test the x_{T} scaling. The scaling exponent n was obtained at $x_{\mathrm{T}} \sim 10^{-2}$ at LHC energies. The measured value $n \sim 5$ is lower than the one reported for RHIC energies and agrees with the NLO pQCD predictions. This confirms the hypothesis that the higher-twist contribution to the hadron cross-section is large and neutral pions and η mesons at high energy collisions are largely produced in hard parton scatterings.

The results presented in this thesis provide input for both theoretical and experimental studies of the properties of strong interactions at high energies. The measured spectra will help to improve the quality of the pQCD calculations by constraining the PDFs and FFs. Also, this measurement allows fine-tuning the PYTHIA Monte-Carlo generator, which is widely used in the collision experiments to estimate the hadron production. The light meson spectra measured at $\sqrt{s} = 13$ TeV provide a baseline for the theoretical comparison of the hadron-production mechanisms in pp and heavy-ion collisions. The reported results also can be used as the reference point for studying the properties of collective effects in Pb–Pb and p–Pb systems.

The parametrizations of the π^0 and η meson yields obtained in the current analysis can be used to calculate the spectra of decay photons produced in pp collisions at $\sqrt{s} = 13$ TeV. These distributions are essential for direct photon signal extraction as π^0 and η meson provide $\sim 98\%$ contribution to the decay photon spectrum. The π^0 and η yields presented in this thesis will be combined with EMCal and PCM measurements to extend the p_{T} range of the light neutral meson spectra. And finally, the presented results are a reference point for studying the PHOS events triggered by energetic particles which will allow extending neutral meson signals up to $p_{\mathrm{T}} \sim 50$ GeV/c.

Appendix A

List of good runs

A.1 LHC16

255275	254983	254984	255242	254604	254606	254608	255249
255251	255252	255253	255255	255256	255177	254621	255466
255008	255009	255010	254629	254630	254378	255111	255276
254381	255407	254640	255240	255154	255283	254644	255467
254646	255159	254648	254649	254394	254395	254396	254653
254654	255167	255171	255173	255176	254476	255180	255182
255280	255440	255442	254419	254422	255447	254479	255162
255248	255398	255079	255465	255082	255463	255085	255086
255247	255091	255350	255351	255402	255011	255415	255418
255419	255420						

Table A.1: The list of runs in LHC16h period.

256219	256223	256225	256227	256228	256231	256283	256284
256289	256290	256292	256297	256299	256302	256307	256309
256311	256357	256363	256364	256365	256366	256368	256371
256415	256210	256212	256213	256215	256282	256287	256361
256362	256417	256418					

Table A.2: The list of runs in LHC16j period.

257682	257684	257685	257687	257688	257689	257692	257697
257724	257725	257727	257733	257734	257735	257737	257754
257757	257765	257773	257797	257798	257799	257800	257803
257804	257850	257851	257853	257893	257901	257912	257932
257936	257937	257939	257957	257958	257960	257963	257986
257989	257992	258003	258008	258019	258039	258041	258045
258048	258049	258053	258059	258060	258062	258063	258107
258108	258109	258113	258114	258117	258178	258197	258198
258202	258203	258204	258256	258257	258258	258270	258271
258274	258278	258280	258301	258302	258303	258307	258332
258336	258359	258388	258391	258393	258399	258452	258454
258456	258477	258498	258499				

Table A.3: The list of runs in LHC16k period.

258883	258884	258885	258886	258889	258890	258919	258920
258921	258923	258926	258931	258962	258964	259086	259088
259090	259096	259099	259117	259162	259164	259204	259261
259263	259264	259269	259270	259271	259272	259273	259274
259302	259303	259305	259307	259334	259336	259339	259340
259341	259342	259378	259381	259389	259394	259395	259469
259473	259477	259649	259650	259668	259697	259703	259704
259705	259711	259713	259747	259750	259751	259752	259756
259788	259789	259792	259822	259841	259842	259860	259866
259867	259868	259888	259961	259979	260010	260011	

Table A.4: The list of runs in LHC16l period.

262395	262396	262397	262398	262399	262418	262419	262422
262423	262424	262425	262426	262428	262430	262450	262451
262487	262489	262490	262492	262528	262532	262533	262537
262563	262567	262568	262569	262570	262571	262572	262574
262578	262583	262593	262624	262628	262632	262635	262705
262706	262708	262713	262717	262723	262725	262727	262768
262776	262777	262778	262842	262844	262847	262849	262853
262855	263487	263490	263497	263529	263647	263652	263654
263657	263662	263663	263682	263689	263690	263691	263737
263739	263741	263743	263784	263785	263786	263787	263790
263792	263803	263810	263813	263823	263824	263829	263830
263861	263863	263866	263905	263916	263917	263920	263977
263978	263979	263981	263984	263985			

Table A.5: The list of runs in LHC16o period.

254128	254147	254148	254149	254174	254175	254178	254193
254199	254204	254205	254303	254304	254330	254331	

Table A.6: The list of runs in LHC16g period.

255011	255010	255009	255008	254479	254476	254396	254395
254394	254393	254390	254385	254381	254378		

Table A.7: The list of runs in LHC16h period, isolated bunches with 1000 ns interval

255615	255614	255592	255591	255582	255577	255543	255542
255540	255538	255537	255535	255534	255533	255583	255539

Table A.8: The list of runs in LHC16i period.

258890	258889	258886	258885	258884	258883

Table A.9: The list of runs in LHC16l period. Isolated bunches with 2500 ns interval

262399	262398	262397	262396	262395

Table A.10: The list of runs in LHC16o period. Isolated bunches with 2500 ns interval

A.2 LHC17

281961	281956	281953	281940	281939	281932	281931	281918
281916	281915	281895	281894	281893	281756	281755	281754
281753	281751	281738	281633	281592	281580	281568	281563
281562	281557	281509	281477	281475	281450	281449	281446
281444	281443	281441	281415	281350	281321	281301	281277
281275	281273	281271	281244	281243	281242	281241	281240
281213	281212	281191	281190	281189	281181	281180	281179
281081	281080	281079	281062	281061	281060	281036	281035
281033	280999	280998	280997	280994	280990	280947	280940
280936	280897	280890	280881	280880	280856	280854	280849
280848	280847	280845	280844	280842	280793	280792	280787
280786	280768	280767	280766	280765	280764	280763	280762
280761	280757	280756	280755	280753	280729	280705	280681
280679	280676	280673	280671	280650	280648	280647	280645
280639	280637	280636	280634	280613	280583	280581	280576
280575	280574	280551	280547	280546	280519	280518	280499
280490	280448	280447	280446	280445	280443	280419	280415
280413	280406	280405	280403	280375	280374	280352	280351
280350	280349	280348	280312	280310	280290	280286	280285
280284	280283	280282					

Table A.11: The list of runs in LHC17o period.

280140	280135	280134	280131	280126	280118	280114	280111
280108	280107	280066	280052	280051	279880	279879	279855
279854	279853	279826	279773	279749	279747	279719	279718
279715	279689	279688	279687	279684	279683	279682	279679
279676	279642	279641	279632	279630	279559	279550	279491
279488	279487	279483	279441	279439	279435	279410	279355
279354	279349	279344	279342	279310	279309	279274	279273
279270	279268	279267	279265	279264	279242	279238	279235
279234	279232	279208	279207	279201	279199	279157	279155
279130	279123	279122	279118	279117	279107	279106	279075
279074	279073	279069	279068	279044	279043	279041	279036
279035	279007	279005	279000	278999	278964	278963	278960
278959	278941	278939	278936	278915	278914		

Table A.12: The list of runs in LHC17m period.

270882	270883	270931	270934	270935	270937	270938	
270940	271005	271006	271008	271009	271013	271015	271021
271026	271028	271288	271289	271369	271373	271377	271378
271379	271381	271382	271383	271384	271419	271444	271448
271449	271451	271743	271768	271774	271777		

Table A.13: The list of runs in LHC17g period.

270667	270665	270663	270661	270601	270598	270581	270544
270543	270542	270535	270531	254128			

Table A.14: The list of runs in LHC17c period.

270865	270861	270856	270855	270854,

Table A.15: The list of runs in LHC17f period.

274442	274390	274387	274386	274385	274364	274363	274360
274357	274355	274352	274351	274329	274283	274281	274280
274279	274278	274276	274271	274270	274269	274268	274266
274264	274263	274259	274258	274232	274212	274174	274148
274147	274125	274094	274092	274064	274063	274058	273986
273985	273946	273943	273942	273918	273889	273887	273886
273885	273825	273654	273593	273592	273591		

Table A.16: The list of runs in LHC17i period.

274671	274669	274667	274657	274653

Table A.17: The list of runs in LHC17j period.

276508	276507	276506	276462	276439	276438	276437	276435
276429	276351	276348	276312	276307	276302	276297	276294
276292	276291	276290	276259	276257	276230	276205	276178
276177	276170	276169	276166	276141	276140	276135	276108
276105	276104	276102	276099	276098	276097	276045	276041
276040	276020	276019	276013	276012	275925	275924	275847
275664	275661	275657	275650	275648	275647	275624	275623
275616	275615	275612	275559	275558	275515	275472	275471
275467	275459	275457	275456	275453	275452	275448	275443
275406	275404	275401	275395	275394	275372	275369	275361
275360	275333	275332	275328	275326	275324	275322	275314
275283	275247	275246	275245	275239	275173	275151	275150
275149	275076	275075	275073	275068	274889	274886	274884
274882	274878	274821	274817	274815	274811	274807	274806
274803	274802	274801	274736	274708	274690		

Table A.18: The list of runs in LHC17k period.

276508	276507	276506	276462	276439	276438	276437	276435
278914	278915	278936	278939	278941	278959	278960	278963
278964	278999	279000	279005	279007	279008	279035	279036
279041	279043	279044	279068	279069	279073	279074	279075
279106	279107	279117	279118	279122	279123	279130	279155
279157	279199	279201	279207	279208	279232	279234	279235
279238	279242	279264	279265	279267	279268	279270	279273
279274	279309	279310	279312	279342	279344	279348	279349
279354	279355	279391	279410	279435	279439	279441	279483
279487	279488	279491	279550	279559	279630	279632	279641
279642	279676	279677	279679	279682	279683	279684	279687
279688	279689	279715	279718	279719	279747	279749	279773
279826	279827	279830	279853	279854	279855	279879	279880
280051	280052	280066	280107	280108	280111	280114	280118
280126	280131	280134	280135	280140			

Table A.19: The list of runs in LHC17l period.

A.3 LHC18

285008, 285009, 285010, 285011, 285012, 285013, 285014, 285015
285064, 285065, 285066, 285106, 285108, 285125, 285127, 285165
285200, 285202, 285203, 285222, 285327, 285328, 285347, 285364
285365, 285396, 285447

Table A.20: The list of runs in LHC18b period.

271868, 271870, 271871, 271873, 271874, 271880, 271881, 271886
271908, 271911, 271912, 271916, 271921, 271925, 271946, 271953
271955, 271962, 271969, 271970, 272018, 272020, 272036, 272038
272039, 272040, 272041, 272042, 272075, 272076, 272100, 272101
272123, 272151, 272152, 272153, 272154, 272155, 272156, 272194
272335, 272340, 272359, 272360, 272388, 272389, 272394, 272395
272399, 272400, 272411, 272413, 272414, 272417, 272461, 272462
272463, 272466, 272468, 272469, 272521, 272574, 272575, 272577
272585, 272607, 272608, 272610, 272620, 272690, 272691, 272692
272712, 272746, 272747, 272749, 272760, 272762, 272763, 272764
272782, 272783, 272784, 272828, 272829, 272833, 272834, 272836
272870, 272871, 272873, 272880, 272903, 272905, 272932, 272933
272934, 272935, 272939, 272947, 272949, 272976, 272983, 272985
273009, 273010, 273077, 273099, 273100, 273101, 273103

Table A.21: The list of runs in LHC18c period.

285978, 285979, 285980, 286014, 286025, 286027, 286028, 286030
286064, 286124, 286127, 286129, 286130, 286159, 286198, 286199
286201, 286202, 286203, 286229, 286230, 286231, 286254, 286255
286257, 286258, 286261, 286263, 286282, 286284, 286287, 286288
286289, 286308, 286309, 286310, 286311, 286312, 286313, 286314
286336, 286337, 286340, 286341, 286345, 286348, 286349, 286350

Table A.22: The list of runs in LHC18d period.

286380, 286426, 286427, 286428, 286454, 286455, 286482, 286501
286502, 286508, 286509, 286511, 286566, 286567, 286592, 286907
286908, 286910, 286911, 286930, 286931, 286932, 286933, 286936
286937

Table A.23: The list of runs in LHC18e period.

274442, 274390, 274387, 274386, 274385, 274364, 274363, 274360
274357, 274355, 274352, 274351, 274329, 274283, 274281, 274280
274279, 274278, 274276, 274271, 274270, 274269, 274268, 274266
274264, 274263, 274259, 274258, 274232, 274212, 274174, 274148
274147, 274125, 274094, 274092, 274064, 274063, 274058, 273986
273985, 273946, 273943, 273942, 273918, 273889, 273887, 273886
273885, 273825, 273654, 273593, 273592, 273591

Table A.24: The list of runs in LHC18i period.

287000, 287021, 287063, 287064, 287066, 287071, 287072
287077, 287137, 287155, 287185, 287201, 287202, 287203
287204, 287208, 287209, 287248, 287249, 287250, 287251
287254, 287283, 287323, 287324, 287325, 287343, 287344
287346, 287347, 287349, 287355, 287356, 287360, 287380
287387, 287388, 287389, 287413, 287451, 287480, 287481
287486, 287513, 287516, 287517, 287518, 287520, 287521
287524, 287573, 287575, 287576, 287578, 287616, 287654
287656, 287657, 287658, 287783, 287784, 287876, 287877
287883, 287884, 287885, 287911, 287912, 287913, 287915
287923, 287941, 287975, 287977

Table A.25: The list of runs in LHC18f period.

288619, 288640, 288642, 288644, 288650, 288687, 288689, 288690
288743, 288748, 288750

Table A.26: The list of runs in LHC18g period.

288804, 288806

Table A.27: The list of runs in LHC18m period.

288861, 288862, 288863, 288864, 288868, 288897, 288902
288903, 288908, 288909

Table A.28: The list of runs in LHC18i period.

288943

Table A.29: The list of runs in LHC18j period.

289165, 289166, 289167, 289169, 289172, 289175, 289176, 289177
289198, 289199, 289200, 289201

Table A.30: The list of runs in LHC18k period.

289240, 289241, 289242, 289243, 289247, 289249, 289253, 289254
289275, 289276, 289277, 289278, 289280, 289281, 289300, 289303
289306, 289308, 289309, 289353, 289354, 289355, 289356, 289363
289365, 289366, 289367, 289368, 289369, 289370, 289373, 289374
289426, 289444, 289462, 289463, 289465, 289466, 289468, 289493
289494, 289521, 289547, 289574, 289576, 289577, 289582, 289625
289657, 289658, 289659, 289660, 289664, 289666, 289721, 289723
289724, 289729, 289731, 289732, 289757, 289775, 289808, 289811
289814, 289815, 289816, 289817, 289818, 289830, 289849, 289852
289854, 289855, 289856, 289857, 289879, 289880, 289884, 289928
289940, 289941, 289943, 289965, 289966, 289971

Table A.31: The list of runs in LHC18l period.

293357, 293359

Table A.32: The list of runs in LHC18n period.

293368, 293386, 293392, 293413, 293424, 293474, 293475, 293494
293496, 293497, 293571, 293573, 293578, 293579, 293582, 293583
293587, 293588, 293686, 293690, 293691, 293692, 293695, 293696
293698, 293740, 293741, 293770, 293774, 293776, 293799, 293802
293805, 293806, 293807, 293809, 293829, 293830, 293831, 293856
293886, 293891, 293893, 293896, 293898

Table A.33: The list of runs in LHC18o period.

294009, 294010, 294011, 294012, 294013, 294128, 294131, 294152
294154, 294155, 294156, 294199, 294200, 294201, 294205, 294208
294210, 294212, 294241, 294242, 294305, 294307, 294308, 294310
294502, 294503, 294524, 294525, 294526, 294527, 294529, 294530
294531, 294553, 294556, 294558, 294562, 294563, 294586, 294587
294588, 294590, 294591, 294593, 294620, 294632, 294633, 294634
294636, 294653, 294703, 294710, 294715, 294716, 294718, 294721
294722, 294741, 294742, 294743, 294744, 294745, 294746, 294747
294749, 294769, 294772, 294774, 294775, 294805, 294809, 294813
294816, 294817, 294818, 294852, 294875, 294877, 294880, 294883
294884, 294916, 294925

Table A.34: The list of runs in LHC18p period.

Appendix B

PHOS QA plots: Cluster Averages

This appendix contains PHOS performance plots for all the run periods used in the analysis. All plots consist of three subplots: the average energy of a cluster, average number of clusters per event and the average number of cells in a cluster. These quantities are plot as a function of ALICE run number (in increasing order). This represents the evolution of PHOS performance of phos in time.

B.1 LHC16

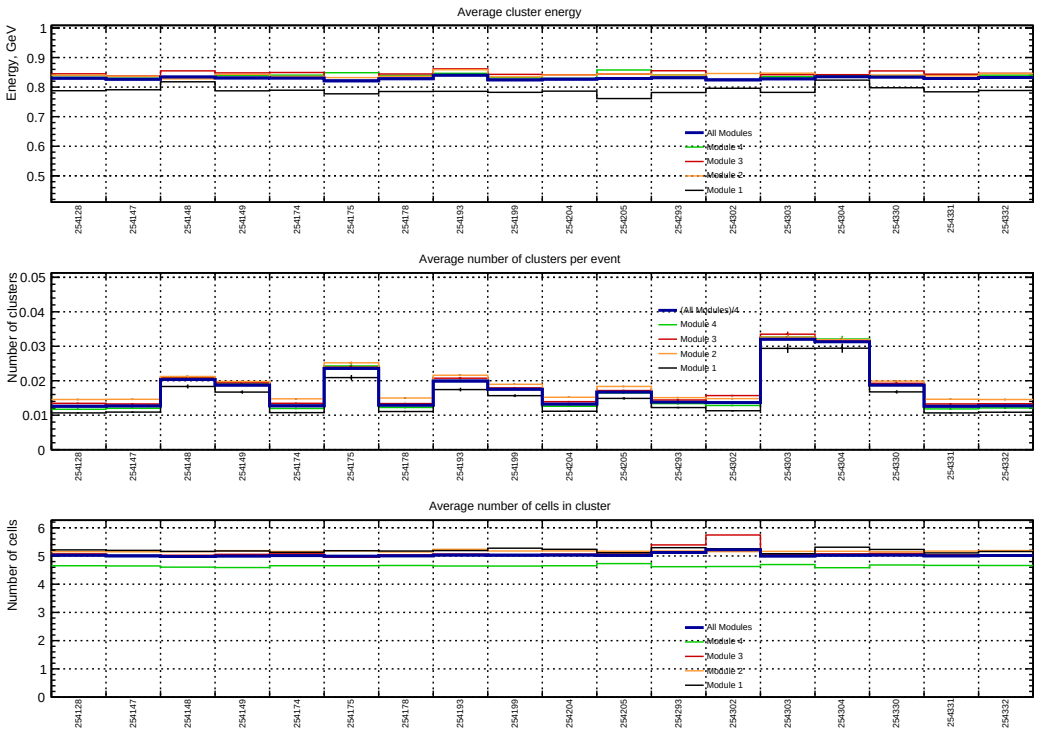

Figure B.1: Cluster averages for `LHC16g` run period.

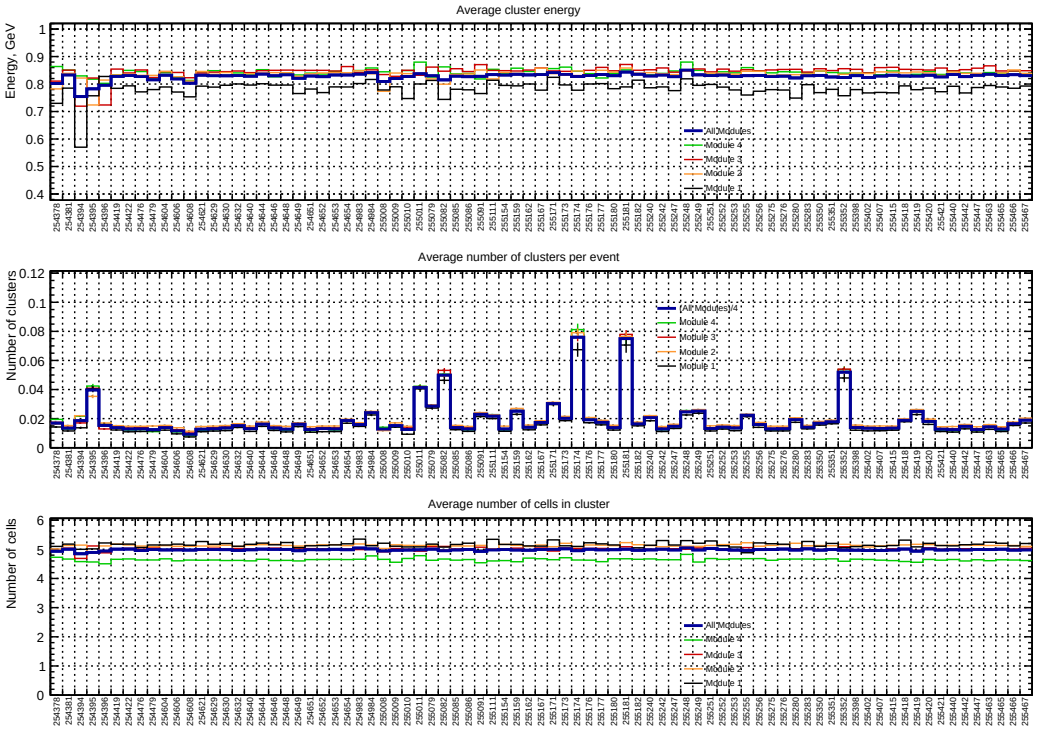

Figure B.2: Cluster averages for `LHC16h` run period.

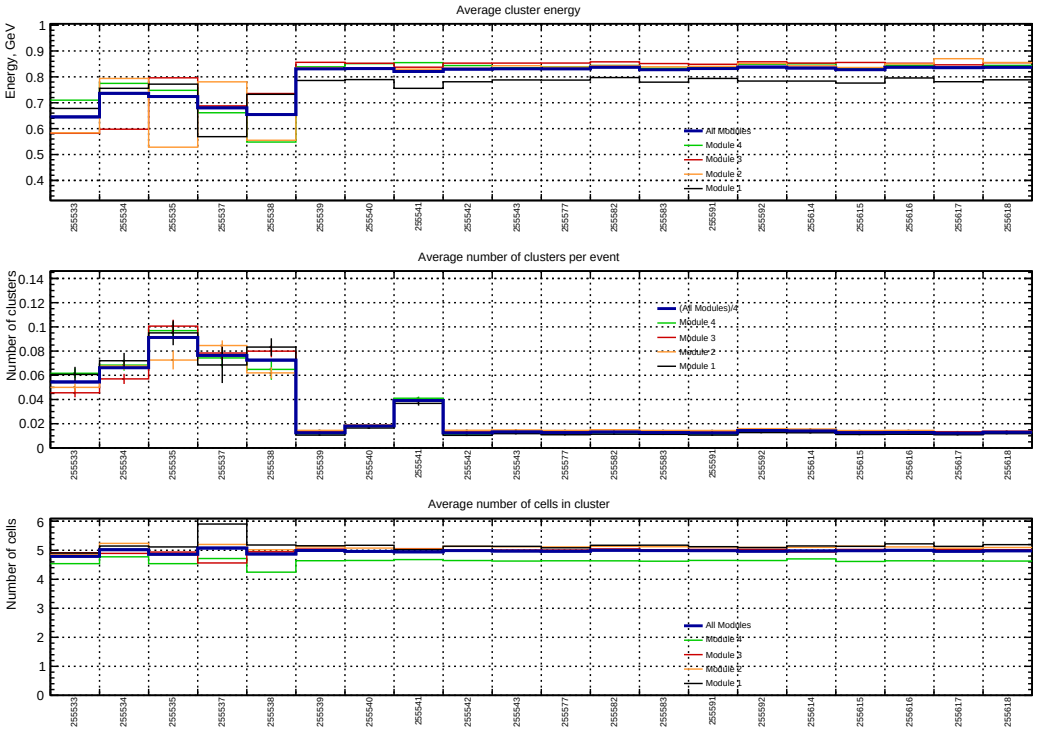

Figure B.3: Cluster averages for `LHC16i` run period.

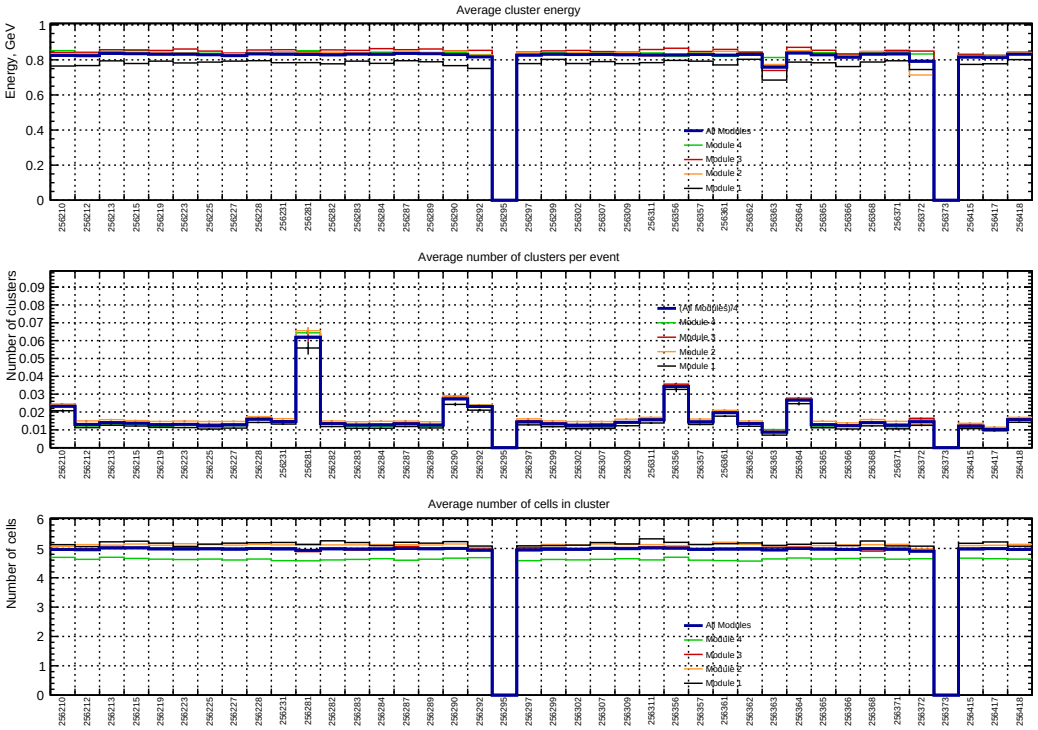

Figure B.4: Cluster averages for `LHC16j` run period.

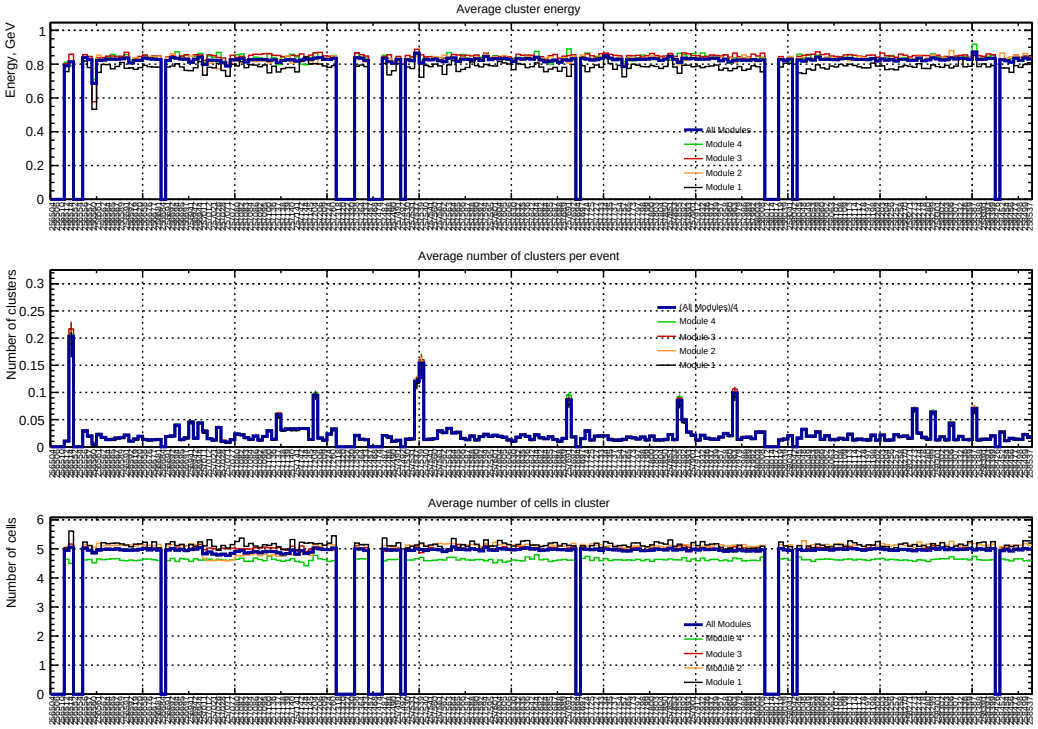

Figure B.5: Cluster averages for `LHC16k` run period.

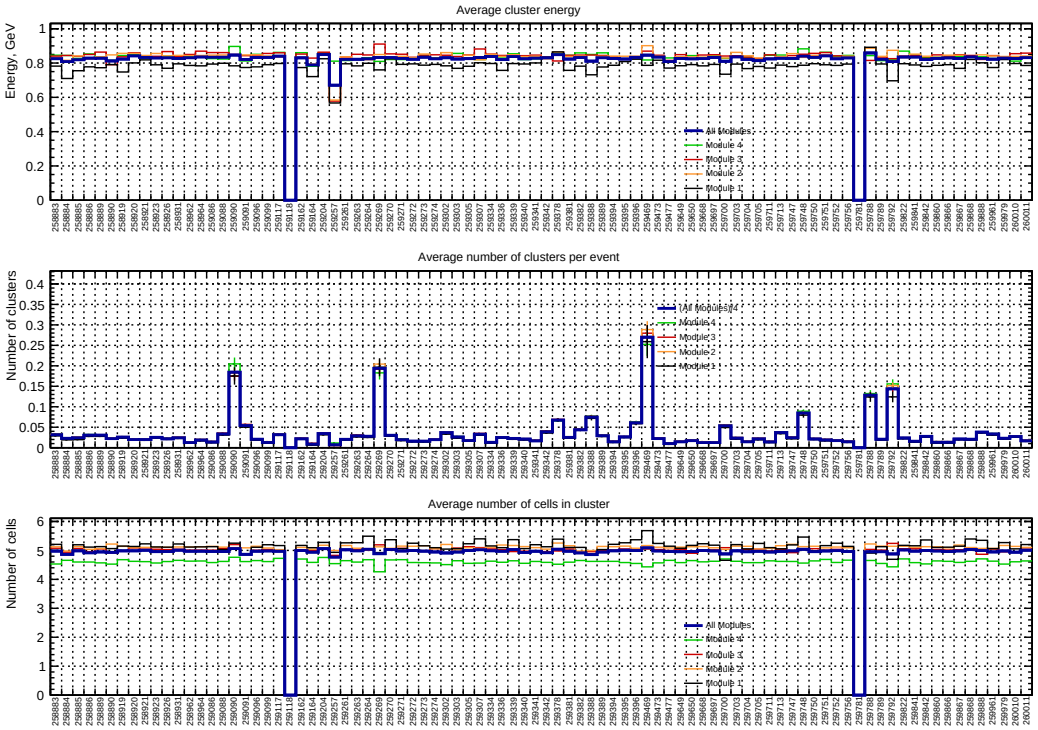

Figure B.6: Cluster averages for `LHC16l` run period.

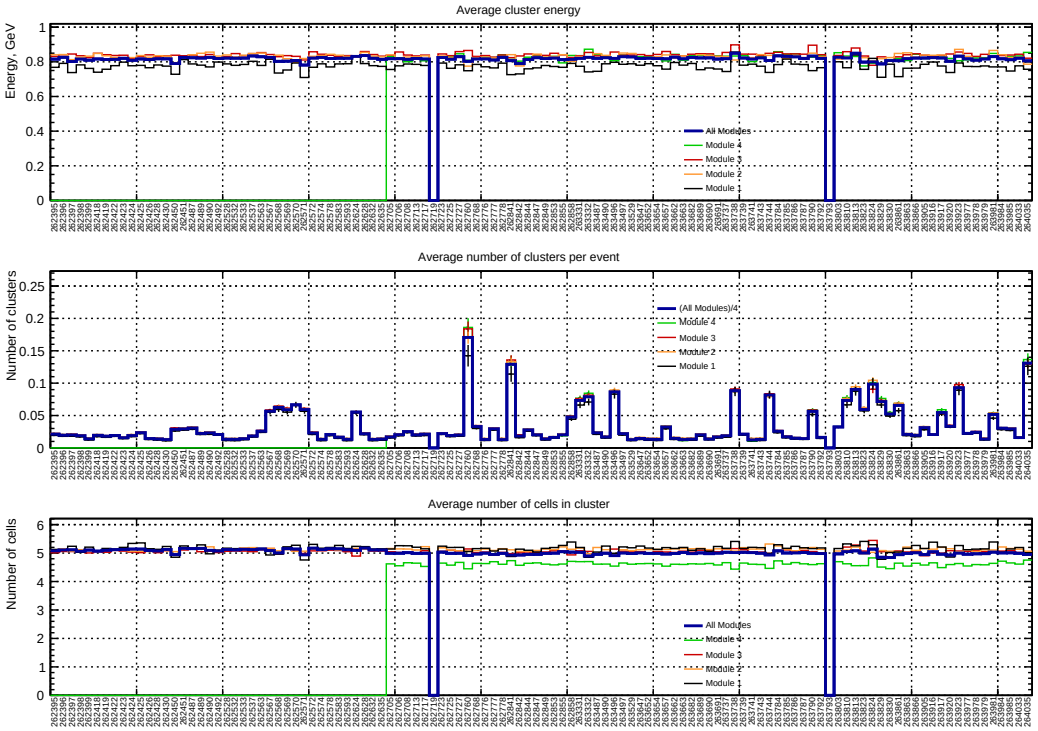

Figure B.7: Cluster averages for `LHC16o` run period.

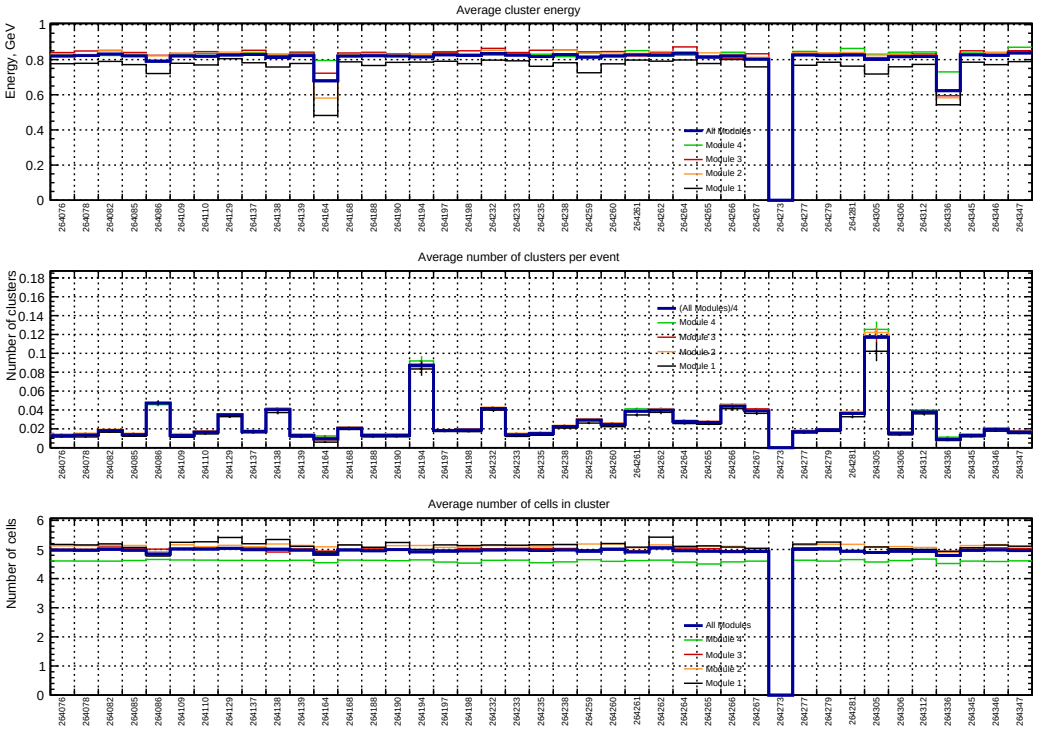

Figure B.8: Cluster averages for `LHC16p` run period.

B.2 LHC17

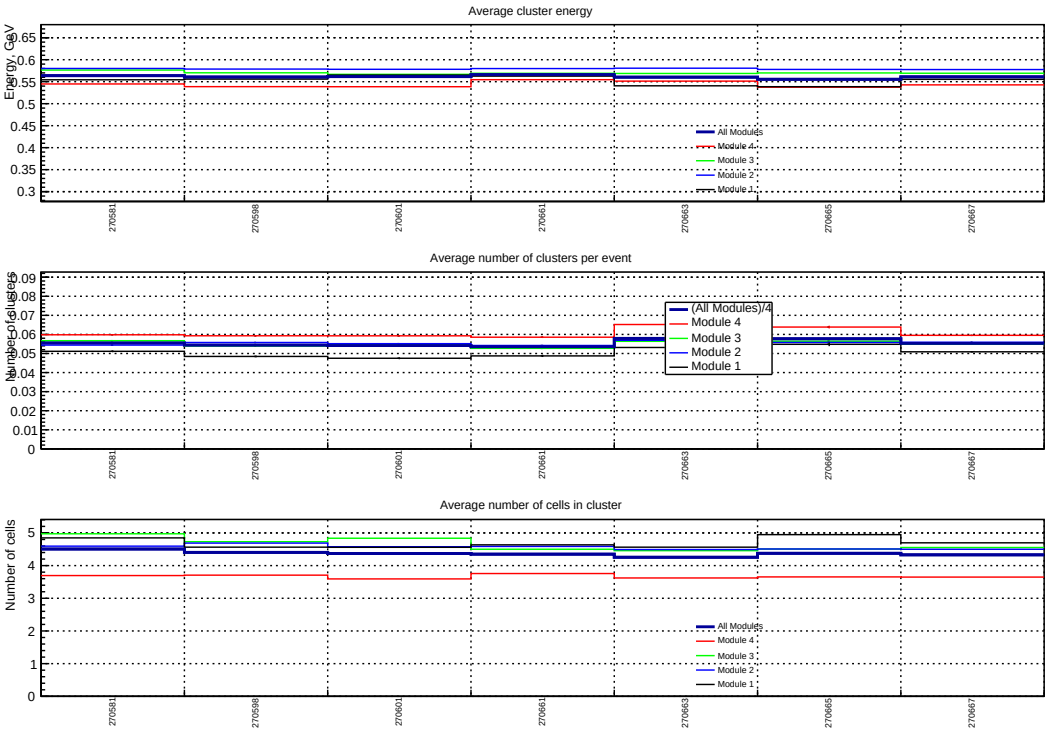

Figure B.9: Cluster averages for `LHC17c` run period.

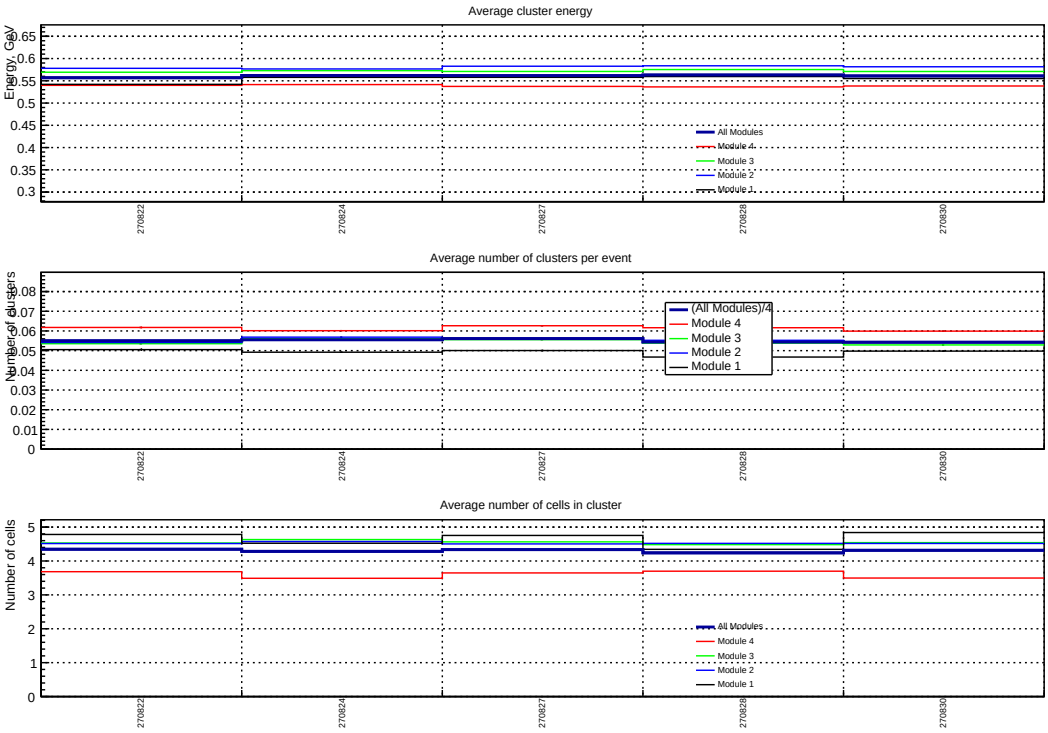

Figure B.10: Cluster averages for `LHC17e` run period.

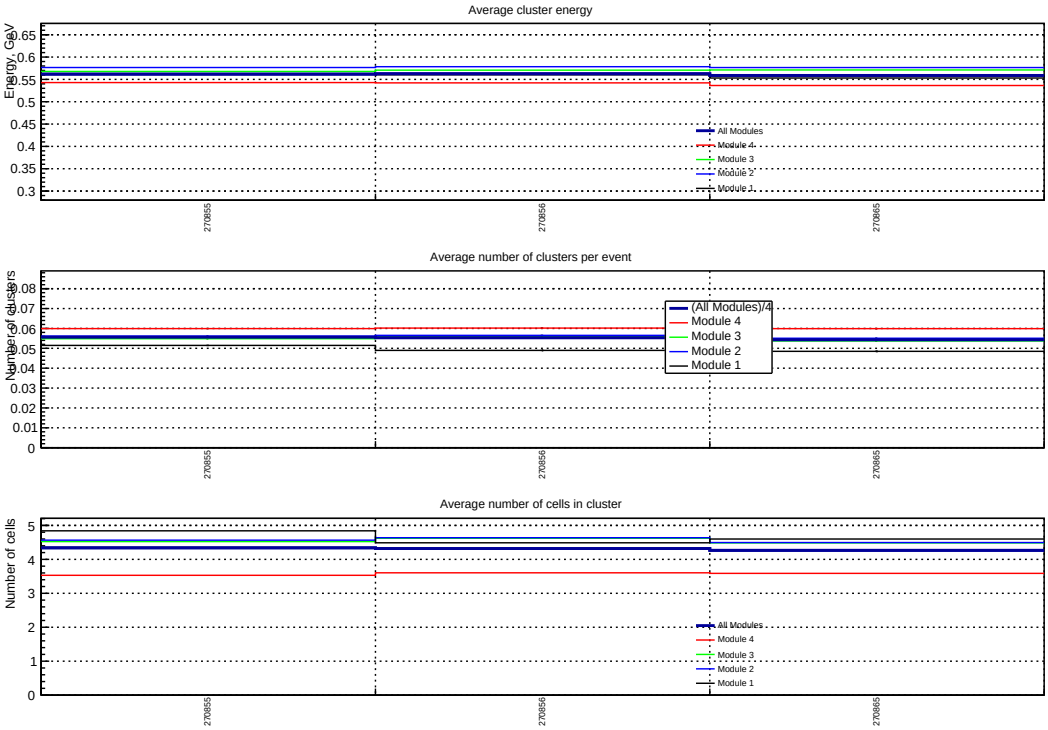

Figure B.11: Cluster averages for `LHC17f` run period.

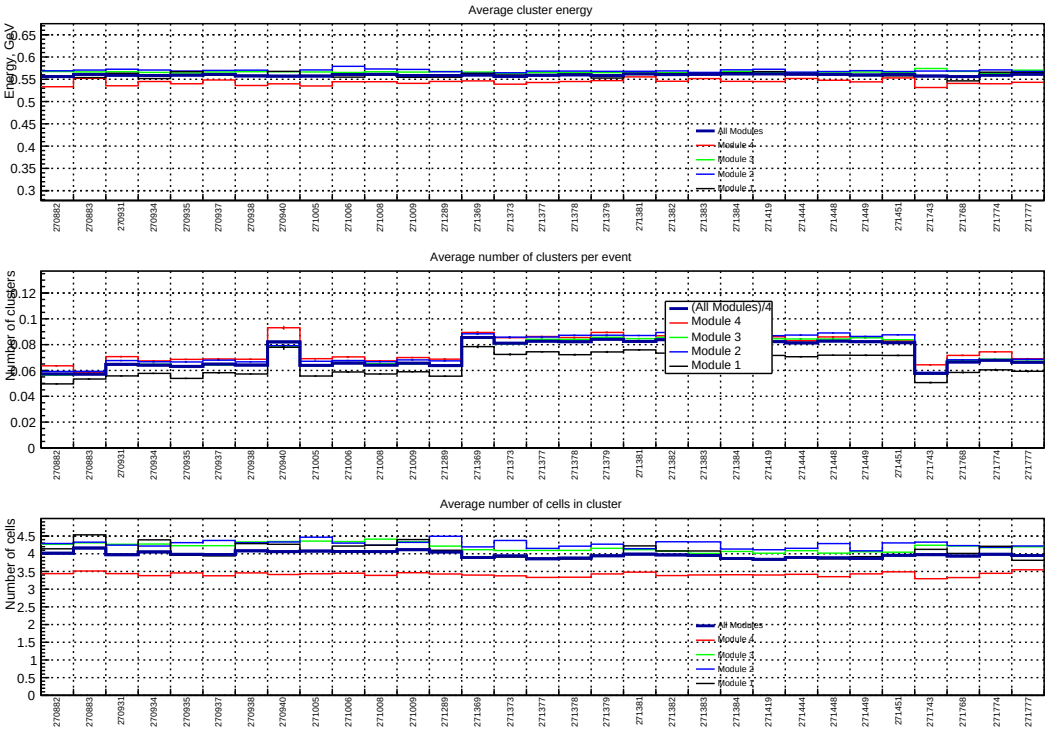

Figure B.12: Cluster averages for `LHC17g` run period.

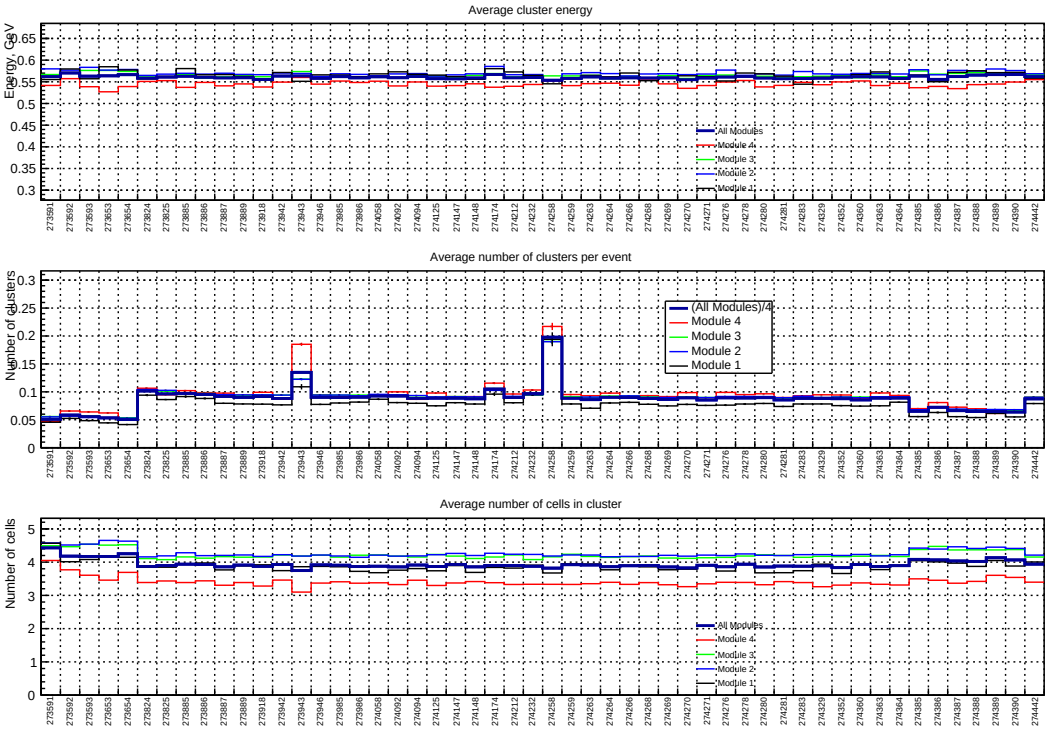

Figure B.13: Cluster averages for `LHC17i` run period.

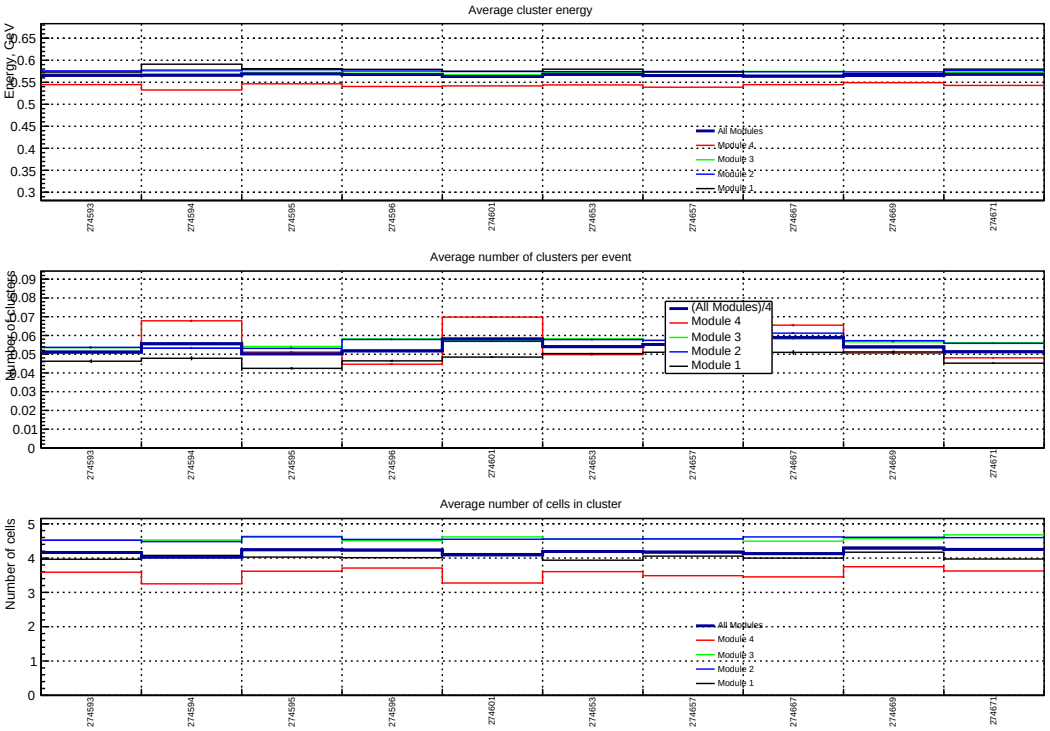

Figure B.14: Cluster averages for `LHC17j` run period.

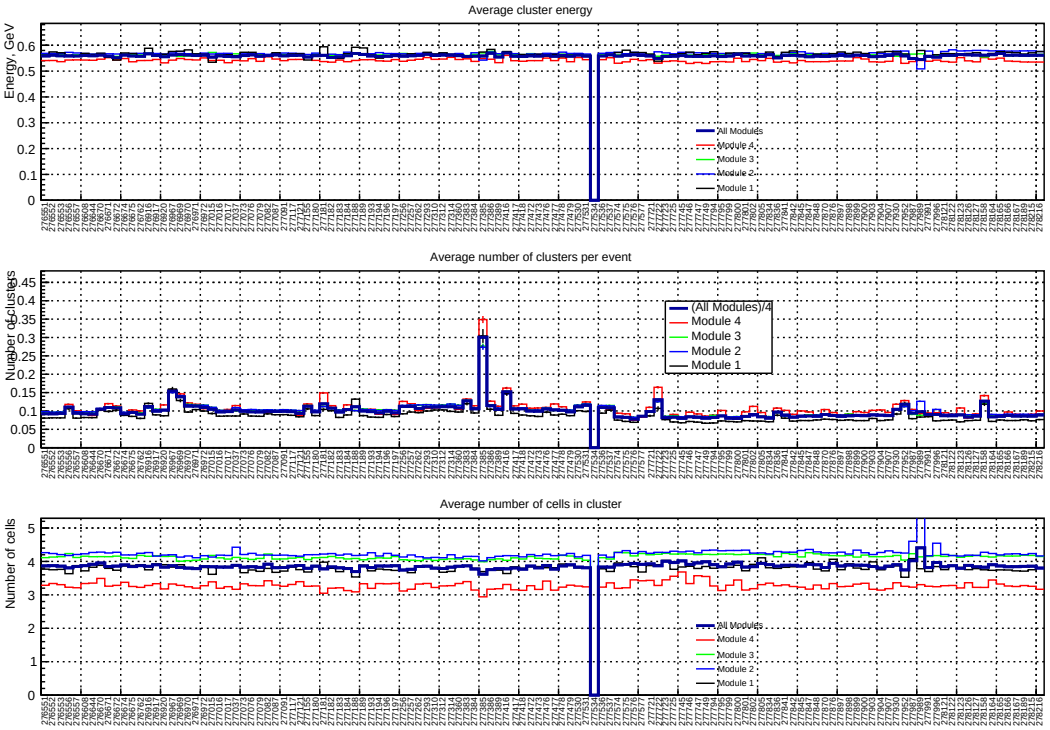

Figure B.15: Cluster averages for `LHC17l` run period.

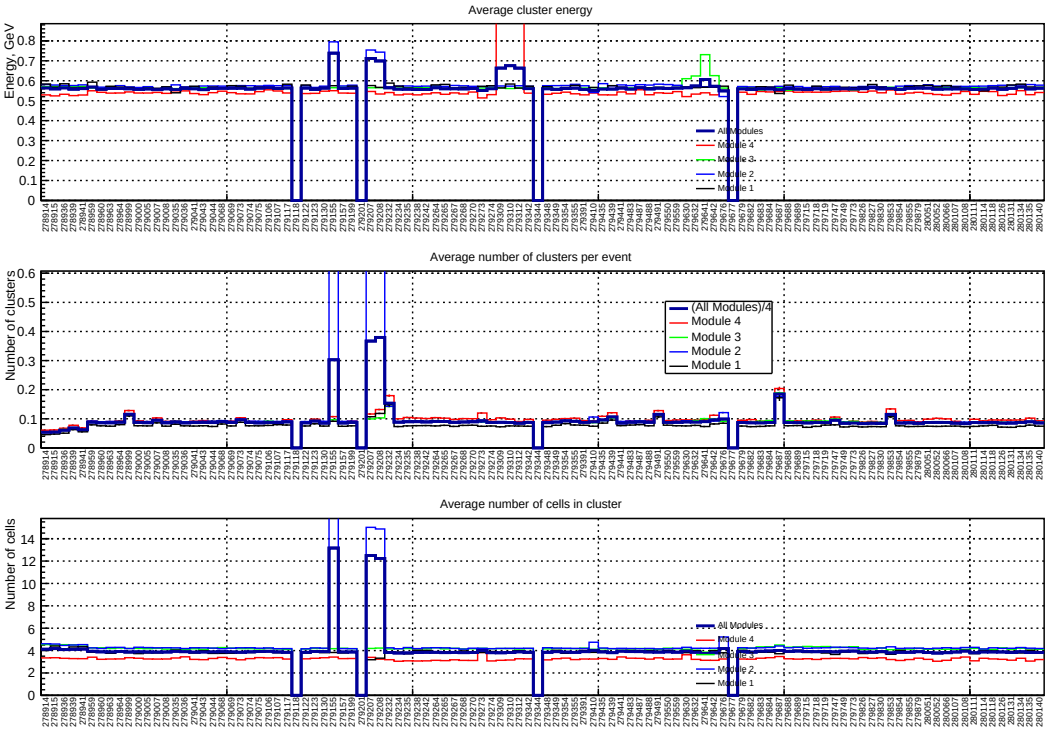

Figure B.16: Cluster averages for `LHC17m` run period, during these periods there were software problems with the detector that resulted in jumps on cluster averages. These runs were excluded from the physics analysis.

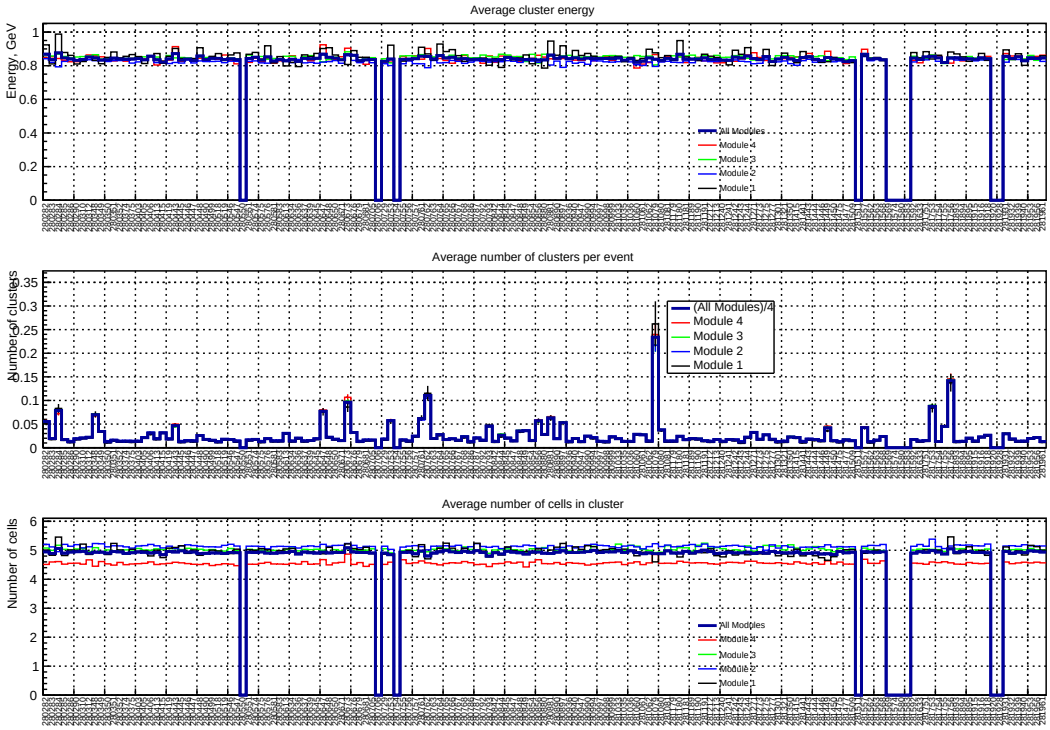

Figure B.17: Cluster averages for `LHC17o` run period. The runs with a very high average number of clusters per event correspond to the very short runs, so the average was not stable.

B.3 LHC18

One of the goals of LHC18 quality assurance analysis was to study the impact of the number of bad channels on the different modules. For this reason, the average number of clusters per event was not normalized by the module acceptance, unlike on the previous plots.

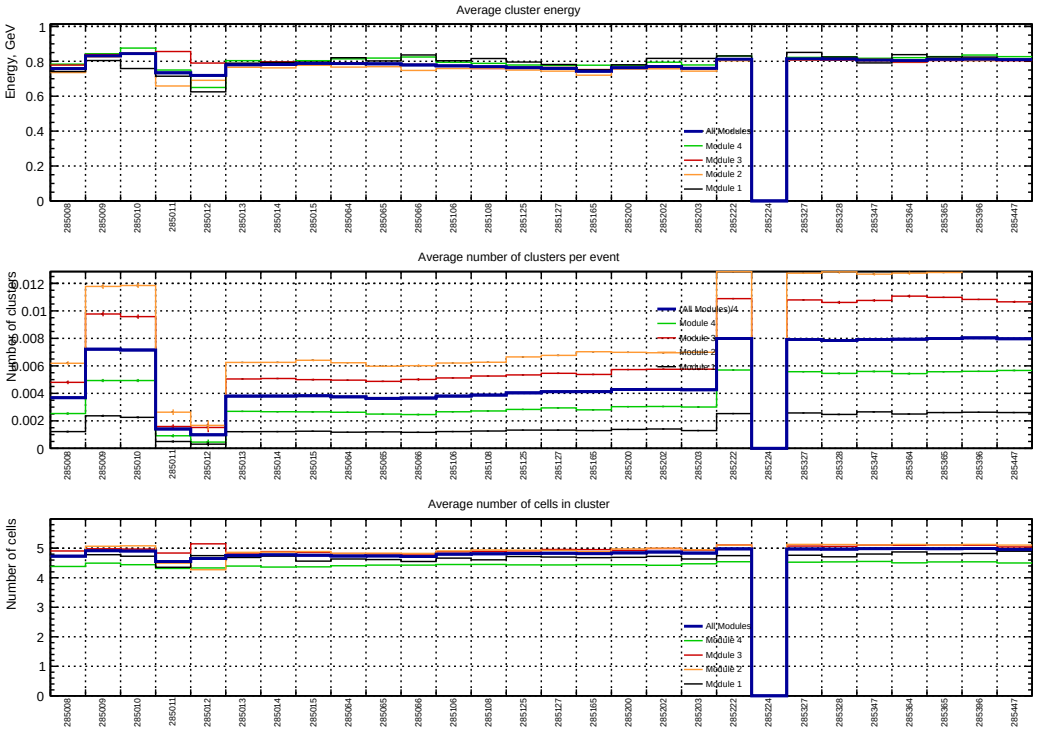

Figure B.18: Cluster averages for `LHC18b` run period.

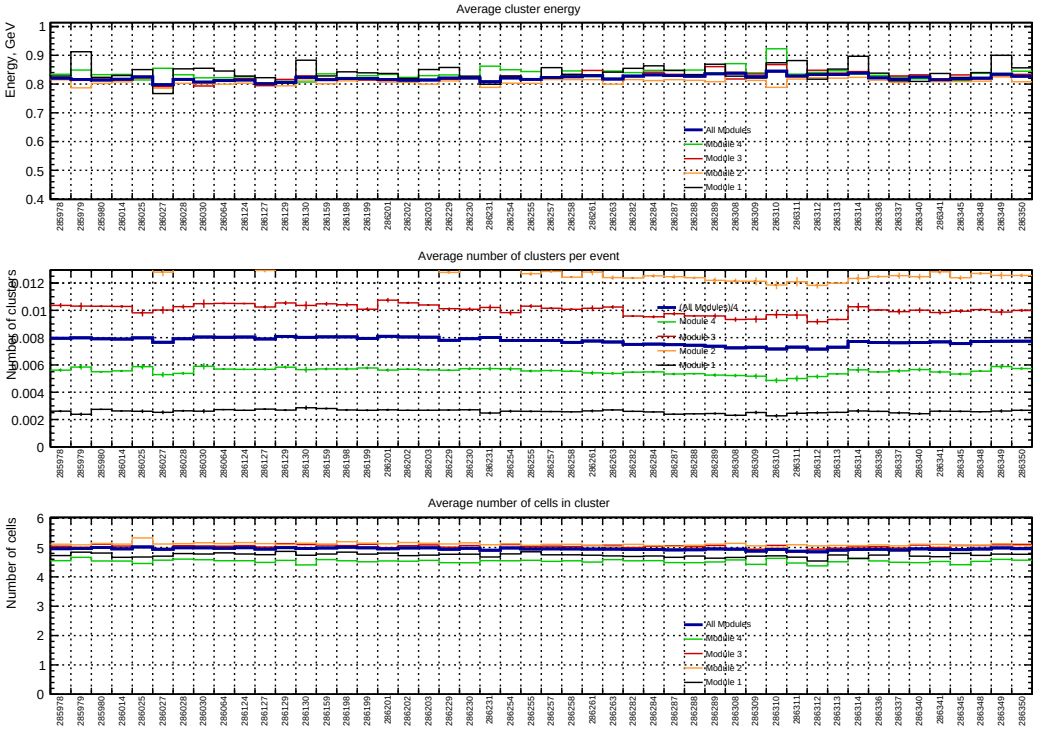

Figure B.19: Cluster averages for `LHC18d` run period.

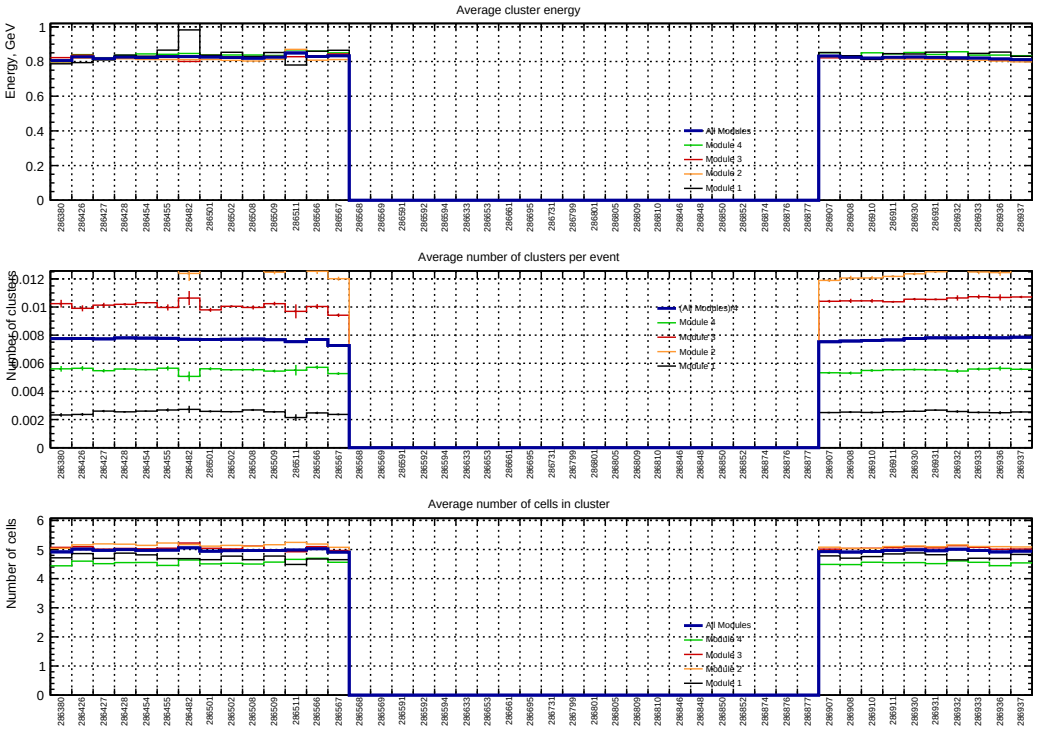

Figure B.20: Cluster averages for `LHC18e` run period. PHOS was not operational for a large period of time during that run period. This corresponds to a gap in the cluster averages.

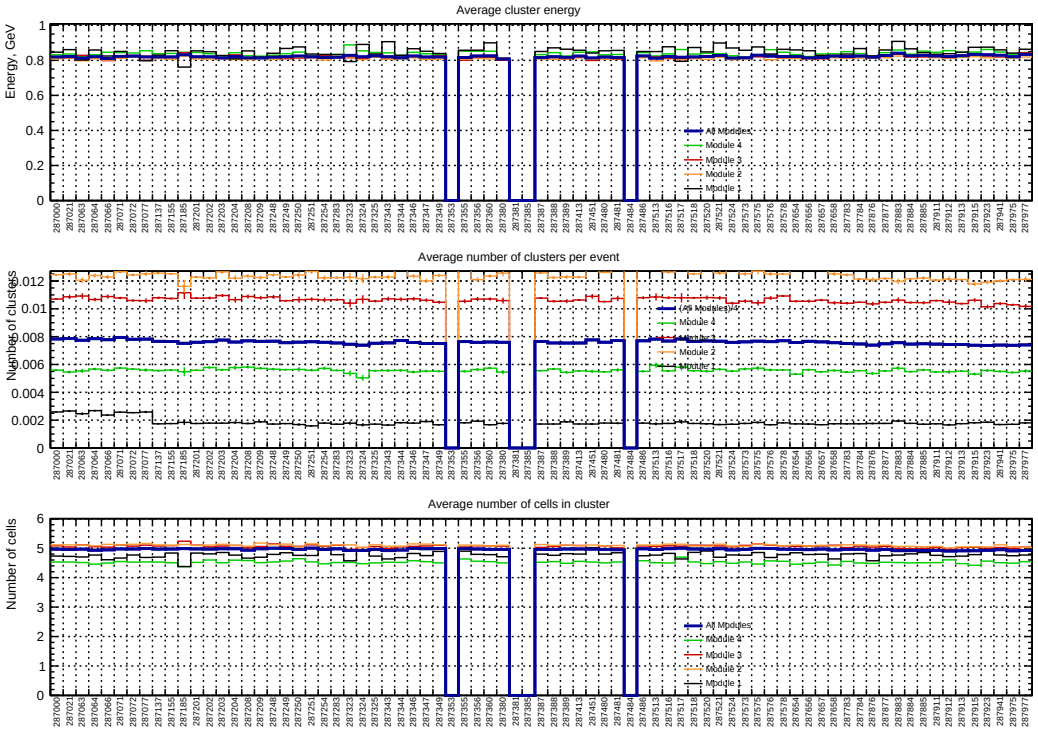

Figure B.21: Cluster averages for `LHC18f` run period.

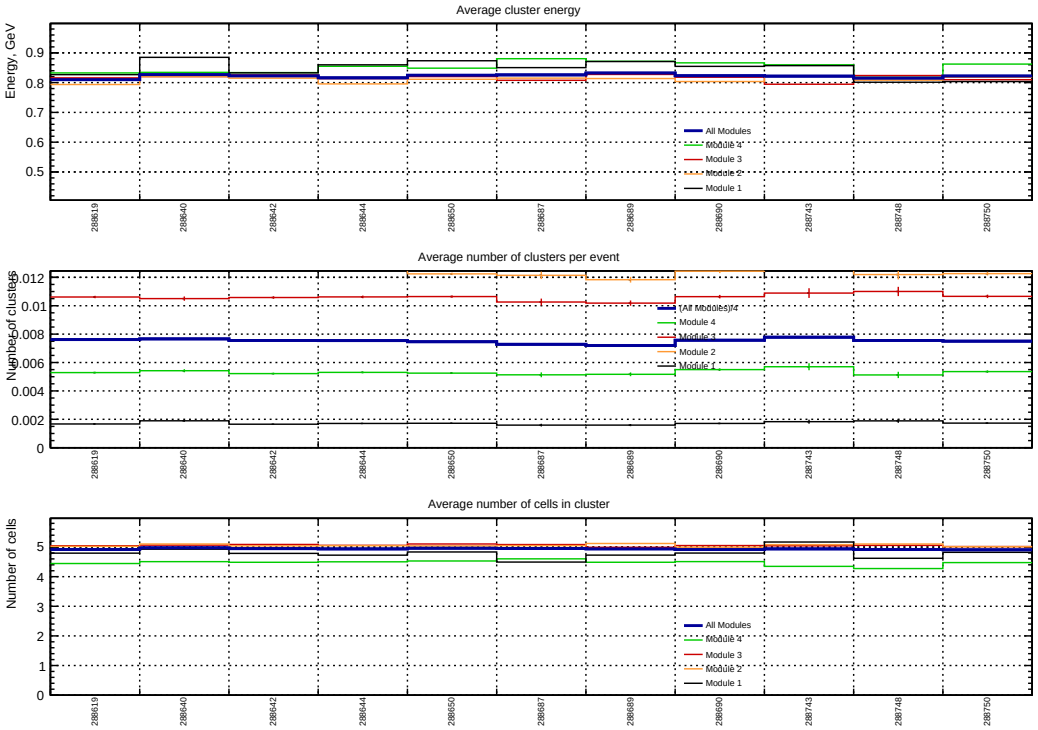

Figure B.22: Cluster averages for `LHC18g` run period.

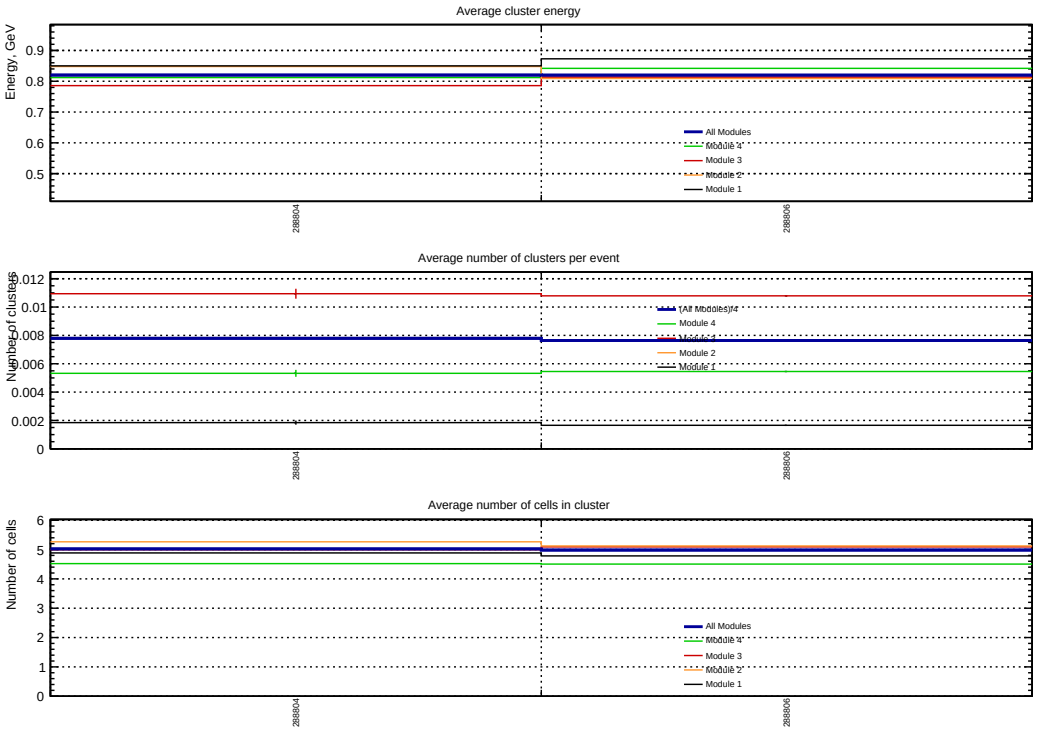

Figure B.23: Cluster averages for `LHC18h` run period. Actually, in this period are only two runs the were reconstructed.

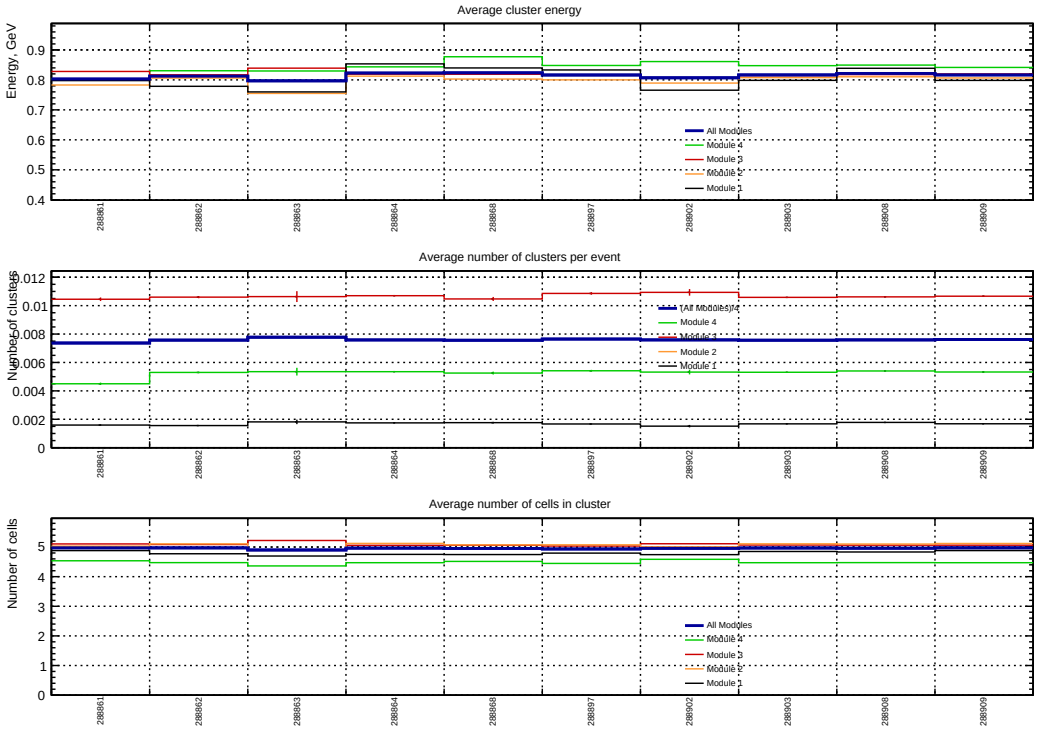

Figure B.24: Cluster averages for `LHC18i` run period.

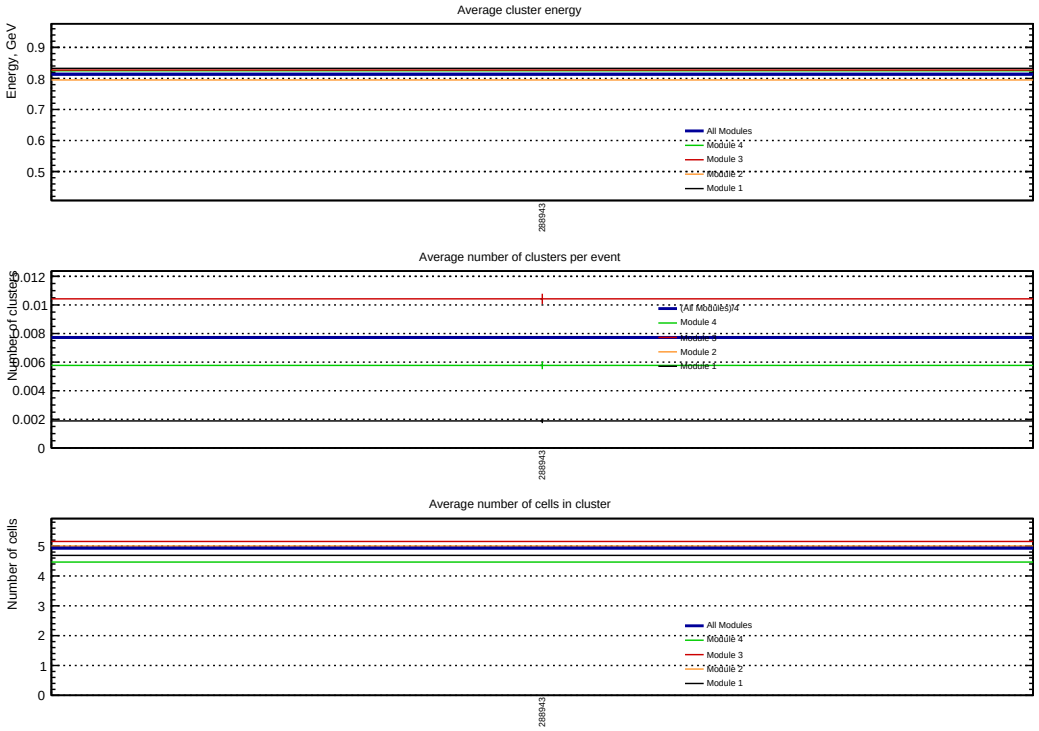

Figure B.25: Cluster averages for `LHC18j` run period. There is a single run reconstructed in this run period.

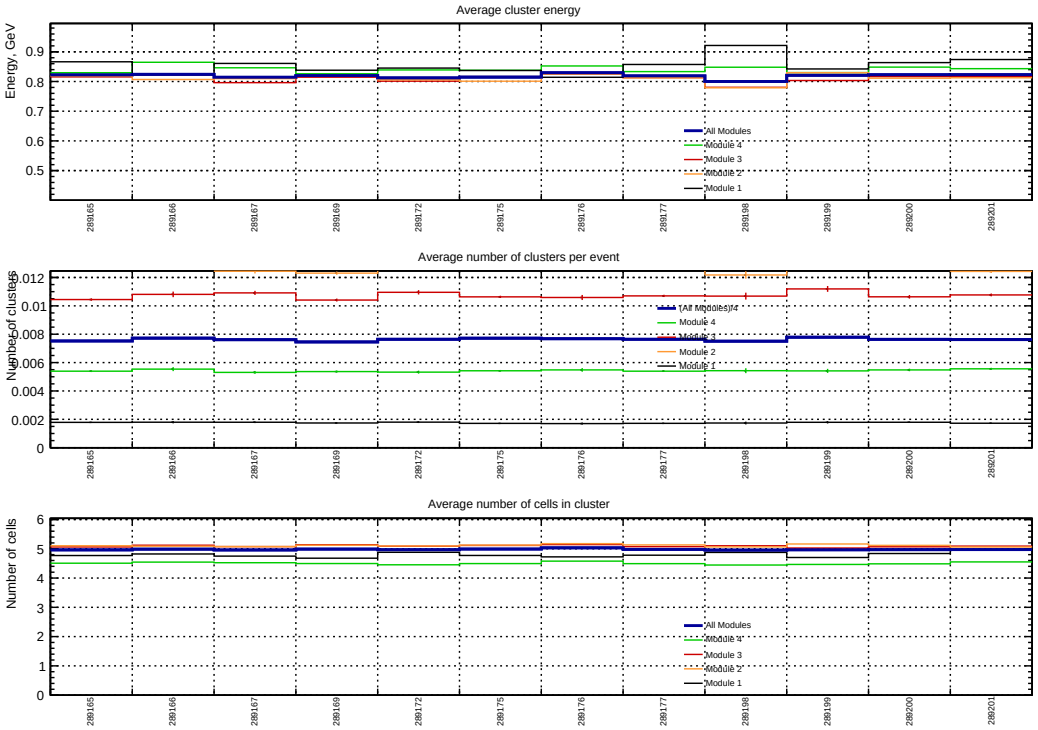

Figure B.26: Cluster averages for `LHC18k` run period.

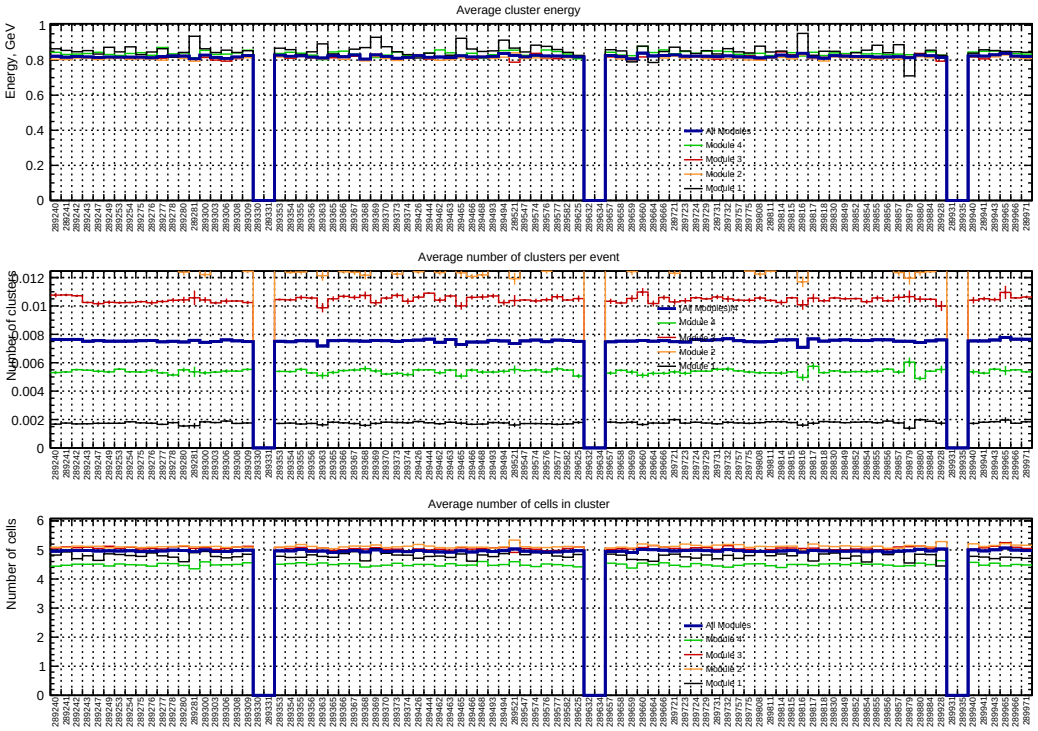

Figure B.27: Cluster averages for `LHC18l` run period.

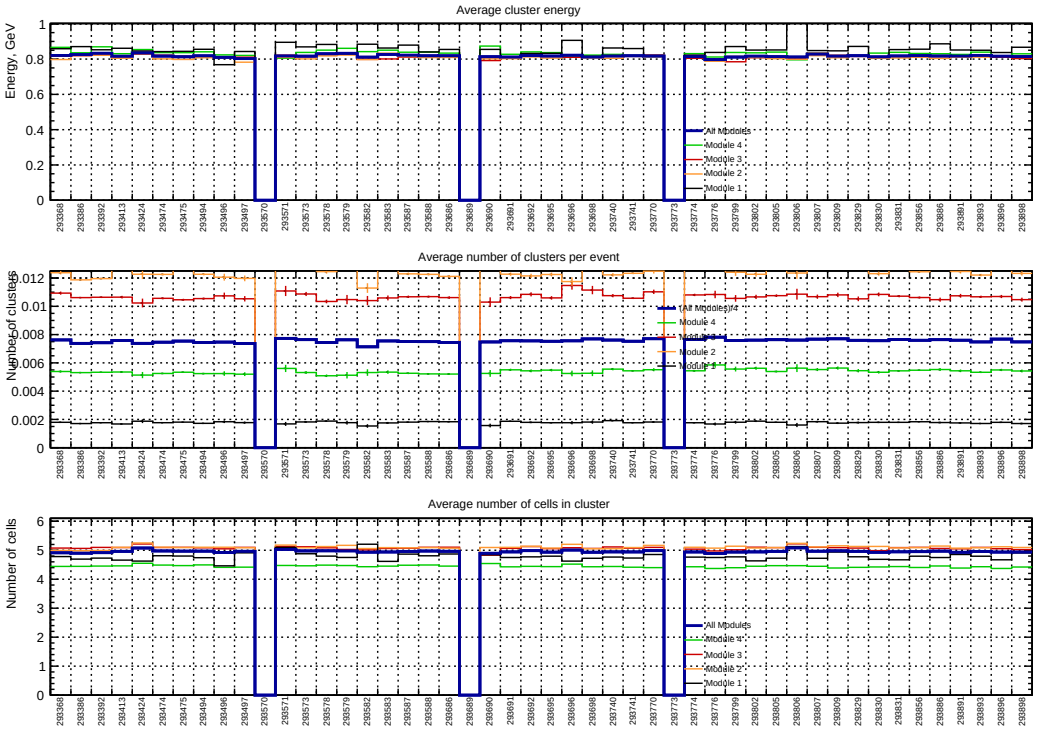

Figure B.28: Cluster averages for `LHC18o` run period.

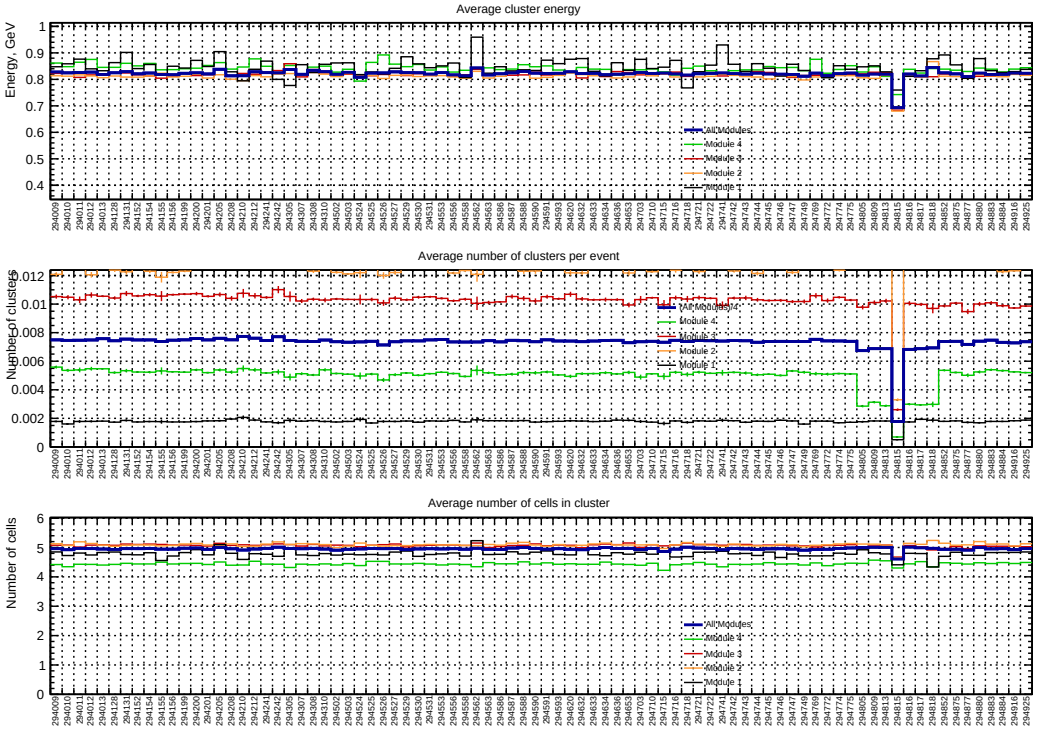

Figure B.29: Cluster averages for `LHC18p` run period.

Appendix C

Invariant mass fits of pp data at $\sqrt{s} = 13$ TeV

This appendix contains the invariant-mass distributions of two-cluster combinations reconstructed with PHOS in pp collisions at $\sqrt{s} = 13$ TeV. The data presented here were obtained by applying all the cuts described in section 3.2.1. The black points represent the invariant-mass distribution itself, while the blue ones correspond to the background estimated via mixing-event technique. The green points are the resulting signal distribution. It was fitted with the combination of Crystal Ball [107] and second-degree polynomial functions plotted with the black dashed line.

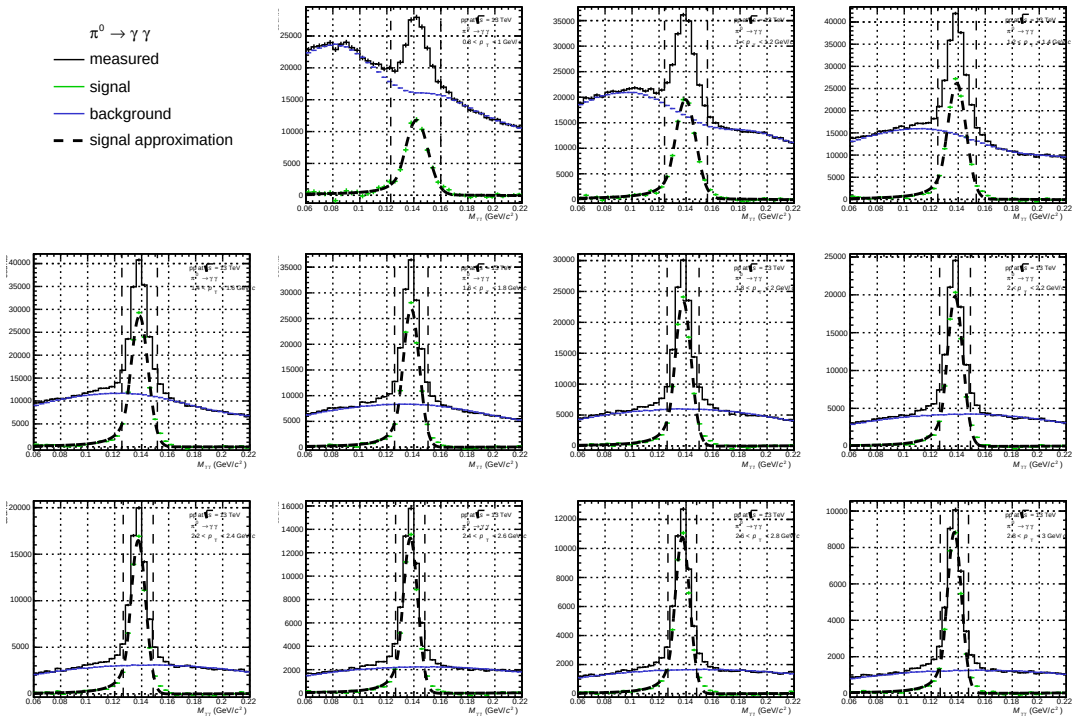

Figure C.1: Two-photon invariant-mass distribution (black points), the combinatorial background (blue points) and the π^0 signal peak (green points) fitted with the combination of second-degree polynomial and Crystal Ball function [107] (black dashed line).

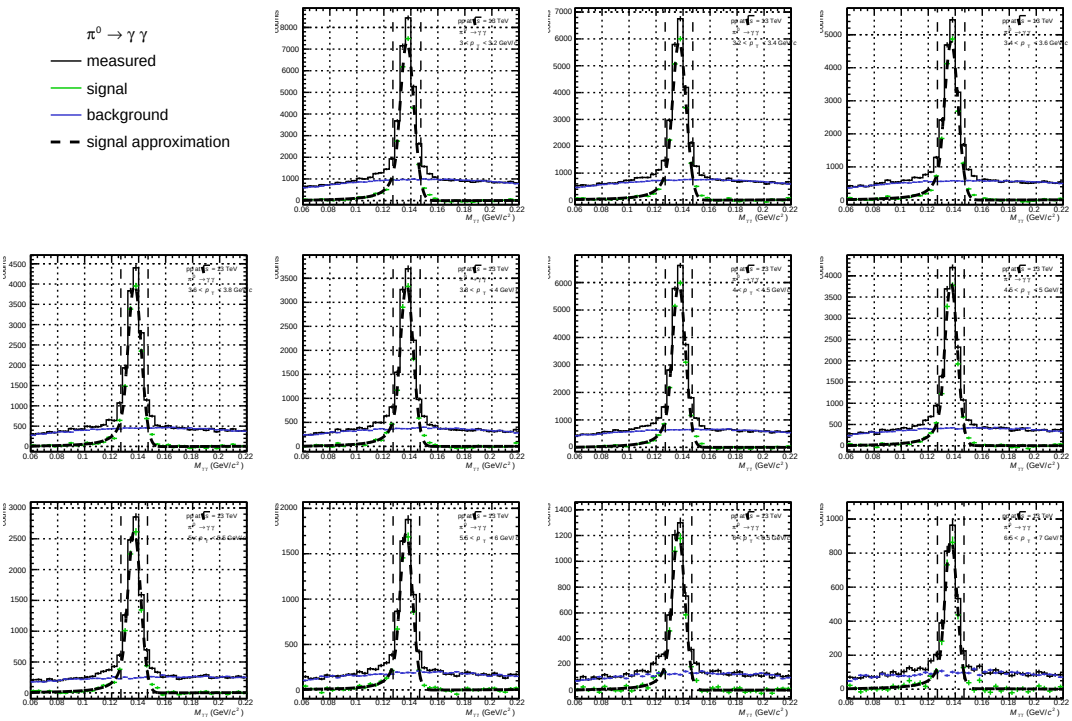

Figure C.2: Two-photon invariant-mass distribution (black line), the combinatorial background (blue line) and the π^0 signal peak (green line) fitted with the combination of second-degree polynomial and Crystal Ball function [107] (black dashed line).

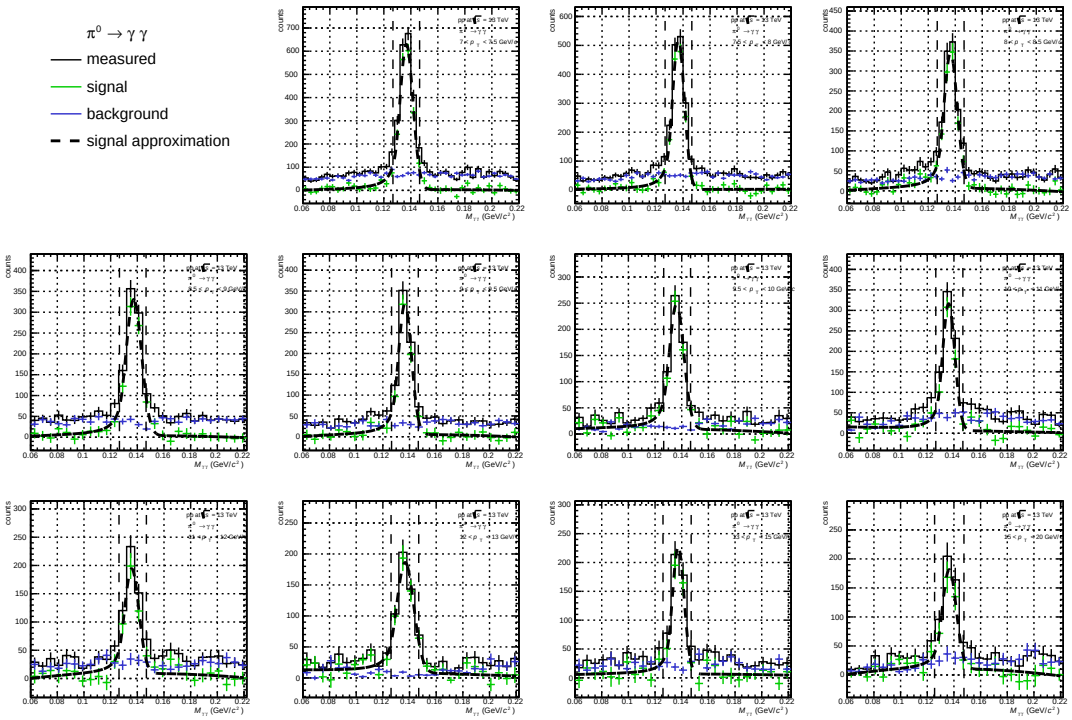

Figure C.3: Two-photon invariant-mass distribution (black line), the combinatorial background (blue line) and the π^0 signal peak (green line) fitted with the combination of second-degree polynomial and Crystal Ball function [107] (black dashed line).

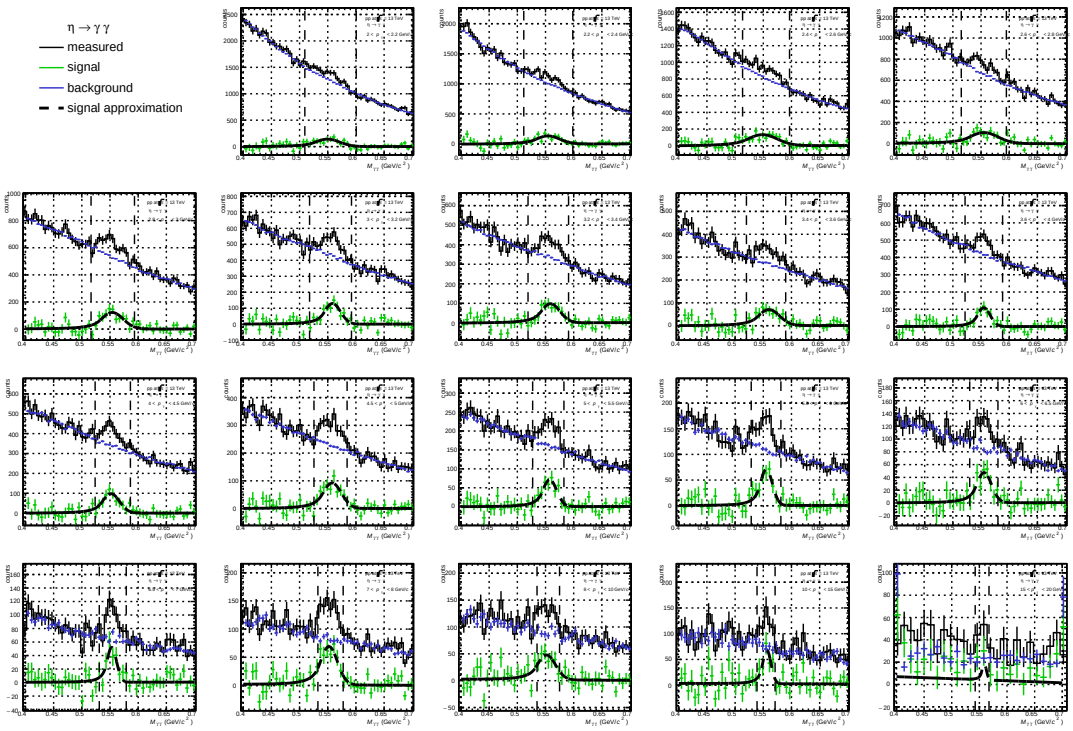

Figure C.4: Two-photon invariant-mass distribution (black line), the combinatorial background (blue line) and the η meson signal peak (green line) fitted with the combination of second-degree polynomial and Crystal Ball function [107] (black dashed line).

Appendix D

Invariant mass fits of Single Particle Monte-Carlo

This appendix contains the invariant-mass distributions of two-cluster combinations reconstructed with PHOS in single-particle Monte-Carlo simulations. They were used to calculate efficiency times acceptance $\varepsilon \cdot A$ factors. The data presented here were obtained by applying all the cuts described in section 3.2.1. The black points represent the invariant-mass distribution itself, while the blue ones correspond to the background approximated with the scond-degree polynomial. The green points are the resulting signal distribution. It was fitted with the combination of Crystal Ball [107] and second-degree polynomial functions plotted with the black dashed line.

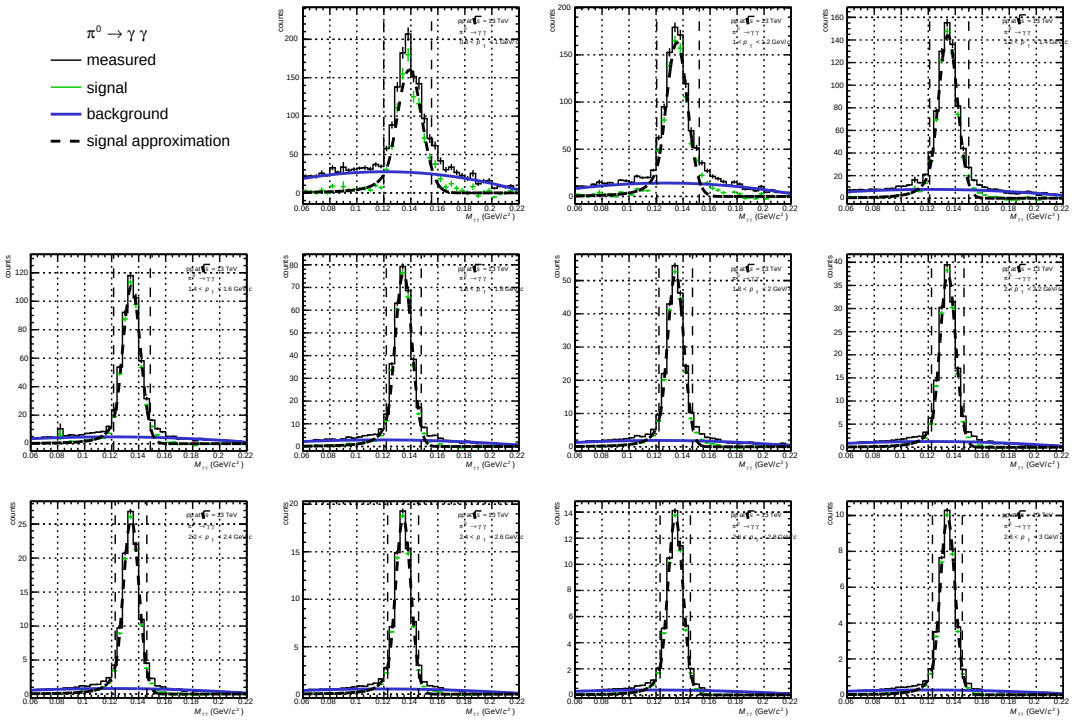

Figure D.1: Two-photon invariant-mass distribution (black points), the combinatorial background (blue line) and the π^0 signal peak (green points) fitted with the combination of second-degree polynomial and Crystal Ball function [107] (black dashed line).

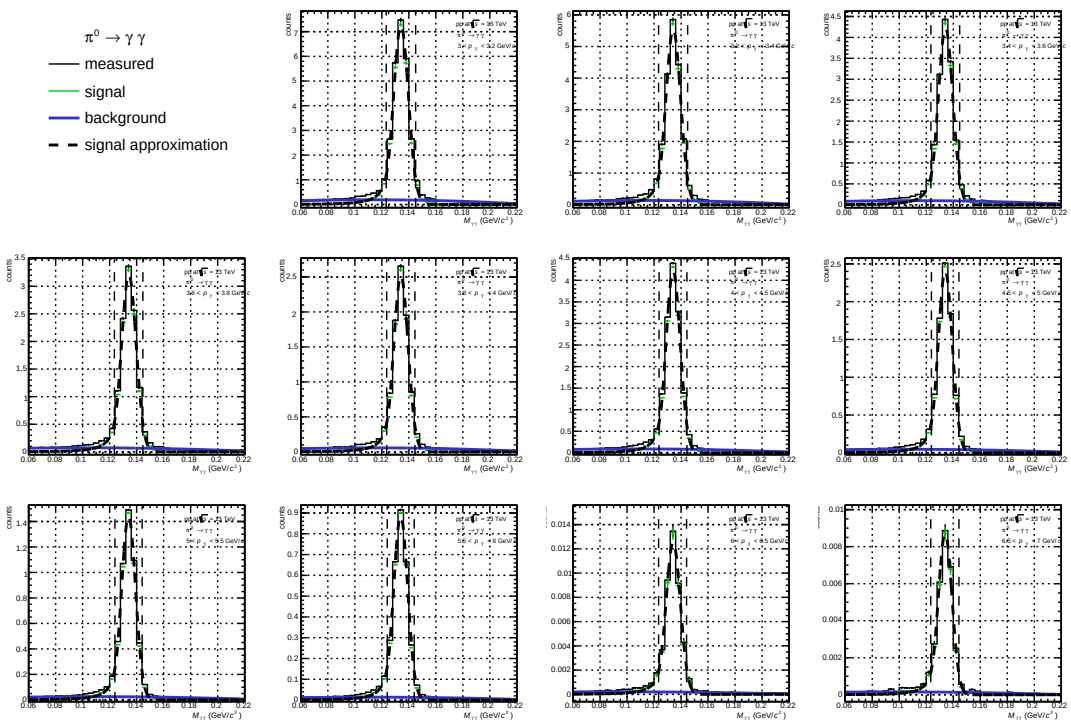

Figure D.2: Two-photon invariant-mass distribution (black points), the combinatorial background (blue line) and the π^0 signal peak (green points) fitted with the combination of second-degree polynomial and Crystal Ball function [107] (black dashed line).

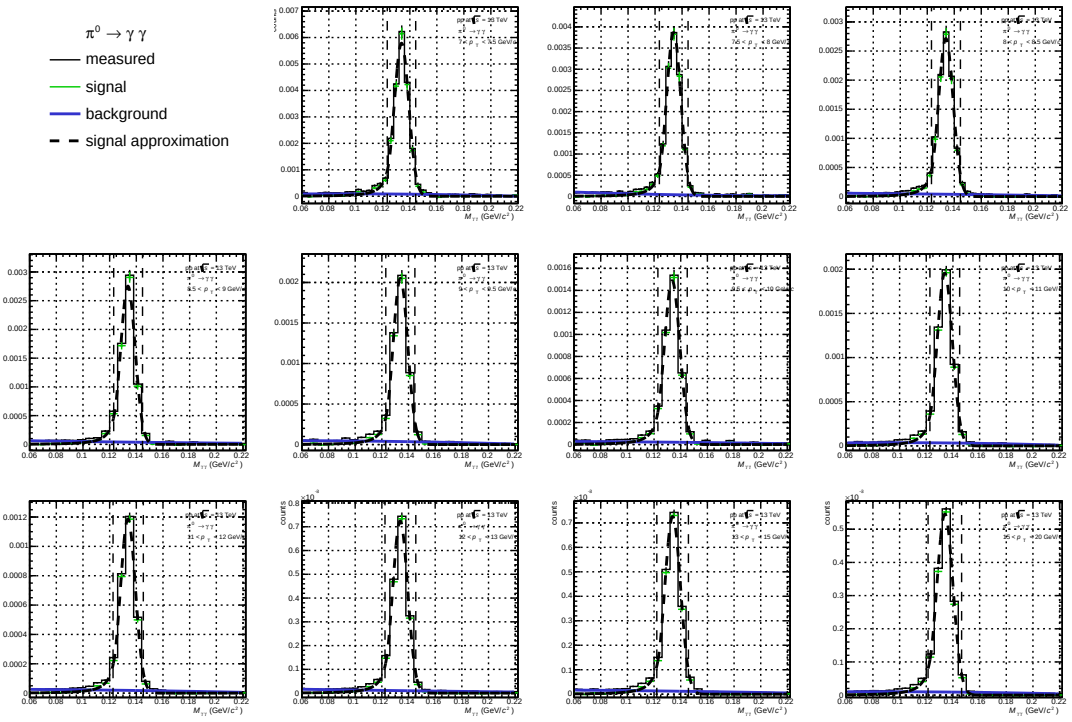

Figure D.3: Two-photon invariant-mass distribution (black points), the combinatorial background (blue line) and the π^0 signal peak (green points) fitted with the combination of second-degree polynomial and Crystal Ball function [107] (black dashed line).

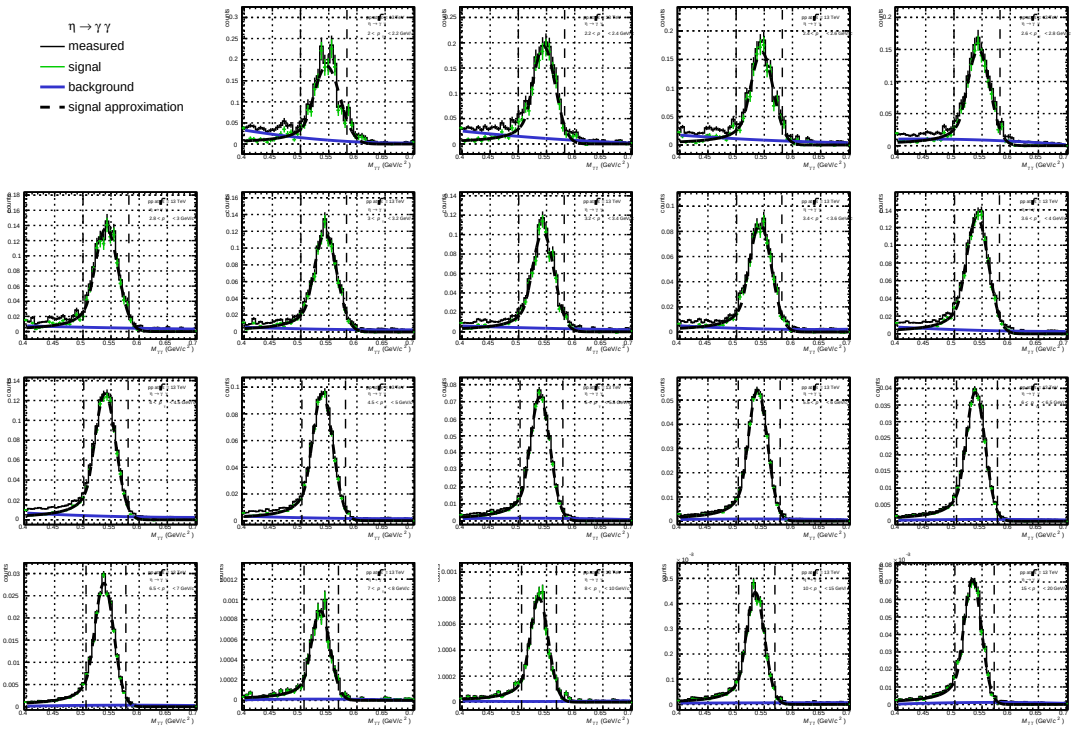

Figure D.4: Two-photon invariant-mass distribution (black points), the combinatorial background (blue line) and the η meson signal peak (green points) fitted with the combination of second-degree polynomial and Crystal Ball function [107] (black dashed line).

Bibliography

[1] **ATLAS** Collaboration, "Observation of a new particle in the search for the Standard Model Higgs boson with the ATLAS detector at the LHC", *Phys. Lett.*, **B716** (1):129, (2012).

[2] **CMS** Collaboration, "Observation of a new boson at a mass of 125 GeV with the CMS experiment at the LHC", *Phys. Lett.*, **B716** (1):3061, (2012).

[3] Masayuki Nakahata et al., "Atmospheric Neutrino Background and Pion Nuclear Effect for Kamioka Nucleon Decay Experiment", *J. Phys. Soc. Jpn.*, **55**, 3786-3805, (1986).

[4] L. Evans and P. Bryant (**CERN** Collaboration), "LHC Machine", *JINST* **3** S08001 (2008).

[5] A. Deur, S. Brodsky, G. F. de Teramond "The QCD Running Coupling", *Progress in Particle and Nuclear Physics* **90** 1 (2006).

[6] R. Bjorklund, W. E. Crandall, B. J. Moyer, H. F. York, "High Energy Photons from Proton-Nucleon Collisions", *Phys. Rev.* **77** 2 (1950) 213-218;

[7] M. Tanabashi et al. (**Particle Data Group**), "Review of Particle Physics", *Phys. Rev. D* **98** 030001 (2018).

[8] E. J. Lofgren, "Experiences with the Bevatron", United States, (1958) https://www.osti.gov/servlets/purl/877349; DOI:10.2172/877349.

[9] A. Pevsner et al., "Evidence for a Three-Pion Resonance Near 550 MeV", *Phys. Rev. Lett.* **7** (1961) 421; DOI:10.1103/PhysRevLett.7.421.

[10] C. G. Callan et al., "High-Energy Electroproduction and the Constitution of the Electric Current", *Phys. Rev. Lett.* **22**, 156, (1969).

[11] J. I. Friedman, "Deep inelastic scattering: Comparisons with the quark model", *Rev. Mod. Phys.* **63**, 597, (1991).

[12] Yu. L. Dokshitser, "Calculation of structure functions of deep-inelastic scattering and e^+e^- annihilation by perturbation theory in quantum chromodynamics", *JETP*, **46**, No. 4, p. 641, (1977).

[13] G.Altarelli et al., "Asymptotic freedom in parton language", *Nucl. Phys. B* **126**, 298, (1977).

[14] A.D. Martin, W.J. Stirling, R.S. Thorne, G. Watt, "Parton distributions for the LHC", *Eur. Phys. J C* **63** 2, 189-285, (2009).

[15] D. de Florian, R. Sassot, M. Epele, R.J. Hernández-Pinto and M. Stratmann, "Parton-to-pion fragmentation reloaded", *Phys. Rev. D* **91** 014035 (2015).

[16] D. de Florian and R. Sassot, "Nuclear parton distributions at next to leading order", *Phys. Rev. D* **69** 074028 (2004).

[17] D. de Florian, R. Sassot and M. Stratmann, "Global analysis of fragmentation functions for pions and kaons and their uncertainties", *Phys. Rev. D* **75** 114010 (2007).

[18] G. J. Donaldson et al., "Inclusive η production at large transverse momenta", *Phys. Rev. Lett.* **40** 684 (1978).

[19] S. S. Adler et al. (**PHENIX** Collaboration), "Midrapidity neutral-pion production in proton-proton collisions at $\sqrt{s} = 200$ GeV", *Phys. Rev. Lett.* **91** 241803 (2003).

[20] S. S. Adler et al. (**PHENIX** Collaboration), "Double Helicity Asymmetry in Inclusive Midrapidity π^0 Production for Polarized proton-proton Collisions at $\sqrt{s} = 200$ GeV", *Phys. Rev. Lett.* **93** 202002 (2004).

[21] S. S. Adler et al. (**PHENIX** Collaboration), "Measurement of transverse single-spin asymmetries for midrapidity production of neutral pions and charged hadrons in polarized proton-proton collisions at $\sqrt{s} = 200$ GeV", *Phys. Rev. Lett.* **95** 202001 (2005)

[22] A. Adare et al. (**PHENIX** Collaboration), "Inclusive cross section and double-helicity asymmetry for π^0 production at midrapidity in p+p collisions at $\sqrt{s} = 510$ GeV", *Phys. Rev. D* **93** 011501(R) (2016).

[23] S. S. Adler et al. (**PHENIX** Collaboration), "Absence of suppression in particle production at large transverse momentum in $\sqrt{s}_{\rm NN} = 200$ GeV $d+$Au collisions", *Phys. Rev. Lett.* **91** 072303 (2003).

[24] S. S. Adler et al. (**PHENIX** Collaboration), "Centrality dependence of π^0 and η production at large transverse momentum in $\sqrt{s}_{\rm NN} = 200$ GeV d+Au collisions", *Phys. Rev. Lett.* **98** 172302 (2007).

[25] S. S. Adler et al. (**PHENIX** Collaboration), "Suppressed π^0 production at large transverse momentum in central Au + Au Collisions at $\sqrt{s}_{\rm NN} = 200$ GeV", *Phys. Rev. Lett.* **91** 072301 (2003).

[26] S. S. Adler et al. (**PHENIX** Collaboration), "Common Suppression Pattern of η and π^0 Mesons at High Transverse Momentum in Au+Au Collisions at $\sqrt{s}_{\rm NN} = 200$ GeV", *Phys. Rev. Lett.* **96** 202301 (2006).

[27] **PHENIX** Collaboration, "Suppression Pattern of Neutral Pions at High Transverse Momentum in Au + Au Collisions at $\sqrt{s}_{\rm NN} = 200$ GeV and Constraints on Medium Transport Coefficients", *Phys. Rev. Lett.* **101** 232301 (2008).

[28] K. Adcox, et al. (**PHENIX** Collaboration), "Suppression of hadrons with large transverse momentum in central Au + Au collisions at $\sqrt{s}_{\rm NN} = 130$ GeV", *Phys. Rev. Lett.* **88** 022301 (2002).

[29] D. Kharzeev, E. Levin and L. McLerran, "Parton saturation and $N_{\rm part}$ scaling of semi-hard processes in QCD", *Phys.Lett.B* **561** 93-101, (2003).

[30] **ALICE** Collaboration, "Neutral pion and η meson production in proton-proton collisions at $\sqrt{s} = 0.9$ TeV and $\sqrt{s} = 7$ TeV", *Phys. Lett. B* **717** 162-172 (2012).

[31] **ALICE** Collaboration, "Neutral pion production at midrapidity in pp and Pb-Pb collisions at $\sqrt{s}_{\rm NN} = 2.76$ TeV", *Eur. Phys. J. C* **74** 3108 (2014).

[32] **ALICE** Collaboration, "Production of π^0 and η mesons up to high transverse momentum in pp collisions at 2.76 TeV", *Eur. Phys. J. C* **77** 339 (2017).

[33] **ALICE** Collaboration, "π^0 and η meson production in proton-proton collisions at $\sqrt{s} = 8$ TeV" *Eur. Phys. J. C* **78** 263 (2018).

[34] T. Sjöstrand, S. Ask, J.R. Christiansen, R. Corke, N. Desai, et al., "An introduction to PYTHIA 8.2", *Comput. Phys Commun.* **191** 159-177 (2015).

[35] **ALICE** Collaboration, "Neutral pion and η meson production at mid-rapidity in Pb-Pb collisions at $\sqrt{s}_{\rm NN} = 2.76$ TeV", *Phys. Rev. C* **98**, 044901 (2018).

[36] A. Bylinkin, N. S. Chernyavskaya, and A. A. Rostovtsev, "Predictions on the transverse momentum spectra for charged particle production at LHC-energies from a two component model", *Eur. Phys. J. C* **75** 166 (2015).

[37] W. Tung, H. Lai, A. Belyaev, J. Pumplin, D. Stump, and C.- P. Yuan. "Heavy Quark Mass Effects in Deep Inelastic Scattering and Global QCD Analysis", *JHEP* **02** 053 (2007).

[38] C. A. Aidala, F. Ellinghaus, R. Sassot, J. P. Seele, and M. Stratmann, "Global Analysis of Fragmentation Functions for Eta Mesons", *Phys. Rev. D* **83** 034002 (2011).

[39] B. I. Abelev et al. (**STAR** Collaboration), "Strange Particle Production in proton-proton Collisions at $\sqrt{s} = 200$ GeV", *Phys. Rev. C* **75** 064901 (2007).

[40] P. Skands, S. Carrazza, and J. Rojo, "Tuning PYTHIA 8.1: the Monash 2013 Tune", *Eur. Phys. J. C* **74** 3024 (2014).

[41] R. Corke, T. Sjötrand, "Interleaved parton showers and tuning prospects", *JHEP* **1103** 032 (2011).

[42] **ALICE** Collaboration, "Neutral pion and η meson production in p–Pb collisions at $\sqrt{s}_{\rm NN} = 5.02$ TeV", *Eur. Phys. J. C* **78**, 624 (2018).

[43] S. Roesler, R. Engel and J. Ranft, "The Monte Carlo Event Generator DPMJET-III", SLAC-PUB-8740 (2000).

[44] Chun Shen, Jean-François Paquet, Gabriel S. Denicol, Sangyong Jeon, and Charles Gale, "Collectivity and electromagnetic radiation in small systems", *Phys. Rev. C* **95** 014906 (2017).

[45] M. Gyulassy and X. N. Wang, "HIJING 1.0: A Monte Carlo Program for Parton and Particle Production in High Energy Hadronic and Nuclear Collisions", *Comput. Phys. Commun.* **83** 307 (1994).

[46] K. Werner, B. Guiot, Iu. Karpenko, and T. Pierog. "Analyzing radial flow features in p–Pb and pp collisions at several TeV by studying identified-particle production with the event generator EPOS3", *Phys. Rev. C* **89** 064903 (2014).

[47] T. Lappi, H. Mäntysaari, "Single inclusive particle production at high energy from HERA data to proton-nucleus collisions", *Phys. Rev. D* **88** 114020 (2013).

[48] B. Jäger, A. Schäfer, M. Stratmann, and W. Vogelsang, "Next-to-leading order QCD corrections to high-$p_{\rm T}$ pion production in longitudinally polarized pp collisions", *Phys. Rev. D* **67** 054005 (2003).

[49] C. Tsallis, "Possible Generalization of Boltzmann-Gibbs Statistics", *J. Statist. Phys.* **52** 479-487 (1988).

[50] A. Morreale on behalf of the **ALICE** collaboration, "Measurement of neutral mesons in pp and Pb-Pb collisions at mid-rapidity with ALICE" (QM2015 Proceedings), *Nucl. Phys. A* **956** 645-648 (2016).

[51] V. Begun, W. Florkowski and M. Rybczynski. "Explanation of hadron transverse-momentum spectra in heavy-ion collisions at $\sqrt{s}_{\rm NN} = 2.76$ TeV within a chemical nonequilibrium statistical hadronization model." *Phys. Rev. C* **90** (2014) 014906

[52] T. Pierog, Iu. Karpenko, J.M. Katzy, E. Yatsenko, K. Werner, "EPOS LHC : test of collective hadronization with LHC data", *Phys. Rev. C* **92** 034906 (2015).

[53] **ALICE** Collaboration, "Production of charged pions, kaons and protons at large transverse momenta in pp and Pb–Pb collisions at $\sqrt{s}_{\rm NN} = 2.76$ TeV", *Phys. Lett. B* **736** 196-207 (2014).

[54] M. Bourquin and J.-M. Gaillard, "A simple phenomenological description of hadron production", *Nucl. Phys. B* **114** 334-364 (1976).

[55] B Alper et al. (**British-Scandinavian** Collaboration), "The Production of Charged Particles with High Transverse Momentum in Proton-Proton Collisions at the CERN ISR", *Nucl.Phys. B* **87** 19 (1975).

[56] G. Gatoff and Cheuk-Yin Wong, "Origin of the soft $p_{\rm T}$ spectra", *Phys. Rev. D* **46** 997 (1992).

[57] J. Schaffner-Bielich, D. Kharzeev, L. McLerran, R. Venugopalan, "Scaling properties of the transverse mass spectra", talk presented at Hirschegg 2002: Ultrarelativistic Heavy-Ion Collisions (2002).

[58] R. Albrecht et al. (**WA80** Collaboration), "Production of η mesons in 200 A GeV/c S+S and S+Au reactions", *Phys.Lett. B* **361** 14-20 (1995).

[59] B. I. Abelev et al. (**STAR** Collaboration), "Strange particle production in p+p collisions at $\sqrt{s} = 200$ GeV", *Phys. Rev. C* **75** 064901 (2007).

[60] S. S. Adler et al. (**PHENIX** Collaboration), "High transverse momentum η production in p+p, d+Au and Au +Au collisions at $\sqrt{s}_{\rm NN} = 200$ GeV", *Phys. Rev. C* **75** 024909 (2007).

[61] T.Sjöstrand, P. Eden, C. Friberg, L. Lonnblad, G. Miu, S. Mrenna and E. Norrbin, ""High-energy physics event generation with PYTHIA 6.1", *Comput. Phys. Commun.* **135** 238-259 (2001).

[62] M. Aguilar-Benitez et al. (**NA27** Collaboration), "Inclusive particle production in 400 GeV/c pp interactions", *Z. Phys. C* **50** 405 (1991).

[63] K. Adcox, et al (**PHENIX** Collaboration), "Formation of dense partonic matter in relativistic nucleus-nucleus collisions at RHIC: Experimental evaluation by the PHENIX collaboration", *Nucl. Phys. A* **757** 184-283 (2005).

[64] R. Witt (**STAR** Collaboration), "Systematics and $m_{\rm T}$ Scaling", Quark Matter Poster (2004).

[65] J. D. Bjorken, "Asymptotic Sum Rules at Infinite Momentum", *Phys. Rev.* **179** 1547 (1969).

[66] S. M. Berman, J. D. Bjorken, and J. B. Kogut, "Inclusive Processes at High Transverse Momentum", *Phys. Rev. D* **4** 3388 (1971).

[67] T. Akesson et al. (**Axial Field Spectrometer** Collaboration) "Large transverse momentum particle production in $\alpha\alpha$ and pp collisions at the CERN ISR", *Nucl. Phys. B* **209** 309-320 (1982).

[68] R. Blankenbecler S. J. Brodsky J.F.Gunion, "Inclusive processes at high transverse momentum", *Physics Letters B* **42** Issue 4 (1972).

[69] R. F. Cahalan, K. A. Geer, J. B. Kogut, L. Susskind, "Asymptotic freedom and the absence of vector gluon exchange in wide angle hadronic collisions", *Phys.Rev. D* **11** 1199 (1975).

[70] B. Alper et al., "Production spectra of $\pi^{\pm}$, $K^{\pm}$, $\rho^{\pm}$ at large angles in proton proton collisions in the CERN Intersecting Storage Rings", *Nucl. Phys. B* **100** 237 (1975).

[71] C. Albajar et al. (**UA1** Collaboration), "A study of the general characteristics of proton-antiproton collisions at $\sqrt{s} = 0.2$ to 0.9 TeV", *Nucl. Phys. B* **335** 261 (1990).

[72] F. Abe et al., "Transverse-momentum distributions of charged particles produced in $p\bar{p}$ interactions at $\sqrt{s} = 630$ GeV and $\sqrt{s} = 1800$ GeV", *Phys. Rev. Lett.* **61** 1819 (1988).

[73] J. Adams et al. (**STAR** Collaboration), "Evidence from d+Au Measurements for Final-State Suppression of High-$p_{\rm T}$ Hadrons in Au +Au Collisions at RHIC", *Phys. Rev. Lett.* **91** 072304 (2003).

[74] S. S. Adler et al. (**PHENIX** Collaboration), "High-$p_{\rm T}$ charged hadron suppression in Au +Au collisions at $\sqrt{s}_{\rm NN} = 200$ GeV", *Phys. Rev. C* **69**, 034910 (2004).

[75] K.J. Eskola, V.J. Kolhinen, and P.V. Ruuskanen, "Scale evolution of nuclear parton distributions", *Phys.Lett.B* **535** 351-371 (1998).

[76] **STAR** Collaboration, "Identified hadron spectra at large transverse momentum in p+p and d+Au collisions at $\sqrt{s}_{\rm NN} = 200$ GeV", *Phys. Lett. B* **637** 161-169 (2006).

[77] S. Catani, M. Fontannaz, J. P. Guillet and E. Pilon. "Cross section of isolated prompt photons in hadron-hadron collisions", *JHEP* **0205** (2002) 028.

[78] **PHENIX** Collaboration, "Enhanced Production of Direct Photons in Au + Au Collisions at $\sqrt{s}_{\rm NN} = 200$ GeV and Implications for the Initial Temperature", *Phys. Rev. Lett.* **104** 132301 (2010).

[79] **ALICE** Collaboration, "Direct photon production in Pb-Pb collisions at $\sqrt{s}_{\rm NN} =$ 2.76 TeV", *Phys. Lett. B* **754** 235-248 (2016).

[80] **PHENIX** Collaboration, "Centrality dependence of low-momentum direct-photon production in Au + Au collisions at $\sqrt{s} = 200$ GeV", *Phys. Rev. C* **91** 064904 (2015).

[81] O. S. Bruning, "LHC Design Report Vol.1: The LHC Main Ring", CERN-2004-003-V1 (2004).

[82] O. S. Bruning, "LHC Design Report Vol.1: The LHC Infrastructure and General Services", CERN-2004-003-V2 (2004).

[83] O. S. Bruning, "LHC Design Report Vol.3: The LHC Injector Chain", CERN-2004-003- V3 (2004).

[84] L. Evans, "THE CERN LARGE HADRON COLLIDER: ACCELERATOR AND EXPERIMENTS", *JINST* **3** S08001 (2008).

[85] **ALICE** Collaboration, "The ALICE Experiment at the CERN LHC", *JINST* **3** S08002 (2008).

[86] **CMS** Collaboration, "The CMS experiment at the CERN LHC", *JINST* **3** S08004 (2008).

[87] **ATLAS** Collaboration, "The ATLAS experiment at the CERN LHC", *JINST* **3** S08003 (2008).

[88] **LHCb** Collaboration, "The LHCb experiment at the CERN LHC", *JINST* **3** S08005 (2008).

[89] **LHCf** Collaboration, "The LHCf experiment at the CERN LHC", *JINST* **3** S08006 (2008).

[90] **TOTEM** Collaboration, "The TOTEM experiment at the CERN LHC", *JINST* **3** S08007 (2008).

[91] **MoEDAL** Collaboration, "The Physics Programme Of The MoEDAL Experiment At The LHC", *C Int.J.Mod.Phys. A* **29** 1430050 (2014).

[92] **ALICE** Collaboration, "ALICE forward detectors: FMD, TO and VO: Technical Design Report", CERN-LHCC-2004-025 (2004).

[93] **ALICE** Collaboration, "ALICE Inner Tracking System (ITS): Technical Design Report", CERN-LHCC-99-012 (1999).

[94] **ALICE** Collaboration, "ALICE time projection chamber: Technical Design Report", CERN-LHCC-2000-001 (2000).

[95] **ALICE** Collaboration, "Measurement of electrons from semileptonic heavy-flavour hadron decays in pp collisions at $\sqrt{s} = 7$ TeV", *Phys.Rev. D* **86** 112007 (2012).

[96] M. Krivda et al. (**ALICE** Collaboration), "The integration of the ALICE trigger system with sub-detectors", *Nuclear Instruments and Methods in Phys. Res. A* **617**, 335 (2010).

[97] D. Evans et al. (**ALICE** Collaboration), "Alice trigger system", *10th Workshop on Electronics for LHC and Future Experiments* 10.5170/CERN-2004-010.277

[98] **ALICE** Collaboration, "Technical design report of the photon spectrometer", CERN-LHCC-99-004 (1999).

[99] M. Yu. Bogolyubsky et al., "A light-emitting diode monitoring system of the PHOS photon spectrometer in the ALICE experiment on the Large Hadron Collider", *Instrum. Exp. Tech.* **55** (2012) 11-21.

[100] P. Cortese et al. (**ALICE** Collaboration), "Technical Design Report of the Trigger Data Acquisition High-Level Trigger and Control System", CERN-LHCC-2003-062, CERN-ALICE-TDR-010 (2004).

[101] D.V. Aleksandrov et al. (**ALICE** Collaboration), "A high resolution electromagnetic calorimeter based on lead-tungstate crystals", *Nuclear Instruments and Methods in Phys. Res. A* **550** 169-184 (2005).

[102] **ALICE** Collaboration, "ALICE luminosity determination for pp collisions at $\sqrt{s} =$ 13 TeV", ALICE-PUBLIC-2016-002 (2016).

[103] S. van der Meer, "Calibration of the efective beam height in the ISR", CERN-ISR-PO-68-31 (1968).

[104] **ALICE** Collaboration, "ALICE luminosity determination for pp collisions at $\sqrt{s}$ = 5, 8 and 13 TeV", (The paper isn't published yet) `https://cds.cern.ch/record/2160174`.

[105] O. Driga, "Data quality assessment for the ALICE PHOS detector", ALICE-INT-2012-006 (ALICE internal note) (2012).

[106] C. W. Fabjan et al. (**ALICE** Collaboration), "ALICE: Physics performance report, volume II", *J. Phys. G* **32** 1295-2040 (2006).

[107] M. J. Oreglia, "A Study of the Reactions $\psi' \to \gamma\gamma\psi$", PhD thesis, SLAC, Stanford University, Stanford, California 94305, (1980).

[108] R. Brun, F. Bruyant, M. Maire, A. McPherson, and P. Zanarini, "GEANT3", CERN-DD-EE-84-1 (1987) BASE001 1–3.

[109] J. Allison et al., "Geant4 Developments and Applications", *IEEE Trans. Nucl. Sci.* **53** 1, 270-278 (2006).

[110] Pranjal Sarma (for the **ALICE** Collaboration), "Production of pions, kaons and protons as a function of charged particle multiplicity in pp collisions at $\sqrt{s} = 13$ TeV with ALICE at the LHC", Poster on "Quark Matter 2018' conference (the paper is under preparation).

[111] **ALICE** Collaboration, "Calibration of the photon spectrometer PHOS of the ALICE experiment", `JINST14P05025e` (2019).

[112] **ALICE** Collaboration, Internal Note, "Analysis of inclusive π^0 production in pp collisions at $\sqrt{s} = 900$ GeV and $\sqrt{s} = 7$ TeV measured with ALICE PHOS", `https://aliceinfo.cern.ch/Notes/node/173`.

[113] **ALICE** Collaboration, "Calibration of the photon spectrometer PHOS of the ALICE experiment", *JINST* **5** 14 (2019) P05025.

[114] D. Sekihata, "Measurement of neutral mesons and direct photons in pp and Pb-Pb collisions at $\sqrt{s}_{\rm NN} = 5.02$ TeV", PhD thesis, ALICE, Hiroshima University (2019).

[115] Tsubasa Okubo, "Study of neutral π^0 meson in $\sqrt{s}_{\rm NN} = 5.02$ TeV p+Pb collisions with PHOS detector at ALICE", PhD thesis, ALICE, Hiroshima University (2017).

[116] **ALICE** Collaboration, " Neutral pion and η meson production in p-Pb collisions at $\sqrt{s}_{\rm NN} = 5.02$ TeV" *Eur. Phys. J. C* **78** 624 (2018).

[117] P. Braun-Munzinger, K. Redlich and J. Stachel, "Particle Production in Heavy Ion Collisions", *Quark Gluon Plasma 3*, edited by R.C. Hwa and X.-N. Wang (World Scientific, Singapore, 2004), pp. 491-599.

A. Andronic, P. Braun-Munzinger and J. Stachel, "Hadron production in central nucleus-nucleus collisions at chemical freeze-out", *Nucl. Phys. A* **772**, 167 (2006).

[118] F. Becattini and G. Passaleva, "Statistical hadronization model and transverse momentum spectra of hadrons in high energy collisions", *Eur. Phys. J. C* **23**, 551 (2002).

F. Becattini, J. Manninen and M. Gazdzicki, "Energy and system size dependence of chemical freeze-out in relativistic nuclear collisions", *Phys. Rev. C* **73**, 044905 (2006).

[119] J. Cleymans, H. Oeschler, K. Redlich and S. Wheaton, "Comparison of chemical freeze-out criteria in heavy-ion collisions", *Phys. Rev. C* **73**, 034905 (2006).

S. Wheaton, J. Cleymans and M. Hauer, "THERMUS – A Thermal Model Package for ROOT", *Comput. Phys. Commun.* **180**, 84-106 (2009).

[120] M. Petran, J. Letessier, J. Rafelski and G. Torrieri, "Share with charm", *Comput. Phys. Commun.* **185**, 2056 (2014).

J. Rafelski, "Melting hadrons, boiling quarks", *Eur. Phys. J. A* **51**, 114 (2015).

[121] S. J. Brodsky and G. Farrar, "Scaling Laws at Large Transverse Momentum", *Phys. Rev. Lett.* **31**, 1153 (1973).

[122] V. Matveev, R. Muradyan, and A. Tavhelidze, "Automodellism in the large-angle elastic scattering and structure of hadrons", *Nuovo Cim. Lett.* **7**, 719 (1973).

[123] R. Hagedorn, "Statistical thermodynamics of strong interactions at high energies", *Nuovo Cim. Suppl.* **3**, 147 (1965).

[124] R. Hagedorn, "Multiplicities, p_{T} distributions and the expected hadron $\rightarrow$ quark - gluon phase transitino", *Riv. Nuovo Cim.* **6** (1983) 1-50.

[125] G. Wilk, Z. Włodarczyk, "Interpretation of the nonextensitivity parameter q in some applications of Tsallis statistics and Lévy distributions", *Phys. Rev. Lett.* **8** 2770 (2000).

[126] M. Rybczyński, Z. Włodarczyk, "Tsallis statistics approach to the transverse momentum distributions in p–p collisions", *Eur. Phys. J. C* **74** 2785 (2014).

[127] S. Grigoryan, "Using the Tsallis distribution for hadron spectra in *pp* collisions: Pions and quarkonia at $\sqrt{s} = 5 - 13000$ GeV", *Phys. Rev. D* **95** 056021 (2017).

[128] P. K. Khandai, P. Sett, P. Shukla, V. Singh, "Hadron spectra in p+p collisions at RHIC and LHC energies", *Int. J. Mod. Phys. A* **28**, 16, 1350066 (2013).

[129] A. Adare et al. (**PHENIX** Collaboration), "Measurement of neutral mesons in $p+p$ collisions at $\sqrt{s} = 200$ GeV and scaling properties of hadron production", *Phys. Rev. D* **83**, 052004 (2011).

[130] I. Sena, A. Deppman, "Systematic analysis of p_{T}-distributions in proton-proton collisions", *Eur. Phys. J. A* **49**, 17 (2013).

[131] J. Cleymans, D. Worku, "The Tsallis Distribution in Proton-Proton Collisions at $\sqrt{s} = 0.9$ TeV at the LHC", *J. Phys. G* **39**, 025006 (2012).

[132] C.-Y. Wong and G. Wilk, "Tsallis Fits to p_{T} Spectra for pp Collisions at LHC", *Acta Phys. Polon. B* **43**, 2047 (2012).

[133] C.-Y. Wong and G. Wilk, "Tsallis fits to p_{T} spectra and multiple hard scattering in *pp* collisions at the LHC", *Phys. Rev. D* **87**, 114007 (2013).

[134] C. Geich-Gimbel, "Particle production at collider energies", *Int. J.Mod. Phys. A* **4**, 1527 (1989).

[135] Z. Koba, H.B. Nielsen, P. Olesen, "Scaling of multiplicity distributions in high energy hadron collisions", *Nucl. Phys. B* **40** 319 (1972).

[136] J. F. Grosse-Oetringhaus, K. Reygers, "Charged-particle multiplicity in proton–proton collisions", *J. Phys G* **37** 083001 (2010).

[137] O. V. Utyuzh, G. Wilk, Z. Włodarczyk, "Multiparticle production processes from the Information Theory point of view", *Acta Phys. Hung. A* **25** 65-81 (2006).

[138] G. Wilk, Z. Włodarczyk, W. Wolak, "Composition of fluctuations of different observables", *Acta Physica Polonica B* **42** 1277 (2011).

[139] G. Wilk, Z. Włodarczyk, "Consequences of temperature fluctuations in observables measured in high energy collisions", *Eur. Phys. J. A* **48**, 161 (2012).

[140] G. Wilk, Z. Włodarczyk, "The imprints of superstatistics in multiparticle production processes", *Central. Eur. J. Phys.* **10**, 568 (2012).

[141] A. A. Bylinkin and A. A. Rostovtsev, "Parametrization of the shape of hadron-production spectra in high-energy particle interactions", *Phys. Atom. Nucl.* **75** 999-1005 (2012).

[142] A. A. Bylinkin, A. A. Rostovtsev, "An analysis of charged particles spectra in events with different charged multiplicity", Institute for Theoretical and Experimental Physics, ITEP, Moscow, Russia (2012). [arXiv:1205.4432v1 [nucl-th]]

[143] V. A. Abramovsky, V. N. Gribov, O. V. Kancheli, "Character of Inclusive Spectra and Fluctuations Produced in Inelastic Processes by Multi - Pomeron Exchange", *Sov. J. Nucl. Phys.* **18** 308-317 (1974).

[144] **ALICE** Collaboration, "Supplemental figures: π^0 and η meson production in proton-proton collisions at $\sqrt{s} = 8$ TeV", ALICE-PUBLIC-2017-009 (2017).

[145] P. Aurenche, M. Fontannaz, J.-Ph. Guillet, B. A. Kniehl, M. Werlen, "Large-p_{T} Inclusive π^0 Cross Sections and Next-to-Leading-Order QCD Predictions", *Eur. Phys. J. C* **13** 347-355 (2000).

[146] H. L. Lai et al. (**CTEQ** Collaboration), "Improved parton distributions from global analysis of recent deep inelastic scattering and inclusive jet data", *Phys. Rev. D* **55** 1280 (1997).

[147] H. L. Lai et al. (**CTEQ** Collaboration), "Global QCD Analysis of Parton Structure of the Nucleon: CTEQ5 Parton Distributions", *Eur.Phys.J C* **12** 375-392 (2000).

[148] L. Bourhis, M. Fontannaz, J.-Ph. Guillet, M. Werlen, "Next-to-leading order determination of fragmentation functions" *Eur. Phys. J. C* **19** 89 (2001).

[149] C. Kourkoumelis et al. (**R806** Collaboration), "Inclusive π^0 production at very large p_{T} at the ISR", *Phys. Lett. B* **84** 271-276 (1979).

[150] D.d'Enterria, "Relevance of baseline hard proton-proton spectra for high-energy nucleus-nucleus physics", *J.Phys. G* **31** 491-512 (2005).

[151] M. Bonesini et al. (**WA70** Collaboration), "High transverse momentum η production in π^-p, π^+p and pp interactions at 280 GeV/c", *Z. Phys. C* **42** 527 (1989).

[152] J. Antille et al. (**UA6** Collaboration), "A measurement of the inclusive π^0 and η production cross sections at high p_{T} in p$\bar{\mathrm{p}}$ and pp collisions at $\sqrt{s} = 24.3$ GeV", *Phys. Lett. B* **194** 568 (1987).

[153] E. Amaldi et al., "Inclusive η production in pp collision At ISR Energies", *Nucl. Phys. B* **158** 1 (1979).

[154] C. Kourkoumelis et al. (**AFS** Collaboration), "Inclusive π^0 production at very large $p_{\rm T}$ at the ISR", *Phys. Lett. B* **84**, 271 (1979); and C. Kourkoumelis et al., "Inclusive η production at high $p_{\rm T}$ at the ISR", *Phys. Lett. B* **84**, 277 (1979).

[155] L. Apanasevich *et al.* (**Fermilab E706** Collaboration), "Production of π^0 and η mesons at large transverse momenta in pp and pBe interactions at 530 GeV/c and 800 GeV/c", *Phys. Rev. D* **68** 052001 (2003).

[156] T. Akesson et al. (**AFS** Collaboration), "A comparison of direct photon, π^0, and η production in p$\bar{\rm p}$ and pp interactions at the CERN ISR", *Phys. Lett. B* **158** 282 (1985).

[157] T. Akesson et al. (**AFS** Collaboration), "Inclusive η production at low transverse momentum in 63 GeV pp collisions at the CERN ISR", *Phys. Lett. B* **178** 447 (1986).

[158] T. Akesson et al. (**AFS** Collaboration), "Production of π^0 and η at 11° in pp collisions at $\sqrt{s} = 63$ GeV", *Z. Phys. C* **18** 5 (1983).

[159] M. Banner et al. (**UA2** Collaboration), "Inclusive particle production in the transverse momentum range between 0.25 and 40 GeV/c at the CERN Sp$\bar{\rm p}$S collider", *Z. Phys. C* **27** 329 (1985).

[160] F. Abe et al. (**CDF** Collaboration), "Prompt photon cross-section measurement in p$\bar{\rm p}$ collisions at $\sqrt{s} = 1.8$ TeV", *Phys. Rev. D* **48** 2998 (1993).

[161] A. Adare et al. (**PHENIX** Collaboration), "Inclusive cross section and double helicity asymmetry for π^0 production in pp collisions at $\sqrt{s} = 62.4$ GeV", *Phys. Rev. D* **79** 012003 (2009).

[162] F. Arleo, S. J. Brodsky, D. S. Hwang, A. M. Sickles "Higher-Twist Dynamics in Large Transverse Momentum Hadron Production", *Phys. Rev. Lett.* **105**, 062002 (2010).